Modeling the Evolution of Galaxy Properties across Cosmic Time with Numerical Simulations

Dissertation Advisor: Professor Lars Hernquist Paul A. Torrey

Modeling the Evolution of Galaxy Properties across Cosmic Time with Numerical Simulations

Abstract

We present a series of numerical galaxy formation studies which apply new numerical methods to produce increasingly realistic galaxy formation models. We first investigate the metallicity evolution of a large set of idealized hydrodynamical galaxy merger simulations of colliding galaxies. We find that inflows of metal–poor interstellar gas triggered by galaxy tidal interactions can account for the systematically lower central oxygen abundances observed in local interacting galaxies. We show the central metallicity evolution during merger events is determined by a competition between the inflow of low–metallicity gas and enrichment from star formation. We find a time-averaged depression in the galactic nuclear metallicity of ~ 0.07 dex for gas–poor disk–disk interactions, which explains the observed close pair mass-metallicity and separation-metallicity relationships.

We then pioneer the impact of a novel hydro solver in our understanding of galaxy gas disk assembly by comparing the structural properties of galaxies formed in cosmological simulations using the smoothed particle hydrodynamics (SPH) code GADGET with those using the moving-mesh code AREPO. We find that the cold gas disks formed using the moving mesh approach have systematically larger disk scale lengths and higher specific angular momenta than their GADGET counterparts across a wide range in halo masses. We articulate the numerical origins of these differences, and

discuss the impact on large body of galaxy formation literature.

We explore the performance of a recently implemented feedback model in AREPO which includes primordial and metal line radiative cooling with self-shielding corrections; stellar evolution with associated mass loss and chemical enrichment; feedback by stellar winds; black hole seeding, growth and merging; and AGN quasar- and radio-mode heating with a phenomenological prescription for AGN electro-magnetic feedback. We demonstrate that our feedback scheme is capable of producing galaxy populations that broadly reproduce the shape of the observed galaxy stellar mass function extending from redshift $z = 0$ to $z = 3$.

Finally, we present a catalog of mock galaxy images based on AREPO full-feedback large-volume cosmological simulations. The resulting mock image catalog is the largest mock galaxy image catalog based directly on hydrodynamical simulations produced to-date. From the catalog it possible to produce color images, perform SED fitting, classify morphology, determine galaxy structural properties, and consider impacts of galaxy viewing angle. Using the images, we explain systematic errors that can result from estimating stellar mass based on a limited set of broadband photometric data.

Contents

Acknowledgments

Embarking on a career in research I could not have asked for better colleagues, mentors, and friends than those that I have found at Harvard. Over the past six years I have grown substantially as a researcher and as a person and I'm most grateful to the folks that have made it possible. Trying to summarize all of the support I've received is not only a difficult task, it is a humbling one. I'm so grateful to all who have helped guide me through graduate school and stood by my side as I took on this very challenging experience, even those who are not mentioned in this brief acknowledgements section.

My thanks goes out first to my advisor, Lars Hernquist, who has been the single biggest reason for my successful venture in graduate school. Lars provided me with scientific guidance, introduced me to members of the field, allowed me to pursue research topics independently, supported my travel, always responded to emails promptly, and regularly managed to find time to meet with me face-to-face. Lars' advising style was an ideal fit for my researching style, and I could not have asked for a better advisor. I feel comfortable leaving graduate school and beginning research as a postdoc because of the research skills that I have developed under Lars' supervision.

I owe substantial gratitude to Mark Vogelsberger and T.J. Cox, both of whom provided hands-on guidance on my research. They taught me the ropes of developing, running, and analyzing numerical simulations. Without their participation and substantial time commitment, the work presented in this thesis would not have been possible. Not only have Mark and T.J. been professional mentors, but they have also become good friends in the process.

In my early career, I've been lucky enough to have helpful guidance provided by outside scientific and professional mentors. Notably, Lisa Kewley, Sara Ellison, and Dave Patton have all closely collaborated on projects that are either included in or closely related to the work presented in this thesis. As observers, they helped give specific and well motivated direction to some of my theoretical studies. Additionally, Arjun Dey, Rob Simcoe, and Chung-Pei Ma all deserve my sincere thanks for providing me with professional guidance through advice regarding the job market, resume development, research project selection, and talk feedback. Through interactions with Chung-Pei and Arjun, I've learned a lot about advising students which I know will serve me well in the future.

I am ever indebted to Jean Collins, Donna Adams, Peg Herlihy, Robb Scholten, Peg Hedstrom, and Nina Zonnevylle for their assistance throughout my time at the CfA. They run the Department of Astronomy and the ITC so smoothly, and have always helped me out with any and all logistical/administrative issue that I've come across with a smile on their face.

During my time at the CfA, I enjoyed the company of a wide range of talented graduate students and post-docs. Thanks to that great network, I soaked up a lot of information about a wide range of science topics, learned by example about the traits that make up a good scientist, and benefited from the ever flowing waterfall of wisdom. In particular, I wanted to acknowledge the graduate students and post-docs who overlapped as members of Lars' group – Greg Snyder, Dylan Nelson, Diego Munoz, Chris Hayward, Laura Blecha, Gurtina Besla, Joshua Suresh, Vicente Rodriguez-Gomez, Claude-Andre Faucher-Giguere and Stephanie Bush. I also wanted to thank my officemates: Bob Penna and Wen-fai Fong. Thanks for putting up with me.

Outside of astronomy, I've had a wonderful set of friends that have made the past six years in Boston very special. Through the roller coaster that is graduate school, I've been able to rely on my friends to keep me in a continuously positive and happy mindset.

And, of course, I would like to give my deepest thanks to my family. Without your endless support, I would not have ever thought of starting – let alone finishing – a Harvard Ph.D. There are countless events in my life that I can identify that have brought me to this point – most of which my family facilitated. Even today, you continue to support me with visits to Cambridge, care packages on holidays, and regular phone calls. But looking back, I would not have done so well in high school, gone to such a great college, started doing research, and ended up at Harvard without the years of time and attention, positive role modeling, and endless encouragement that you guys gave me growing up. I am the person I am today because of you. And, while I don't expect you to understand all of the research presented in this thesis, I do hope you know that none of it would have been possible with you.

Chapter 1

Introduction

> "Begin at the beginning," the King said very gravely, "and go on till you come to the end: then stop."
>
> — Lewis Carroll, Alice in Wonderland

1.1 Background and General Motivation

Cosmological simulations are the largest scale simulations run in any of the physical sciences. A central goal of these simulations is to assemble a self-consistent and detailed understanding of how the universe evolved from the nearly homogenous matter distribution observed soon after the big bang, to the beautiful and highly complex distribution of galaxies seen in the local universe. This is achieved by generating initial conditions that mimic the physical state of the Universe at some early time and evolving them forward while modeling the physical process (e.g., gravity and hydrodynamics) that drive galaxy formation. Such an approach has the potential the yield a predictive

theory of galaxy formation, where simulations can make clear statements about the expected buildup of stars in galaxies, the enrichment or gas in and around galaxies, or the evolution of galactic morphological classes. Due to advances in available computational power, numerical techniques, and precision cosmology, we have recently come into a strong position to assemble some of the most detailed and physically valid models of galaxy formation ever produced.

The past decade has ushered in the era of precision cosmology where we have a remarkably accurate and precise understanding of the initial conditions for our Universe. Roughly a decade ago the first results of the Wilkinson Microwave Anisotropy Probe (WMAP) were published, which revealed the physical state of the Universe just a few hundred thousand years after the big-bang (Spergel et al. 2003). While modest modifications to the derived cosmological parameters will be made over time by increasingly advanced instruments (e.g., PLANK; Planck Collaboration et al. 2013), a relatively clear consensus picture for physical state of the Universe just after recombination has now emerged. The observed temperature fluctuations in the Cosmic Microwave Background (CMB) can be used to directly reconstruct the scale and magnitude of density fluctuations in the matter distribution in the early Universe – allowing initial conditions to be constructed for cosmological simulations. Coupling precision cosmology measurements with robust numerical gravity solvers has driven the emergence of a coherent theoretical picture for the formation of dark matter haloes – the host sites of galaxy formation (e.g., Springel et al. 2005c; Boylan-Kolchin et al. 2009; Klypin et al. 2011).

While our understanding of dark matter halo assembly if fairly robust, substantial uncertainty still surrounds the evolution of the luminous components of galaxies (i.e. gas

and stars) owing to additional complexities associated with baryonic physics. The most basic and under-appreciated of these uncertainties is in the discretization scheme used on the hydrodynamic equations of motion. It is now well established that some methods for solving the hydrodynamic equations of motion commonly adopted in numerical simulations have very serious inaccuracies associated with resolving instabilities or fluid phase boundaries (e.g., Agertz et al. 2007; Sijacki et al. 2012). While there are a number of idealized code comparison studies, limited studies have been carried out to translate the impact of hydro solver inaccuracies on the formation of simulated galaxies. The main barrier to performing such a seemingly important study is that hydro solvers can typically only be compared between fundamentally different simulation codes, where much more than the hydro solver is varied (e.g., the time stepping scheme, the form of the initial conditions, gas cooling methods, gravity solver, etc.). While one can identify differences in the results between methods (e.g., Frenk et al. 1999), unambiguously pinning down the root cause of these differences has been an elusive goal. As a result, the full extent to which known inaccuracies in existing and commonly used hydro solvers impact galaxy formation models has remained poorly known. Using a pair of codes that remain nearly identical with the exception of their hydrodynamic solvers, we are now in a position to make definitive statements about the role that hydrodynamic processes play in galaxy assembly and cosmological simulations.

Beyond hydrodynamic methods, galaxy formation models rely upon a wide range of uncertain physical processes (e.g., radiative cooling of gas, formation of stars, gas heating from supernovae, energetic feedback effects of supermassive black holes, etc.) to form realistic galaxy populations. Simulations of individual galaxies have demonstrated that the implementation details of these processes – especially those related to feedback

– will impact the resulting galaxy mass and morphological evolution (e.g., Governato et al. 2007; Agertz et al. 2011; Guedes et al. 2011; Scannapieco et al. 2012). It has also been shown that the formation history (including, e.g., the accretion or merger history) impacts the resulting galaxy stellar mass and morphological evolution (e.g., Marinacci et al. 2014). It is therefore difficult to disentangle the influence of uncertain feedback processes versus galaxy assembly history when only a small set of systems are studied. In principle, we can remove this degeneracy by applying a uniform and comprehensive physical model to a large ensemble of galaxies in full-volume (as opposed to zoom-in) cosmological simulations. However, very few full-volume cosmological simulations that contain both a trustworthy hydrodynamic solver and comprehensive feedback model have ever been carried out (let along run down to redshift $z = 0$). This limits the model predictions that can be made based on previous generations of galaxy formation simulations, which we are now in a position to correct.

A final level of uncertainty surrounds the comparison of galaxy formation models against observations. Comprehensive galaxy formation models can aid in the interpretation of extragalactic observations. However, forging an even-handed link between simulated and observed galaxy populations is difficult because even the most basic of physical quantities (e.g., galaxy stellar mass) have substantial uncertainties associated with their observational determination (e.g., Conroy et al. 2009). Bridging the gap to make modern galaxy formation models widely accessible in a form that is directly comparable to observations can add value to existing and on-going extragalactic observational campaigns, while identifying unambiguously success and shortcomings of the models. Building upon the recent advancements to hydrodynamic methods and galaxy formation feedback modeling, we are now in a position to translate our seemingly

realistic simulated galaxy populations into mock observations for direct comparison against real data.

In this thesis, we make contributions to all of the previously discussed galaxy formation model uncertainties. We do this by employing simulations as numerical experiments where we can control the properties of the adopted hydrodynamical solver or modify the included list of physical processes. We run simulation to observe the resulting impact on the galaxy population to learn where and how model components influence galaxy assembly. We then translate the simulation results into mock images in a publicly accessible database, which has the potential to act as a powerful new tool available to observers to interpret extragalactic data.

Two types of numerical experiments are presented in this thesis: idealized merger simulations and full-volume cosmological simulations. The idealized merger simulations have the advantage that we can systematically control many aspects of the galaxy initial conditions (e.g., bulge-to-disk ratios, disk scale lengths, etc.) allowing us to understand in detail how all aspects of a galaxy's properties and merger configuration impact the system's evolution. However, the merger simulations lack proper cosmological context and will therefore not capture, e.g., late time accretion of intergalactic medium (IGM) gas after the merger is complete. At the other extreme, cosmological simulations allow us to capture the proper cosmological context of galaxy formation, but with substantially less flexibility. Galaxy properties (e.g., bulge-to-disk ratios, disk scale lengths, etc.) self-consistently evolve as model predictions, but not necessarily in a way that is consistent with observed galaxy populations. In full-volume cosmological simulations our typical approach is to modify the input physics (e.g., the strength or speed of star formation driven winds) and observe the resulting impact on simulated galaxy

populations. We start this thesis work by using targeted merger simulations to address the role of mergers in driving galactic gas-phase metallicity evolution and move on to full volume cosmological simulations to place our galaxy formation numerical experiments into a more complete cosmological picture.

1.2 Galactic Heavy Element Distribution

Heavy elements – which are produced in stars and returned to the interstellar medium (ISM) at late states in stellar evolution – are observed within the dense star forming ISM in galaxies, in the circumgalactic medium (CGM), and in the diffuse IGM. The distribution of heavy elements and the metallicity of gas in and around galaxies contains information about recent gas flows and gas mixing efficiency. We can therefore use the heavy elements as effective gas tracers, to probe how gas is accreting into and being ejected from galaxies. An interesting problem is the role that galaxy mergers play in inducing gas inflows to drive starburst and active galactic nuclei (AGN) activity. The heavily obscured and kinematically complex nuclear regions of local merging galaxies make observations of nuclear gas inflows difficult. However, signatures of a recent gas inflow can be observed by examining the evolving nuclear metallicity and metallicity gradient of interacting systems. Using idealized merger simulations we studied the link between merger induced gas inflows and the observed depressed nuclear metallicity in interacting galaxies.

The second chapter of this thesis describes our efforts to understand the role that mergers play in shaping the mass-metallicity relation. We investigate the metallicity evolution of a large set of simulations of colliding galaxies with models that include

radiative gas cooling, star formation, feedback, and a new stochastic method for tracking the mass recycled back to the ISM from stellar winds and supernovae. We provide a physically motivated picture to link together the influence of merger–induced inflows, chemical enrichment from ongoing star formation, gas consumption, and galactic winds in determining the nuclear metallicity evolution. We find that the evolving central metallicity during galaxy mergers is determined via a competition between the inflow of low–metallicity gas and enrichment from star formation. An average depression in the nuclear metallicity of ~ 0.07 dex is found for gas–poor disk–disk interactions. Gas–rich disk–disk interactions, on the other hand, typically have an enhancement in the central metallicity that is positively correlated with the gas content. We show that the simulations fare reasonably well when compared to the observed mass–metallicity and separation–metallicity relationships.

The major assumption that enters into the idealized galaxy merger simulations is the setup of the initial conditions. Idealized galaxies with exponentially decaying stellar and gaseous disks and metallicity gradients are manually prescribed. We would also like to understand the origin and evolution of (i) the mass-metallicity relation and (ii) galactic metallicity gradients. Unfortunately the idealized merger simulations lack the appropriate cosmological context to study these problems. These problems can be studied in fully cosmological simulations where late type spirals self-consistently build up their gaseous and stellar disks while self enriching with heavy elements over cosmic time.

Historically, forming diverse morphological populations (i.e. forming both disks and spheroids simultaneously) in cosmological simulations has been a notoriously difficult problem. While part of the problem is an incomplete knowledge of the role that feedback plays in delaying stellar mass buildup in galaxies, part of the problem can be attributed to

residual uncertainty in the role that hydrodynamics play in gas disk formation. Although we can write down the relevant inviscid hydrodynamical equations that we would like to apply within a simulation, there exist several ways to discretize these equations and implement them into the simulation code. This is not a benign issue: the formation of gas disks (and consequently metallicity gradients, etc.) in galaxies is sensitive to the applied hydrodynamical solver. Before we can study topics like metallicity gradient buildup in disk galaxies, we must first ensure that the fundamental and well understood components of our simulations – including gravity and hydrodynamics – are handled accurately. The third through fifth chapters of this thesis therefore shift focus from idealized merger simulations, to full volume cosmological simulations where we employ a novel hydro solver to study galaxy formation.

1.3 Gas Disk Formation in AREPO

Traditionally there are two methods for numerically solving hydrodynamic equations in astrophysics: Lagrangian and Eulerian methods. The basic approach of Lagrangian methods is to discretize a fluid into a series of mass elements (fluid particles) that move according to a discretized form of the hydrodynamic equations of motion. In a common Lagrangian based technique known as Smoothed Particle Hydrodynamics (SPH), a spline smoothing kernel is used to define hydrodynamic quantities such as density based on the local distribution of resolution elements. Lagrangian methods have a number of inherent advantages for galaxy formation problems. One of their advantages is that they naturally enhance resolution within regions of high gas density. Specifically, as gas cools and collapses into dark matter potential wells, the density of gas increases and the

physical scales of relevance grow smaller. SPH methods handle this naturally because mass elements follow the fluid flow, and therefore naturally increase the number of resolution elements present in dense regions. Additionally, SPH based methods naturally permit arbitrary geometry. There are no grids or preferred directions, and the fluid elements can be distributed with arbitrary geometry – including vacuum or periodic boundary conditions – without problems. Finally, SPH based methods are naturally galilean invariant. This implies that hydrodynamic phenomena – such as shocks or instabilities – will be handled equally well independent of the bulk velocity of the object of interest. This can be an important consideration in structure formation simulations where matter over densities around groups and clusters can cause large scale bulk motion of the galaxies and IGM around them. Due to their robust nature, SPH hydro solvers were common among early galaxy formation simulation efforts.

Whereas Lagrangian methods discretize the fluid into a series of mass elements that move with the fluid, the defining characteristic of Eulerian methods is to divide the simulation domain into discrete volume elements. The fluid's motion is then tracked relative to this grid by solving the Riemann problem at each cell face to determine the amount of mass, momentum, and energy that is transferred across the boundary. Typically, cartesian grids are used in galaxy formation simulations. Adaptive Mesh Refinement (AMR) simulation allow grids of increasing spacial resolution to be applied to enhance resolution within targeted areas of a simulation. Importantly, the Riemann solvers applied in AMR simulations are designed to handle hydrodynamical phenomena very accurately – allowing them to capture shocks, instabilities, and phase boundaries properly.

Lagrangian and Eulerian methods have complimentary strengths and weaknesses in

terms of their ability to accurately handle galaxy formation problems. While Eulerian methods are better equipped to handle the hydrodynamic phenomena which are important to galaxy formation, Lagrangian methods are naturally suited for the arbitrary geometry, large and localized bulk motions (without introducing galilean invariance), and wide dynamic mass and spatial dynamic range. It has been shown, for example, that the hydro solver applied within the SPH simulation code GADGET-2 fails to resolve Kelvin-Helmholtz and Rayleigh-Taylor instabilities, even at very high resolutions (Agertz et al. 2007). Conversely, it has been shown that instabilities are suppressed in AMR simulations when a bulk fluid motion is introduced (Springel 2010a) and that galaxies tend to align with the grid axes within AMR simulations (Hahn et al. 2010).

Just four years ago, a fundamentally new hydrodynamical method was introduced to the galaxy formation community by Volker Springel within the simulation code AREPO (Springel 2010a). The novel aspect of AREPO is that it solves the hydrodynamic equations on a moving mesh. In detail, mesh generating points – with associated mass, momentum, and energy – are allowed to move throughout a simulation domain according to the local bulk fluid motion as in a Lagrangian method. However, when it comes time to solve the hydrodynamic equations, the simulation volume is partitioned into a set of discrete volume elements via a Voronoi tessellation based on the distribution of mesh generating points. The Riemann problem is then solved across all faces of the resulting unstructured mesh to update the fluid properties as in Eulerian methods. It has been shown that this approach preserves the principle advantages of both the Lagrangian and Eulerian methods (Springel 2010a; Sijacki et al. 2012). AREPO is the first code to couple this sort of hydro solver to an accurate gravity solver, allowing it to be applied to galaxy formation problems.

In Chapter 3, we present a practical comparison of the structural properties of gas disks formed in cosmological simulations using the SPH code GADGET with those using the moving-mesh code AREPO. Both codes employ identical gravity solvers and the same sub-resolution physics but use very different methods to track the hydrodynamic evolution of gas. This permits us to isolate the effects of the hydro solver on the formation and evolution of galactic gas disks in GADGET and AREPO haloes with comparable numerical resolution. We show that the cold gas disks formed using the moving mesh approach have systematically larger disk scale lengths and higher specific angular momenta than their GADGET counterparts across a wide range in halo masses. For low mass galaxies differences between the properties of the simulated galaxy disks are caused by an insufficient number of resolution elements which lead to an artificial angular momentum transfer in the SPH calculation (described in detail in the body of the thesis). We find that galactic disks formed in massive halos, resolved with $\geq 10^6$ particles/cells, are still systematically smaller in the GADGET run by a factor of ~ 2. The reason for this is twofold: *i)* the excessive heating of haloes close to the cooling radius due to spurious dissipation of the subsonic turbulence in GADGET reduces the supply of gas which can cool and settle onto the central disk; *ii)* the efficient delivery of low angular momentum gaseous blobs to the bottom of the potential well results in the centrally concentrated gas disks in GADGET simulation. While this large population of gaseous blobs in GADGET originates from the filaments which are pressure confined and fragment due to the SPH surface tension while infalling into hot halo atmospheres, it is essentially absent in the moving mesh calculation, clearly indicating numerical rather than physical origin of the blob material.

Since the GADGET-AREPO comparison was first published, additional scrutiny has

been given to the hydro methods employed by the SPH galaxy formation community. New formulations of SPH equations of motion (Saitoh & Makino 2013; Hopkins 2013) and/or modifications to the artificial viscosity or conductivity (Read & Hayfield 2012; Hobbs et al. 2012) have been proposed to help correct some of the most glaring issues presented in Chapter 3 of this thesis.

1.4 Feedback

Strong feedback is now widely believed to be an important part of galaxy formation. In Chapter 3 we present simulations without strong feedback to facilitate a clear numerical comparison of hydrodynamical methods. As a result, the galaxy populations built in these simulations form stars far too efficiently compared to observations. Comparing these first simulations against observations would reveal poor matches to, e.g., the cosmic star formation rate density, galaxy stellar mass function, and Tully-Fisher relation. In order to perform meaningful comparisons between simulations and observations, we must incorporate feedback effects to help galaxies regulate their growth.

To achieve this goal, we developed a feedback model that could be applied in full-volume cosmological simulations where the spatial resolution is roughly a kiloparsec in scale. This is challenging because many (if not all) of the physical phenomena that are responsible for driving outflows in galaxies (e.g., supernova, radiation pressure, etc.) act on scales well below this resolution limit. Our feedback model is therefore formulated as a numerically convergent sub-grid model, where we try to capture the effects of various feedback channels, without needing to explicitly resolve the physical phenomena that drive them. The development of a comprehensive feedback module in AREPO was led

by Mark Vogelsberger and presented in Vogelsberger et al. (2013). Testing the impact of the feedback model parameters (e.g., wind velocity) on the resulting galaxy populations (e.g., galaxy stellar mass function, Tully-Fisher relation, etc.) was the subject of a separate paper which is included in this thesis as Chapter 4.

In Chapter 4, we present a multi-epoch analysis of the galaxy populations formed within the cosmological hydrodynamical simulations presented in Vogelsberger et al. (2013). These simulations explore the performance of the updated AREPO feedback model including primordial and metal line radiative cooling with self-shielding corrections; stellar evolution with associated mass loss and chemical enrichment; feedback by stellar winds; black hole seeding, growth and merging; and AGN quasar- and radio-mode heating with a phenomenological prescription for AGN electro-magnetic feedback. We illustrate the impact of the model parameter choices on the resulting simulated galaxy population properties at high and intermediate redshifts. We demonstrate that our scheme is capable of producing galaxy populations that broadly reproduce the shape of the observed galaxy stellar mass function extending from redshift $z = 0$ to $z = 3$. We also characterize the evolving galactic B-band luminosity function, stellar mass to halo mass ratio, star formation main sequence, Tully-Fisher relation, and gas-phase mass-metallicity relation and confront them against recent observational estimates. This detailed comparison allows us to validate elements of our feedback model, while also identifying areas of tension (e.g., the shape and normalization of the mass-metallicity relation and normalization of the star formation main sequence) that will be addressed in future work.

Although there are areas where the resulting "fiducial" model fails to match observations precisely, the point can easily be argued that the cosmological simulations

run using AREPO with our new feedback model do the best job to-date matching such a wide range of observable properties at so many different epochs.

1.5 Illustris Mock Image Catalog

The Illustris simulation is a single massive cosmological simulation that employed the full-feedback model explored in Chapter 4 within large volume at high mass and spatial resolution. The larger simulation volume allows us to explore the evolution of more massive galaxies/groups/clusters, as well as sample a wider range of environments. The simulation was run in a periodic box of size $L = 75h^{-1}$ Mpc with 1820^3 dark matter and baryon resolution elements. At the writing of this thesis, it is the largest and most well resolved full volume cosmological hydrodynamical simulation ever completed.

A powerful and unique aspect of the Illustris simulations is its ability to produce a wide range of realistic galaxy types. Early explorations of the simulated galaxy populations showed that the simulation contained star forming disks along side red and dead ellipticals. Owing to the large simulation volume, one can also find quenched/red disks within the haloes of massive systems, stellar shells formed during dry mergers, and tidal features in interacting systems. We can use this simulated galaxy population to provide tools for interpreting extragalactic observations. This can be done by matching observed galaxies to simulated systems with similar properties, where we have full access to the formation history, subsequent evolution, and complete cosmological context of each galaxy. Matching can be performed by constructing mock galaxy SEDs and/or galaxy images using stellar population synthesis models.

In chapter 5 of this thesis, we use the simulated galaxies from the Illustris simulation, to produce mock images from several viewing angles in 36 broadband filters for each galaxy. With this mock dataset, it possible to produce color images, perform SED fitting, classify morphology, determine galaxy structural properties, and consider impacts of galaxy viewing angle. The principle component of all images is stellar light assigned using stellar population synthesis models based on the age and metallicity properties of stars in each galaxy. Each galaxy is therefore assigned an SED that properly reflects its stellar metallicity distribution and star formation history with self-consistent contributions from starbursts, mergers, and periods of quiescence. Line emission from HII regions as well as dust obscuration is considered in the images to assess the impact on SED derived galaxy stellar masses. The main result of the paper is the presentation of the largest publicly accessible online mock image database made directly from hydrodynamical galaxy formation simulations containing more than 40,000 galaxies and spanning more than two orders of magnitude in stellar mass. Of these, $\sim$1,000 galaxies are well resolved with more than 10^5 star particles. In this chapter, we describe the format and access to the data to facilitate direct comparison with observations, present science applications of the images, and discuss potential extensions of the current dataset.

The potential applications of the Illustris Simulation Observatory are fairly extensive. We outline some of these possibilities briefly in Chapter 5, but we also revisit this topic in the conclusions.

Chapter 2

The Metallicity Evolution of Interacting Galaxies

P. Torrey, T. J. Cox, L. Kewley, & L. Hernquist

The Astrophysical Journal, Vol. 746, No. 1, pp. 19, 2012

"Everything should be made as simple as possible, but no simpler. "

— Albert Einstein

2.1 Introduction

The nuclear metallicities of star-forming galaxies are characterized by a mass-metallicity relation (hereafter, MZ Lequeux et al. 1979; Rubin et al. 1984; Tremonti et al. 2004). Contributing to the scatter in the MZ relation are interacting galaxies, which are consistently lower in central metallicity than non–interacting systems of equivalent

mass, as first noted by Kewley et al. (2006), and later confirmed for ultraluminous infrared galaxies (ULIRGs) (Rupke et al. 2008), close pairs in SDSS (Ellison et al. 2008; Michel-Dansac et al. 2008; Peeples et al. 2009; Sol Alonso et al. 2010), and local, low mass systems (Ekta & Chengalur 2010). Observations such as these are most naturally explained as the result of vigorous merger–induced inflows of gas (Barnes & Hernquist 1991, 1996) which rearrange the initial metallicity gradient (Shields 1990; Belley & Roy 1992; Zaritsky et al. 1994; MacArthur et al. 2004) and "dilute" the nuclear metallicity (Kewley et al. 2006). In this sense, the same gas that drives nuclear starbursts (Mihos & Hernquist 1994b, 1996; Iono et al. 2004) and triggers central AGN activity and black hole growth (Di Matteo et al. 2005; Springel et al. 2005b; Hopkins & Hernquist 2006; Hopkins et al. 2007a), also results in suppressed nuclear metallicity.

Simulations of merger-driven inflows of gas naturally predict a flattening of the initial metallicity gradient (Perez et al. 2006; Rupke et al. 2010a; Perez et al. 2011), which has now been observed in a number of colliding systems (Kewley et al. 2010; Rupke et al. 2010b). However, more than hydrodynamics are at play in determining the nuclear metallicity evolution. To further our understanding, we should consider ongoing star formation with associated chemical enrichment, feedback from star formation and AGN activity, and the interchange of material between the stellar and gaseous phases as stars are born and later return material to the interstellar medium.

The four main processes responsible for the evolution of the nuclear metallicity are gas inflows, chemical enrichment from star formation, gas consumption, and galactic outflows. These effects compete with one another to influence the nuclear metallicity, making it difficult to determine their relative importance a priori. Numerical simulations have only recently been used to quantify the detailed impact of these effects on metallicity

gradients and nuclear metallicities of interacting pairs. Rupke et al. (2010a) simulated colliding galaxies without chemical enrichment to explore dynamically induced changes in metallicity gradients, finding that a drastic flattening can occur, accompanied by a drop in the nuclear metallicity. Montuori et al. (2010) and Perez et al. (2011) performed simulations with star formation and chemical enrichment and found similar results to Rupke et al. (2010a), but noted that the dip in the nuclear metallicity values can be counteracted by chemical enrichment from star formation. These simulations have refined our knowledge of the depressed MZ relation.

In this paper, we explore the evolution of the nuclear metallicity during mergers using numerical simulations which include cooling, star formation, stellar feedback, and black hole growth and AGN feedback. Our approach allows us to systematically investigate the importance of gas inflows, chemical enrichment from star formation, gas consumption as a result of star formation, and galactic outflows. In order to unambiguously determine the role of metal enrichment, we have developed a stochastic method to recycle stellar particles back to the interstellar medium without requiring inter-particle mass mixing. The stochastic gas recycling method, which is designed by analogy to the widely used stochastic star formation method, has attributes that are distinct from kernel weighted mass return, making it particularly useful for our study.

We consider a range of situations with systematically varied parameters to enhance our understanding of metallicity evolution as a natural extension of the merger process. We find that, for systems modeled after those in the local Universe, the main driver behind changes to the nuclear metallicity is the flow of low metallicity gas to the nuclear regions, or metallicity dilution. However, we identify two previously under-appreciated effects that influence the strength of this dilution: locking of gas and metals in the

stellar phase, and gas and metal removal via stellar-driven winds. We also find that, for systems modeled after high redshift galaxies, the main driver of the nuclear metallicity shifts to chemical enrichment. In these simulations, the nuclear metallicity increases, contrary to what is observed in the local Universe, suggesting that the interacting galaxy MZ relation may evolve differently at high redshifts.

We compare our simulations directly to observations by synthesizing a population of progenitor galaxies with properties consistent with observed samples and show that the empirical depression in the close-pair mass-metallicity relation can be reproduced while accounting for chemical enrichment. We find good agreement between our simulations and observations for both the interacting galaxy mass-metallicity relation and separation-metallicity relation.

2.2 Methods

We employ a library of merger simulations carried out using the N-body/Smooth Particle Hydrodynamics (SPH) code GADGET-2 (Springel 2005). GADGET-2 is based on a formulation of SPH (Springel & Hernquist 2002) which conserves both energy and entropy simultaneously (when appropriate). In addition to accounting for gravity and hydrodynamics, our simulations also include a sub-grid two-phase model of star formation, supernova feedback, radiative cooling of gas, and star formation driven winds (Katz et al. 1996; Springel & Hernquist 2003a, hereafter SH03). These features give a working description of the multiphase nature of the interstellar medium (e.g. McKee & Ostriker 1977) without explicitly resolving the various phases. Supermassive black hole sink particles are included in our simulations and have both accretion and

thermal feedback associated with them, but their presence does not influence any results presented in this paper.

The simulations presented here also include a novel method for returning gas to the interstellar medium (ISM) from (prompt) supernovae and asymptotic giant branch (AGB) winds. While the main body of our simulations code has been used for numerous other studies (see, e.g., Cox et al. 2006a,b; Robertson et al. 2006a,b,c), the inclusion of time–delayed gas recycling is a new feature which is described.

2.2.1 The Basic Model: SH03

The primary astrophysical processes modeled in our simulations – including cooling, star formation, feedback, and galactic winds – are included as in the SH03 model. Because these processes are discussed extensively in that paper we review them only briefly here.

The instantaneous rate of star formation for an SPH particle is given by

$$\frac{dM_*}{dt} = \frac{M_c}{t_*} \tag{2.1}$$

where M_* is the stellar mass, M_c is the mass of cold gas (i.e. some fraction of the SPH particle's mass that is in the cold phase as determined via the sub-grid model prescription of SH03), and t_* is a characteristic star formation timescale. We adopt a value $t_* = 4.5$ Gyrs so that our simulations are consistent with the Kennicutt-Schmidt relation (Schmidt 1959; Kennicutt 1998; Cox et al. 2006b). Star formation is assumed to only take place in gas which has densities above a set threshold, which in our case is 0.5 cm^{-3}.

Equation 2.1 is used as the basis for a Monte Carlo method for actually converting

SPH particles to star particles. Each SPH particle is assigned a probability of turning into a star particle as follows:

$$p_* = \left[1 - \exp\left(-\frac{\Delta t}{t_{\rm SFR}}\right)\right] \tag{2.2}$$

where Δt is the current simulation time step, and $t_{\rm SFR} = M_{gas}/(dM_*/dt)$ is the star formation timescale. A particle is converted if a random number drawn between 0 and 1 is less than Eq. 2.2.

The instantaneous rate of mass launched in star formation driven winds is given by

$$\frac{dM_w}{dt} = \gamma \frac{dM_*}{dt} \tag{2.3}$$

where dM_*/dt is the local star formation rate and γ is the mass entrainment efficiency. We typically take $\gamma = 0.3$, which is the mean value for luminous infrared galaxies measured by Rupke et al. (2005b), and the resulting winds are ejected at $v_{\rm w} = 242$ km/sec.

Equation (2.3) is used as the basis for a Monte Carlo method for wind generation. The associated probability of launching a particle in a wind is given by

$$p_w = \left[1 - \exp\left(-\frac{\Delta t}{t_w}\right)\right] \tag{2.4}$$

where $t_w = M_{gas}/(dM_w/dt)$. Particles put into winds receive a velocity kick and are not allowed to interact with the surrounding medium while they leave their host environment. In principle, gas particles launched by winds may still contribute to the nuclear gas phase metallicity. However, in practice, these particles very quickly leave the nuclear regions, and no longer contribute to the nuclear metallicity.

2.2.2 Gas Recycling

While models for star formation and feedback are ubiquitous in the current generation of numerical simulations, it is much less common to include the recycling of mass and metals which are lost from evolving stellar populations, a fundamental process in the enrichment of the interstellar and intergalactic mediums. The few models that do include this "gas recycling" typically do so in a continuous fashion, during which, at every time step, a small fraction of mass and metals is transferred from a single stellar particle to a set of nearest SPH neighbors (e.g. Steinmetz & Mueller 1994; Kawata 2001; Kawata & Gibson 2003; Okamoto et al. 2005; Scannapieco et al. 2005; Stinson et al. 2006; Tornatore et al. 2007; Wiersma et al. 2009b; Montuori et al. 2010; Perez et al. 2011). This approach can accurately track the spatial and temporal distribution of mass and metals at a reasonable computational cost, but unfortunately, because particles can exchange mass with many neighbors, at many different times, it is impossible to trace the exact origin of any particular mass or metal element.

Given a desire to unambiguously track the origin and evolution of interstellar metals, the work presented here adopts a stochastic approach to gas recycling (e.g. Lia et al. 2002; Martínez-Serrano et al. 2008). This less-used approach is designed to mirror the stochastic star formation scheme that is typically implemented in numerical simulations. While stochastic star formation probabilistically converts SPH particles into a fixed number of collisionless stellar particles based upon the star-formation rate, our stochastic gas recycling converts stellar particles into SPH particles based upon theoretical mass return rates for a simple stellar population. When used in conjunction, these methods can accurately track the temporal and spatial interchange of baryonic material between

stellar populations and the interstellar medium, a necessary element to any study of the evolution of interstellar metals.

In our stochastic approach, the probability of turning an individual star particle into an SPH particle at any given time step is given by

$$p_{recy} = \left[1 - \exp\left(-\frac{\Delta t}{t_{recy}}\right)\right] \tag{2.5}$$

where Δt is the current simulation time step, and

$$t_{recy} = \frac{M_*(t)}{dM_{gas}/dt}. \tag{2.6}$$

Here, $M_*(t)$ is the expected stellar mass at time t, and dM_{gas}/dt is the mass return rate at the same time. While the physical mass of the stellar particle in the simulation remains constant, the expected stellar mass identifies the amount of mass that would have been returned to the ISM if we implemented continuous gas recycling. We should make clear that there are no hybrid particles in the simulation, so the expected stellar mass has no influence on the simulations dynamics. It is necessary, however, for Eq. 2.6 to use the expected stellar mass in order for the stochastic recycling routine to reproduce the desired Starburst99 gas recycling rate in the simulations.

In practice, the simulation selects a random number between 0 and 1, and performs the particle conversion if this number is less than p_{recy}. We calculate the mass return rate, dM_{gas}/dt, directly from Starburst99 synthetic population models (Leitherer et al. 1999; Vázquez & Leitherer 2005; Leitherer et al. 2010). These models include gas recycling contributions from core collapse supernova and asymptotic giant branch (AGB) winds, but do not include contributions from Type Ia supernovae. At each time step, stellar particles are assigned a mass return rate determined by their age, metallicity, and

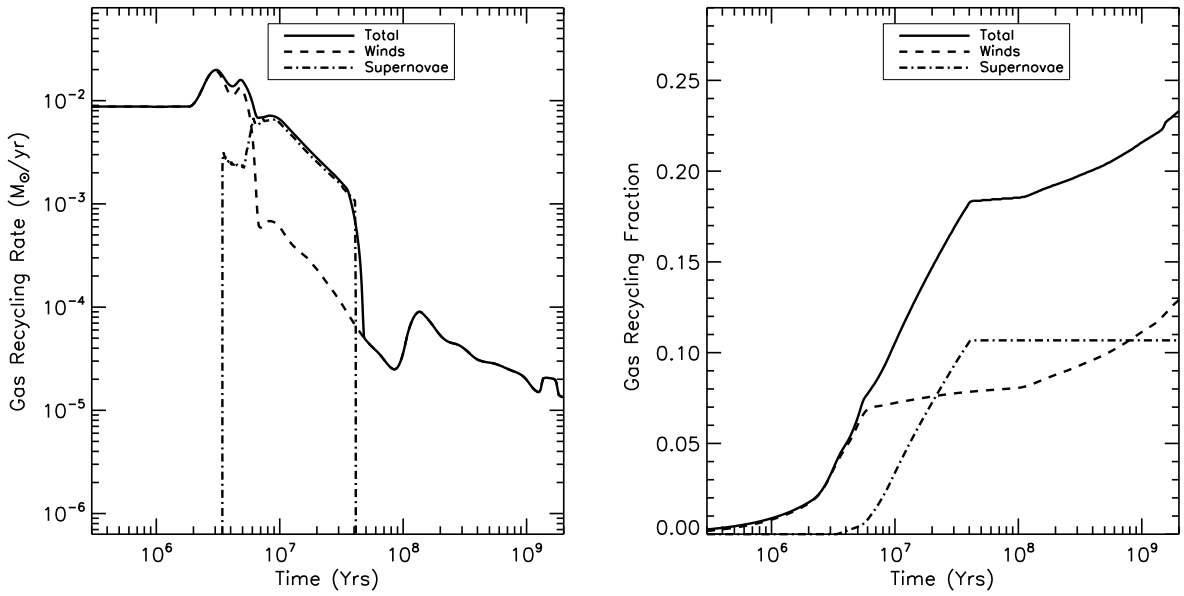

Figure 2.1.—: The mass recycling rate (left) and integrated mass recycling fraction (right) from a Starburst99 model for a $10^6 M_\odot$ stellar population with a Kroupa IMF.

an initial mass function (Υ). For the simulations presented here, we choose a Kroupa initial mass function with solar metallicity. The resulting mass return rate, and mass return fraction are demonstrated in Figure 2.1.

While it will be fruitful to explore variations in the mass return according to varying IMF assumptions, real–time metallicity information, or even easily parameterized functional forms of mass return that include Type Ia supernovae (see, e.g., Jungwiert et al. 2001; Leitner & Kravtsov 2011) we choose to allow variations in mass return through a simple scale factor to the return rate shown in Figure 2.1. Specifically, we define a scalar, ζ, and employ a mass return rate normalized as such

$$\frac{dM_{gas}}{dt} = \left(\frac{\zeta}{\frac{1}{M_*} \int_0^\infty f_{sb99}(t, Z, \Upsilon) dt} \right) f_{sb99}(t, Z, \Upsilon), \tag{2.7}$$

where $f_{sb99}(t, Z, \Upsilon)$ is the mass return rate from Starburst99 as shown in Figure 2.1. The expected stellar mass in Eq. 2.6 is then calculated as

$$M_*(t) = M_0 - \int_0^t \frac{dM_{gas}}{dt'} dt', \tag{2.8}$$

where M_0 is the original mass of the stellar particle. We note that for large values of ζ, and for old stellar ages, $M_*(t)$ can become negative, yielding unphysical negative values for t_{recy} and consequently a negative probability p_{gas}. This situation is non-catastrophic, however, because, in practice, it leads to an immediate conversion of this stellar particle to SPH.

The parameter ζ allows us to control the timescale and efficiency of gas recycling. For example, the Kroupa IMF we employ dictates that 37% of the stellar mass will be returned to the ISM after 10 Gyr. Setting $\zeta = 0.37$ makes the normalization unity and the recycling therefore tracks exactly what is shown in Fig. 2.1. Setting $\zeta = 1$ will

produce complete (i.e., 100%) recycling of the stellar mass within 10 Gyr, while $\zeta = 100$ effectively yields the instantaneous recycling approximation with all the stellar mass being returned within $\sim 3 \times 10^6$ Yr. Finally, and perhaps obviously, setting $\zeta = 0$ turns off recycling altogether giving us the flexibility to study the impacts of varying amounts of recycling on metallicity evolution.

When a star particle is returned to the gas phase, the particle type is instantly converted from stellar to gas at the end of the current time step. The fields which are defined for both SPH particles and star particles, such as the position, velocity, mass, metallicity, etc., remain unchanged during the conversion. For concreteness, the metallicity of a particle remains unchanged during the transition to or from the stellar state. The metallicity increases while in the gas phase (according to Eq 2.9), but remains fixed while in – or making transitions to and from – the stellar state.

SPH quantities must be initialized for the newly converted gas particle. In principle, we could set these fields to properly reflect the physical state of the gas being returned and explore the feedback implications that naturally result from this gas recycling model. However, in practice, we are resolution-limited, we already include feedback according to the SH03 model, and our primary concern is representing the overall mass-budget faithfully. To this end, we give a newly formed SPH particle properties that will allow it to quickly homogenize into the surrounding medium. In particular, the entropy is set equal to that of gas at a temperature of $T = 50,000$ K and a density (chosen to be the star formation critical density) of $\rho = 0.5$ cm^{-3}. It is important to note that our simulations are nearly invariant to our choice of these values. Changing the initial entropy by an order of magnitude in either direction yields no obvious differences in the simulations. In effect, this implementation of gas return serves to provide a passive

source of gas for our evolving system, without providing strong feedback.

During both star formation and gas recycling events, no particle splitting occurs. As such, the total number of baryon particles (stars and gas) is conserved throughout the simulation. Effectively, baryon particles are permitted to flip back and forth between the gas and stellar phases, according to the star formation and gas recycling rates. Because baryon particle number is conserved and no mass is transferred between particles, mapping a particle's initial position to a final position a trivial task, regardless of the number of times it was it was turned into a star particle or returned to the gas phase. Using this stochastic gas recycling method provides the distinct advantage that we can retrace all mass to a unique initial position regardless of the star formation or gas recycling history.

2.2.3 Metallicity Enrichment

We implement a method for calculating the metal enrichment based on the instantaneous star formation rate to determine the metallicity enrichment rate. Unlike star formation, galactic winds, and gas return, metal enrichment is carried out in a continuous fashion, where the metal formation rate is given by

$$\frac{dM_Z}{dt} = y\frac{dM_*}{dt} \tag{2.9}$$

and y is the metal yield and dM_*/dt is the instantaneous star formation rate. For our simulations, we use a fixed yield of $y = 0.02$. The metallicity will increase wherever there is ongoing star formation, as determined via the SH03 star formation model. As such, diffuse gas will not be star forming, and will therefore not enrich (see SH03 for details). The scalar metallicity is updated at each time step using an Eulerian integration

scheme. This scalar metallicity does not track independent species, but instead provides a single metallicity value proportional to the integrated star formation rate. This metal enrichment scheme is strictly independent of our gas recycling routine.

The metallicity enrichment does not affect the evolution of the simulation because there are no metallicity dependent dynamical processes included, such as metal line cooling. Because no mixing is allowed, nearby particles may have large metallicity variations. This is not problematic, as long as we interpret the metallicity at a given location to be a kernel weighted average of nearby particles, as is traditional for determining fluid quantities in SPH. Mixing would homogenize the individual particle metallicities, while leaving the average value of the kernel weighted metallicity unchanged.

Using this enrichment scheme, we are able to cleanly decompose the metallicity of an SPH particle into contributions from its initial metallicity and star formation history. More important, we are able to scale our metal yield and modify our initial metallicity setup in our post-processing analysis, without requiring additional simulations. This is possible because all of the gas content of an SPH particle has an unambiguous and unique initial location and star formation history, which is not true when particle mass mixing is used. In later sections, our ability to arbitrarily modify initial metallicity gradients of our progenitor galaxies is critical in allowing us to thoroughly sample the range of metallicity gradients of our progenitor galaxies, without large computational requirements.

2.3 Isolated Galaxies

In our analysis, we take the nuclear region of a galaxy to be a sphere of radius 1 kpc about the galactic center. We determine the nuclear metallicity from the star formation rate weighted average of all gas particles inside this sphere. A 1 kpc spherical region is used for consistency with the observations of Kewley et al. (2006). However, it should also be noted that our results would not fundamentally change for slightly larger or smaller definitions of the nuclear region.

We use star formation rate weighted averages to mimic observations of HII regions, which naturally select star forming gas. Unless otherwise stated, all nuclear metallicities quoted in this paper are gas-phase and star formation rate weighted. In particular, the central depressions in gas-phase metallicity presented here should not be confused with enhancements in stellar metallicity seen in late-stage mergers and relaxed elliptical galaxies. These increases in stellar metallicity are relics from the merger-driven starbursts that leave behind central stellar cusps in merger remnants (Mihos & Hernquist 1994a; Hopkins et al. 2008b) and elliptical galaxies (Hopkins et al. 2009a,c). These starbursts occur at late stages in a merger, following coalescence, from enriched, star-forming gas, yielding a central population of young, metal-enhanced stars (see, e.g. Figs. 27 and 28 in Hopkins et al. 2009a).

The star formation rate weighted nuclear metallicity is defined as

$$\bar{Z} = \frac{\int_V \dot{\rho}_* \left(\vec{r}\right) Z \left(\vec{r}\right) dV}{\int_V \dot{\rho}_* \left(\vec{r}\right) dV} \tag{2.10}$$

where $\dot{\rho}_* \left(x, y, z\right)$ is the star formation rate density, $Z \left(x, y, z\right)$ is the fraction of gas-mass in metals, and the integral is performed over the 1 kpc spherical region about the galaxy's

center. The star formation rate density is calculated as

$$\dot{\rho}_* (\vec{r}) = \sum_j \frac{dM_{*,j}}{dt} W (|\vec{r} - \vec{r}_j| , h_j) \tag{2.11}$$

where $W (|\vec{r} - \vec{r}_j| , h_j)$ is a smoothing kernel function, h is a smoothing length, and dM_*/dt is a particle's instantaneous star formation rate (discussed in §2.2.1). For our analysis, we use a galaxy's central black hole to define the galactic center; however, our results are unchanged if we use the potential minimum, or any other reasonable measure of the galactic center. This approach neglects projection effects, but instead provides information about the "true" nuclear region.

The metallicity of each SPH particle consists of two separate contributions: an initial metallicity and an enriched metallicity. The initial metallicity of an SPH particle is completely determined by the particle's initial radial position (discussed in §2.3.1) and is unchanging in time, while the enriched metallicity grows owing to star formation. The metallicity of an SPH particle as a function of time is given by

$$Z_{gas} (t) = Z_{init} + \frac{y}{M_{gas}} \int_0^t \frac{dM_*(t')}{dt'} dt' \tag{2.12}$$

where $dM_*(t')/dt'$ is the particle's complete time dependent star formation rate history. The integration of the rightmost term in Eq. 2.12 should be carried out starting at the beginning of the simulation (i.e. $t = 0$), regardless of whether a particle has been recycled or not. Since $dM_*(t')/dt'$ is non-zero only when a particle is actively star forming (i.e. in the gas state and above the star formation threshold density), periods of time when a particle is in the stellar state or below the star formation threshold density (see §2.2.1) will not contribute to Eq. 2.12.

The metallicity of the nuclear region is calculated similarly to the metallicity of an individual SPH particle, with an additional sum over an ensemble of particles weighted

by their star formation rates. We explicitly break the nuclear metallicity into two components

$$\bar{Z} = \frac{\sum_i Z_{i,init}\dot{M}_{*,i}}{\sum_i \dot{M}_{*,i}} + \frac{\sum_i Z_{i,enrich}\dot{M}_{*,i}}{\sum_i \dot{M}_{*,i}} \tag{2.13}$$

where the sum is performed over the particles that fall within the nuclear region. The first term contains the contribution from the initial metallicity gradient of our progenitor galaxies while the second term contains the contribution from star formation induced metallicity enrichment. For clarity throughout, we call the first term the "dynamical metallicity", as it is a dynamical result of the initially assumed metallicity gradient, while we call the second term the "enriched metallicity", as it is a product of metal enrichment. For concreteness, the metallicity gradients for one of our "C" isolated galaxies evolved in isolation for 2 Gyrs is shown in Figure 2.3 with contributions from the dynamical and enriched components explicitly shown (see §2.3.2).

2.3.1 Isolated Galaxy Setup

The isolated galaxies used in this paper are modeled following the analytical work of Mo et al. (1998) employing the procedure outlined in Springel et al. (2005b). Our fiducial galaxy consists of a dark matter halo, an embedded rotationally supported exponential disk, a stellar bulge, and a central supermassive black hole.

We construct a set of four isolated galaxies with total system masses ranging from $\sim 10^{11} M_\odot$ to $\sim 10^{12} M_\odot$, as outlined in Table 2.1. Although varied in mass, all systems are constructed to be self-similar in order to isolate the effects of mass from other quantities that may correlate with mass in observed systems. The total mass of the disk (stars and gas combined) is chosen to be a constant fraction (4.0%) of the halo mass

Table 2.1:: Progenitor Disk Properties

Disk Identifier	Total Halo Mass [$M_\odot$]	Initial Stellar Mass [$M_\odot$]	Initial Disk Gas Fraction	h [kpc]	N_{Halo}	N_{gas}	N_{stars}
A	2.3×10^{11}	1.1×10^{10}	10%	2.4	532,500	30,000	145,500
B	5.1×10^{11}	2.4×10^{10}	10%	3.2	532,500	30,000	145,500
C	9.5×10^{11}	4.4×10^{10}	10%	3.9	532,500	30,000	145,500
D	13.5×10^{11}	6.2×10^{10}	10%	4.4	532,500	30,000	145,500
C2	9.5×10^{11}	4.0×10^{10}	20%	3.9	532,500	40,000	135,500
C3	9.5×10^{11}	3.2×10^{10}	40%	3.9	532,500	60,000	115,500
C4	9.5×10^{11}	2.4×10^{10}	60%	3.9	532,500	80,000	95,500

for all progenitor galaxies, with four settings for the initial gas fraction (8%, 20%, 40%, and 60%). All halos have spin parameters equal to $\lambda = 0.05$, which effectively sets the disk radial scale length. The initial stellar disk scale height is set to a fixed fraction (0.2) of the initial disk scale length, while the gaseous scale height is determined by satisfying hydrostatic equilibrium (Springel et al. 2005b). Stellar bulges are included as part of the fiducial galaxy setup and are given a fixed fraction (1%) of the system mass. The resulting disk setup has a Toomre Q parameter that varies as a function of galactocentric radius, but is everywhere greater than unity – indicating stability against axisymmetric perturbations.

The dark matter halos follow Hernquist (1990) profiles with concentration indices of $c = 10$. The stellar and gaseous disk components are modeled with exponential surface density profiles

$$\Sigma_{*,g}(r) = \frac{M_{*,g}}{2\pi h^2} \exp\left(-\frac{r}{h}\right) \tag{2.14}$$

where $M_{*,g}$ is the total mass of stars and gas in the disk, respectively, and h is their common scale length set by the disk's angular momentum (Mo et al. 1998; Springel & White 1999). Stellar bulges are taken to be spherical Hernquist (1990) profiles, where the bulge scale length is given in terms of the halo scale length, $a_b = 0.2a$, and the bulge mass fraction to be 1% of the halo mass.

The initial metallicity profile of our progenitor galaxies enters as an assumption. We model the metallicity profile of the disk as an exponential

$$Z(r) = Z_0 \ \exp\left(-\frac{r}{h_z}\right) \tag{2.15}$$

where the central metallicity, Z_0, and the metallicity scale length, h_z, are chosen to be consistent with observations. Isolated galaxies show dispersion in their radial metallicity

gradients. We could include this dispersion in our simulations by adding in a Gaussian error term to Eq. 2.15; However, no dispersion is used when setting the initial metallicity profile for our isolated galaxies because this would add an extra element of uncertainty into our models and add noise to our results, without yielding systematic changes or further insight.

We assume that Oxygen makes up 30% of the metals by mass. The constant Oxygen mass fraction is a necessary assumption of our models, because we track only one scalar metallicity value. We note that our results are not particularly sensitive to our choice of the Oxygen mass fraction, since this is merely a normalization of the overall metallicity.

We fix the central metallicity values to the observed relation of Tremonti et al. (2004) so that the central metallicity is given in terms of the stellar mass

$$12 + \log(O/H) = -1.492 + 1.847x - 0.08026x^2 \tag{2.16}$$

where $x = \log_{10} M_*$. Initially, we use the exact value given by equation (2.16) when discussing the process of nuclear metallicity evolution in §2.4. However, in §2.5 we pick the central metallicity of each progenitor galaxy from a Gaussian distribution with a standard deviation, $\sigma = 0.1$ dex, taken from Tremonti et al. (2004). Similarly, we use the average result from Zaritsky et al. (1994) of $h_z = h/0.2$ in §2.4. However, in §2.5 we pick the slope of the metallicity gradient from a Gaussian distribution with a standard deviation of $\sigma = 0.3h_z$.

2.3.2 Isolated Galaxy Evolution

While the metallicity evolution of isolated galaxies is not the focal point of this paper, we take a moment in this section to demonstrate that our galaxy models are indeed stable, and evolve very little in isolation. We specifically demonstrate that the galaxy models do not develop strong bars since these structures can lead to significant radial inflows of gas. Such processes obscure the true origin of any central metallicity evolution, and what is specifically a result of the merger.

The evolved gas surface density, seen in Figure 2.2, demonstrates that our disks are both stable and free of strong bars over at least 2 Gyrs, the typical duration of the galaxy major mergers we study. As a result, the metallicity gradients of our isolated systems evolve very little, as seen in Figure 2.3. We further demonstrate the characteristics of our isolated disks in Figure 2.4 where we show the star formation rates and gas fractions for the C2, C3, and C4 systems.

To understand where the small amount of metallicity evolution does come from, Figure 2.3 also shows the evolution of the initial metallicity gradient, or the "dynamical" metallicity (middle panel), and the contribution from ongoing star formation, or the "enriched" metallicity (right panel). From this information it is easy to see that the small increase in central metallicity and gradient is a result of chemical enrichment from ongoing star formation, while the initial metallicity gradient remains nearly unchanged.

Motivation to emphasize the stability of our initial disk models stems from the fact that the disks used in previous studies (e.g. Montuori et al. 2010) appear to be bar unstable over short timescales (see their Figure 2 in their Appendix). These bars result in strong radial mixing and a flattening of their radial metallicity profiles (see Figure 1 in

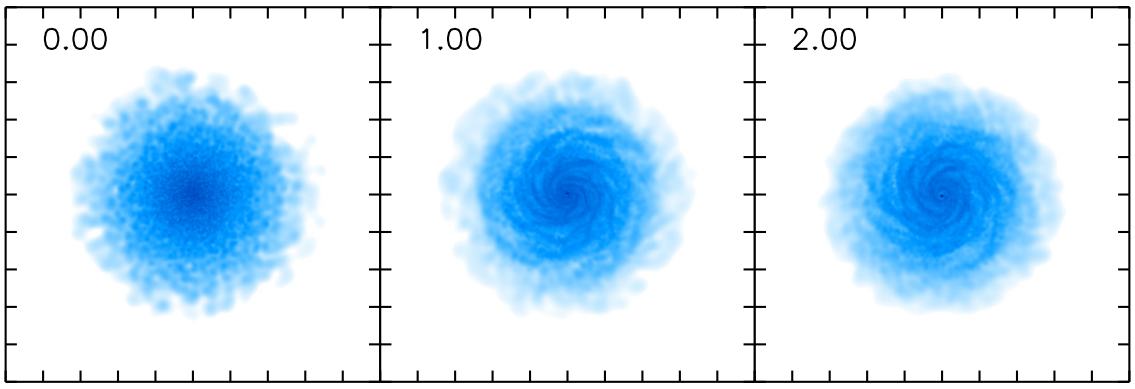

Figure 2.2.—: The gas surface density is shown for our isolated "C" disk evolved for 2 Gyrs. The disks evolve stably and without bar formation or significant radial gas inflow for 2 Gyrs.

their Appendix). While bar induced gas inflows are indeed a valid physical mechanisms for modifying the nuclear metallicity, we wish to eliminate this complication from our study to make our results easier to interpret.

The evolution of the nuclear metallicity of the four progenitor disks, described in Table 2.1, are demonstrated in Figure 2.5. The nuclear metallicity of all isolated disks is well described by a mild and monotonic increase over at least 2 Gyrs. The steady behavior of the isolated galaxy nuclear metallicity ensures that any strong changes during the merger simulations are a product of the merger process, rather than disk instability.

While exploring the behavior of isolated disks, we can also demonstrate the effects and capabilities of stochastic gas recycling. When evolving the "C" systems (i.e. C2, C3, and C4 from Table 2.1) we vary the gas recycling parameter and examine the resulting gas fraction and star formation rate evolution. The results, shown in Figure 2.4, demonstrate that the gas is locked into stars more efficiently when the gas recycling parameter is small. As a result, the star formation rates, which largely depend on the amount of gas available for star formation, are consistently larger for increasing values of the gas recycling parameter. Simulations that use efficient gas recycling maintain larger gas fractions and star formation rates throughout the simulation.

In the limit of very large gas recycling parameters, all newly formed stellar material is quickly returned to the ISM. As a result, the gas fraction for large gas recycling parameters stays nearly constant. The corresponding star formation rates slowly increase as gas naturally cools and condenses over time.

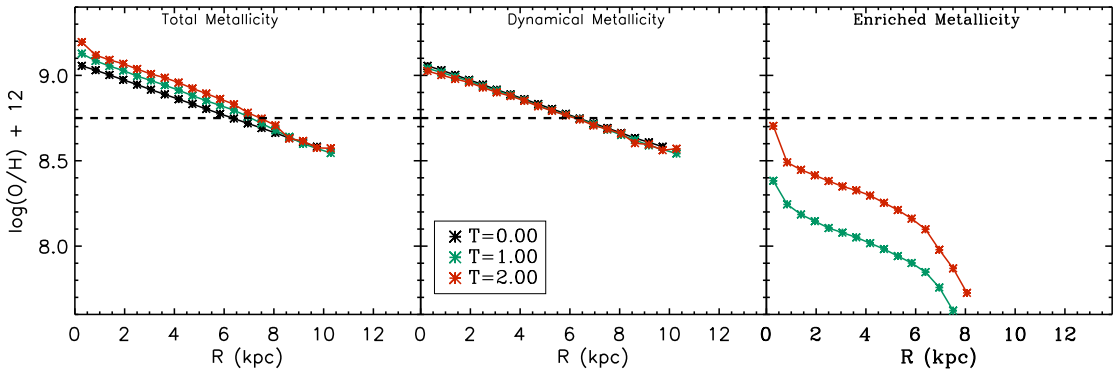

Figure 2.3.—: Metallicity profiles for the "C" isolated galaxies evolved for 2 Gyr. The total (left), dynamical (center), and enriched (right) metallicities are shown separately. The horizontal dashed line denotes the mean initial metallicity for the disk. The stability of the dynamical metallicity indicates that radial gas flows are minimal in our isolated systems, while the total metallicity gradient increases over time owing to chemical enrichment.

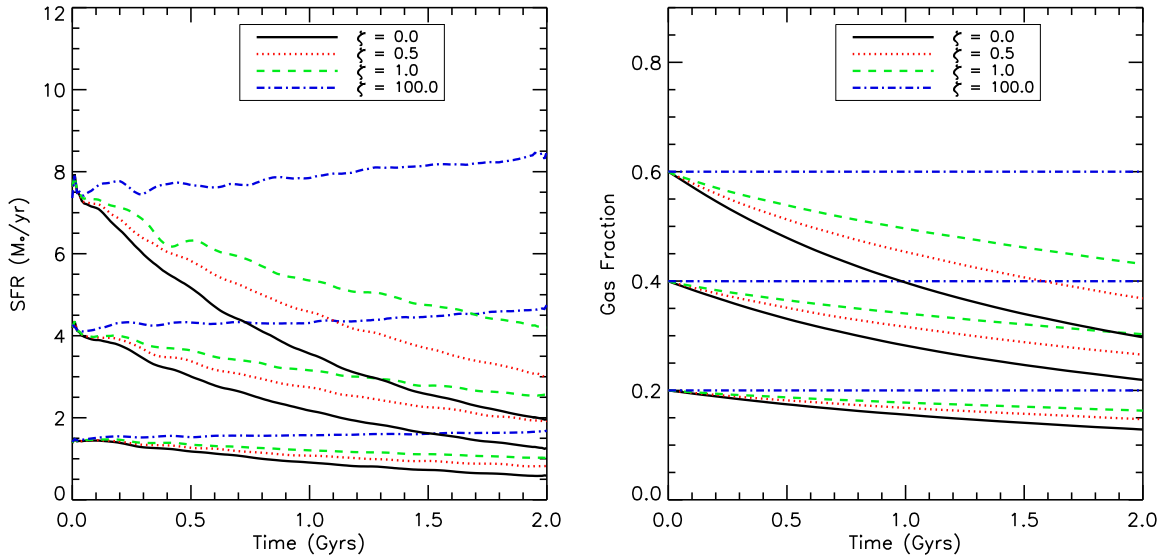

Figure 2.4.—: Star formation rates and gas fractions for the C2, C3, and C4 systems evolved for 2 Gyrs with varying gas recycling parameters. The gas return parameters, identified in the legend, are varied from $\zeta = 0.0$ (i.e. no gas recycling) to $\zeta = 100.0$ (i.e. nearly instantaneous recycling). Unless otherwise noted, subsequent sections and simulations use $\zeta = 0.3$, which is the unscaled value taken from the Starburst99 simulations.

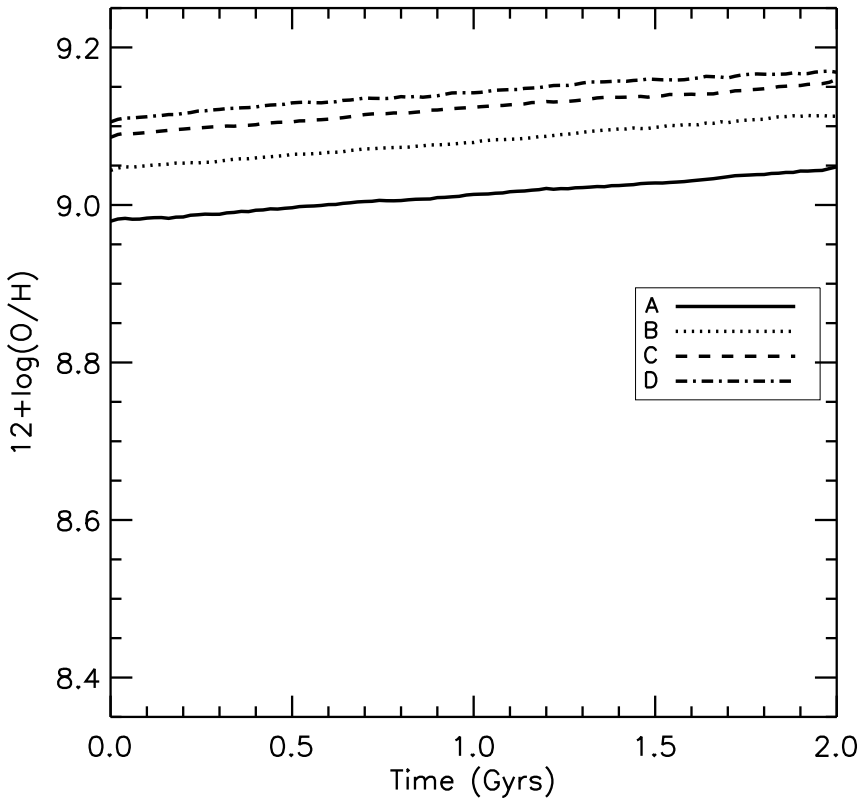

Figure 2.5.—: Nuclear metallicities for the A, B, C, and D, isolated galaxies evolved for 2 Gyrs is shown. The nuclear metallicity of our isolated model galaxies increases monotonically with time owing to chemical enrichment, as demonstrated in Figure 2.3

2.4 Merging Galaxies

While keeping all of the conventions for nuclear metallicity defined in §2.3, we now consider the evolution of galactic nuclear metallicity for merging systems. Since our interacting systems are spatially extended and overlap substantially during the interaction, they do not follow Keplerian trajectories. However, we use the terminology of Keplerian orbits to clearly describe the merger setup.

To completely specify our merging setup, we must specify the properties of the merger orbit (2 parameters), and the relative orientation of each galaxy with respect to the orbit (2 parameter for each galaxy). We start by specifying that the systems will be on zero energy orbits (i.e. eccentricity value of unity for Keplerian objects). The orbital angular momentum is then set by picking a value for the impact parameter, assuming Keplerian trajectories (the "real" impact parameter found in the simulations will be larger than this value). We hold the impact parameter fixed (5 kpc) for all simulations. The spin angular momentum vector of each galaxy is varied with respect to the orbital angular momentum vector according to the orientations detailed in Table 2.2 as visually depicted in Figure 2.6.

The parameter space of mergers is quite large. To explore this parameter space, without using an excessively large number of simulations, we first perform a detailed exploration of a single case. We then systematically vary merger parameters, such as the disk orientation, progenitor disk mass, merger mass ratio, orbital angular momentum, and so forth. While this does not necessarily cover all of merger parameter space, it does enable us to paint a coherent picture detailing the relation between the evolution of the merger and the evolution of the nuclear metallicity.

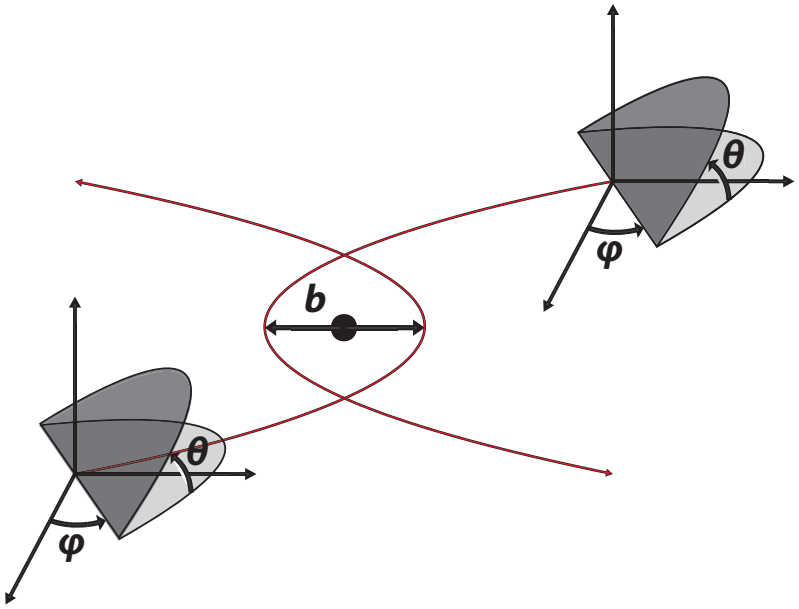

Figure 2.6.—: Schematic representation of the merger setup. Our coordinate system is defined by the plane of the merger orbit, and each disk's orientation is independently adjusted with respect to this plane.

Table 2.2:: Orbital Orientations

Orientation Identifier	θ_1 [deg]	ϕ_1 [deg]	θ_2 [deg]	ϕ_2 [deg]
a	90	90	0	0
b	180	0	0	0
c	180	0	180	0
d	90	0	0	0
e	30	60	-30	45
f	60	60	150	0
g	150	0	-30	45
h	0	0	0	0
i	0	0	71	-30
j	-109	90	71	90
k	-109	-30	71	-30
l	-109	30	180	0
m	0	0	71	90
n	-109	-30	71	30
o	-109	30	71	-30
p	-109	90	180	0

We select our fiducial galaxy merger to be two identical "B" disks merging on the "e" trajectory (see Tables 2.1 and 2.2). This setup is neither average nor special, and is simply selected to demonstrate in detail the relationship between the merger state and evolution of the nuclear metallicity. While §2.4.1 is restricted to understanding a single merger evolution, §2.4.2-2.4.4 show that much of the nuclear metallicity evolution can be understood in terms of generic merger properties that will continue to drive the nuclear metallicity evolution as we move beyond this fiducial setup.

2.4.1 Metallicity Evolution in Merging Systems

In stark contrast to the isolated systems presented in §2.3.2, the nuclear metallicity of interacting galaxies is a complicated function of time, as shown in Figure 2.7. Moreover, there is a clear change in the evolutionary behavior of the nuclear metallicity following pericenter passage when the disks stop behaving like isolated systems, and enter a period of evolution dominated by the merger dynamics.

Before delving further into the merger details, we note that there is a characteristic "double dip" shape to the nuclear metallicity evolution. This is caused by the ongoing competition between metallicity dilution and chemical enrichment. While the exact evolutionary track shown here is specific to this particular merger setup, the characteristic double dip in the metallicity will appear repeatedly in many other cases. In general, galactic close passages lead to gas inflows (yielding inflows of low metallicity gas) which are quickly followed by star formation (yielding chemical enrichment).

During the period of time between first pericenter passage and final coalescence, the nuclear metallicity evolution is driven by: 1) Radial inflows of low metallicity gas caused

by the tidal interaction, 2) Chemical enrichment caused by star formation activity, 3) Locking of metals and gas in the stellar phase, and 4) Removal of gas and metals via galactic winds. The combined effect of these four mechanisms, which are discussed in detail in the following sub-sections, determines the relative importance of metallicity dilution and chemical enrichment, which ultimately decide when and where the nuclear metallicity will be diluted or enhanced.

Metallicity Dilution and Chemical Enrichment

The influence of radial gas inflows and chemical enrichment are demonstrated in Figure 2.8, which shows the galactic separation, rate of change of nuclear metallicity, nuclear star formation rate, and nuclear gas inflow rate. In terms of basic merger properties, there is an influx of gas following first pericenter passage and periods of gas inflow associated with each additional close passage. These gas inflows give rise to high nuclear star formation rates. While these previous points have been studied extensively in other papers (Barnes & Hernquist 1991, 1996; Mihos & Hernquist 1994b, 1996; Iono et al. 2004), we instead focus here on the influence that these generic merger properties have on the evolution of the nuclear metallicity. Specifically, times of strong gas inflow correspond to periods of nuclear metallicity depression, while high star formation activity aligns with nuclear metallicity enhancement. These qualitative relationships remain true as the merger parameters are varied.

Previous studies have found that the depression in the nuclear metallicity is correlated with the mass of gas that migrated to the nuclear region (Rupke et al. 2010a). This result is reproduced in our simulations when we neglect star formation

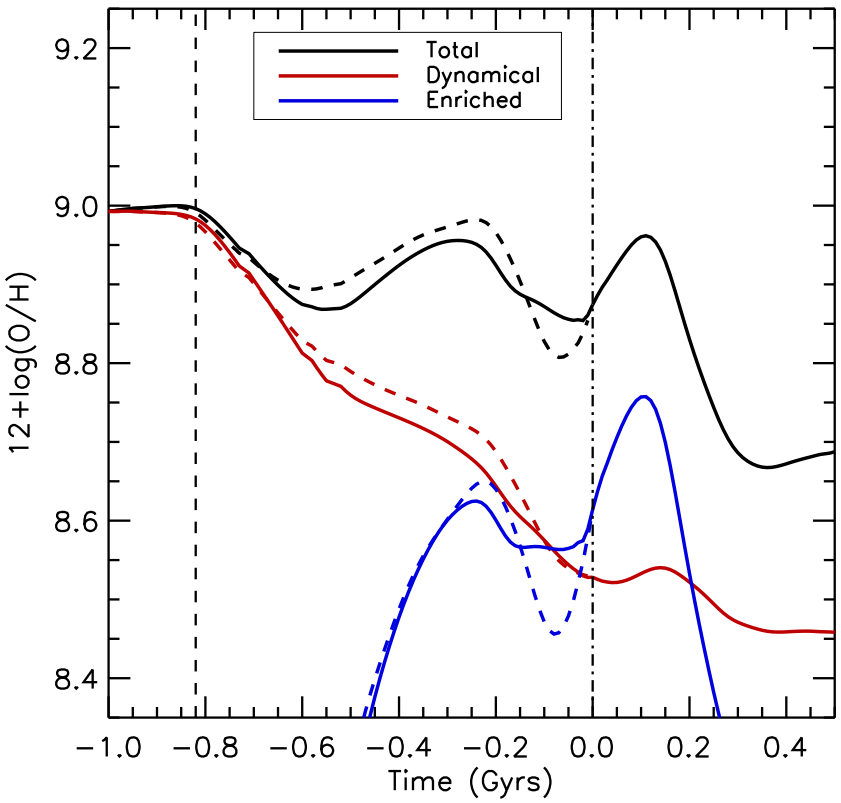

Figure 2.7.—: The total (black), dynamical (red), and enriched (blue) nuclear metallicities as a function of time for the "BBe" merger simulation. The two disks, which do not have identical metallicity evolutionary tracks, are distinguished by the solid and dashed lines. First pericenter passage and final coalescence are marked with vertical dashed and dot-dashed lines, respectively.

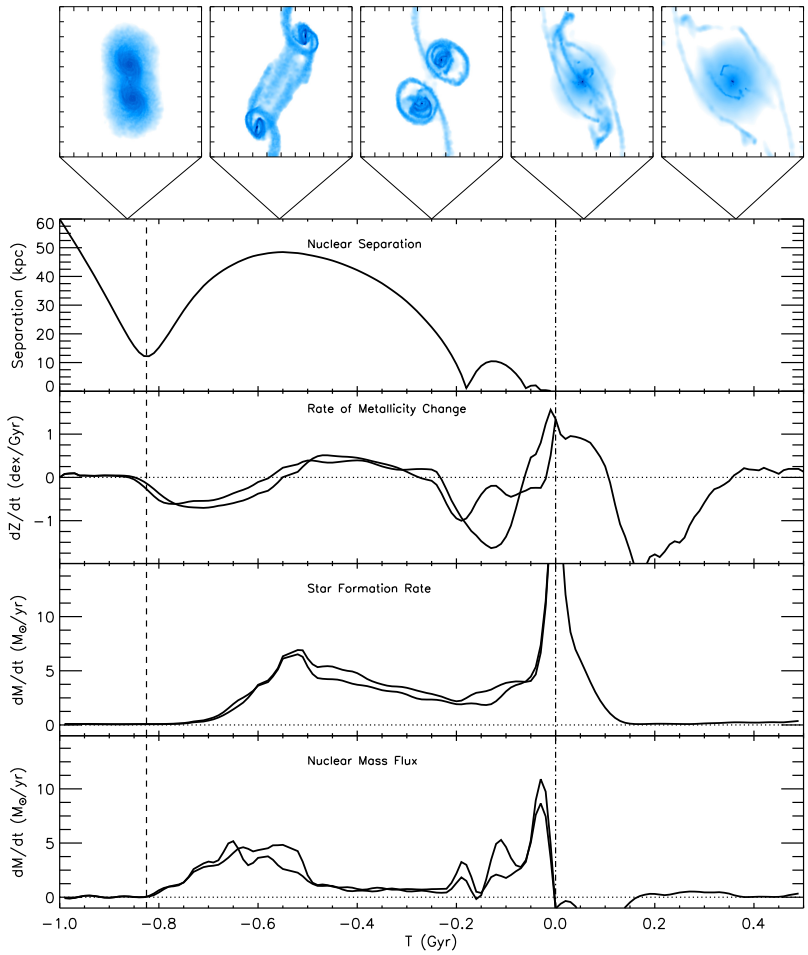

Figure 2.8.—: Several diagnostics for assessing the metallicity evolution of our fiducial merging system are shown. The top row shows contour plots of the gas density, with lines indicating the stage of the merger. From top to bottom, the subsequent time series show the galactic nuclear separation, the rate of change of the nuclear metallicity, nuclear star formation rate, and nuclear gas inflow rate. Pericenter passage and final coalescence are denoted by dashed and dot-dashed lines, respectively. In general, periods of ongoing nuclear metallicity dilution can be associated with strong nuclear gas inflows, while times of ongoing nuclear metallicity enhancement are associated with high nuclear star formation rates.

(similar to the red line in Figure 2.7) and is a clear-cut demonstration of metallicity dilution. However, when we also consider contributions from chemical enrichment and the consumption of gas via star formation, this correlation disappears.

Inspection of Figure 2.8 shows that, in general, periods of strong gas inflow occur simultaneously with times of ongoing nuclear metallicity depression. Similarly, periods of high star formation give rise to enhancements in the nuclear metallicity. Interestingly, neither the nuclear star formation rate nor the nuclear mass inflow rate correlate well with the rate of change of the nuclear metallicity because they exchange roles playing the dominate driver of the nuclear metallicity throughout the merger. The reason is that metallicity dilution, chemical enrichment, locking of gas in the stellar phase, and galactic winds all influence metallicity evolution. While more involved parameters (e.g. the difference between the star formation and nuclear mass inflow rate) yield better, albeit imperfect, correlations, these trends can be misleading and they tend to over-complicate a fairly simple point. In particular, changes to the nuclear metallicity at any time during the interaction can be understood by examining the nuclear star formation and gas inflow rates. Furthermore, the nuclear star formation and gas inflow rates are naturally explained via the well studied merger process.

From this single merger example, it seems plausible that the role of metallicity dilution and chemical enrichment are natural consequences of the merger process. However, by inspection of Figure 2.7, neither effect is overwhelmingly dominant. Hence, in the following analysis we pay attention not only to metallicity dilution and chemical enrichment, but also effects such as the locking of gas in stars and the launching of galactic winds that work to modulate the efficiency of these processes. Instead of searching for correlations between the changes in the metallicity and these distinct

processes, we vary parameters in our simulations to test their influence on the evolution of the nuclear metallicity.

Gas Consumption

Any process that can modify the gas reservoir in the nuclear region can affect the metallicity measurement. Here, we consider the influence of locking gas in the stellar phase when determining the evolution of the nuclear metallicity. Star formation lowers the reservoir of gas in the nuclear region, and hence amplifies the effect of metallicity dilution that occurs when low metallicity gas floods the central region. While this is definitely a physical effect, its magnitude will be misjudged if the simulations do not properly account for gas recycling. Using the stochastic gas recycling method outlined in §2.2.2, we are able to modulate the efficiency with which gas becomes locked in the stellar phase without changing our star formation efficiency or feedback prescriptions. Instead, we change the gas recycling parameter, allowing gas to be returned from the stellar state back to the ISM.

We first consider a simulation where newly formed stellar material is instantaneously returned to the ISM, such that no gas will be trapped in the stellar phase. At the opposite extreme, we perform a simulation with star formation, but no gas recycling (i.e. $\zeta = 0.0$), which would trap the largest amount of gas in the stellar phase. In between these extremes, we consider three values for the gas recycling fraction, ζ, that show how the nuclear metallicity evolution changes as the efficiency with which gas is locked in the stellar state is varied.

When the gas recycling parameter is set to very large values, the resulting enriched

metallicity becomes unphysically high. This occurs when many generations of star formation are allowed to occur over very short timescales as the gas is quickly recycled into the ISM repeatedly. However, the resulting dynamical metallicity remains physical and meaningful, as it describes the change in the nuclear metallicity that will occur as a function of the efficiency with which material is locked in the stellar phase. In fact, dynamical metallicity given by our simulation with instantaneous gas recycling (see the black line in the center panel of Figure 2.9) is very similar to the results of Rupke et al. (2010a). These simulations capture changes to the nuclear metallicity caused by dilution without any contributions or contamination from the creation of stars. In this case, the nuclear metallicity is well-correlated with the mass of gas in the nuclear region, as noted by Rupke et al. (2010a, see their Fig. 2). This indicates that the initially high nuclear metallicity is diluted by inflows of low metallicity gas. However, as the gas recycling parameter is dialed back to lower values, gas is more efficiently trapped in the stellar phase which increases the effect of metallicity dilution.

The simulation with star formation and no gas recycling brackets the upper end for the amount of gas that can be trapped in the stellar phase. In this case, the dynamical metallicity (red dotted line in the center plot of Figure 2.9) is lower than the dynamical metallicities of all other simulations and falls $\sim$0.2 dex below that of the nuclear metallicity with instantaneous recycling. This difference is caused purely by the effect of locking gas in the stellar state. When no gas recycling is used, a substantial fraction of the inner gaseous reservoir is converted into the stellar state, allowing influx of low metallicity gas to have stronger influences. In addition, the enriched metallicity is lower than any other simulation because the resulting star formation rates are lower when gas is efficiently locked in the stellar state. The resulting total metallicity is below

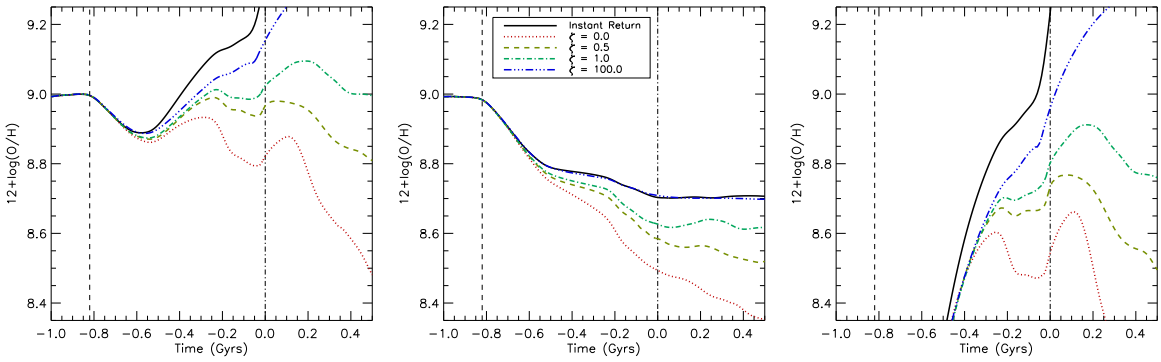

Figure 2.9.—: The total (left), dynamical (center), and enriched (right) nuclear metallicities as a function of time for "BBe" merger simulations are shown. The various lines show the nuclear metallicity evolution with several values of the gas recycling coefficient as well as complete and instantaneous gas recycling. For very large values of the gas recycling coefficient (i.e. $\zeta >> 1$), stellar particles are returned to the gas phase quickly. As the gas recycling coefficient is increased, the results approach the case of instantaneous and complete gas recycling. First pericenter passage and final coalescence are marked with vertical dashed and dot-dashed lines, respectively.

the total metallicity where gas recycling is used.

As gas recycling is included at intermediate values, both the dynamical metallicity and enriched metallicity increase. The increase in the dynamical metallicity for larger gas return fractions is well-motivated by the simple physical arguments presented above. Specifically, increasing the gas recycling fraction lowers the efficiency with gas is depleted from the nuclear region into the stellar state. Hence, as the gas recycling fraction is increased, the mass of gas in the inner reservoir increases, and the influence of metallicity dilution is decreased.

The increase in the enriched metallicity for larger gas return fractions is similarly explained. Gas that resides in the nuclear region will tend to remain there for longer periods of time (on average) and achieve higher instantaneous and integrated star formation rates (hence, higher metallicities). While this sheds light on the influence of gas recycling, we would like to use physically motivated values for the gas recycling fraction in what follows. We take the unscaled Starburst99 mass return fraction as the fiducial mass return fraction used for the remainder of this paper.

Galactic Winds

Galactic winds are thought to play a leading role in the evolution of the distribution of metals throughout cosmic time. Starburst–driven, or AGN–driven winds are a ubiquitous phenomena that act to transport metals from the depths of galaxies into the interstellar, or intergalactic medium (see, e.g., Veilleux et al. 2005, for a comprehensive review). Galactic winds may also play a prominent role in shaping the mass–metallicity relationship (see, e.g., Davé et al. 2006) and because galaxy mergers induce episodes

of enhanced star formation, they may also induce periods of significant feedback and galactic outflows thereby altering the central metallicity evolution of galaxy mergers.

In the context of this paper, galactic winds can remove gas from central regions and modify the reservoir of material contributing to the nuclear metallicity (Perez et al. 2011). In this capacity, the influence of galactic winds is identical to the locking of gas in the stellar state. To demonstrate the impact of galactic winds on the nuclear metallicity, we present a set of simulations where we vary the mass entrainment, γ. In these simulations we do include gas recycling at the fiducial level, but note that the our conclusions are unchanged if this effect is turned off.

The dynamical metallicity is not substantially affected by galactic winds. Since star formation is already fairly efficient at locking gas in the stellar state, galactic winds provide only an incremental modification to this effect. However, notable changes occur in the enriched metallicity. Specifically, the enriched metallicity is depressed for large values of the mass entrainment because gas with high star formation rates is either quickly converted into the stellar phase or launched in a wind. Therefore, the integrated star formation rates and enriched metallicity values for gas particles remains lower, on average, for higher mass entrainment values.

The resulting nuclear metallicity, shown in Figure 2.10, is depressed as mass entrainment is increased. This change is primarily caused by changes to the enriched metallicity. However, there is one additional effect that distinguishes galactic winds from locking of material in the stellar phase. While gas that is permanently locked in the stellar state will forever be unable to contribute to the nuclear metallicity or star formation, gas that has been launched in a wind will ultimately fall back onto the disk,

or even into the nuclear region. We see this effect having an influence in the enriched metallicities of the highest mass entrainment value simulations at late times. Specifically, as gas inflow from previously ejected wind material falls upon the nuclear region, the star formation rates and enriched metallicities are pushed toward higher values.

It should be noted that the galactic wind launching prescription used in this work does not describe a situation where the galactic wind predominately ejects enriched gas. In other words, the metallicity of the wind is the same as the ambient metallicity of the star forming region from which the wind was launched. This prescription could underestimate the efficiency with which metals are pushed out of a galaxy and into the intergalactic medium. However, this wind launching prescription is straightforward to understand and has the direct and notable effect of removing gas from the nuclear region.

Galactic winds do little to change the radial rearrangement of gas which attends a galaxy merger, as shown by the relative insensitivity of the dynamical metallicity to the efficiency of the winds. The only appreciable effects are on the enriched metallicity. In the following analysis, we take $\gamma = 0.3$ as the fiducial mass entrainment value (Rupke et al. 2005b).

2.4.2 Disk Spin Orientation

While the previous analysis focused on a single merger setup, the effect of merger orientation can be tested using a set of identical "B" galaxies merging from 16 orientations (a-p, as detailed in Table 2.2). All orientations maintain unique metallicity evolutions, as the specifics governing the magnitude and timing of the gas inflows and starbursts are orientation dependent. Here we will consider which aspects of our fiducial merger's

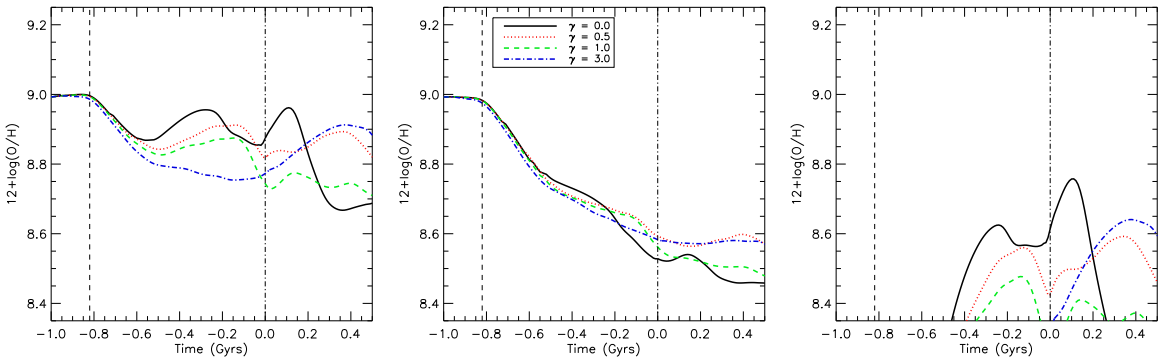

Figure 2.10.—: The nuclear metallicities are shown for varied wind launching efficiencies. First pericenter passage and final coalescence are marked with vertical dashed and dot-dashed lines, respectively.

metallicity evolution are found to hold for various merger orientations. To test this, we first examine the metallicity evolution for the four orientations shown in Figure 2.11.

As is evident from this figure, three of the four disks show strong depressions in their nuclear metallicity following pericentric passage. This is caused by the strong tidal interaction and resulting gas inflows which are a natural byproduct of the merger process. The disk not experiencing a post pericentric nuclear metallicity depression is identified as being on a nearly retrograde orientation. More concretely, the induced gas inflow following pericenter passage is found to be small compared to the other systems. The idea that some orientations, specifically those on retrograde orbits, have suppressed responses during pericentric passages has been studied previously (Toomre & Toomre 1972; D'Onghia et al. 2010), and we note that the metallicity evolution is affected accordingly in the cases where strong post-pericenter passage responses are not found.

Subsequent depressions in the nuclear metallicity, can be identified as occurring during periods of strong gas inflow caused by close encounters. For the "e" and "h" orientations, only one additional close encounter occurs before proceeding to coalescence. However, for the "f" orientation, three metallicity dips can be seen. These metallicity dips are natural products of this particular merger orientation, which leads to three distinct pericenter passages before the galaxies ultimately coalesce. While a hard and fast rule governing the metallicity depression's dependence on merger orientation cannot be given, two statements can be made: most orientations undergo a metallicity depression following pericentric passages (unless the tidal interaction is sufficiently suppressed), and most orientations show metallicity depressions immediately preceding final coalescence. Both of these statements are demonstrated in figure 2.11, where three of four (e,f, and h; not k) orientations show post-pericentric dips in their nuclear metallicity and three of

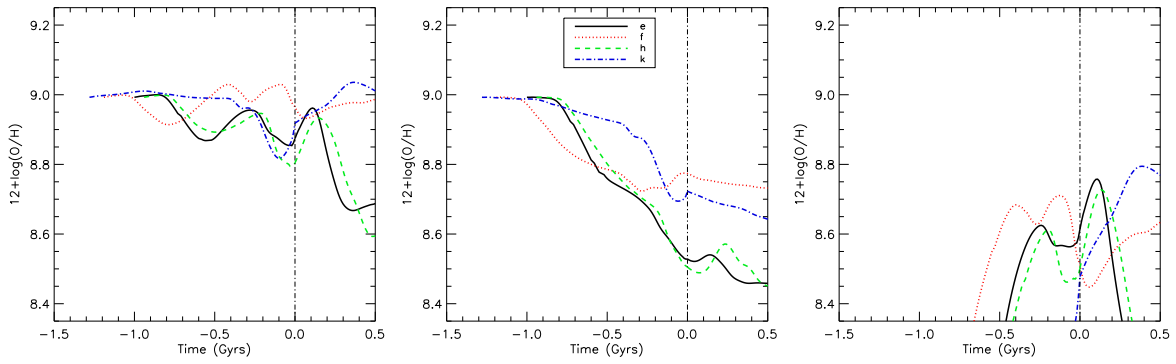

Figure 2.11.—: The nuclear metallicity evolution for four identical initial progenitor disks, set on four distinct merging trajectories, all aligned with final coalescence at $t = 0$, as indicated by the dot-dashed vertical line. Each orientation has a unique metallicity evolution, but all share common features. First, depressions of the nuclear metallicity are common following any pericentric passage (though not all pericenter passages induce nuclear metallicity depressions, as demonstrated by the "k" orientation). Second, depressions of the nuclear metallicity are common preceding final coalescence.

four (e, k, and h; not f) orientations show dips in their nuclear metallicities preceding final coalescence.

If we identify the merging time, t_m, to be the time between pericenter passage and final coalescence, we can average the metallicity evolution for several orientations to get an orientation averaged progression of the nuclear metallicity during the merger. Figure 2.12 shows the mean nuclear metallicity evolution for all 16 orientations, with the solid region indicating the 1σ variations. Despite the variation that occurs in the nuclear evolutionary tracks for individual orientations, the mean result has a well-defined pattern with reasonably small dispersion and a clear interpretation. Specifically, there are two notable metallicity depressions caused by gas inflows, one following pericentric passage and one preceding black hole coalescence, with a chemical enrichment induced peak separating in between. Also shown in Figure 2.12 is the average dynamical metallicity. Here we can see that simulations without chemical enrichment substantially under-predict the resulting nuclear metallicity. However, even when chemical enrichment is included, the mean nuclear metallicity is depressed throughout the interaction.

2.4.3 Progenitor Masses

We examine the effect that system mass has on the nuclear metallicity evolution using a set of major mergers (i.e. 1:1 mass ratios) with progenitor galaxies of varying mass. As detailed in §2.3.1, the four galaxies used in this paper are constructed to be self-similar. Hence, the mass study performed here isolates the influence of merger mass from other parameters that may scale with mass (e.g. gas fraction, galaxy structure, etc.).

We use four orientations in each mass bin (the “e”, “f”, “h”, and “k” orientations),

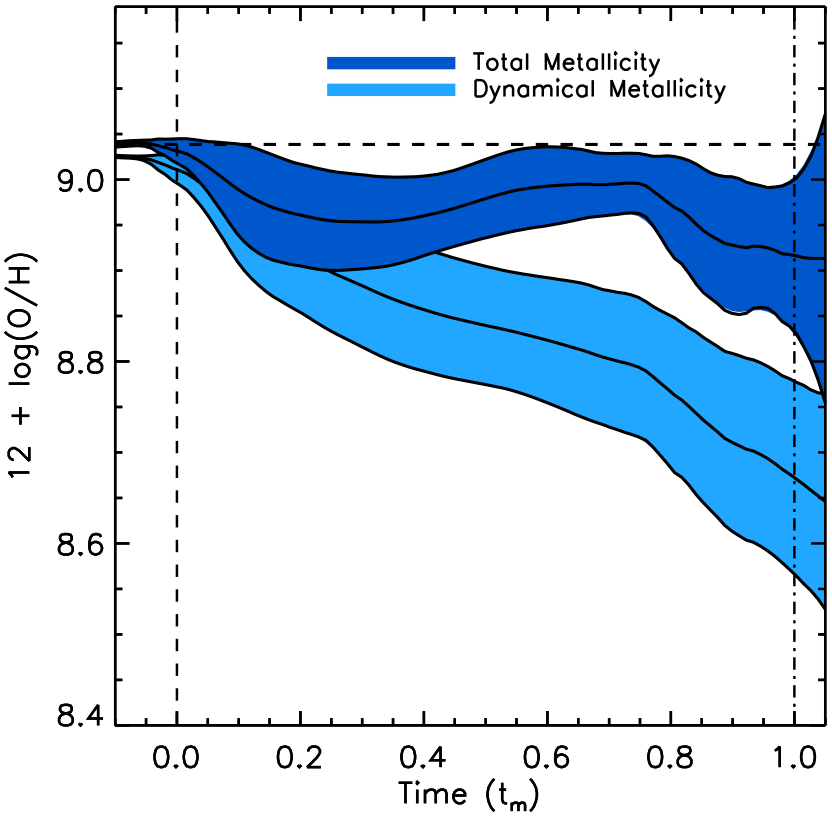

Figure 2.12.—: The average metallicity evolution for a set (orientations a-p) of major mergers with identical progenitor galaxies on different merger orientations. The dark blue region denotes the mean nuclear metallicity plus the one sigma variation for BB galaxy mergers on all 16 orientations. The light blue region shows the nuclear metallicity for the same mergers when chemical enrichment from star formation is neglected. First pericenter passage and final coalescence for all orientations are denoted by the vertical dashed and dot-dashed lines, respectively.

and average the resulting metallicity evolutionary tracks. The result, shown in Figure 2.13, is that the shape of the evolutionary track is nearly preserved, while the magnitude of the depression depends weakly on mass. We note that the preserved shape of the metallicity evolution supports our argument in the previous sections that the metallicity evolutionary track is a natural byproduct of the generic merger process. This indicates that, within the limited range of galaxy masses that are used here, the system mass is not a major consideration in determining the nuclear metallicity evolution.

2.4.4 Gas Fraction

Initial gas fraction is an important parameter to consider in nuclear metallicity evolution. For higher gas fraction galaxies that, by definition, have lower initial stellar mass, two basic changes occur: The initial nuclear metallicity of the system, as prescribed by the MZ relation, is lowered (decreasing the importance of the dynamical metallicity), and higher star formation rates occur (increasing the importance of chemical enrichment). The combined result, as discussed in this section, is that the nuclear metallicities of interacting systems at higher gas fractions tend to evolve to larger values, rather than decreasing, in contrast to their lower gas fraction counterparts.

We first consider the nuclear metallicity evolution for a series of disks with varied initial gas fractions (8, 20, 40, and 60%). We merge together these systems on the "e", "f", "h", and "k" orientations. If we initialize the metallicity properties of these disks using the local MZ relation, an assumption that we will relax later in this section, we can track the metallicity evolution and plot the change in the nuclear metallicity, as in Figure 2.14. This shows that the depressions in the nuclear metallicity that occurred for

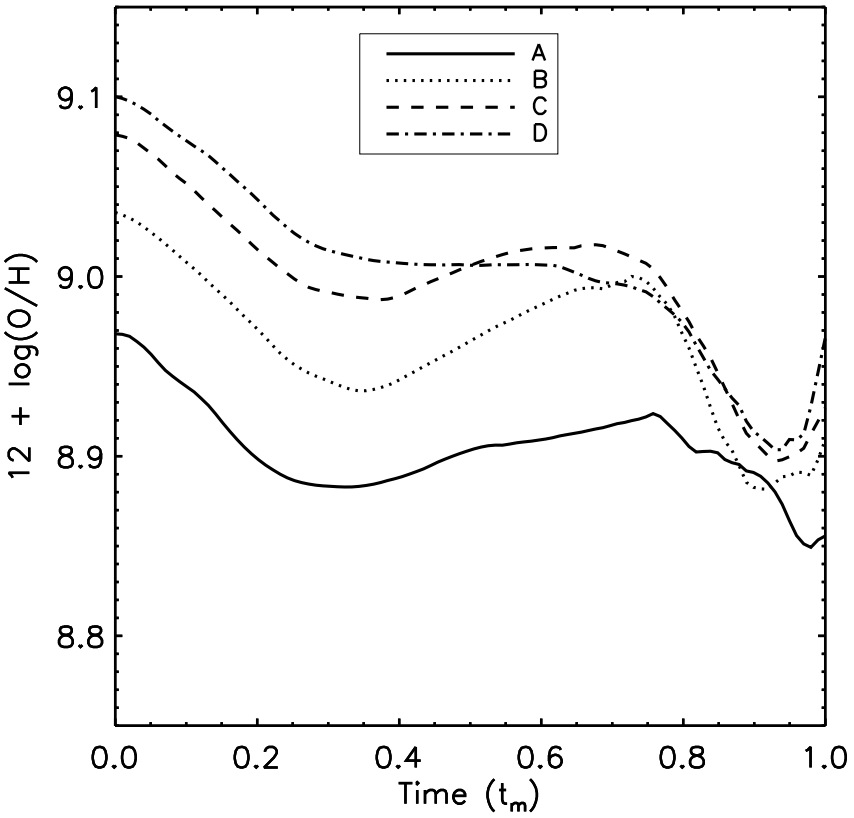

Figure 2.13.—: The average metallicity evolution for a set (the e, f, h, and k orientations) of major mergers in four mass bins.

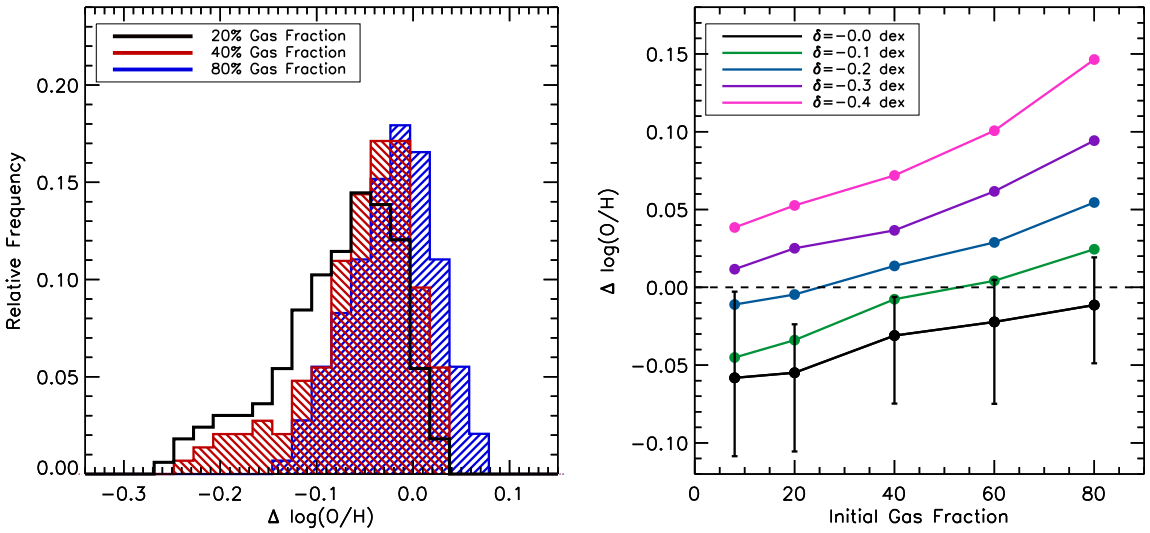

Figure 2.14.—: The distribution of changes in the nuclear metallicity for various gas fraction disks (left) and the median change in the nuclear metallicity as a function of gas fraction (right). The offset to the local MZ relation that was used is given by δ in the legend (i.e. $\delta = -0.3$ is consistent with the $z > 2$ MZ relation of Erb et al. (2006a)).

the low initial gas fractions considered in the previous sections shift toward less negative, or even positive values, as the initial gas fraction is raised. This transition is caused by the increasing dominance of the enriched metallicity over the dynamical metallicity, primarily owing to the higher star formation rates in the higher gas fraction systems.

These highest gas fraction systems, however, are not natural analogs to galaxies in the local Universe. Therefore, our choice to initialize the metallicity properties of these systems using the local MZ relation comes into question. Instead, we should consider an MZ relation better suited for higher redshifts. A full theoretical understanding of the origin of the MZ relation has not yet been obtained, however, cosmological simulations indicate that the shape of the MZ relation is achieved at early times (i.e. z>6) and that galaxies move along this MZ relation toward higher stellar mass, while the amplitude of the MZ relation slowly increases over time (Davé et al. 2006), in broad consistency with observations (Erb et al. 2006a; Maiolino et al. 2008). Without committing ourselves to a single choice for the high redshift MZ relation, we can re-initialize the metallicity properties of our galaxies using an MZ relation that is offset by a constant fixed value, δ, toward lower metallicities.

Since our simulations have no metallicity dependence, re-normalizing the MZ relation has no effect on the enriched metallicity, but lowers the impact of the dynamical metallicity. The result, shown in the right panel of Figure 2.14, is that as the the MZ relation is shifted to lower metallicities, the change in the nuclear metallicity is expected to become increasingly positive. For all choices for the initial MZ relation, the higher gas fraction systems have a median change in metallicity that is more positive than their low gas fraction counterparts.

Using the local MZ relation (i.e. the black line in Figure 2.14) for systems with relatively low gas fractions, we find that negative changes to the nuclear metallicity are expected in a merger. This is consistent with the observed lowering of the MZ relation. However, as we move to higher gas fractions, or MZ relations better suited for higher redshifts, we find that increases to the nuclear metallicity are expected. This result is caused by shifting the dominant driver of the nuclear metallicity from metallicity dilution to chemical enrichment. Moreover, if the gas content is sufficiently high, the galactic stellar component cannot efficiently torque down the gas, resulting in moderated early stage inflows (Hopkins et al. 2009b).

The same merger fundamentals apply to low and high gas fraction disks, independent of their initial metallicities, but the relative increase in the role of chemical enrichment with respect to the dynamical metallicity causes higher redshift or gas fraction systems to increase their nuclear metallicities during the merger process.

Without being overly restrictive about our choice for initial gas fraction or offset from the local MZ relation, high-redshift, gas-rich galaxies are expected to have median increases in their nuclear metallicity when undergoing a merger. Based on this evidence, we predict that the depression that occurs in the MZ relation during galaxy mergers and interactions in the local Universe would not occur at higher redshift. Instead, increases in the MZ relation are expected.

2.5 Comparison with Observations

Much work in recent years has gone into observationally classifying the metallicity of interacting or close pair galaxies in the nearby Universe (Kewley et al. 2006; Ellison et al. 2008; Peeples et al. 2009; Sol Alonso et al. 2010). In this section we compare our results directly with these observations. To facilitate this comparison, we parameterize the evolution of the nuclear metallicity in terms of the galactic projected separation. We define the projected separation as $s = r\cos(\xi)$ with ξ being a uniformly distributed random number between 0 and 2π. Since all of our systems are, by definition, interacting systems, this projected separation neglects contributions from truly non-interacting systems. We present the mass-metallicity (MZ) and separation-metallicity (SZ) relations for a simulated population of interacting galaxies.

For these comparisons, we generate a population of progenitor galaxies that contain the metallicity properties of observed field galaxies (Shields 1990; Belley & Roy 1992; Zaritsky et al. 1994; MacArthur et al. 2004). We use a Gaussian distribution for the nuclear metallicity selection with a mean value consistent with the MZ relation of Tremonti et al. (2004) with a constant standard deviation across mass bins of $\sigma = 0.1$ dex. The metallicity scale length is taken from a Gaussian distribution with a mean gradient consistent with Zaritsky et al. (1994) of $h_z = h/0.2$ with $\sigma = 0.3h_z$.

The initial metallicity properties of each galaxy in each snapshot are assigned based on the above criteria. Our ability to pick metallicity properties of the progenitor disks in our post-processing analysis is a consequence of not having a dynamical dependence on metals or allowing mixing. This lets us sample the parameter space of initial disk metallicity properties thoroughly, without re-running simulations.

2.5.1 The Mass-Metallicity Relation for Interacting Galaxies

The MZ relation for our simulated interacting galaxies is shown in Figure 2.15. We select galaxies with projected separations less than 30 kpc – the same as was used in Ellison et al. (2008). We plot the MZ relation in Figure 2.15. The result is a depressed MZ relation with an average depression of 0.07 dex, which is in agreement with the observed depression of 0.05-0.10 dex (Ellison et al. 2008).

Unlike luminosity, which can increase dramatically during merger induced starburst activity, the stellar mass of an interacting galaxy will change only by a modest factor. Therefore, the evolution of galaxies on the MZ relation is driven by changes to the nuclear metallicity, not stellar mass. In the simulation analysis, we are able to quickly determine a system's stellar mass. The stellar masses for the close pair systems included in the Ellison et al. (2008) sample have had their stellar masses determined via optical and IR colors (Kauffmann et al. 2003; Tremonti et al. 2004) which have been shown to compare well with the spectrally-determined stellar masses (Drory et al. 2004). Assuming that the observationally determined stellar masses are not strongly affected by ongoing starburst activity, the depression in both the observed and simulated MZ relation is being caused entirely by changes to the nuclear metallicity – not by changes in the galactic luminosity or stellar mass.

The depression in our simulated MZ relation would be slightly smaller if we included a set of field galaxies that lie on the MZ relation, but appear close in projected separation (i.e. if we included a population of interlopers). This result gives a comprehensive reproduction of the depression in the MZ relation for interacting galaxies that accounts for all relevant physics and the intrinsic scatter in the initial metallicity properties of the

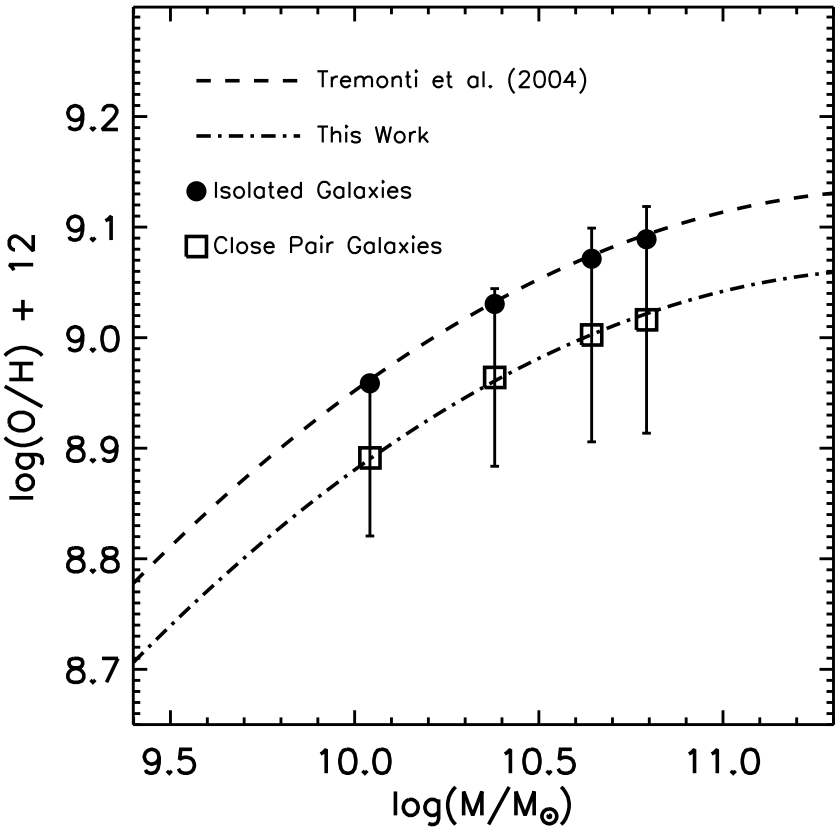

Figure 2.15.—: The simulated mass-metallicity relationship for interacting galaxies is shown. The progenitor galaxy MZ relationship from Tremonti et al. (2004) is indicated along with the second order best fit from our simulation results.

progenitor galaxies, while covering a reasonable portion of merger phase space.

2.5.2 Separation vs Metallicity

Figure 2.16 shows an example of two galaxies ("C" galaxies) from one merger simulation (the "e" orientation) moving in separation–metallicity (SZ) space as they approach coalescence. The evolution can be broken down into four distinct stages, as marked by arrows in Figure 2.16. First, the galaxies approach first pericenter passage at relatively constant nuclear metallicities. Second, the galaxies separate as gas inflows dilute their nuclear metallicity. Third, the galaxies begin falling back together, with star formation causing a significant amount of chemical enrichment. And, finally, the galaxies undergo strong gas inflows that further dilute their nuclear metallicities as they approach coalescence.

The details of this SZ evolution will change substantially with the merger orientation. However, we can gather from Figure 2.11 that all four stages of this evolution will be somewhat generic. Namely, galaxies will present constant nuclear metallicities as they approach each other for the first time, and strongly depressed nuclear metallicities as they approach final coalescence, with mildly depressed nuclear metallicities in between.

Using the evolutionary track of 2.16, we can develop some expectations for the distribution of galaxies in SZ space. Clearly, we expect close pair galaxies to show depressed nuclear metallicities. In addition, we can expect depressed metallicities out to large galactic separations. While the largest nuclear metallicity depressions are expected around close separations, widely separated interacting galaxies show mildly depressed nuclear metallicities after interacting with their companion. The observability of these

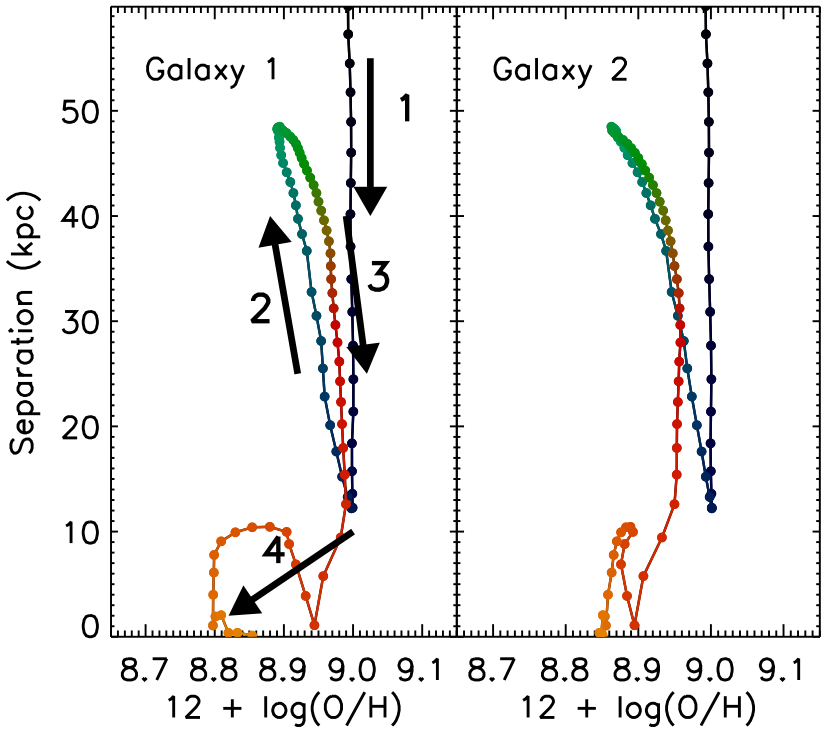

Figure 2.16.—: The evolution of two galaxies from one merger simulation are shown. The numbered arrows follow the evolution of the galaxies as they: 1) Approach first pericenter passage with an unchanging nuclear metallicity, 2) increase their separation while diluting the nuclear metallicity, 3) come together for the second time with notable contributions to the nuclear metallicity from star formation, and 4) lower their nuclear metallicity as they approach final coalescence.

trends can be assessed by using our entire merger library and converting real-separations into projected separations.

The distribution of all simulated galaxies in SZ space is shown in Figure 2.17 along with data from Kewley et al. (2006). The distribution of our simulated galaxies, shown with the colored contours in the lower half of Figure 2.17, coincide with many of the observed systems, which is demonstrated in the histogram in the top half of Figure 2.17. There is a trend toward lower metallicities with close separations. However, this trend is very mild and the most-extreme low-separation low-metallicity objects from the observed sample are not reproduced by our models. Despite this difference, it should be noted that our simulations agree with the majority of the observed objects from Kewley et al. (2006), and, there is a systematic but subtle drop in the simulated nuclear metallicity as the galaxies decrease their projected separation.

We note that the overall distribution of simulated galaxies in SZ space is relatively featureless, as evidenced by the contours in Figure 2.17. The nuclear metallicity depressions present at both small and large separations in Figure 2.16 are washed out as a result of projecting the physical separations, the wide variety of metallicity dilution versus separations that result from different spin–orbit couplings, and the scatter in the initial nuclear metallicities as prescribed by the mass-metallicity relation. In addition, while late stage mergers (e.g., stage 4 in Figure 2.16) present the largest depressions in nuclear metallicity, they only last for a short period of time compared to the overall merger process. Since we place equal weight on every timestep for every simulation when determining the distribution of simulated galaxies in Figure 2.17, the highly-depressed late-stage mergers will naturally have a less dramatic impact.

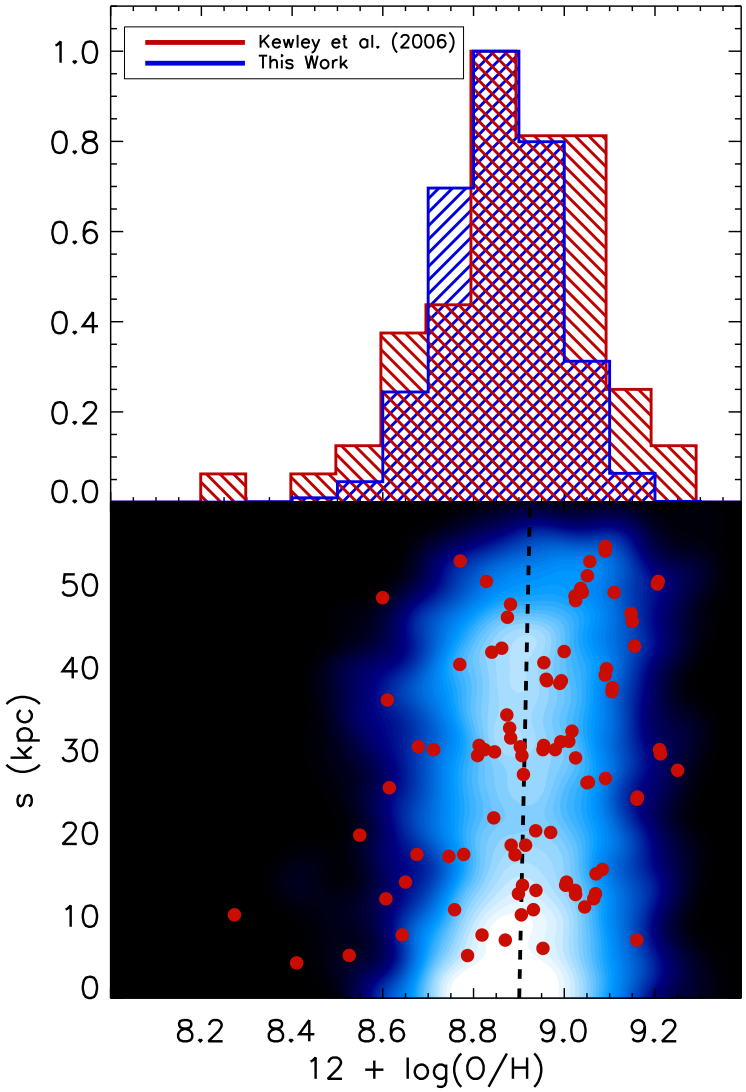

Figure 2.17.—: The relative frequency of galaxies in metallicity space (top) and the simulated separation-metallicity relationship along with the data from Kewley et al. (2006) (bottom) are shown. The majority of observed points from Kewley et al. (2006) are coincident with our simulated galaxies, with the exception of the low-metallicity, low-separation tail. Our simulated galaxies show a depression in the nuclear metallicity for close pair galaxies, however this depression is less dramatic than is required to explain the low-metallicity, low-separation tail observed in Kewley et al. (2006).

Several factors can influence the distribution of our model galaxies in SZ space. In particular, the (in)completeness of our merger library and the metal enrichment scheme will influence the resulting SZ relation. We discuss both of these factors in the following subsections, so that we may better understand the disagreement between our models and the observations at low separations and low metallicities. However, we also note that additional observations would help clarify how common these low-separation, low-metallicity objects are.

Merger Library Completeness

Although the merger library used in this work was fairly comprehensive, there is a significant portion of merger parameter space that has not been explored. Perhaps this could explain why we do not reproduce the low-separation, low-metallicity objects. We can describe our exploration of merger parameter space with two components: Variations of initial isolated galaxies models and merger configuration parameters.

Additional merger configurations (i.e. variations to the orbital orientation and angular momentum) are unlikely to yield surprising results. Out of all of our merger simulations, a maximum depression of about 0.3 dex was found, with many depressions being must less drastic. To achieve the lowest-metallicity objects found in Kewley et al. (2006), depressions of $\sim$ 0.6-0.7 dex would be required. It seems unlikely that the isolated galaxy models used in this study will reproduce very low metallicity objects, even with a more extensive exploration of merger orientations.

On the other hand, galaxy models that are significantly different from the ones used in this study, such as low mass galaxies, could fill out a new region in SZ space. For

example, galaxies with initial stellar masses of $M_s \sim 10^9 M_\odot$ will have initial nuclear metallicities of $12 + \log(O/H) \sim 8.6$ and could have their nuclear metallicities depressed to $\sim$ 8.3 or 8.4 during the merger. More generally, it seems likely that the lowest metallicity objects of Kewley et al. (2006) are likely merging systems that had low metallicities prior to the onset of the merger which may be a reasonable possibility given the low B-band luminosities associated with these objects. These systems may be reproduced by our simulations when we include a more extensive set of initial galaxy models.

Approximating Delayed Mixing

Although oxygen abundances are well-approximated by an instantaneous enrichment model, this does not necessarily imply that metals produced in SNe instantaneously migrate to HII regions. Specifically, we can relax our assumption that the metallicity of an SPH particle should be instantaneously identical to the metallicity of an HII region. Our analysis calculated the nuclear metallicity from the current metallicities of gas particles. While the metals produced in core collapse supernovae are quickly returned to the ISM ($\sim 10^7$ years) and supernovae remnants cool and fade into the ambient ISM over similar timescales ($\sim 10^6$ years), there could then be some additional delay before this gas is sufficiently mixed with the surrounding medium and ends up in HII regions. In particular, we expect the metals produced by SNe to affect the *next* generation of HII regions. As a first approximation, this does not require a change to our simulations, but rather a change to our post-processing analysis.

We can define an effective HII region metallicity that is given by the metallicity that

the SPH particle had one generation of star formation ago. If the number of generations of star formation is given by

$$N_*(t) = \frac{1}{M}\int_0^t \frac{dM_*}{dt'}dt' \tag{2.17}$$

where M is the particle mass, then the effective HII region metal content is given by

$$M'_Z(t) = \begin{cases} M_{Z,init} + yM\left(N_* - 1\right) & \text{if } N_* \geq 1 \\ \\ M_{Z,init} & \text{if } N_* < 1 \end{cases} \tag{2.18}$$

which reflects the particle's metallicity one generation of star formation in the past.

This delayed chemical enrichment scheme gives an SZ relation, shown in Figure 2.18, which has a low metallicity tail that is qualitatively similar to the observed galaxies. This does not imply that our previous calculation of the nuclear metallicity using the non-delayed chemical enrichment values were incorrect, but rather that the assumption of instantaneous transition of metals into HII regions may be overly restrictive. This is a plausible explanation, provided that the associated delay-times are reasonable estimates for the timescale over which SN ejecta would mix and diffuse into the ISM.

If we parameterize an effective HII region metallicity in terms of a delay-time, rather than an integrated star formation rate, we can get an estimate for the required delay time. Rather than neglecting the enrichment from the last generation of star formation, we neglect the enrichment that occurred over the past t_d years. The effective metal content of a particle is then given by

$$M'_Z(t) = \begin{cases} M_{Z,init} + y\int_0^{t-t_d} \frac{dM_*}{dt'}dt' & \text{if } t \geq t_d \\ \\ M_{Z,init} & \text{if } t < t_d \end{cases} \tag{2.19}$$

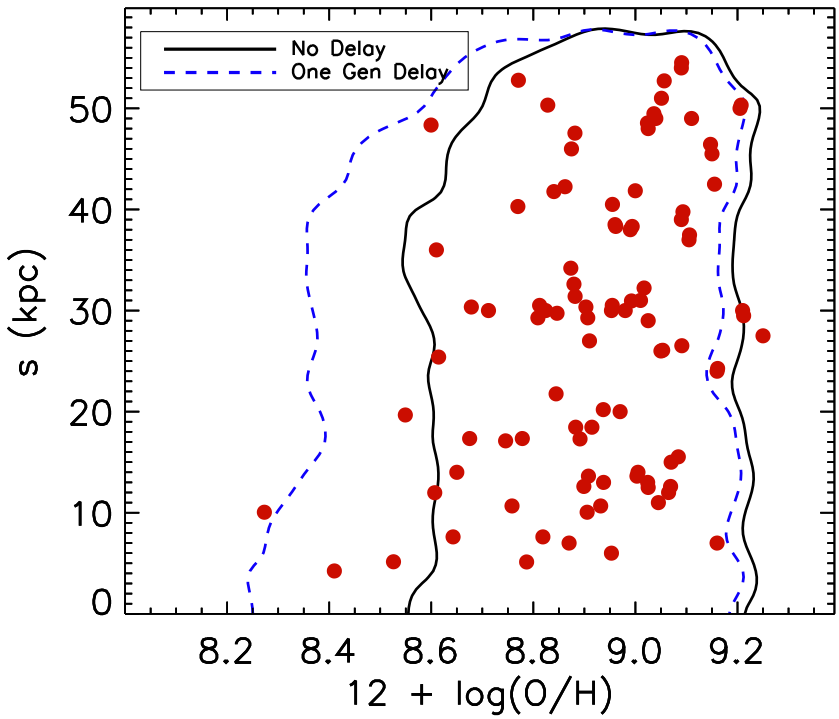

Figure 2.18.—: The simulated separation-metallicity relationship is shown using a delayed chemical enrichment scheme. Newly formed metals are allowed to contribute to the HII region metallicity measurements only after the SPH particle in which they reside undergoes an integrated star formation rate equal to its own mass. This effectively delays metal enrichment by one generation.

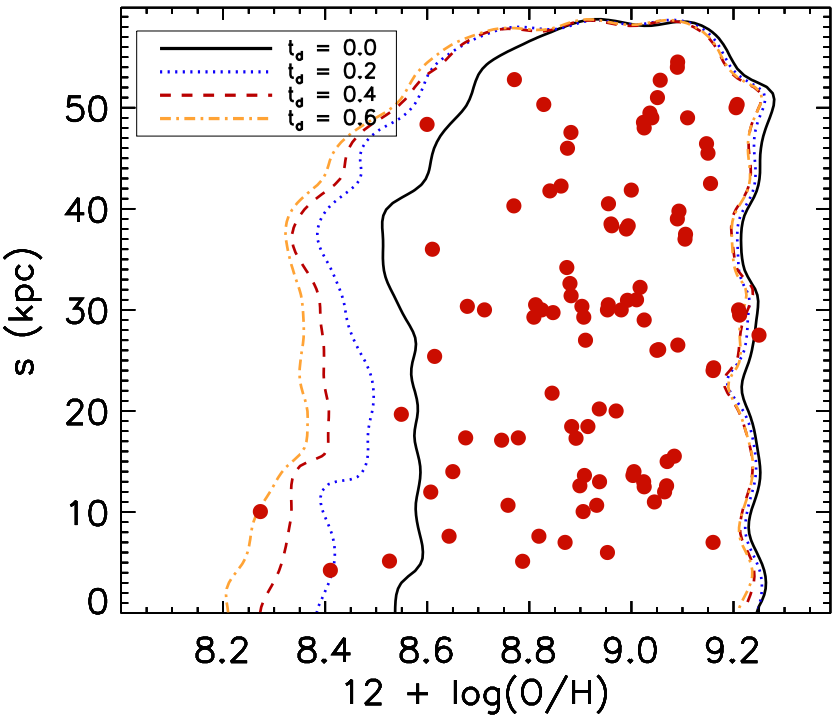

Figure 2.19.—: The simulated separation-metallicity relationship is shown using a delayed chemical enrichment scheme. Newly formed metals are allowed to contribute to the HII region metallicity measurements after a specified delay time, t_d, in Gyrs.

where t_d is the assumed time delay.

This time delayed chemical enrichment scheme gives an SZ relation, shown in Figure 2.19, where larger delay times lead to systematic decreases in the inferred metallicity of close pairs. This is similar to those seen in Figure 2.18, but with an explicit time dependence. The delay times required for our simulations to match observations is of the order of a few 10^8 years, which is comparable to estimates for the metal mixing timescale of newly produced metals into the ISM (Oey 2003; Scalo & Elmegreen 2004). We conclude that delaying the transfer of metals from SN remnants to HII regions is important to consider; however, it is unclear whether these long mixing times are appropriate for the extreme environments in merging galaxy nuclei where external forces, gas inflows, high gas densities, and large star formation rates are present.

2.6 Discussion

2.6.1 Predictions for Galaxies with High Gas Content

The results of § 2.4.4 demonstrate that the merger–induced metallicity evolution is heavily dependent upon gas content, specifically, higher gas fraction disks produce less nuclear metallicity depression than lower gas fraction disks (see, e.g., Fig. 2.14). In the extreme, high gas content mergers may even yield significant *enhancements* of central metallicity, a result that emerges both because of the increased impact of enrichment from star formation as well as because nuclear gas inflows are suppressed when the gas fraction is very high (Hopkins et al. 2009b).

As a consequence of these trends, we expect that the nuclear metallicities of gas–rich merging galaxies will be similar to, or greater than, an appropriately matched quiescent sample. This is in contrast to the depression of nuclear metallicity observed in low gas–content mergers which was the focus of this paper. Such considerations may be applicable at high redshift where current observations suggest that galaxies contain significantly higher gas fractions (Tacconi et al. 2010; Erb et al. 2006b) and suppressed metallicity at fixed galaxy mass (Erb et al. 2006a; Maiolino et al. 2008) or for less–massive gas–rich galaxies in the local universe (Catinella et al. 2010).

The predicted metallicity enhancements in gas–rich merging systems was also noted in a recent paper by Perez et al. (2011) using similar methods. While both works observed similar metallicity enhancements, the timing was not identical, and purported cause of these effects were very different. The Perez et al. (2011) model shows rapid metallicity enhancement during early stages of the merger primarily as a result of rapid star formation owing to disk instabilities in the gas–rich system (see, e.g., their Figs. 8 and 9). Such effects occur prior to, or during the early stages of the merger and are therefore decoupled from the final coalescence stage. In our model, the gas–rich disks are designed to be stable a priori, and therefore the metallicity enhancements are driven by intense star formation triggered by the merger. While the end result is the same, namely metallicity enhancements, the relative timing and strength of the vigorous star formation, the metallicity dilution owing to inflows, and the metallicity enhancement owing to star formation are fundamentally different, and therefore potentially discernible via observations.

We caution, however, that the galaxy merger simulations carried out here may require some generalization before they are directly applicable at high redshifts. Effects

such as the higher UV background, higher merger rate, and direct fueling of low metallicity gas via the surrounding intergalactic medium at high redshifts may be of significant influence in the observed metallicity of galaxies. And numerical uncertainties, such as the proper treatment of feedback from star formation and accreting black holes will invariable need to be explored.

2.6.2 Future Considerations: An Improved Chemical Enrichment Model

By comparing our models of interacting galaxies to the observed mass-metallicity (MZ) and separation–metallicity (SZ) relations we have refined our understanding of the factors at play during the metallicity evolution of galaxies. It is crucial to point out (yet rarely done so), however, that numerical results such as ours are based upon the ability to robustly track a number of complicated and interrelated astrophysical processes. While we consider our sub–resolution models to be well motivated and well tested, we admit that there are straightforward improvements to these models which will allow for more stringent tests of our physical picture. We now take a moment to outline these future improvements to our models.

The chemical enrichment model employed here tracks a global metallicity through a single scalar variable that is continuously updated assuming that the entire solar yield (assumed to be a mass fraction of 0.02) is instantaneously recycled within a single star–forming fluid element (i.e., an SPH particle). We admittedly note the simplicity of this model, but consider the ease with which it is implemented, the straightforward analysis it allows, and its inherent self–consistency as distinct advantages of this

approach. The instantaneous recycling approximation is also justified because we compare to oxygen derived metallicities, and oxygen is thought to be recycled on a short ($\sim 10^7$ years) timescale through core–collapse supernovae. Moreover, in a practical sense, similar models have been employed in nearly every SPH code over the last two decades which makes our results easy to gauge within the existing theoretical framework.

There are, however, avenues in which distinct progress can be made to our chemical enrichment model. Efforts toward this end have been pioneered by a number of authors over the last ∼5-10 years (see, e.g., Kawata 2001; Tornatore et al. 2007; Scannapieco et al. 2005; Oppenheimer & Davé 2008; Kim et al. 2009, to name a few) by employing two common features: metallicity–dependent cooling, and more complex enrichment schemes that explicitly track various species and their time–dependent release. Our gas recycling scheme is particularly well-suited for including mass return by a single stellar population. As individual star particles are converted back to interstellar gas, they can straightforwardly carry with them the appropriate enrichment from Type I and II supernovae as well as mass–loss from massive young stars and asymptotic giant branch stars. Such an approach is necessary to study trends in abundance ratios, such as those observed in the centers of elliptical galaxies.

Additional accuracy may also be gained by including sub–resolution models for the turbulent diffusion of metals (see, e.g., Wadsley et al. 2008; Shen et al. 2010). Coupled to an advanced enrichment algorithm, a physically motivated procedure for diffusing metals will allow enrichment to occur locally but still have global influences if conditions warrant. Such methods have been shown to be important for tracking metallicity in cosmological simulations (e.g., Shen et al. 2010) and we intend to assess their influence in isolated and merging galactic systems.

Finally, the comparisons between the models and the observations can be significantly improved by actually tracking the detailed line emission using 3D radiative transfer (Jonsson et al. 2010). As efforts to produce data cubes with full spatial and spectral information are developed (e.g. Rich et al. 2010), full metallicity maps can be produced and directly compared to our simulations. Radiative transfer in our simulations will shed light on any additional information that may be encoded in the line profiles and allow for a more even–handed comparison.

2.7 Conclusion

Using numerical simulations, we have investigated the impact that mergers have on galactic nuclear metallicity. Our models include the capability of describing star formation, chemical enrichment, gas recycling, and star– formation driven winds. The analysis performed here relies upon the ability to accurately track the spatial and temporal return of metals to the ISM enabled by our stochastic gas–recycling algorithm within GADGET (see § 2.2.2).

One of the primary results of this work is to reinforce the notion that galaxy mergers, and their attending gravitational tidal forces, generate significant inflows of gas shown explicitly in Figures 2.11 and 2.12 (see also Rupke et al. 2010a; Montuori et al. 2010; Perez et al. 2011). These inflows transport metal–poor gas into the nuclear region and reinforce the generic connection between close galaxy interactions and nuclear metallicity dilution – no matter how many close passages occur.

Merger–induced gaseous inflows are, however, not the only factor influencing the

nuclear metallicity, and this paper quantifies the competing effects of enrichment from star formation (§ 2.4.1), gas consumption (§ 2.4.1), and galactic winds (§ 2.4.1). Our models provide a physical template to understand nuclear metallicity evolution and lead us to conclude that merger–induced metallicity dilution and chemical enrichment from star formation drive the nuclear metallicity, while gas consumption and galactic winds play a secondary role to modulate the efficiency of the primary processes.

We have made a distinct effort in this work to directly compare our models to observations, allowing us to validate the physical evolutionary model that we have presented and associate observable trends with the various stages of the merger evolution. We find that the merger–induce depressions of nuclear metallicity are typically ~ 0.07 dex, an offset similar to that observed to the mass–metallicity relation for close pairs in SDSS (Ellison et al. 2008). The models also demonstrate that central depressions of metallicity are time–dependent owing to the specific merger orbit, the galaxies' spin–orbit coupling, and varying structural properties of the galaxies. When compared to the observed separation–metallicity relation of Kewley et al. (2006), the models generally show a similar trend to produce lower central metallicities at smaller separations. The precise role of interactions is difficult to discern, however, because of the significant scatter in the relations (see 2.17 and the discussion in §2.5.2). Future comparisons in which galaxies are morphologically classified according to merger stage, or separated according to IR luminosity or star–formation rate may be better suited to isolated the true effects of the interaction.

This work also demonstrates that the progenitor gas content can have a profound influence on the resulting merger–induced metallicity dilution. Mergers between gas–rich progenitors can yield systematic metallicity enhancement, as opposed to metallicity

dilution (see § 2.4.4, and specifically Fig. 2.14). In our picture, central metallicity enrichment comes from vigorous merger–induced star formation that can compensate for, and eventually overcome the merger–induced inflow of metal–poor gas. This view is slightly different than put forth in recent work by Perez et al. (2011), which argues that disk instabilities and clump formation drive rapid star formation and subsequent metal enrichment. But once these processes occur, which is typically early in the merger process, the story becomes similar to when the galaxies have low gas content. By studying the detailed correlations between merger stage, pair separation, central metallicity, and metallicity gradients, in both observations and the models, future work will allow for a better understanding of the (merger and enrichment) processes at work.

Chapter 3

Moving-mesh cosmology: properties of gas discs

P. Torrey, M. Vogelsberger, D. Sijacki, V. Springel, & L. Hernquist

Monthly Notices of the Royal Astronomical Society, Vol. 427, No. 3, pp. 2224, 2012

> "Never interrupt your enemy when he is making a mistake."
>
> — Napoleon Bonaparte

3.1 Introduction

A primary goal of cosmological simulations is to self-consistently reproduce the variety of galaxy morphologies observed in the local Universe. While the formation of dark matter haloes via gravitational collapse has been simulated in great detail using N-body

simulations (e.g., Springel et al. 2005c; Boylan-Kolchin et al. 2009; Fosalba et al. 2008; Teyssier et al. 2009; Klypin et al. 2011), modeling the evolution of the luminous components of galaxies has lagged behind due to the intrinsic complexity of gas dynamics and star formation. Early efforts to incorporate baryonic processes into cosmological simulations accounted for gas cooling, but did not include star formation or related feedback effects. These studies found that cooling gas accreted into dark matter haloes would quickly lose angular momentum and fall to the centre of the potential (Navarro & Benz 1991; Katz & Gunn 1991; Navarro & White 1994). The forming objects had disk-like morphologies, but with low specific angular momenta, and with most of the gas residing in a central spheroid rather than a rotationally supported disk, unlike most observed late-type galaxies. It was argued that the efficient angular momentum loss was largely a consequence of the early collapse and formation of proto-galactic clouds which were able to efficiently transfer their angular momentum to the dark matter haloes by dynamical and hydrodynamical friction during merger and accretion events.

A large number of subsequent disk formation studies have attempted to diagnose and fix this so-called "angular momentum catastrophe". Most proposed solutions are centered around preventing the gas from cooling and forming stars too efficiently at high redshift. In a simple experiment, Weil et al. (1998) showed that if gas cooling is prevented until $z = 1$, stellar disks could form with specific angular momenta consistent with observed spiral galaxies. The two widely advocated mechanisms to mitigate gas over-cooling are heating by an ultraviolet (UV) radiation field and feedback associated with star formation. The UV background (Quinn et al. 1996; Navarro & Steinmetz 1997; Hoeft et al. 2006) has been shown to inhibit the accretion of cold gas by low mass haloes, but does not appear to provide a full solution to the angular momentum problem. Star

formation with associated feedback has also been identified as a heating mechanism which might prevent early collapse (e.g. Thacker & Couchman 2000, 2001; Maller & Dekel 2002; Abadi et al. 2003; Robertson et al. 2004; Okamoto et al. 2005; Scannapieco et al. 2008) or efficiently remove low angular momentum material (e.g. Governato et al. 2010; Guedes et al. 2011) which allows less centrally concentrated disks to form. Although strong feedback can improve galactic disk formation, it is not immediately clear that this is the only solution to the angular momentum problem or if other numerical artifacts remain adversely affecting the formation of rotationally supported galaxies.

There are some well studied issues with the standard density formulation of SPH – which is the most commonly employed SPH formulation for cosmological simulation codes – that can cause spurious angular momentum transfer from gas disks. Okamoto et al. (2003) showed that gas disks embedded in a diffuse hot halo would systematically loose angular momentum due to spurious hydrodynamical torques, an effect that is particularly severe at low resolution (see also Commerçon et al. 2008). However, this problem is resolution dependent, and Governato et al. (2004) illustrated this point by presenting disk galaxy formation simulations in a ΛCDM context – without invoking strong feedback – to show that angular momentum loss could be substantially reduced by increasing the mass and spatial resolution. Similarly, Kaufmann et al. (2007) used idealized inside-out disk formation simulations to show that while spurious hydrodynamical angular momentum loss dominates at low particle resolutions, using $> 10^6$ SPH particles in each simulated galaxy can make the unphysical hydrodynamical torques subdominant.

Unfortunately, the very high resolution criteria specified in Kaufmann et al. (2007) make the near-term feasibility of carrying out full cosmological box simulations with

standard SPH poor. As a result, many recent galaxy formation studies have adopted the "zoom-in" technique, where a single galaxy can be simulated at a very high mass and spatial resolution (e.g. Guedes et al. 2011; Agertz et al. 2011). Some of these efforts have led to the formation of galaxies that share many properties in common with our own disk-dominated Milky Way. However, Agertz et al. (2011) argued that – even though they were successful in reproducing a Milky Way type disk galaxy – the properties of their simulated galaxies depend heavily on the choice of the star formation threshold, formation efficiently, feedback parameters, and other poorly constrained star formation related parameters. Since "zoom-in" simulations are limited in their scope to one halo at a time, it becomes difficult to judge if the same simulation parameters (e.g., star formation threshold, etc.) would validly reproduce the wide range of observed galaxy morphologies or observationally constrained quantities such as the global star formation rate at different redshifts. So, while "zoom-in" simulations are a very useful numerical tool to understand how individual galaxies form and evolve, it is necessary to perform large cosmological box simulations, where a wide variety of structures should naturally form which can then be compared directly to the wealth of observational galaxy data. Simulations of representative samples of the Universe permit us to test more clearly the impact of poorly constrained simulation parameters on structure formation by exploring the evolution of a full ensemble of galaxies, rather than one individual object. Once it becomes feasible to produce a large ensemble of realistic galaxies in a cosmological context, we will have a powerful tool to address questions about the driving forces behind galaxy morphological evolution that would complement the efforts of "zoom-in" simulations.

Another issue that exists in standard density SPH is the formation of dense gas

"blobs" (Kaufmann et al. 2006; van de Voort et al. 2011; Kereš & Hernquist 2009; van de Voort & Schaye 2012a), that form via numerical thermal instability that occurs in the absence of thermal conductivity (Hobbs et al. 2012). For example, Kaufmann et al. (2006) presented simulations of inside-out disk formation and found a population of dense gas blobs efficiently accreted onto their central forming galaxy. These blobs – which are not found in adaptive mesh refinement simulations (Joung et al. 2012) or more modern SPH algorithms where entropy mixing is included via thermal conductivity (Hobbs et al. 2012) – deliver a substantial amount of gas to forming galaxies, making them capable of impacting the structural properties of galactic gas disks (Sijacki et al. 2012; Hobbs et al. 2012).

One way to improve the prospects of carrying out reliable cosmological simulations without relying on substantial increases in available computational power is to improve the accuracy of the hydro solver for a fixed resolution or computational cost. For example, the primary reason for the required high resolution in Kaufmann et al. (2007) is to decrease the importance of spurious hydrodynamical torques that occur at sharp density boundaries between dense galactic gas disk and the surrounding hot gas haloes. However, if one could remove the source of the spurious hydrodynamical torques and improve the thermal mixing properties, then it may be possible to relax the high resolution criteria to a more attainable level. It is possible that this could be achieved by either modifying the SPH algorithm (e.g. Ritchie & Thomas 2001; Price 2008; Wadsley et al. 2008; Heß & Springel 2010; Read et al. 2010; Abel 2011; Saitoh & Makino 2013; Hopkins 2013) or by moving to a grid based code where these spurious hydrodynamical torques are not expected to occur (e.g. Okamoto et al. 2003). Indeed, in a recent study by Scannapieco et al. (2012) it has been shown for a single galaxy simulated at a high

resolution via a zoom-in technique that the choice for the adopted hydro solver can impact the galaxy morphology.

In this paper, we explore the formation of gas disks in two cosmological simulations: one using a traditional density based SPH formulation as implemented in GADGET (Springel 2005) and one using a novel moving-mesh grid-based hydrodynamical solver as implemented in AREPO (Springel 2010a). Both GADGET and AREPO are massively parallel hydrodynamical simulation codes that use the same gravity solver and sub-grid physics, allowing us to isolate the impact of the hydro solver at an equivalent number of initial resolution elements and nearly equivalent computational cost. We study cosmological simulation runs with the two codes and find that the gas disk scale lengths associated with the cold gas disks formed in AREPO are systematically larger than their GADGET counterparts. We discuss the reasons for these differences including the impact of the numerical resolution. The work described here is an extension of the analysis presented in Kereš et al. (2012) which discussed the properties of galaxies and haloes. In this work, we focus specifically on the properties of gas disks that form within the two simulations and compare their structural properties.

This paper is structured as follows. In Section 2, we summarize the numerical methodology. We then present our results for the gas disk properties in Section 3, and discuss the causes for the differences in Section 4. Finally, we summarize our findings in Section 5.

3.2 Methods

We consider the simulations presented in Vogelsberger et al. (2012), which were performed with the cosmological codes GADGET (Springel 2005) and AREPO (Springel 2010a). These simulations follow structure formation in an $L = 20\,\mathrm{Mpc}\ h^{-1}$ box assuming a standard ΛCDM cosmology ($\Omega_\Lambda = 0.73$, $\Omega_0 = 0.27$, $h = 0.7$, $\sigma_8 = 0.8$). The simulations contain $N_{\mathrm{DM}} = 512^3$ dark matter particles and an equivalent number of gas resolution elements at the start of the simulation, giving a mass resolution of $m_{\mathrm{DM}} = 3.722 \times 10^6 h^{-1} M_\odot$ and $m_{\mathrm{gas}} = 7.444 \times 10^5 h^{-1} M_\odot$ (note that the gas resolution element mass can change in AREPO due to mass advection across cell boundaries, but all cells maintain a mass within a factor of 2 of this target value). A comoving gravitational softening length of $\epsilon = 1 h^{-1}$ kpc was used.

3.2.1 Comparison Parameter Selection

A central premise for our comparison is that GADGET and AREPO are very similar simulation codes which allows us to hold a large number of simulation parameters and procedures the same. In addition to containing the same gravity solver, the prescriptions for the radiative cooling of gas (Katz et al. 1996), the evolution of the ionizing background radiation field (Faucher-Giguère et al. 2009), and star formation with associated feedback (Springel & Hernquist 2003a) are identical. The fundamental difference between the codes lies in their handling of gas hydrodynamics. While GADGET uses a standard density based smoothed particle hydrodynamics (SPH) technique to evolve the gas, AREPO solves the fluid equations using an exact Riemann solver on a moving unstructured mesh based on a Voronoi tessellation. AREPO has a number of

advantages over the standard SPH method due to its ability to, e.g., capture shocks more accurately and better resolve fluid instabilities (Springel 2010a; Sijacki et al. 2012; Springel 2010b). In particular, AREPO can handle weak shocks more reliably than standard SPH codes which wash these features out because of the effects of artificial viscosity (see, e.g., Keshet et al. 2003). Also, with respect to Eulerian adaptive mesh refinement (AMR) codes used in cosmology, AREPO employs a more accurate gravity solver (see, e.g., O'Shea et al. 2005) and a spatial refinement that is continuous with the motion of the fluid. Although these traits have been demonstrated in isolated test problems (Springel 2010a; Sijacki et al. 2012), we would like to understand how these numerical effects can impact the evolution of galaxies in cosmological simulations. Furthermore, because the same gravity solver and sub-grid physics prescriptions are used, we avoid some of the uncertainties that remain in code comparisons where these are allowed to vary (e.g., Frenk et al. 1999).

For our comparison, we choose to have both codes start from identical initial conditions and have the same initial number of resolution elements ($N_{\rm DM} = 512^3$, $N_{\rm gas} = 512^3$). From a practical standpoint, using the same number of initial resolution elements leads to comparable computational cost for the two codes (with the AREPO simulation taking $\sim 30\%$ more CPU time). This is an important consideration, because it is the CPU expense which sets limits on the size and complexity of simulations that can be run. However, since the two codes have roughly comparable CPU consumption for the same number of resolution elements, we simply note that neither code has a distinct advantage in this area.

From a more physical standpoint, using the same number of initial resolution elements results in similar mass resolutions between the two codes. For the dark matter

component where no inter-particle mass transfer is required, both simulations share identical mass resolutions. For the baryon component, the SPH particles in GADGET have a fixed mass in time while the cells in AREPO have a time dependent mass due to mass advection to their neighbors when solving the Riemann problem across cell boundaries. We note, however, that we have included a refinement/de-refinement scheme that maintains all hydro cells in our AREPO simulation within a factor of two of the SPH particle mass in our GADGET simulation (Vogelsberger et al. 2012). As a result, both simulations share similar (although not identical) mass resolutions. As discussed in Vogelsberger et al. (2012), we emphasize that the fixed particle mass in SPH is connected to inaccuracies made in solving the continuity equation, preventing this algorithm from correctly handling mixing.

Since the dark matter components in both simulations evolve similarly (with some potential differences resulting from the influences of the baryon components), the same large scale structure and halo properties are present in both simulations (Vogelsberger et al. 2012). As a result, we can compare gas disks which reside in a set of matching haloes that are identified as being present in both simulations. Figures 3.1 and 3.2 illustrate this point for two matching haloes taken from our simulations. In these nested maps of the projected gas surface density, it can be seen that the distribution of gas on large scales is similar in the two codes (see the leftmost panels of Figures 3.1 and 3.2). This is an expected result, as the gas distribution traces the dark matter distribution on large scales. However, as one examines the distribution of gas on galactic scales (as shown in the central and rightmost panels), it becomes clear that there are prominent differences between the two codes. Specifically, while the gas in the GADGET simulation is distributed in a large number of compact and dense clumps, in AREPO gas has a

much smoother distribution. Further inspection of Figures 3.1 and 3.2 shows that in the central region there are three galaxies – highlighted by red circles – in the process of merging. The effects of their mutual interaction can be seen in the case of AREPO, where tidal features are visible. Although these galaxies are present in GADGET as well, tidal features are much less prominent because the gas is more centrally concentrated and less rotationally supported. Perhaps the most striking finding from Figures 3.1 and 3.2, results from a comparison of the galaxy located nearest to the origin in these plots. While this object appears as a smooth, spatially extended disk in AREPO, the same object in GADGET is better described as a featureless blob.

Figures 3.1 and 3.2 summarize the motivation for this work. Even though these simulations have been initiated from the same initial conditions, share the same feedback prescriptions, and use the same number of initial resolution elements, the detailed morphological properties of the gas distribution on galactic scales can be very different. This is a very important point, because it indicates that the hydro solver has a significant impact on the gas properties. While these differences can be fairly easily identified from the gas surface density maps, a primary goal of this paper is to produce a detailed quantitative comparison of the sizes of the gas disks based on a large sample of galaxies matched between the two simulations.

3.2.2 Gas Disk Analysis

In what follows, we contrast gas disks that form in the GADGET and AREPO cosmological simulations. To facilitate this comparison, we first identify a sample of matched galaxies from the two simulations. We start by building a catalog of all structure in the each

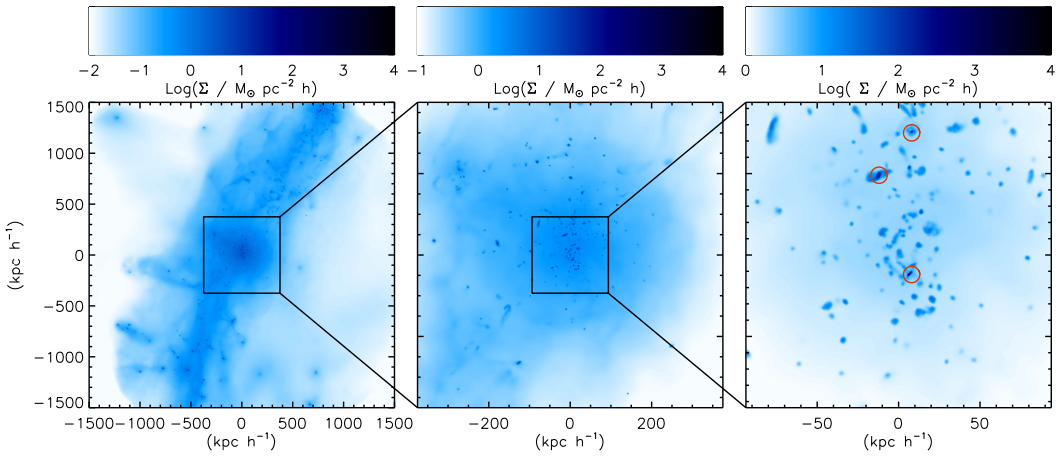

Figure 3.1.—: Maps of the projected gas surface density for one object in the GADGET simulation at redshift $z = 1$. The central object has a halo mass of $M = 2 \times 10^{12} h^{-1} M_{\odot}$. Three nested views are shown to give a clear picture of the gas distribution over a large range of spatial scales. In the rightmost panel, the gas distribution around the central galaxy can be seen to be fairly clumpy and the galaxies themselves appear fairly compact. In this image, three galaxies are in the process of merging, which we have identified with red circles. It is helpful to directly compare this plot to Figure 3.2, which shows the same maps for the AREPO simulation.

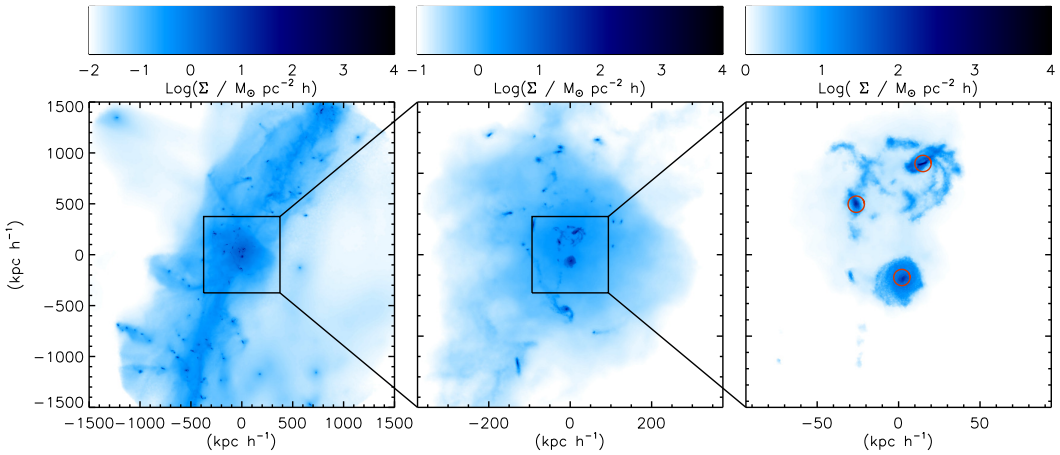

Figure 3.2.—: Same as Figure 3.1, but for the AREPO simulation. In contrast to Figure 3.1, the gas distribution around the central galaxy in the rightmost panel has much fewer gas clumps. The three galaxies that are in the process of merging are highlighted with red circles.

simulation independently using the SUBFIND tool (Springel et al. 2001). We assemble a population of "matching" haloes by finding objects in the GADGET and AREPO simulations that have the same total mass to within 10% and potential minimum locations that are not offset by more than 25% of their half mass radii. We remove any pairs where the centre of mass is offset by more than $10\,h^{-1}$kpc from the most tightly bound particle in either halo, as this may be an indication of a merging system. These selection criteria yield 1367 matching haloes in both simulations with total halo masses above $10^{10}h^{-1}\,\mathrm{M}_\odot$ at redshift $z = 0$. Figures 3.3 and 3.4 show examples of the local gas density around a series of five such matching objects in GADGET and AREPO at redshift $z = 0$ and $z = 2$, respectively.

In addition to showing differences in the spatial distribution of gas, the gas component of galaxies formed in GADGET and AREPO also differ kinematically. Figure 3.5 shows the maps of the gas surface density for an example matched galaxy with vectors indicating the local gas velocity field. Based on the topology of the velocity field, it is evident that the large gas disk in AREPO shows clear rotation about the disk's center. In contrast, the velocity field of the central galaxy for the same halo in the GADGET simulation, exhibits much lower level of circulation.

To analyze the gas disk properties, we identify the gravitationally bound cold and dense gas within each halo. We distinguish the diffuse hot halo from the colder, more dense rotating gas disk by making a cut in the $T - \rho$ phase diagram at

$$\log_{10}\left(\frac{T}{[\mathrm{K}]}\right) = 6 + 0.25\log_{10}\left(\frac{\rho}{10^{10}[\mathrm{M}_\odot\ h^2\ \mathrm{kpc}^{-3}]}\right). \tag{3.1}$$

Our subsequent analysis depends on first removing the hot halo component before measuring the disk surface density profile. However, our results are not very sensitive to

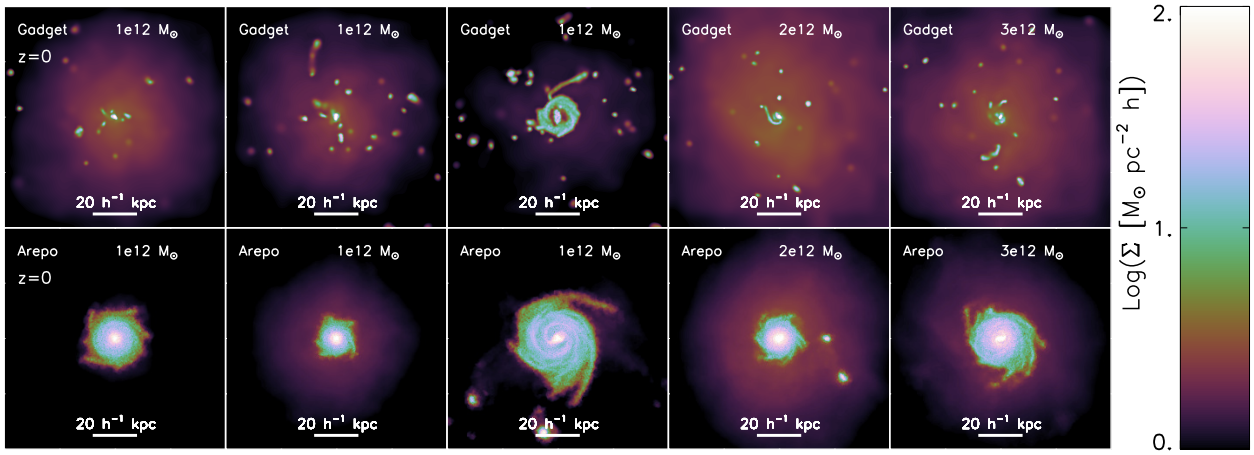

Figure 3.3.—: Projected gas surface density maps of 5 matched objects in GADGET and AREPO chosen at redshift $z = 0$ with host halo masses $\sim 10^{12} h^{-1} \mathrm{M}_{\odot}$. There are clear differences in the extent of the central gas disk. In addition, the prevalence of dense gas blobs is much higher in the GADGET simulation.

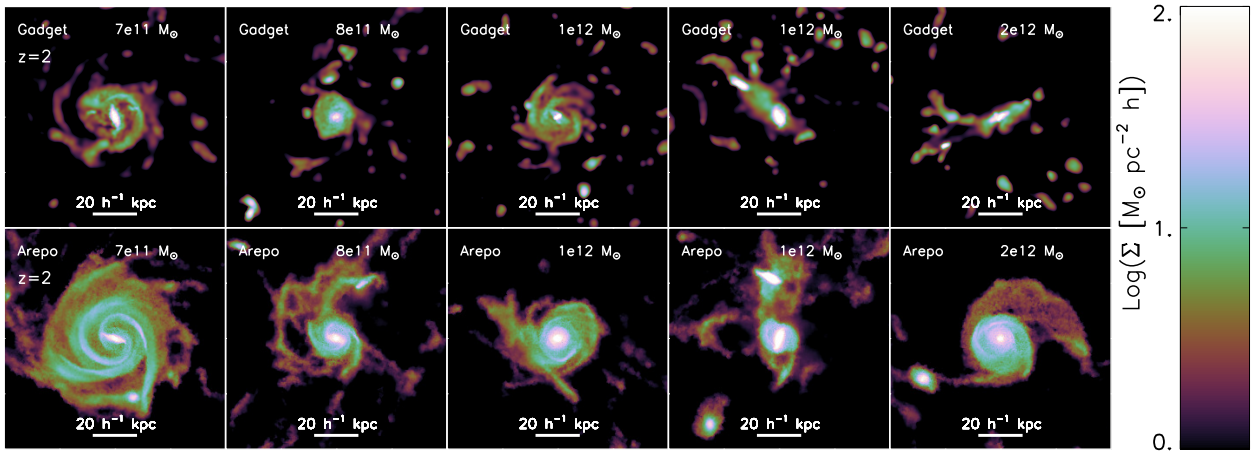

Figure 3.4.—: Projected gas surface density maps of 5 matched objects in GADGET and AREPO chosen at redshift $z = 2$ with host halo masses $\sim 10^{12}h^{-1}\mathrm{M}_{\odot}$. There are clear differences in the extent of the central gas disk. In addition, the prevalence of dense gas blobs is much higher in the GADGET simulation.

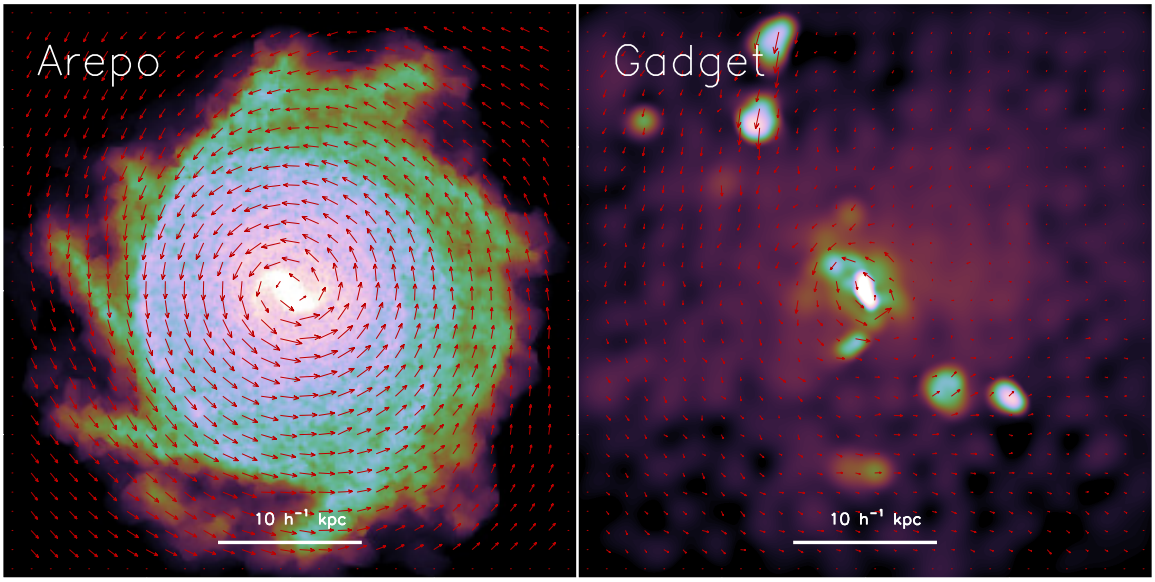

Figure 3.5.—: Maps of the projected gas surface density for a typical matched galaxy in a $M_{\rm Halo} = 10^{12} M_{\odot}$ halo. Red overplotted arrows denote the local gas velocity field. The AREPO galaxy (left panel) is significantly more rotationally supported than its GADGET counterpart (right panel).

this particular cut in the phase diagram (i.e. moving the normalization of this cut up or down by a factor of 5 would not change our conclusions). The remaining cold and dense gas is translated to place the centre of mass at the origin and rotated to align the net gas angular momentum vector in the $\hat{z}$ direction.

Before moving forward, we note that the definition of cold/dense gas cut defined in equation (3.1) can select material which is not part of the central gas disk. In particular, we find that high mass haloes in GADGET contain a population of low mass cold gas clumps which have no associated dark matter overdensity. The rightmost panel in Figure 3.1 shows an example of these gas clumps outside of the central object and a similar population of clumps can be found in all massive (i.e. $\sim 10^{12}h^{-1}M_{\odot}$) haloes in the GADGET run. We note that such clumps are also seen in simulations of galaxy formation carried out with other SPH codes (e.g. Okamoto et al. 2008; Guedes et al. 2011). Most of these clumps are not part of the galactic disk – many of them have entered the halo for the first time, have not yet had any contact with the central galaxy, and are on very non-circular trajectories. However, the density and temperature of these clumps allows them to be selected as "disk mass" according to the definition outlined in equation (3.1).

In principle, we could remove these cold gas clumps by imposing some additional criteria in our "disk gas" selection, e.g., we could require disk gas to be on nearly circular trajectories or link together the central disk using a friends-of-friends (FOF) algorithm. Nonetheless, at this point we choose not to impose any additional selection criteria for two reasons. First, we find that de-selecting clump material can be sensitive to the details of the clump removal technique that we use. For example, while running a FOF algorithm on the cold and dense gas can efficiently remove clumps that are more

than 15 or 20 h^{-1} kpc from the central galaxy, removing the most centrally located gas clumps can depend on our choice for the linking length. Second, since these clumps are only present in GADGET, we find that removing them tends to decrease the disk scale lengths obtained for massive GADGET galaxies without having any noticeable impact on the same objects in AREPO. Since one of the conclusions in this paper is that gas disks formed in GADGET are indeed more centrally concentrated than those formed in AREPO, we have tried to avoid any steps in our analysis that could be perceived as artificially pushing us toward that result. Thus, in the following section on gas disk properties, we leave these clumps in our definition of disk mass and save additional discussion about their origin and impact for section 3.4.3.

3.3 Disk Comparison

To find the average surface density profile for gas disks, we stack the profiles for all objects in a given halo mass range. A representative set of stacked surface density profiles is shown in Figure 3.6. We find the best-fit exponential profile

$$\Sigma(r) = \Sigma_0 \exp(-r/R_{\rm d}) \tag{3.2}$$

for each surface density profile via a chi-squared minimization. Note from Figure 3.6 that most of the profiles can be fit using a single exponential. However, almost all profiles are distinctly steeper in the inner regions, and this is especially pronounced for GADGET galaxies. This compact central feature is typically associated with a slowly rotating spheroidal component. Since we are primarily interested in the structure of the spatially extended disks and because this inner region is not well-resolved in our current simulations (the softening length is $1\,h^{-1}\,$kpc co-moving, with gravity becoming

fully Newtonian after $2.8\,h^{-1}\,\mathrm{kpc}$, co-moving, for the spline softening employed here (Hernquist & Katz 1989)), we perform fits by both including and excluding the central $2.8\,h^{-1}\,\mathrm{kpc}$. We check the quality of each fit by comparing the integral of the best fit surface density profile in the fitted region to the true disk mass measured in the simulation. We note that when we exclude the central region all fits for both GADGET and AREPO return the cold, dense gas mass (as defined by equation 3.2) within 10%, indicating that our prescribed exponential functions are serving as good representations of the actual stacked surface density profiles. When we include the central region, the GADGET fits underestimate the disk mass by ∼20-30% while the AREPO fits underestimate the disk mass by ∼10%. This difference – which is more pronounced for GADGET – is caused by a concentration of material in the central region.

The distribution of best fit parameters, Σ_0 and R_d, of the exponential surface density profiles are shown in Figure 3.7. We have performed the fits when including (left panel) and excluding (right panel) the central region. We find the GADGET best-fit central densities are systematically lowered when we exclude the central region, while the AREPO central densities changes less. This is a result of the fact that, on average, GADGET objects contain a larger fraction of their gas in the central region. More importantly, we find that the distribution of disk scale lengths is systematically different between the GADGET and AREPO galaxies, with the AREPO galaxies being described by larger scale lengths regardless of whether we account for the central region. This is a central result of this paper, and confirms the idea that the AREPO disks are larger based on visual inspection of the gas surface density maps. We emphasize that changing the number of galaxies in each stacked surface density profile, the exact normalization of our cold/hot phase boundary cut, or other detailed aspects of the analysis does not

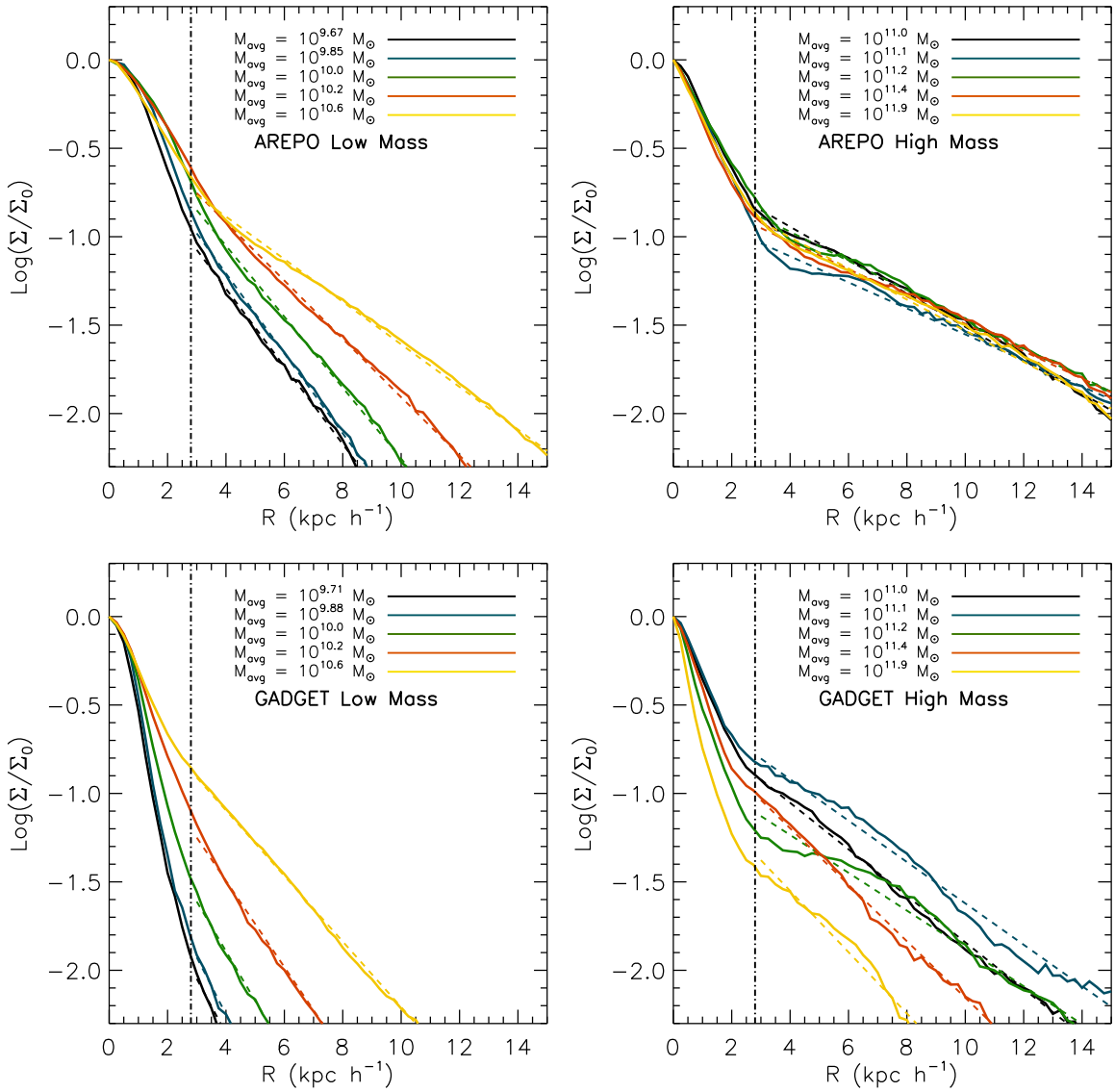

Figure 3.6.—: Stacked mass profiles at $z = 0$ for the low mass AREPO objects (top left), high mass AREPO objects (top right), low mass GADGET objects (bottom left) and high mass GADGET objects (bottom right). The true mass profiles are shown as solid lines, while the best fit exponential functions are shown as dashed lines. Each colour corresponds to an average surface density profile for all galaxies in a given halo mass range, with the average halo mass, $M_{\rm avg}$, indicated in the legend. The vertical dot-dashed lines denote the spatial scale over which the gravitational potential is softened, i.e. $2.8\,h^{-1}$ kpc, co-moving.

affect this conclusion.

Figure 3.7 shows clearly the average offset toward larger disk scale lengths for the AREPO gas disks, we find it instructive to show the best-fit exponential disk scale lengths as a function of host halo mass. Figure 3.8 shows the disk scale lengths (including the central $2.8\,h^{-1}\,\mathrm{kpc}$) as a function of halo mass at redshifts $z = 2$ and $z = 0$ in the left and right panels, respectively. This allows us to see more clearly how the gas disks from the two codes compare to one another at a fixed halo mass. For each bin we show disk scale length values obtained by first stacking the objects and then fitting the exponential surface density profiles (continuous lines), and by computing the median disk scale length from a set of individually fit galaxy surface density profiles (dashed lines). Hatched regions mark 25% and 75% of the distribution for the individually fit profiles. Regardless of the adopted procedure, the AREPO galaxies have larger scale lengths than their GADGET counterparts at both redshifts and for all halo masses. From Figure 3.8, it results that the AREPO disks are between 1.5 to 2 times larger than their GADGET counterparts.

We note that for objects with a halo mass $M > 10^{11.5} h^{-1}\ M_{\odot}$ there is a discrepancy between the disk scale lengths obtained using our stacking procedure with respect to the median disk scale lengths obtained from individual objects in the GADGET simulations. The reason for this discrepancy is the presence of cold gas blobs surrounding the central gas disk. As discussed in the previous section, since these blobs are cold and dense they are included in our definition of "disk gas". Stacking many objects with a large population of blobs can then systematically bias the estimate of the disk scale length. Thus we note that the apparent trend of the disk scale length with the halo mass at the

high mass end in the GADGET simulations as seen in the lower right panel of Figure 3.8 is affected by the presence of cold blobs. For these high mass systems, the central disks are just not well described by single exponential profiles. An analogous population of cold gas blobs is not present in the AREPO simulation. This is the primary reasons why the solid and dashed lines – representing the stacked best fit disk scale length and median of individually fit disk scale lengths – are in better mutual agreement for AREPO galaxies.

Differences between the GADGET and AREPO galaxies can also be seen via a histogram of the gas specific angular momentum, as shown in Figure 3.9. In this plot, where the specific angular momentum distribution for the example galaxies illustrated in Figure 3.5 is shown, there is a clear distinction between the two codes. The AREPO galaxy shows a narrow distribution around j_{circ} with most of the gas on circular orbits, and thus rotationally supported. The GADGET galaxy instead exhibits a much wider distribution around $j_z/j_{circ} = 1$ due to the significant gas component which is on highly non-circular orbits, with some material even counter-rotating, as evidenced by negative j_z/j_{circ} values.

Figure 3.10 shows the specific angular momenta of the gas disks and of all baryons as a function of galaxy baryon mass. The hatched regions indicate where actual spiral and elliptical galaxies are located, as noted by Fall (1983). We have verified that the recent observational sample of Courteau et al. (2007) falls within the hatched region occupied by spirals. We find the specific angular momenta of the cold gas and stellar material in the AREPO simulation to be significantly larger than that of the GADGET objects. The larger specific angular momenta of the AREPO galaxies indicates that they are more rotationally supported, which accounts for their larger disk scale lengths.

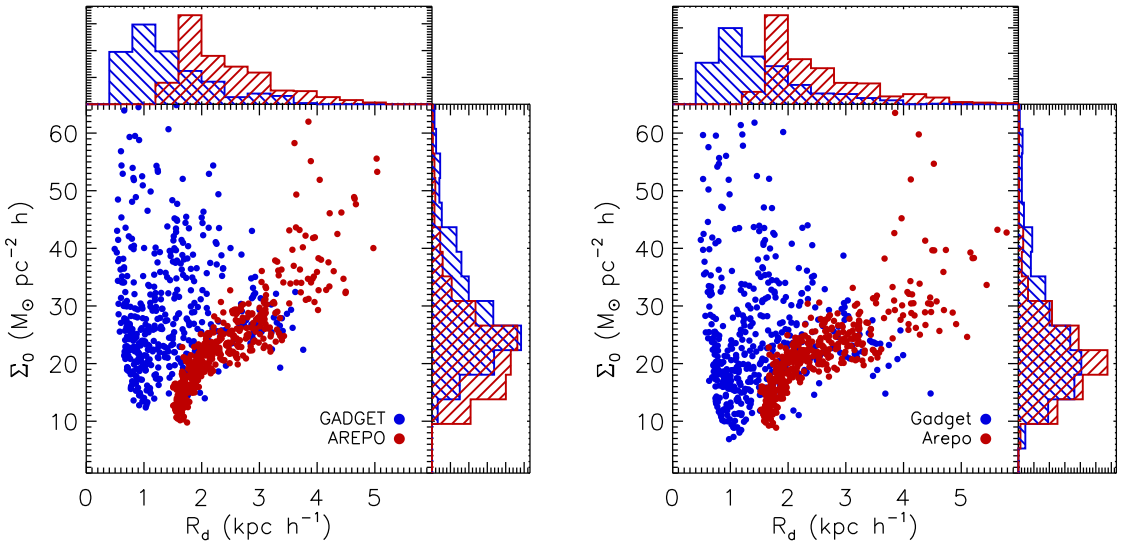

Figure 3.7.—: The best fit exponential surface density profile parameters to the whole disk (left) and with the central region excluded (right). The distribution of best fit parameters for $R_{\rm d}$ and Σ_0 is illustrated in the histograms. Clearly, AREPO objects have larger disk scale lengths than their GADGET counterparts. Including or excluding the central region does not alter this conclusion.

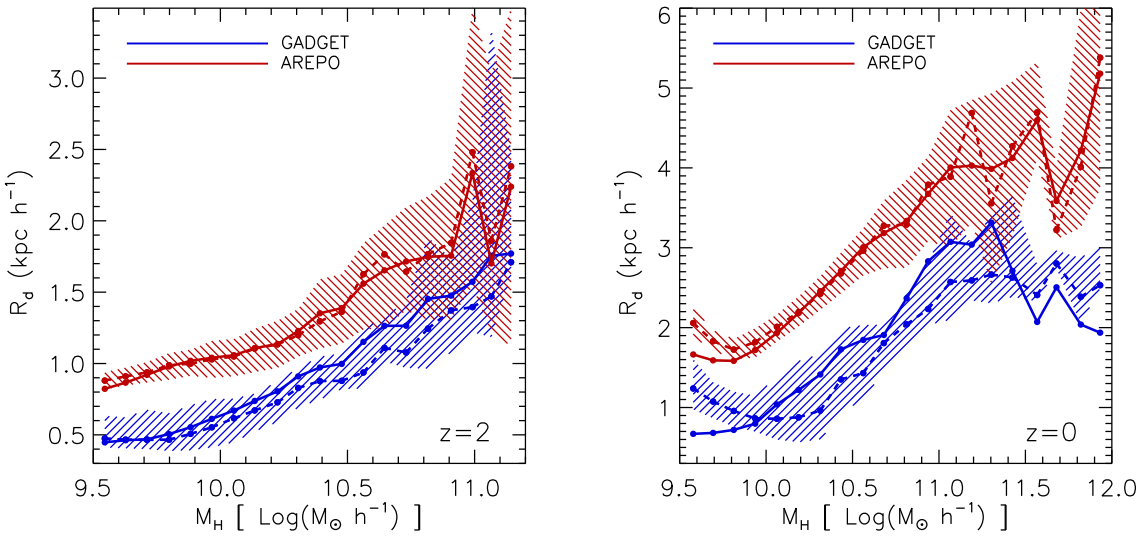

Figure 3.8.—: The best fit exponential disk scale lengths (in physical units) as a function of halo mass for GADGET and AREPO objects at $z = 2$ (right) and $z = 0$ (left). Continuous lines indicate $R_{\rm d}$ values for the stacked galaxies in each mass bin, while dashed lines denote the median $R_{\rm d}$ obtained by fitting exponential profiles to individual objects. Hatched regions are 25% and 75% of the distribution. The AREPO disks are substantially larger at all halo masses and at both redshifts.

3.4 Origin of the Discrepancies

In this paper we have presented a comparison of gas disks formed in cosmological simulations (Vogelsberger et al. 2012) performed with the SPH based code GADGET and the moving-mesh code AREPO. Both codes use an identical gravity solver and include the same physical processes (e.g., cooling, sub-grid model for star formation and feedback), but use fundamentally different hydro solvers. Whereas GADGET uses an SPH approach to evolve the gas, AREPO uses a finite volume scheme on a moving Voronoi mesh.

Our primary conclusion is that the cold gas disks that form with AREPO are described by notably different surface density profiles than disks formed using GADGET. We showed that, on average, the cold gas disks in AREPO simulations have significantly larger scale lengths compared to a matched sample of GADGET disks. Consistently, we also find higher specific angular momenta for the AREPO disks. Now that we have identified systematic differences in the disk scale lengths and angular momenta we discuss their principle numerical origins and address ways in which the discrepancies may be reduced.

3.4.1 Spurious Hydrodynamical Torques

It is well-known that conventional formulations of SPH suffer from artificial angular momentum transport at phase boundaries – like the hot halo cold-disk transition. For example, Okamoto et al. (2003) showed that SPH simulations are prone to angular momentum transfer at this interface and that this can have implications for disk formation in cosmological simulations. Moreover, Okamoto et al. (2003) demonstrated

that shearing flows at phase boundaries are more accurately captured in grid-based hydro solvers. Thus, this is one particular area where we expect that the hydro solver included in AREPO should yield more accurate results compared to GADGET.

One solution to this problem is to completely decouple the "hot" and "cold" particle neighbor searches (Okamoto et al. 2003; Marri & White 2003). In principle, this modification does a better job at estimating the local gas density using only particles that are in the same phase allowing for a cleaner separation of multi-phase gas boundaries. Since this will eliminate all hydrodynamical interactions between the hot and cold phase the spurious loss of angular momentum will be eliminated. However, decoupling the neighbor searches for particles based on their phase could also lead to artificial suppression of other physical phenomena that rely on direct interaction of multi phase gas such as ram pressure stripping or shock capturing (see, e.g., the discussion in Marri & White 2003, for their procedure to address this issue).

Another solution proposed is to increase the simulation resolution substantially (Okamoto et al. 2003; Kaufmann et al. 2007). Increasing the resolution will reduce the influence of the pressure gradient mis-estimation that occurs at density phase boundaries in standard SPH (see e.g. Agertz et al. 2007). Kaufmann et al. (2007) tested the impact of resolution on idealized inside-out disk formation simulations using SPH and found that by increasing the number of SPH particles in a halo above 10^6 the artificial hydrodynamical angular momentum loss became subdominant to other torquing mechanisms. This problem is less severe (if present at all) in grid based codes like AREPO where both density phase boundaries and shearing flows are more accurately handled (Okamoto et al. 2003; Agertz et al. 2007; Sijacki et al. 2012). As a result, simulated gas disks in GADGET rapidly loose their angular momentum unless they have

a very large number of resolution elements while the same gas disks are able to evolve without such severe angular momentum loss at the same resolution in AREPO.

Since this artificial angular momentum transport is most prominent at low resolution, this is the main reason for the differences seen between the disk scale lengths of GADGET and AREPO objects at relatively low masses (i.e. $< 10^{11} h^{-1}\ M_{\odot}$) and will contribute to the loss of angular momentum for higher mass systems (i.e. $< 10^{12} h^{-1}\ M_{\odot}$). We note that the most massive haloes considered in our current paper approach the resolution criteria set forth by Kaufmann et al. (2007) (i.e. $\sim 10^6$ particles per halo), so we do not expect spurious hydrodynamical angular momentum loss to be the dominant problem in our high mass simulated objects. However, for the low mass objects in our simulation which are by definition more poorly resolved, spurious angular momentum loss is bound to have a substantially larger impact. This conclusion is supported by examining the specific angular momentum content of the GADGET and AREPO galaxies – as shown in Figure 3.10 – which demonstrates that the discrepancy between the two codes is larger for low mass galaxies.

The resolution dependence of spurious hydrodynamical angular momentum transport demonstrated in Kaufmann et al. (2007) implies that increasing the resolution of our GADGET simulations by an appropriate factor (an increase in the number of SPH particles of 10^3 would give us the desired 10^6 particles per halo at the low mass end) could improve the agreement between GADGET and AREPO. In fact, since massive galaxies are assembled via hierarchically merging smaller objects together, it is necessary to have $> 10^6$ SPH particles in all haloes – including low mass systems – to avoid spuriously loosing angular momentum in low mass systems that will ultimately become part of a well resolved, high mass galaxies (Kaufmann et al. 2007). This is seemingly in

accord with the results of very high resolution "zoom-in" simulations (e.g. Governato et al. 2004) that have found the angular momentum loss in gas disks formed in standard SPH simulations can be substantially reduced by increasing the particle resolution. However, while the 10^6 SPH resolution elements per halo is a reasonable requirement for "zoom-in" simulations, this same requirement is not yet feasible for intermediate and low mass haloes in full cosmological box simulations. In that sense, we consider it an advantage that grid based codes such as AREPO do not suffer from this spurious hydrodynamical angular momentum loss even at resolutions well below 10^6 particles per halo.

3.4.2 Gas Heating and Cooling

Although GADGET and AREPO share the same prescriptions for radiative gas cooling, non-adiabatic heat sources and mixing at phase boundaries can cause differences in the growth of galactic gas disks. Vogelsberger et al. (2012) presented an analysis of the evolving thermodynamic gas properties in our cosmological simulations. One conclusion from this analysis is that the cooling in AREPO is more efficient than in GADGET, which is driven primarily by differences in the cooling rates of diffuse halo gas. There are two main reasons for the differences in these cooling rates which are discussed in detail in Vogelsberger et al. (2012) and summarized here.

The first reason is differences in dissipative heating in haloes driven by the presence of turbulent energy. Bauer & Springel (2012) performed a comparison of the properties of simulated driven turbulence using GADGET and AREPO and found that while the two codes produce similar velocity and density power spectra for high mach numbers

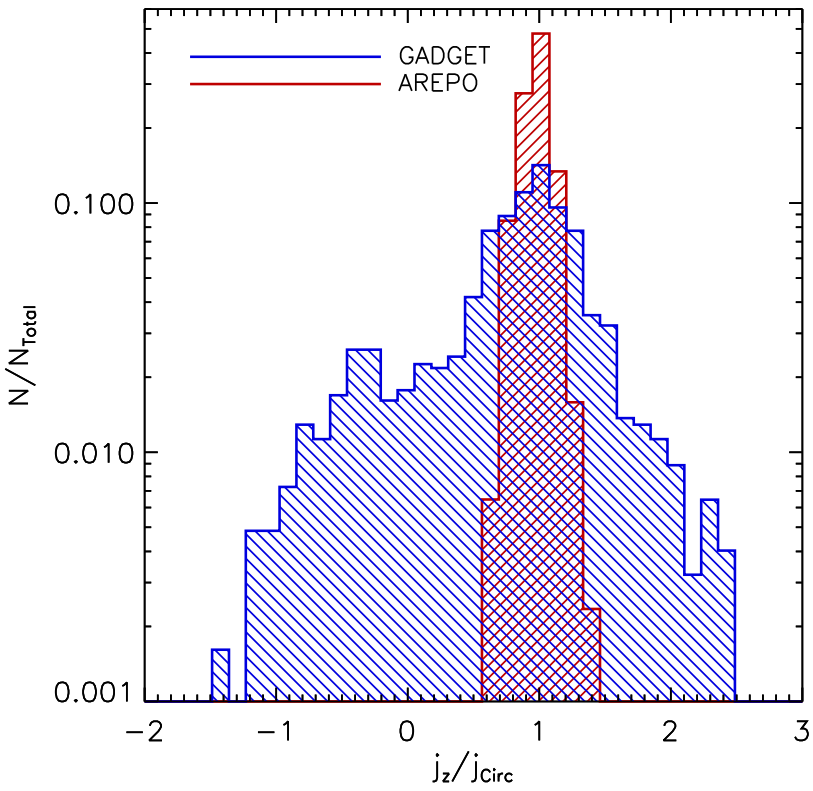

Figure 3.9.—: The distribution of specific angular momenta in the disk for a typical matched galaxy in a $M_{\rm Halo} = 10^{12} M_{\odot}$ halo. On the x-axis the ratio of the $\hat{z}$-component of the specific angular momentum to the expected specific angular momentum for a particle at that location on a circular orbit is shown. Both codes exhibit distributions that peak about 1, which corresponds to a rotationally supported gas disk. However, while the AREPO disk shows a narrow distribution, with most gas being on nearly circular orbits, the GADGET object has a much wider distribution, with some gas on highly non-circular trajectories.

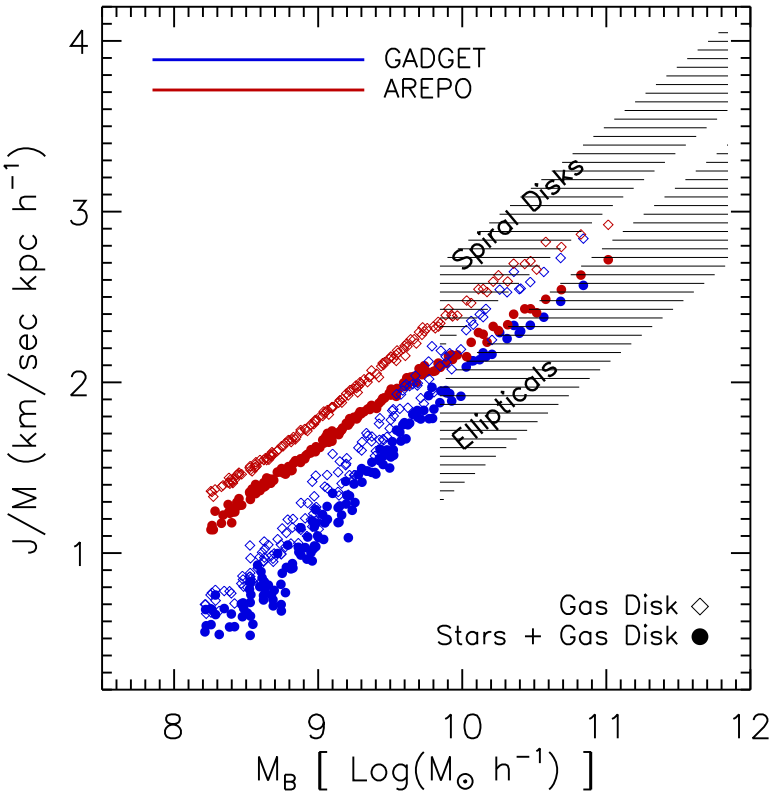

Figure 3.10.—: Specific angular momentum as a function of baryon mass for the gas (diamonds) and baryons (filled circles) for the matched sample of AREPO and GADGET galaxies. Hatched regions denote locations of spirals and ellipticals on this diagram as defined by Fall (1983).

(i.e. for highly supersonic driven turbulence), there are prominent differences in the way turbulent power cascades to smaller scales in the subsonic regime. In AREPO, a Kolmogorov-like turbulent cascade is recovered which transports energy to smaller spatial scales. However, in GADGET, the turbulent large scale eddies are quickly dissipated close to the cooling radius and transformed into incoherent small-scale velocity noise which is converted into thermal energy as the velocity noise is damped out via artificial viscosity. This heats gas and inhibits cooling in GADGET haloes, driving part of the difference in the cooling rates seen in Vogelsberger et al. (2012).

The second reason stems from differences in mixing between the two codes, especially at density phase boundaries. For low mass galaxies, the gas cooling timescale in the halo is relatively short, such that the material is able to cool onto the central galaxy with similar efficiency in both codes. However, for a typical massive galaxy in our simulations, the diffuse halo gas becomes sufficiently hot and the gas cannot cool rapidly due to radiative losses. However, mixing that occurs around in-falling substructures as cool gas is hydrodynamically stripped can substantially lower the local cooling timescale (Marinacci et al. 2010). Idealized tests of gas stripping (Agertz et al. 2007; Sijacki et al. 2012) show that this mixing will be suppressed in GADGET.

A similar mixing boundary layer can develop at the interface of the central gas disk and the diffuse hot halo. This shearing phase boundary can generate mixing via Kelvin-Helmholtz instabilities which will be poorly resolved in GADGET (Okamoto et al. 2003). Although the diffuse halo gas sitting just above the gas disk boundary may have long cooling times, continued efficient hot-mode gas accretion can be facilitated by mixing at this boundary. Sijacki et al. (2012) demonstrated this point by examining the cooling rates of gas in an idealized gas sphere with GADGET and AREPO. They find that

the cooling rates are nearly identical when no gas rotation is included, which validates that the cooling prescriptions in both codes are in fact functionally identical. However, when the same test is repeated with gas rotation the cooling rates for the two codes became discrepant, with AREPO cooling more efficiently. The more efficient cooling only sets in once a substantial amount of gas settles into a rotationally supported disk that can interact with the ambient halo gas. Kereš et al. (2012) present evidence for enhanced cooling of this same sort in massive galaxies in the cosmological simulations by noting that the hot haloes in AREPO have cooler cores compared to GADGET and the gas in AREPO tends to be on radially inward trajectories – both of which are consistent with a scenario of less subsonic turbulence dissipation and of increased cooling in a mixing boundary layer between the diffuse halo gas and dense gas disk.

The combined effect of "extra heating" in GADGET from the poorly resolved turbulent power cascade and "extra cooling" in AREPO from better resolution of mixing at phase boundaries explain the global thermodynamic differences seen in Vogelsberger et al. (2012). This also explains part of the differences in disk scale lengths that we see in this paper. Notably, high mass galaxies in AREPO will be more efficient at accreting material from the hot halo at late times which will help them maintain a gas rich disk.

It is worth noting that several proposals have been put forward to improve the mixing at phase boundaries in SPH, which may bring the two codes into better agreement. For example, it has been suggested that by including a thermal conductivity term contact discontinuities and instabilities can be more accurately handled (e.g., Price 2008; Wadsley et al. 2008), which would improve the mixing picture with respect to the standard SPH. Alternatively, moving away from the density based formulation of SPH to an energy or pressure formulation can substantially reduce the artificial surface tension

at contact discontinuities, which can help to resolve instabilities and mixing with higher accuracy (e.g., Ritchie & Thomas 2001; Saitoh & Makino 2013). In particular, Hopkins (2013) has recently shown how such a formalism can be derived from a variational principle, as in Springel & Hernquist (2002), resulting in a fully conservative version of SPH. Other changes, such as modifying the shape of the adopted smoothing kernel with a substantial increase in the number of neighbors used in the hydro calculations, or modifying the momentum equation evaluated in the code, have all also shown promise in improving the performance of SPH at resolving instabilities (e.g., Abel 2011; Read et al. 2010).

3.4.3 Cold Clumps

One important issue contributing to the differences in the disk scale lengths for high mass objects in GADGET and AREPO is the efficient accretion of low angular momentum gas via dense clumps. These clumps can be quite easily identified using projected surface density maps of the gas around relatively massive galaxies residing in $\sim 10^{12}\mathrm{M}_{\odot}$ haloes in GADGET as is shown in Figure 3.3 and 3.4 at redshift $z = 0$ and $z = 2$, respectively. In contrast, very few blobs are present in the AREPO galaxies aside from discrete objects which we have identified to be subhaloes with clearly associated dark matter components.

Identifying Clump Material

We can identify the clump particles by noting that they are overdense relative to the ambient hot halo density, colder than the ambient hot halo temperature, and do not have any substantial dark matter overdensity associated with them. To demonstrate this

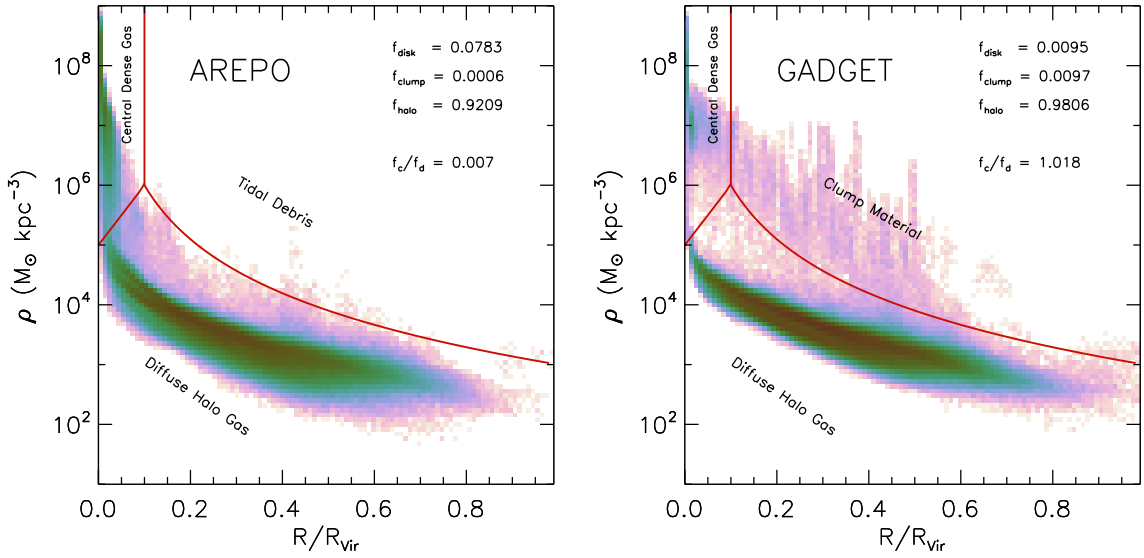

Figure 3.11.—: The distribution of gas in the 5 matched haloes between 10^{12} and $3 \times 10^{12} h^{-1}$ $M_\odot$ in AREPO (left) and GADGET (right). Red lines mark the boundaries we have chosen to separate the diffuse halo gas, central dense gas, and clump material are described in detail in the text. The fraction of gas that resides in the disk, $f_{\rm disk}$, halo, $f_{\rm halo}$, and clump, $f_{\rm clump}$ regions are reported on each panel. Finally, the ratio of the clump gas mass to the disk gas mass, $f_{\rm c}/f_{\rm d}$ is also shown.

point, Figure 3.11 shows a 2-D histogram of the material that is part of the primary subhalo (as identified via SUBFIND) in the 5 matched haloes between $10^{12}h^{-1}$ $M_\odot$ and $3 \times 10^{12}h^{-1}$ $M_\odot$ at redshift $z = 0$ in density-radius space (also shown in Figure 3.3). Although the clumps can be as or even more prominent at higher redshifts, here we focus on this mass range and redshift in our analysis here for demonstrative purposes.

We can place rough boundaries to break the density-radius space down into three physically meaningful components: central dense gas, diffuse hot halo gas, and cold/dense blobs. The central dense gas – which has been the subject of most of this paper – is concentrated into a relatively small region at small radii and has high density

$$M_{\rm disk} = M\left(\frac{r}{R_{\rm vir}} < 0.1, \rho > 10^{\frac{5+r}{(0.1R_{\rm vir})}}\left[\frac{{\rm M}_\odot h^2}{{\rm kpc}^3}\right]\right). \quad (3.3)$$

The dense clumps are identified as dense material outside of the noted central dense gas region, i.e.,

$$M_{\rm clump} = M\left(\frac{r}{R_{\rm vir}} > 0.1, \rho > \frac{10^3}{(r/R_{\rm vir})^3}\left[\frac{{\rm M}_\odot h^2}{{\rm kpc}^3}\right]\right). \quad (3.4)$$

Finally, we assign all other material to be part of the diffuse hot halo which is characterized by relatively low density.

The fraction of mass that resides in each region is noted on both panels of Figure 3.11. In both GADGET and AREPO over 90% of the gas mass associated with these systems resides in the diffuse halo region. Vogelsberger et al. (2012) and Kereš et al. (2012) analyzed the hot halo gas and found that more hot halo gas is present and that the temperature of this gas is hotter in GADGET compared to AREPO. This is consistent with our discussion from the previous section on the increased artificial heating in GADGET and increased mixing induced cooling in AREPO.

The central dense region in AREPO contains about 8% of the total gas mass,

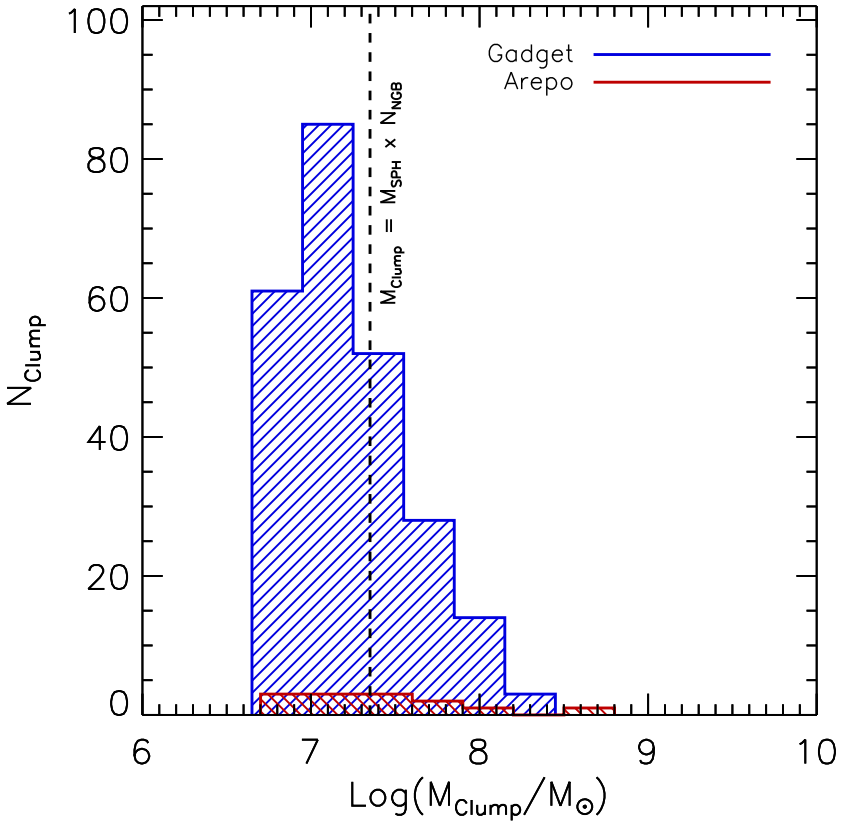

Figure 3.12.—: The distribution of clump masses is shown for GADGET (blue) and AREPO (red). We find that there is a substantially larger population of clumps in the GADGET simulation, and that these clumps build up around the mass resolution limit of our simulation which is marked by the vertical dashed line. We emphasize that the few "clumps" found in the AREPO simulation are actually tidal features or recently stripped cold gas, which are identified as clump material according to our imposed density threshold. The overwhelming majority of the GADGET gas clumps do not contain dark matter and are not associated with infalling substructure or tidal features, as can be gleaned from Figures 3.1 and 3.3.

compared to about 1% in GADGET. We identify two simple reason for this difference. First, more gas is able to cool into this region in AREPO for the reasons discussed in the previous section. Second, we find that the AREPO galaxies are able to maintain larger amounts of gas in this region because the dense gas resides in a rotationally supported disk with intermediate star formation rates. In contrast, we find that the GADGET galaxies in these massive systems contain most of their gas mass in a very centrally concentrated region with high densities, which efficiently convert the gas supply into stars.

We now turn to the "clump material" portion of this diagram. As we described earlier, material that resides in this region is far away from the central galaxy, but very dense compared to the ambient halo gas. Interestingly, we find a substantial population of cold clump gas in the GADGET objects that is not found in the AREPO systems. In terms of the fractional mass distribution, $\sim 1\%$ of the gas mass is in this region for the GADGET systems, while a negligible fraction is in the same region for AREPO objects. Furthermore, of the small gas fraction that does reside in this region for the AREPO objects, most of this material is associated with tidal features or recently stripped cold gas from infalling satellites.

To quickly estimate the potential impact of these clumps on the growth of the central disk, we report the ratio of clump mass to disk mass in Figure 3.11. In GADGET we find that a comparable amount of mass is in the central dense region as in the clump region. In other words, if these clumps are able to efficiently migrate toward the central object – which we will soon argue is the case – then they are capable of contributing a substantial amount of cold, low-angular momentum material to the central galaxy. We note that although these quoted fractional mass distributions depend on our choice for

the boundary locations shown in Figure 3.11, our conclusion that there is a substantial amount of mass in the clump region for the GADGET objects in this mass range is robust to any reasonable changes in the boundary definition.

Clump Associations

To classify these clumps, we select all overdense particles according to the cut presented in Figure 3.11 and group these particles using a Friends-of-Friends (FOF) algorithm with a linking length of $l = 3h^{-1}$ kpc yielding a set of particles belonging to each clump. Each clump then has a well defined position, velocity, and mass.

One quantity of interest is the dark matter overdensity associated with these clumps. Since we have included only material that is bound to the primary halo within our FOF group, we expect that well defined substructure (e.g., in-falling dwarf galaxies) will have already been removed. We can verify that this is the case by checking the dark matter overdensity associated with each clump, and comparing it to the spherically averaged dark matter density at the clump's position. In practice, we do this by finding the volume associated with the N^{th} nearest dark matter particle from the clump's center of mass, and compare that to the spherically averaged dark matter density measured in a thin shell at the same radius as of the clump. Although we have verified that this method would allow us to clearly identify substructure, we do not find any clumps in our sample with significant associated dark matter overdensities. We have repeated our overdensity test using $N^{th} = 64, 100, 500$ without any change in our results.

The mass spectrum for these blobs is shown in Figure 3.12. We find that the majority of the blobs contain just above or below 32 particles, which corresponds to

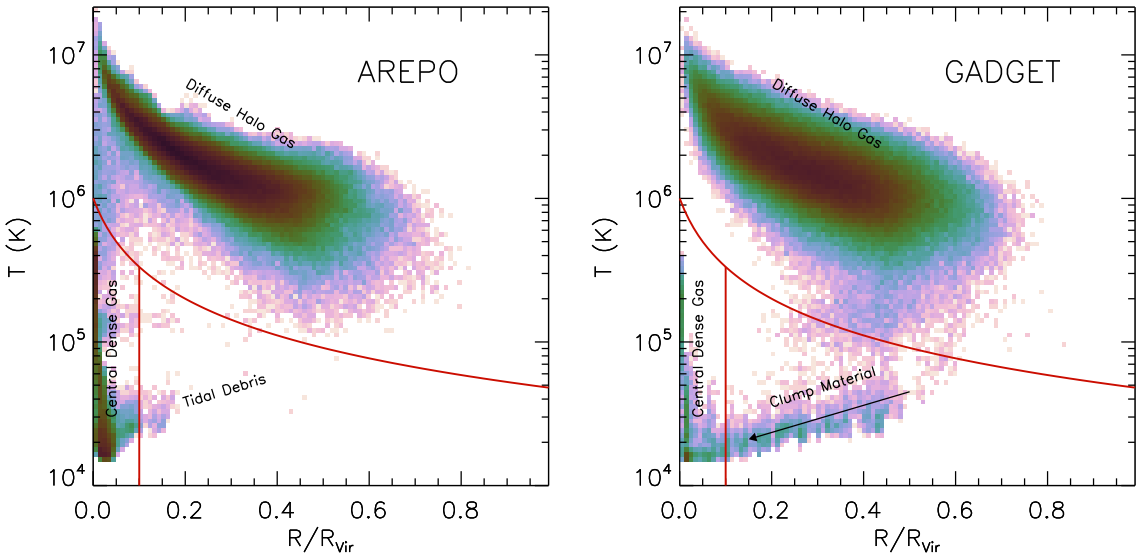

Figure 3.13.—: Temperature distribution of bound gas in the 5 matched haloes between 10^{12} and $3 \times 10^{12} h^{-1} \mathrm{M}_{\odot}$ in AREPO (left) and GADGET (right). Red lines mark the boundaries we have chosen to separate the diffuse halo gas, central dense gas, and clump material.

the number of nearest neighbors used in our SPH simulation as denoted by the vertical dashed line in Figure 3.12. Clumps tend to build up around the resolution limit of our simulation and as we have verified the mass spectrum changes accordingly if we increase or decrease the number of nearest neighbors. Although we do find a very small number of low mass cold and dense gas patches in the AREPO simulation, we note that these features are characteristically distinct from the cold gas clumps in GADGET. Specifically, these cold gas patches tend to be associated with tidal features or recently stripped gas from infalling satellites. So, while these cold gas patches meet the density based selection criteria that we have implemented and do not contain any clearly associated dark matter overdensity, we emphasize that their origin is very different from the large population of cold gas clumps that are seen the GADGET simulation.

Clump Origin and Trajectory

The origin of these clumps can be determined by tracing clump particles back in time. We find that the clump particles originate in very mild gas over-densities within the filamentary structures of the intergalactic medium (IGM). As material in these filaments falls into the hot halo environment that surrounds central galaxies in massive objects, mild over-densities are amplified via hydrostatic pressure confinement. We find that the maximum past temperature of the clumps is well below the halo virial temperature, indicating that the blobs did not form via cooling instability of gas overdensities present in the hot halo (as studied in, e.g., Kaufmann et al. 2006), but rather remained cold during their accretion from the IGM. This point is demonstrated in Figure 3.13 which shows a 2-D histogram of the distribution of gas in radius-temperature space for 5 matched objects with halo masses just above $M = 10^{12} h^{-1}\ M_{\odot}$ at redshift $z = 0$.

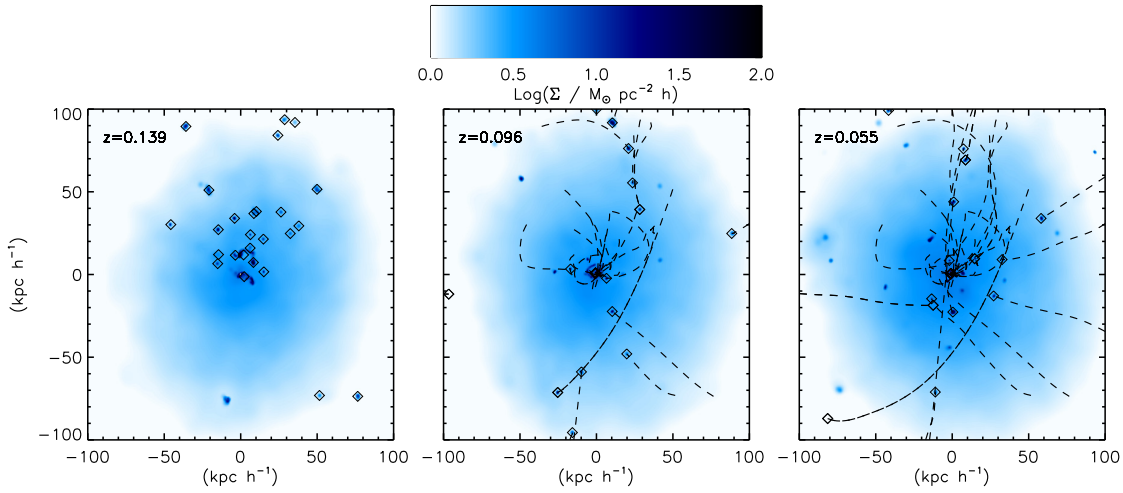

Figure 3.14.—: Maps of the gas surface density showing the trajectories of cold, dense gas clumps for a $\sim 10^{12}h^{-1}\ M_{\odot}$ halo in the GADGET simulation at redshifts $z = \{0.130, 0.096, 0.055\}$ (left, central and right panel, respectively). A population of clumps (marked with diamond symbols) are identified in the leftmost panel and tracked forward in time. Dashed lines are denoting their trajectories. The vast majority of the clumps shown are moving toward the central galaxy on nearly radial trajectories, and are able to merge with the central galaxy. Thus, the clumps effectively provide a source of cold, low angular momentum material in the innermost regions, which is of entirely numerical origin.

As labeled within the plot the trajectory for clumps can be readily identified for the GADGET haloes, which allows cold material to migrate from large radii to the central object without ever heating substantially. No analogous migration trajectory exists for the AREPO systems. The clump formation picture we have discussed here is consistent with the clump formation scenario outlined in Kereš et al. (2009), where an analogous population of cold gas clumps were found originating from IGM filaments. Also in agreement with Kereš et al. (2009), we find an accretion rate from these cold clumps in our GADGET simulation of $\dot{M}_{\rm gas} \sim 0.5 M_{\odot}{\rm yr}^{-1}$ at redshift $z = 0$ for $M = 10^{12} h^{-1}\ M_{\odot}$ systems.

As a clump is gravitationally accelerated toward the halo center, the clump should begin to be disrupted and mixed via ram pressure stripping and the Kelvin-Helmholz and Rayleigh-Taylor instabilities. However, it is well known that these instabilities are poorly resolved and that ram pressure stripping is underestimated in the standard density formulation of SPH. In particular, Agertz et al. (2007) and Sijacki et al. (2012) presented numerical experiments that showed cold blobs have artificially long survival times in SPH codes, while grid based codes like AREPO shred these clumps over substantially shorter timescales consistent with analytic expectations. As a result, mild over-densities in the accreting filamentary material are condensed and fragmented into a population of high density cold clumps that have substantially longer survival times in the GADGET simulation compared to AREPO. Since idealized numerical experiments have shown that the survival timescale for cold gas blobs in GADGET is artificially long compared to analytic expectations, we argue that the survival of these blobs in our GADGET cosmological simulations is a consequence of the same SPH deficiencies.

When the clumps enter the virial radius for the first time, they have non-zero

orbital angular momenta about the halo's center of mass that is consistent with other recently accreted material. However, as the clumps pass through the halo gas, they loose their angular momentum efficiently due to spuriously strong hydrodynamic drag forces (Tittley et al. 2001) and dynamical friction. This loss of angular momentum puts the clumps on increasingly radial trajectories and allows them to merge with the central object after only one or two orbits. Thus, the clumps become an efficient source of cold, low angular momentum gas feeding the central galaxy.

Figure 3.14 specifically highlights the trajectories of a population of clumps in time. A set of cold, dense gas clumps are identified in the leftmost panel of Figure 3.14 and their subsequent trajectories are marked with dashed lines in the central and rightmost panels. By inspection of the marked clump trajectories, it can be seen that many clumps move on nearly radial trajectories and eventually merge with the central galaxy. Although each clump has a relatively low mass ($\sim 10^7 - 10^8 h^{-1}\ M_\odot$ – see Figure 3.12), a sufficiently large number of clumps fall into the central galaxy on a characteristic time scale of $\sim$ 1Gyr. Thus, their cumulative mass amounts to a substantial fraction of the central galaxy gaseous mass. Furthermore, given that they arrive on nearly radial trajectories with low angular momentum, the clumps act as an efficient delivery source of low angular momentum fuel to the central galaxy.

A similar population of blobs can be seen in the gas distribution for relatively massive haloes (i.e. $\sim 10^{12} h^{-1}\ M_\odot$) in independent studies that used similar versions of GADGET (e.g., van de Voort et al. 2011; Kereš & Hernquist 2009; van de Voort & Schaye 2012a). This is an interesting point because the mass resolution used in van de Voort et al. (2011) is about a factor of 2 worse than the resolution used in our present study, and the resolution used in Kereš & Hernquist (2009) is a factor of 7 better. Both of

these studies find that these clumps result from fragmented IGM filaments that are able to survive until they merge with the central gas disk. Despite their substantially higher resolution, Kereš & Hernquist (2009) find that these clumps tend to form just above the resolution limit of their simulation – implying a significant change in the clump mass spectrum from what we have found here.

Recently, Hobbs et al. (2012) have made use of a new flavor of SPH (Read & Hayfield 2012) to study the formation and impact of "blobs" in standard SPH simulations and found their origin to lie in artificial thermal instabilities that can originate from a small number of particles with low entropies with respect to their neighbors. Since the standard formulation of SPH in GADGET lacks any inter-particle fluid mixing, these artificial thermal instabilities are allowed to grow and ultimately form a population of dense gas clumps. Hobbs et al. (2012) show that this artificial thermal instability can be averted by including thermal conductivity (e.g., Price 2008). This issue does not arise with AREPO because cells exchange entropy with their neighbors when mass is advected across cell boundaries, which results in a physically motivated homogenization of the fluid entropy. The presence of these clumps in independent numerical studies of varying resolution (e.g. van de Voort et al. 2011; Kereš & Hernquist 2009; van de Voort & Schaye 2012a) seems to imply that these clumps will continue to form and survive at higher resolution even though the specific properties, such as the mass spectrum, will change unless modifications are made to the standard SPH hydro solver.

3.5 Conclusions

Here we presented a comparison project aimed at studying the properties of gas disks formed in cosmological simulations performed with two very different hydrodynamical codes – GADGET and AREPO. Our comparison started from an identical set of initial conditions which were evolved forward in time with the two codes which have the same gravity solver and while holding fixed the initial number of resolution elements, and radiative cooling, star formation and feedback prescriptions. However, GADGET and AREPO adopt very different approaches for solving the hydrodynamic equations. While GADGET uses a standard density formulation of SPH, AREPO solves the fluid equations using a Riemann solver on an unstructured moving mesh. In many ways, the hydro solver included in AREPO has accuracy advantages over the SPH solver used in GADGET which can be clearly demonstrated in, e.g., idealized shock tube tests, driven turbulence tests, and hydro instability tests. The goal of our comparison was to understand the impact of the hydro solver on the formation of gas disks in fully cosmological simulations at a comparable resolution. Our primary conclusions are as follows:

- After fitting the gas disks with best-fit exponential surface density profiles, we find that the AREPO gas disks are systematically larger than their GADGET counterparts. This corresponds to gas disks in GADGET having lower specific angular momentum compared to the matching set of disks formed in AREPO simulation.

- The primary reason responsible for the differences in gas disk scale lengths between the two codes changes as a function of the number of resolution elements and physical environment of the host halo.

- For low mass objects, low resolution leads to spurious angular momentum transport from the cold disk to the diffuse hot halo in the GADGET simulation. This spurious angular momentum loss is a well-known and documented issue, which can be alleviated by moving to increasingly higher resolution in test problems or "zoom-in" simulations. However, for large cosmological box simulations, like those we have presented here, the resolution needed to suppress this spurious angular momentum loss is not yet attainable. Grid based codes – such as AREPO – are not expected to suffer from this same problem and can therefore provide a more accurate answer for the same number of resolution elements and comparable CPU time.

- Poorly resolved subsonic turbulence in GADGET results in dissipative heating of the gas near the cooling radius. This inhibits the accretion of gas onto the central galaxy. In the presence of turbulent energy, AREPO correctly recovers a cascading Kolmogorov-like power spectrum, so no analogous artificial heating source is present.

- For high mass objects, the cooling timescale of hot halo gas can become comparable to the Hubble time which effectively shuts off fresh gas accretion. However, mixing at density phase boundaries – such as the interface between the cold gas disk and the hot halo – can substantially increase the gas cooling rates. This allows for more gas to cool onto the disk in AREPO given that the mixing at phase boundaries is suppressed in GADGET.

- For high mass objects, the efficient delivery of low angular momentum gas in the form of cold gas clumps causes the central gas disks in GADGET to be much more

centrally concentrated than in AREPO. These clumps form from fragmented IGM filaments and rapidly migrate to the potential minimum as they loose their angular momentum to hydrodynamic drag against the ambient hot halo. The absence of these blobs in AREPO is attributed to the efficient disruption of clumps via ram pressure stripping and the Kelvin-Helmholtz and Rayleigh-Taylor instabilities – all of which are poorly handled in GADGET.

Chapter 4

A model for cosmological simulations of galaxy formation physics: multi-epoch validation

P. Torrey, M. Vogelsberger, S. Genel, D. Sijacki, V. Springel, & L. Hernquist

Monthly Notices of the Royal Astronomical Society, Vol. 438, No. 3, pp. 1985, 2014

> "It is only through labor and painful effort, by grim energy and resolute courage, that we move on to better things."
>
> — Theodore Roosevelt

4.1 Introduction

Cosmological simulations are among the most powerful tools available for studying the non-linear regime of cosmic structure formation. While dark matter only simulations have

built a solid foundation for our understanding of the origin of haloes via gravitational collapse (e.g., Springel et al. 2005c; Boylan-Kolchin et al. 2009; Fosalba et al. 2008; Teyssier et al. 2009; Klypin et al. 2011), applying their findings to our understanding of the observable Universe (i.e. luminous galaxies) requires modelling of baryonic physics as well. Although semi-analytic (e.g., White & Frenk 1991; Kauffmann et al. 1999; Hatton et al. 2003; Kang et al. 2005; Somerville et al. 2008; Guo et al. 2011, 2013) and halo occupation distribution (e.g., Vale & Ostriker 2004; Conroy et al. 2006; Behroozi et al. 2013; Moster et al. 2013) models can estimate galaxy properties based on dark matter only simulations, the most direct and self-consistent way to explore the evolution of observable galaxies theoretically is by including baryons in the simulations (e.g. Katz et al. 1992, 1996; Weinberg et al. 1997; Murali et al. 2002; Springel & Hernquist 2003b; Kereš et al. 2005; Ocvirk et al. 2008; Crain et al. 2009; Croft et al. 2009; Schaye et al. 2010; Oppenheimer et al. 2010; Vogelsberger et al. 2012).

The main challenge for any large-scale galaxy formation model is accurately handling the baryonic physics and including proper forms of feedback to regulate star formation. Galaxy formation simulations lacking strong feedback substantially overproduce stars, leading to galaxies with too high baryon fractions (e.g., White & Frenk 1991; Balogh et al. 2001; Scannapieco et al. 2012). This problem is most pronounced for the highest and lowest mass systems, where star formation is known to be relatively inefficient (e.g., Behroozi et al. 2013, and references therein). The problem can be remedied by introducing sources of feedback which either eject gas from galaxies or heat it to prevent continued accretion from the halo. Two commonly employed strong feedback mechanisms are star formation (Dekel & Silk 1986; Thacker & Couchman 2000; Springel & Hernquist 2003a; Kawata & Gibson 2003; Stinson et al. 2006; Scannapieco

et al. 2008; Dalla Vecchia & Schaye 2008; Okamoto et al. 2010; Stinson et al. 2013) and black hole growth (Springel et al. 2005b; Kawata & Gibson 2005; Di Matteo et al. 2005; Thacker et al. 2006; Sijacki et al. 2007; Okamoto et al. 2008; Kurosawa & Proga 2009; Booth & Schaye 2009; Debuhr et al. 2011; Dubois et al. 2012).

Winds driven by star formation are a consequence of energy and/or momentum injection from newly formed stellar populations into the interstellar medium (ISM). Observations indicate that star forming galaxies show signs of outflowing material (e.g., Heckman et al. 2000; Rupke et al. 2002, 2005a), and that the velocity of the outflowing wind material may scale with the mass of the galaxy (Martin 2005). Including winds in large-scale cosmological simulations requires sub-grid models because the detailed ISM structure remains unresolved (Hopkins et al. 2012a, 2013a,b). Several types of explicit wind models have been developed including hydrodynamically decoupled winds (Springel & Hernquist 2003a), injecting thermal energy while shutting down cooling (Stinson et al. 2006, 2013), imposing a minimum temperature threshold for supernovae energy injection (Dalla Vecchia & Schaye 2012) or adding blast particles to launch a Sedov-Taylor blast wave (Dubois & Teyssier 2008). These wind prescriptions vary in their formulations, but all of them eject material from galaxies based on the local star formation rate and they have all been shown capable of regulating the growth of low mass galaxies in large scale simulations (e.g., Davé et al. 2011b; Kannan et al. 2014; Ocvirk et al. 2008).

Feedback from active galactic nuclei (AGN) is the result of energy and/or momentum injection that occurs as gas accretes onto the galaxy's central super-massive black hole (BH). This is thought to be responsible for the rapidly-moving outflows that can be inferred from UV and X-ray observations of galaxies that host AGN (Chartas et al.

2002; Pounds et al. 2003; Reeves et al. 2003). It has been shown that AGN feedback is critical for shutting down star formation (e.g., Springel et al. 2005b,a; Croton et al. 2006; Hopkins et al. 2006; Sijacki et al. 2007; Hopkins et al. 2008a; Booth & Schaye 2009; McCarthy et al. 2010) and setting up self-regulated black hole growth (Di Matteo et al. 2005; Hopkins et al. 2006, 2007a,b, 2008c; Di Matteo et al. 2008; Younger et al. 2008; Sijacki et al. 2009).

Over the last few years, there have been many studies of galaxy formation using large-scale hydrodynamical simulations. For example, Schaye et al. (2010) presented a suite of smoothed particle hydrodynamics (SPH) simulations (the "OWLS" project) to explore the impact of various physical effects, like stellar and AGN feedback, on the resulting galaxy population. The simulations were used to examine, among other things, the evolution of the cosmic star formation rate (Schaye et al. 2010), observational signatures of the warm-hot intergalactic medium (Tepper-García et al. 2011, 2012), and the rates and modes of gas accretion into dark matter haloes (van de Voort et al. 2011; van de Voort & Schaye 2012b; van de Voort et al. 2012). More recently, Davé et al. (2011b) used SPH simulations to investigate the impact and importance of stellar winds. They found that stellar winds are able to reproduce the faint-end of the $z = 0$ galaxy stellar mass function, while also leading to appropriate levels of enrichment in the inter galactic medium (Oppenheimer & Davé 2008; Oppenheimer et al. 2009). Even more recently, it was shown (Kannan et al. 2014) that large-scale hydrodynamical simulations are capable of producing galaxy stellar mass functions and stellar mass to halo mass relations that are consistent with observations by enforcing strong (Stinson et al. 2006) and early (Stinson et al. 2013) stellar feedback.

In the "GIMIC" project (Crain et al. 2009), roughly spherical volumes of size

$L \sim 20h^{-1}$ Mpc drawn from regions of various over-densities in the Millennium simulation were re-simulated at high resolution. This work has been used to study systematic variations in galaxy formation that scales with large scale environment (Crain et al. 2009), the formation (Font et al. 2011) and structure (McCarthy et al. 2012a) of galactic stellar haloes, and the characteristics (McCarthy et al. 2012b) and origin (Sales et al. 2012) of disk galaxies. The "Mare-Nostrum Horizon" (Ocvirk et al. 2008) is perhaps the largest, high-resolution, full-volume cosmological simulation run and it was performed using the Adaptive Mesh Refinement (AMR) simulation code RAMSES (Teyssier 2002). This simulation was used to study the mode of gas accretion into galaxies (Ocvirk et al. 2008) and the angular momentum evolution of high redshift galaxies (Danovich et al. 2012). Other simulations aimed at studying galaxy formation in large volumes have been carried out using RAMSES by Hahn et al. (2010) and Few et al. (2012).

Recently, a moving-mesh hydro solver was developed and incorporated into the hydrodynamical simulation code AREPO (Springel 2010a). This method combines advantages of traditional Lagrangian hydro solvers (e.g., continuous resolution enhancement, adaptive geometry, Galilean invariance) with the strengths of Eulerian hydro solvers (e.g., instability handling, shock capturing, phase boundary resolution). It has been demonstrated that the hydro solver used in AREPO can lead to systematic changes in the properties of galaxies formed in cosmological simulations. In particular, the hot-haloes of galaxies are found to contain less hot gas (Vogelsberger et al. 2012) because it is able to cool efficiently onto the central gas disk (Sijacki et al. 2012; Kereš et al. 2012). This leads to an increase in hot-mode gas accretion rates (Nelson et al. 2013) and the creation of large, gas disks (Torrey et al. 2012). However, the first cosmological simulations published with this code lacked strong feedback, and therefore formed stars

far too efficiently compared to actual galaxies.

The goal of this paper is to test and demonstrate the ability of the AREPO code to produce realistic galaxy populations directly in cosmological simulations by including realistic feedback processes. This paper builds on the work presented in Vogelsberger et al. (2013, hereafter, Paper I) where a detailed description of our galaxy formation model for the moving mesh code AREPO was presented for the first time. In Paper I, the framework of our approach was described in detail and a set of cosmological simulations were presented. The strength of the star formation driven winds and the AGN feedback parameters were tuned as to accurately reproduce the evolving cosmic star formation rate density and the redshift $z = 0$ galaxy stellar mass function. The metal content of ejected wind material was set to ensure a reasonable normalization of the redshift $z = 0$ mass-metallicity relation. These relations, as well as several other redshift $z = 0$ relations that were not used to tune the feedback model (e.g., the Tully-Fisher relation and luminosity functions) were presented in Paper I. The primary goal in what follows is to extend the analysis of Paper I by benchmarking the performance of our galaxy formation models against observational constraints at intermediate and high redshifts. This allows us to understand if the simulated galaxy populations are forming and evolving in a manner consistent with observations.

The structure of this paper is as follows: In Section 2 we describe the simulations that we have used, including a brief description of our general methods and the various feedback mechanisms included in our simulations. We present results of the build-up of stellar mass in Section 3, the evolution of the galactic and global star formation rates in Section 4, and the evolution of the mass-metallicity relation and Tully-Fisher relation in Section 5. We discuss our results and conclude in Section 6.

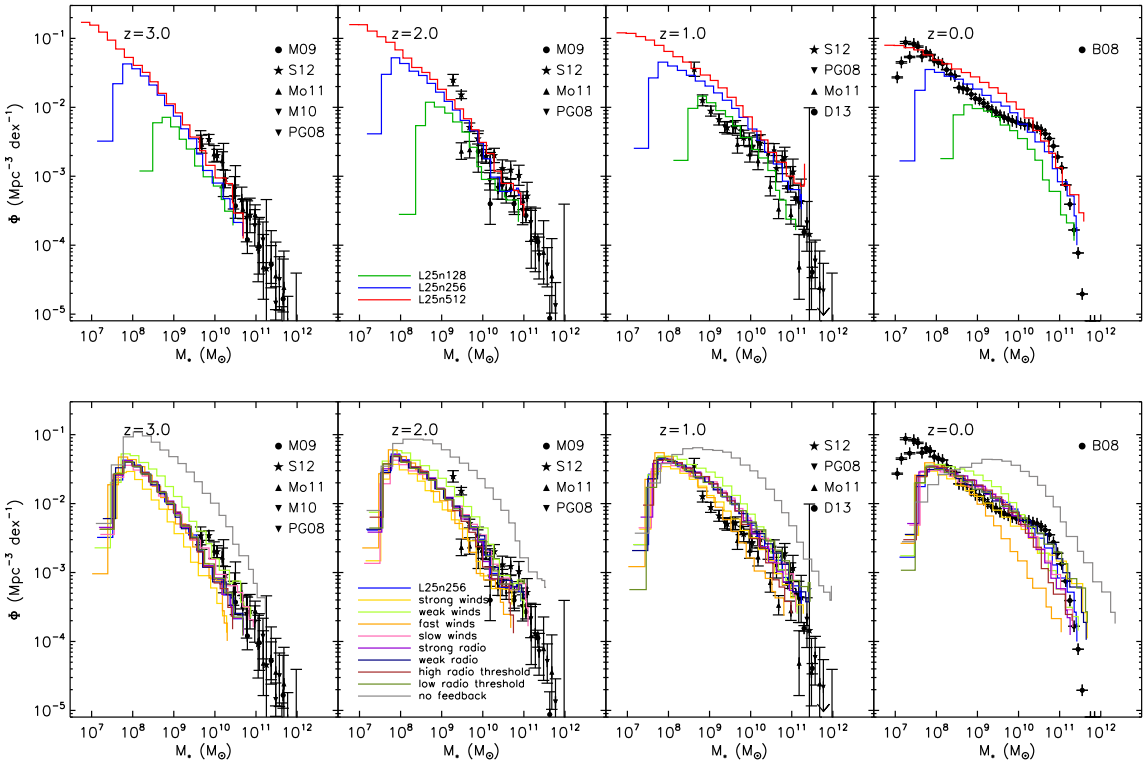

Figure 4.1.—: The simulated galaxy stellar mass function (GSMF) is shown for three different resolution simulations (top panel, solid coloured lines) and several variations of our feedback model (bottom panel, solid coloured lines) along with data points from observations at four different redshifts (as indicated). The "no feedback" simulation (grey line, bottom plot) provides a poor match to observations, underscoring the need for strong feedback to regulate the growth of galaxies. Many of the feedback models are able to alleviate the overproduction of stellar mass, including the high resolution fiducial model (red line, top plot) which provides reasonable agreement in the overall shape and normalization of the GSMF compared against observations. This includes a flattening of the low mass end of the GSMF that occurs towards late times, along with a sharp cutoff for massive systems.

4.2 Methods

The simulation suite used in this paper as well as a detailed description of our numerical methods have been discussed extensively in Paper I. We review briefly the main components of the galaxy formation model here.

All simulations used in this paper, apart from the 'no-feedback' run, include the same physics: gravity, hydrodynamics, radiative gas cooling, star formation with associated feedback, and AGN feedback. The gravity and hydrodynamics implementation are described in Springel (2010a) and Vogelsberger et al. (2012). Radiative gas cooling for hydrogen and helium is carried out according to Katz et al. (1996) taking into account the presence of a cosmologically evolving ultraviolet background (Faucher-Giguère et al. 2009), which has been calibrated to match the mean transmission of the Lyman-alpha forest at redshifts $z = 2 - 4.2$ (Faucher-Giguère et al. 2008b,a), HeII reionisation by $z \sim 3$ (McQuinn et al. 2009), and complete HI reionisation by $z = 6$. In addition, the metal line contribution to the cooling rate (under the assumption of ionization equilibrium) is tabulated as a function of gas density, temperature, redshift-dependent background radiation, and metallicity using the photoionisation code CLOUDY (Ferland et al. 1998, 2013) and added to the primordial cooling rate. We correct both cooling contributions for self-shielding (Rahmati et al. 2013).

Star formation is modelled using a slightly modified version of the Springel & Hernquist (2003a) subgrid model which pressurises gas above the specified star formation density threshold and converts gas into stars according to a density based prescription that is tuned to recover the observed Kennicutt-Schmitt (Kennicutt 1998; Schmidt 1959) relation for star forming gas assuming an equation of state parameter of $q_{\rm eos} = 1.0$. Here,

we have employed an equation of state parameter of $q_{\rm eos} = 0.3$, which has allows for resolution of internal disk structures yet prevents artificial gas fragmentation (Springel et al. 2005b; Robertson et al. 2006a) and is also consistent with a value derived in the high-resolution ISM simulations of Hopkins et al. (2012b).

Stellar mass loss and metal enrichment are carried out by calculating the mass and composition of ejected material from aging stellar populations at each time-step. To achieve this, we adopt a Chabrier (2003) initial mass function (IMF), the stellar lifetime function from Portinari et al. (1998), and the chemical yields for asymptotic giant branch (AGB) stars (Karakas 2010), core collapse supernovae (Portinari et al. 1998), and Type Ia supernovae (Thielemann et al. 1986). The star formation driven wind model uses a stochastic approach, similar to Springel & Hernquist (2003a), to launch wind particles out of star forming regions. Recently launched wind particles are hydrodynamically decoupled until they propagate out of the dense ISM. We adopt a variable wind speed that drives winds at a velocity based on the local dark matter velocity dispersion (e.g., Oppenheimer & Davé 2006, 2008). The mass loading factor is adjusted appropriately based on the local velocity dispersion such that an equal amount of energy is transferred to the ISM per unit star formation rate (SFR) (Okamoto et al. 2010). We have introduced a wind metal loading factor, $\gamma_{\rm w}$, which is set independently from the wind mass loading factor, $\eta_{\rm w}$. The wind metal loading factor defines the relationship between the metallicity of newly created wind particles, $Z_{\rm w}$, and the metallicity of the ambient ISM, $Z_{\rm ISM}$, such that $Z_{\rm wind} = \gamma Z_{\rm ISM}$. We adopt a metal loading factor of $\gamma_{\rm w} = 0.4$ which allows for reasonable matches to the local and high redshift mass-metallicity relation and halo gas enrichment.

We adopt a unified model for quasar (Springel et al. 2005b; Di Matteo et al. 2005,

2008), radio (Sijacki et al. 2007), and radiative AGN feedback. The quasar mode self-regulates the black hole growth by injecting thermal energy around the black hole at a rate proportional to the black hole accretion rate. For lower accretion rates (in Eddington units), off-center radio-mode bubbles are generated. The AGN radiative feedback prescription provides a novel way for black holes to impact the gas state at large distances by suppressing gas cooling. While the majority of the gas in our cosmological box cools under the assumption of being exposed to a uniform UV background, the cooling rate of gas near BHs is calculated from a combination of both the uniform UV background and the ionising radiation field of nearby AGN.

All of the simulations in this paper were performed in periodic boxes of size L = 25 h^{-1}Mpc. The number of dark matter elements remains constant throughout the simulation with a particle mass dependent on the simulation resolution as noted in Table 4.1. The mass within individual resolution elements for the gas changes as material is advected across cell boundaries and the number of gas elements changes as cells can be converted into collisionless stellar particles and accreted by black holes. However, we include a cell (de-)refinement scheme (Vogelsberger et al. 2012) which enforces that all cells remain within a factor of two of a specified target mass so that the total number of baryonic elements in our simulations (star particles and gas cells) remains close to its initial value. All simulations use initial conditions generated at redshift $z = 127$ based on a CAMB linear power spectrum. The adopted cosmological parameters are $\Omega_{m0} = 0.27$, $\Omega_{\Lambda 0} = 0.73$, $\Omega_{b0} = 0.0456$, $\sigma_8 = 0.81$, and $H_0 = 100\,h\,\mathrm{km\,s^{-1}\,Mpc^{-1}} = 70.4\,\mathrm{km\,s^{-1}\,Mpc^{-1}}$ ($h = 0.704$), which were chosen to be consistent with the WMAP7 measurements of Komatsu et al. (2011).

We study two types of simulations in this paper, both of which were described in

Paper I. The first is a set of cosmological simulations of size L = 25 h^{-1}Mpc that initially contain 256^3 DM particles and 256^3 gas cells, and in which we vary the parameter choices for our feedback model. The impact of these feedback parameter variations on the redshift $z = 0$ galaxy population was discussed in Paper I, and we extend this discussion here by comparing the simulated galaxy populations with high redshift data. The second set of simulations employs our fiducial feedback model at three different resolutions, and are labelled L25n128, L25n256, and L25n512. All our simulations are summarised in Table 4.1.

We use the SUBFIND algorithm (Springel et al. 2001) to identify gravitationally bound groups of dark matter, stars, and gas. We treat each self-bound group as a galaxy, and calculate its properties based on the SUBFIND (sub) halo catalogue. For the stellar mass, we could in principle take a sum over all stellar particles associated with the group. However, a non-negligible fraction of stellar mass in massive systems resides in a diffusely distributed component, as seen in observations of groups and clusters (e.g., Zibetti et al. 2005; McGee & Balogh 2010) and simulations (e.g., Murante et al. 2004, 2007; Rudick et al. 2006; Puchwein et al. 2010; Puchwein & Springel 2013). This is an important point because: (i) intra-cluster light is not traditionally counted as contributing to the central galaxy's mass and (ii) some of the intra-cluster light may fall below observational limits. To take this into account, we define the galactic stellar mass as the sum of stellar mass within twice the (total) stellar half mass radius. This has only a small effect on the stellar mass measurements for low mass systems, but can reduce the intra-cluster mass contributions in more massive systems. We have checked that our adopted definition of galactic stellar mass gives a similar result compared to what would be obtained if we used an observationally motivated surface brightness cut for massive systems (e.g.,

Rudick et al. 2006). For the halo mass we adopt the $M_{200,\mathrm{crit}}$ value, which is defined as the sum of all mass within a sphere where the halo's average density is 200 times the critical density.

4.3 The Stellar Content of Galaxies

The shape of the galaxy stellar mass function (GSMF) is determined by a combination of the underlying DM (sub)halo mass function (HMF), and the efficiency with which stars are formed in those haloes. As noted previously, including winds driven by star formation is critical to reproducing the evolving number density of low mass galaxies (Oppenheimer et al. 2010; Bower et al. 2012; Puchwein & Springel 2013) while AGN feedback can quench star formation in massive haloes, establishing a high mass cutoff in the GSMF (Croton et al. 2006; Hopkins et al. 2008a; Gabor et al. 2011; Bower et al. 2012; Puchwein & Springel 2013). Both of these feedback processes have been included in our simulations as described in the previous section, and as has already been shown in Paper I the model included in our simulations is capable of producing reasonable matches to the GSMF at redshift $z = 0$. In this section, we focus on the evolution of the GSMF with time, and compare the simulation results with several recent observations (summarised in Table 4.2). We have applied appropriate correction factors to all observational stellar mass and star formation rate measurements so that all results are now appropriate for a Chabrier (2003) initial mass function (IMF).

A comparison of the simulated GSMF with observations is presented in Figure 4.1. The bottom panel of Figure 4.1 shows the simulated GSMF for several variations of our feedback model. Most of the feedback models provide satisfactory fits to the redshift

name	volume $[(h^{-1}\,\mathrm{Mpc})^3]$	cells/particles	ϵ $[h^{-1}\,\mathrm{kpc}]$	$m_{\mathrm{DM}}/m_{\mathrm{target}}$ $[h^{-1}\,\mathrm{M}_\odot]$	physics
L25n512	25^3	2×512^3	0.5/1.0	$7.33 \times 10^6/1.47 \times 10^6$	fiducial
L25n256	25^3	2×256^3	1.0/2.0	$5.87 \times 10^7/1.18 \times 10^7$	fiducial
L25n128	25^3	2×128^3	2.0/4.0	$4.69 \times 10^8/9.43 \times 10^7$	fiducial
stronger winds	25^3	2×256^3	1.0/2.0	$5.87 \times 10^7/1.18 \times 10^7$	$\mathrm{egy_w}/\mathrm{egy_w^0} = 6.0$
weaker winds	25^3	2×256^3	1.0/2.0	$5.87 \times 10^7/1.18 \times 10^7$	$\mathrm{egy_w}/\mathrm{egy_w^0} = 1.5$
faster winds	25^3	2×256^3	1.0/2.0	$5.87 \times 10^7/1.18 \times 10^7$	$\kappa_{\mathrm{w}} = 7.4$
slower winds	25^3	2×256^3	1.0/2.0	$5.87 \times 10^7/1.18 \times 10^7$	$\kappa_{\mathrm{w}} = 1.85$
stronger radio	25^3	2×256^3	1.0/2.0	$5.87 \times 10^7/1.18 \times 10^7$	$\epsilon_{\mathrm{m}} = 0.7$
weaker radio	25^3	2×256^3	1.0/2.0	$5.87 \times 10^7/1.18 \times 10^7$	$\epsilon_{\mathrm{m}} = 0.175$
high radio threshold	25^3	2×256^3	1.0/2.0	$5.87 \times 10^7/1.18 \times 10^7$	$\chi_{\mathrm{radio}} = 0.1$
low radio threshold	25^3	2×256^3	1.0/2.0	$5.87 \times 10^7/1.18 \times 10^7$	$\chi_{\mathrm{radio}} = 0.025$
no AGN	25^3	2×256^3	1.0/2.0	$5.87 \times 10^7/1.18 \times 10^7$	winds; no AGN feedback
no feedback	25^3	2×256^3	1.0/2.0	$5.87 \times 10^7/1.18 \times 10^7$	no winds; AGN feedback

Table 4.1:: Summary of the different cosmological simulations as originally described in Paper I, and as referenced throughout this paper. The L25n128, L25n256, L25n512 simulations employ the fiducial physics parameters shown in Table 1 of Paper I. The remaining simulations explore variations in our feedback model parameters at the intermediate resolution. Parameters that are varied are indicated in the last column.

$z = 3$ GSMF. The one exception is the "strong winds" simulation, which suppresses the stellar mass growth of galaxies slightly too efficiently, and lowers the normalization of the simulated GSMF. By redshift $z = 2$ the offset of the strong wind model is less distinct, and all of the feedback runs provide good fits to the observational data, especially compared to the "no feedback" case. At redshift $z = 1$ most of the feedback models deviate from observations in the normalization of the GSMF at the low mass end. This is an indication that low mass systems in our simulations are building up their stellar mass at this epoch more efficiently than observations indicate. The exception is the "fast wind" model, which produces a GSMF that is offset toward lower normalizations (compared to the other feedback models), consistent with observations. By redshift $z = 0$, this normalization offset is reduced for most of the feedback models, as the observed number density of low mass systems has substantially increased, while the number density of these same objects has remained fairly constant in the simulations. While the "fast wind" simulation provided the best fit to the GSMF at redshift $z = 1$, this same simulation now strongly underproduces galaxies just below the knee of the GSMF.

Our simulation shows an appropriate exponential cut-off in the GSMF at low redshift for massive galaxies. The simulation box used here is too small to identify this exponential cutoff clearly at early redshifts. Where it is seen, the exponential drop is driven by efficient AGN radio-mode feedback in our simulations which suppresses star formation in massive systems (Croton et al. 2006; Hopkins et al. 2008a; Guo et al. 2010; Bower et al. 2012; Puchwein & Springel 2013). The exact location of this cutoff depends on choices for the AGN radio feedback strength and accretion threshold, as discussed in Paper I. Obtaining this cutoff is important because it indicates that all haloes will

Table 4.2:: Observational references for the galaxy stellar mass function data used in Figure 4.1.

Source	Observed Redshift Range	Plotted Redshift Panel	Original IMF
Baldry et al. (2008)	$z < 0.05$	$z = 0$	diet Salpeter
Pérez-González et al. (2008)	$0.0 < z < 0.2$	$z = 0$	Salpeter
	$1.0 < z < 1.3$	$z = 1$	Salpeter
	$2.0 < z < 2.5$	$z = 2$	Salpeter
	$3.0 < z < 2.5$	$z = 3$	Salpeter
Marchesini et al. (2009)	$2.0 < z < 3.0$	$z = 2$	Kroupa
	$3.0 < z < 4.0$	$z = 3$	Kroupa
Marchesini et al. (2010)	$3.0 < z < 4.0$	$z = 3$	Kroupa
Mortlock et al. (2011)	$1.0 < z < 1.5$	$z = 1$	Salpeter
	$2.0 < z < 2.5$	$z = 2$	Salpeter
	$3.0 < z < 3.5$	$z = 3$	Salpeter
Santini et al. (2012)	$1.0 < z < 1.4$	$z = 1$	Salpeter
	$1.8 < z < 2.5$	$z = 2$	Salpeter
	$2.5 < z < 3.5$	$z = 3$	Salpeter
Davidzon et al. (2013)	$0.9 < z < 1.1$	$z = 1$	Chabrier

have reasonably sized stellar components associated with them. This allows for a clear connection between the properties (i.e. the growth rates, concentrations, morphologies, etc.) of observable galaxies and their host dark matter haloes.

The resolution dependence of the simulated GSMF is shown for the fiducial feedback model in the top panel of Figure 4.1. We note three points regarding the numerical convergence of the simulated GSMF. First, any resolution effects become increasingly prominent toward late times. Although all three resolution simulations agree fairly well at redshift $z = 3$, the redshift $z = 0$ agreement is less good. As a result, the high resolution low redshift GSMF sits above the observed GSMF relation. Second, while there is an offset between the normalizations of the lowest resolution (128^3) simulation and the higher resolution simulation GSMFs which is visible at late times, the offset between the intermediate (256^3) and high (512^3) resolution simulations GSMFs is smaller. This indicates that our results are converging numerically. Third, the GSMF for high mass systems (e.g., $M_* > 10^{10} M_\odot$) shows little offset at any redshift for the two highest resolution simulations, which indicates these systems are numerically converged. In fact, it is likely that the GSMF is converged down to even lower masses (e.g., $M_* > 10^9 M_\odot$) for our highest resolution simulations. However, we could only demonstrate this point by presenting an even higher resolution simulation, which is beyond the scope of this paper.

A clear characterisation of the performance of our various feedback models can be obtained by independently assessing the evolution of the slope and normalization of the low mass end of the GSMF. As mentioned above, the majority of our feedback models appear to overproduce the number density of low mass galaxies at redshift $z = 1$. The right panel of Figure 4.2 highlights this by showing the number density evolution of simulated low mass galaxies (in the same particular mass bin used in Weinmann

et al. 2012). Weinmann et al. (2012) argued that the shape of the low mass galaxy number density evolution in previous semi-analytic and hydrodynamical modeling is characteristically distinct from that of the observations, indicating that the models were not using wind prescriptions capable of decoupling the galaxy stellar mass growth from the underlying halo mass growth. Here, we find that all of our feedback choices lead to a very flat evolution in the number density of these low mass systems past redshift $z = 1$. Variations in our adopted wind model set the normalization of the low redshift number density plateau, but do not strongly impact the slope. Whereas the "weak winds" model leads to a higher number density of low mass systems, the "strong winds" model decreases the number density of low mass systems. Since all of our models plateau in their low mass number density at late times while the observations indicate an increasing number density of these systems, it is unlikely that any simple variation in our wind model could reproduce the observed redshift $z = 1$ and $z = 0$ low mass galaxy number densities simultaneously. It is worth noting here that, as expected, variations in the adopted black hole feedback model parameters have negligible impact on the evolution of the simulated low mass galaxy population.

The left panel of Figure 4.2 demonstrates the resolution dependence of the number density evolution of low mass galaxies. All resolution simulations show the same characteristic evolutionary shape. Higher resolution simulations produce slightly higher normalizations, due to increases in the star formation efficiency in low mass galaxies. The magnitude of this resolution dependence decreases towards better resolved systems. The highest resolution model passes above most of the low redshift data points and misses the intermediate redshift data points. This may be an indication that our models require more efficient suppression of star formation in low mass systems at these

redshifts. But, as discussed above, while simply tuning up the strength of our wind feedback model could correct the normalization of the low mass galaxy number density at either low or intermediate redshifts, we cannot correct the normalization at both epochs simultaneously.

The slope of the low mass end of the GSMF is observed to flatten towards low redshifts. The slope of the low mass end of the simulated GSMF mimics this observed flattening. Fitting a Schechter (1976) function to the simulated GSMF explicitly demonstrates this evolution. The right panel of Figure 4.3 shows the low mass end slope, α, compared to observational results for the various feedback model parameterisations. Here we note that Pérez-González et al. (2008) caution that their estimations of the low-mass end slope of the GSMF above redshift $z \gtrsim 2$ could be affected by incompleteness. Thus, as indicated in the legend of Figure 4.3, we have removed the $z > 2$ slope calculations of Pérez-González et al. (2008). Most of the simulations are clustered around a single evolutionary track that traces the observed low mass end slope evolution. We do not show a best fit α value for the "no feedback" simulation because the low redshift GSMF is not well described by a single Schechter function. The most substantially offset model is the "fast wind" model, which has a steeper slope than observations (see Figure 4.1 and discussion above). All of the other feedback models produce evolving low mass end slopes which are similar to the observations.

There is no major resolution dependence to this result, as demonstrated in the left panel of Figure 4.3. The fiducial feedback model yields very similar low mass end GSMF slopes for all three resolutions. In particular, the intermediate and high resolution runs show very similar low redshift behaviour, indicative of numerical convergence.

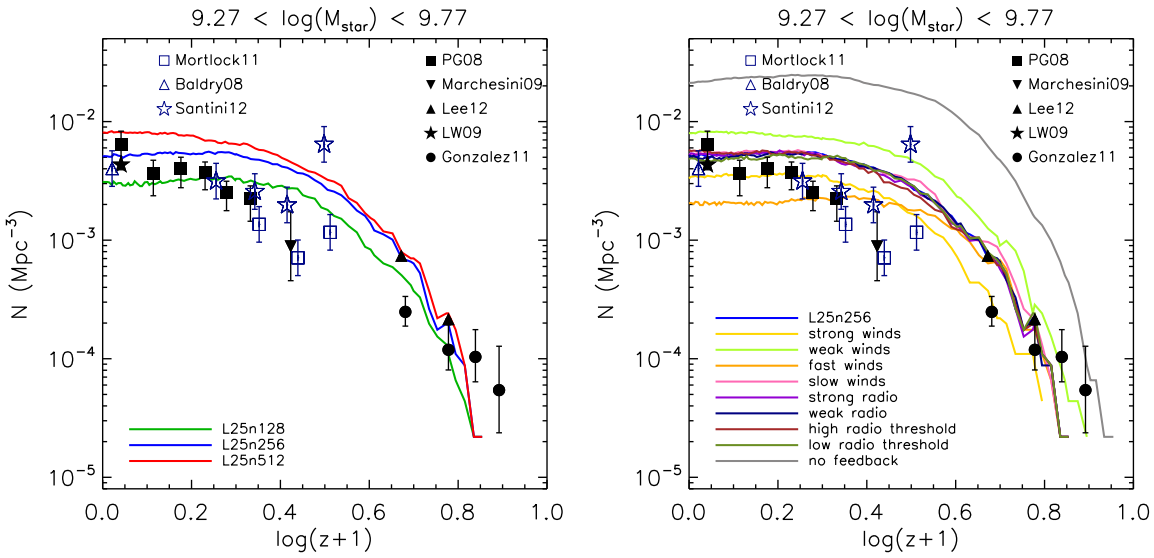

Figure 4.2.—: The evolution of the number density of low mass galaxies is shown for three different resolutions (left) and our varied feedback models (right). The black symbols show the data taken directly from the Weinmann et al. (2012) paper, while the blue points show additional data points assembled by interpolating/extrapolating the GFMS data used in Figure 4.1 of this paper. As in many semi-analytic and hydrodynamic models, low mass systems are being assembled too early, leading to an overproduction of these systems by redshift $z \sim 1$, with little evolution in their number density thereafter. Variations in the feedback parameters lead to adjusted normalizations for the late time number density plateau, without substantially impacting the late time slope.

4.3.1 Luminosity Function

Comparing our simulated GSMFs to observations implicitly assumes that the observed spectra can be converted into stellar mass measurements accurately. Stellar mass measurements are typically obtained from observations by employing stellar population synthesis models (e.g., Leitherer et al. 1999; Bruzual & Charlot 2003; Le Borgne et al. 2004) and assuming some star formation history and IMF. However, there are a number of uncertainties associated with observationally determined stellar mass measurements, and so some caution should be taken when comparing to theoretically determined stellar mass measurements (Mitchell et al. 2013). Instead of considering the stellar mass function comparison of the previous subsection alone, it is useful to also consider how the luminosity functions compare between the simulations and observations. To facilitate this comparison, we assign broad band luminosities to all star particles in each galaxy via the Bruzual & Charlot (2003, hereafter BC03) catalogues after taking into account the star particle's age, initial stellar mass, metallicity, and assuming a Chabrier (2003) IMF. To start, we neglect the impact of dust attenuation, and tabulate each galaxy's luminosity as the sum of the contributions from all of its star particles.

Paper I showed a comparison between the luminosity functions produced by our simulations and the local SDSS g-, r-, i-, and z-band measurements. To extend the comparison of the observed and simulated results to higher redshift, we consider the rest-frame B-band luminosity function versus redshift as shown in Figure 4.4. Observational data points are included for comparison as outlined in Table 4.3. As in Figure 4.1, the top panel of Figure 4.4 shows the resolution dependence of the simulated redshift dependent luminosity function while the bottom panel shows the impact of the

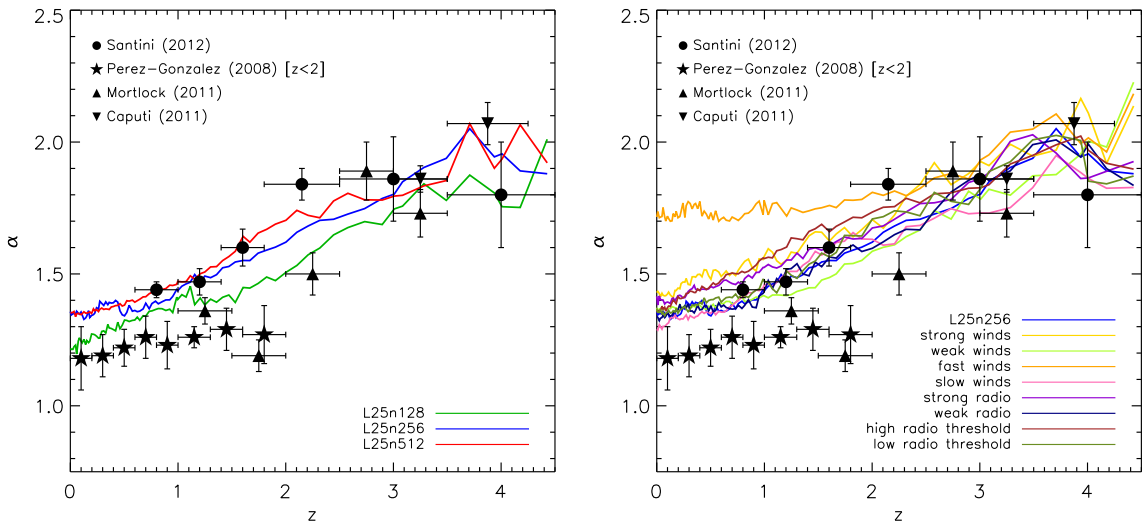

Figure 4.3.—: The evolution of the low mass end slope of the galaxy stellar mass function is shown for three different resolutions (left) and our varied feedback models (right). We have obtained the α slope value by performing an RMS minimisation to determine the best fit Schechter function parameters. Observational estimates of α from the literature are also shown.

feedback model parameter choices on the simulated luminosity function.

The luminosity function is impacted by feedback in a very similar way to the GSMF. Most of the feedback models provide satisfactory fits to the redshift $z = 3$ luminosity function, though the observational luminosity function is offset towards marginally brighter values. Since no substantial offset exists in the redshift $z = 3$ GSMF simulation/observation comparison at the same number density, this may be an indication that our simulated systems need marginally higher star formation rates (i.e. have somewhat younger stellar populations) to better match the B-band luminosity function. This, however, may give rise to other tensions in either the global star formation rate density or star formation main sequence relations which we discuss in the next section. It is also possible that omitting non-stellar sources of luminosity (e.g., AGN) could be leading to an underestimation of simulated galaxies true B-band luminosities.

At redshifts $z = 2$ and $z = 1$ we find very good agreement between the simulated and observed luminosity functions in terms of overall shape and normalization for most of the feedback models. The two clear outlier simulations are the "no feedback" case (which allows for efficient star formation in all galaxies, making haloes/galaxies of a given number density too bright) and the "fast wind" case (which suppresses star formation in massive systems too efficiently, and therefore underproduces bright objects). As with the GSMF, the various model parameter choices for the AGN feedback have little impact here, because of the lack of very massive/bright objects in our small simulation volume. By redshift $z = 0$, there is a broader spread in the luminosity functions that result from the different models, with the best agreement to the observed B-band luminosity

function being given by our fiducial "L25n256" model, as discussed in Paper I.

The resolution dependence of the simulated luminosity function is demonstrated for our fiducial feedback model in the top panel of Figure 4.4. There is a slight increase in the normalization of the luminosity function for higher resolution simulations, however this normalization offset is small between the intermediate and high resolution cases. Overall, the similarity of the intermediate and high resolution simulations indicates reasonable numerical convergence for our fiducial feedback model.

To this point, we have neglected the impact of dust attenuation which can have a substantial impact on the measured B-band luminosity function (e.g., Tuffs et al. 2004; Pierini et al. 2005). We can approximate the dust attenuation correction to the simulated B-band luminosity function using the simple model of Charlot & Fall (2000). Charlot & Fall (2000) provides an empirically based model to approximate the reddening of stellar populations based on their ages alone (i.e. without explicit information about the gas or dust distribution around these light sources). The dust attenuated B-band luminosity functions from our models are shown in the top panel of Figure 4.4 as a series of colored dashed lines. The size of the correction is $\sim$0.5 magnitudes, and pushes our models away from the observations at all redshifts. This exacerbates the previously discussed shortfall of our models with respect to the bright end of the luminosity function at redshift $z = 3$, and creates a similar issue at lower redshifts. However, the normalization and slope of the faint end of the luminosity function remains almost unchanged where our models continue to provide a good match to the observations. More detailed modeling of the dust attenuation will be considered in future work via three-dimensional radiative transfer to self-consistently determine line-of-sight attenuation factors under more explicit assumptions (e.g., the dust-to-gas ratio) which may validate or correct the

luminosity functions presented here.

In general, the simulated luminosity functions agree well with observations up to redshift $z = 3$. Perhaps this is somewhat expected, given that: (i) we have already shown reasonable agreement in the stellar mass function and (ii) we are converting stellar masses into broad band luminosities using similar techniques that observers use to convert broad band luminosities into stellar masses. Moreover, it has been shown previously in semi-analytic models that good matches can be achieved to the evolving B-band luminosity function by accounting for the finite recycling time for previously ejected wind material (Henriques et al. 2013) as is done in our simulations (see discussion in Oppenheimer & Davé 2008, for more details on the recycling time for wind material). The two most obvious ways that we could have achieved agreement in the stellar mass functions without obtaining similar agreement in the luminosity functions is by forming galaxies in our simulation with very different star formation histories from that assumed by observational models, or, if our assumption of neglecting dust attenuation failed severely. It is unlikely that we have formed galaxy populations with very different formation histories because, as we will show in the next section, the simulated global SFR as well as the simulated star formation main sequence both follow observations reasonably well. While we have not carried out a full radiative transfer calculation to determine the impact of dust attenuation, we have shown that our fiducial models only slightly undershoot the observational measurements of the B-band luminosity function when we approximate dust attenuation via the simple model of Charlot & Fall (2000).

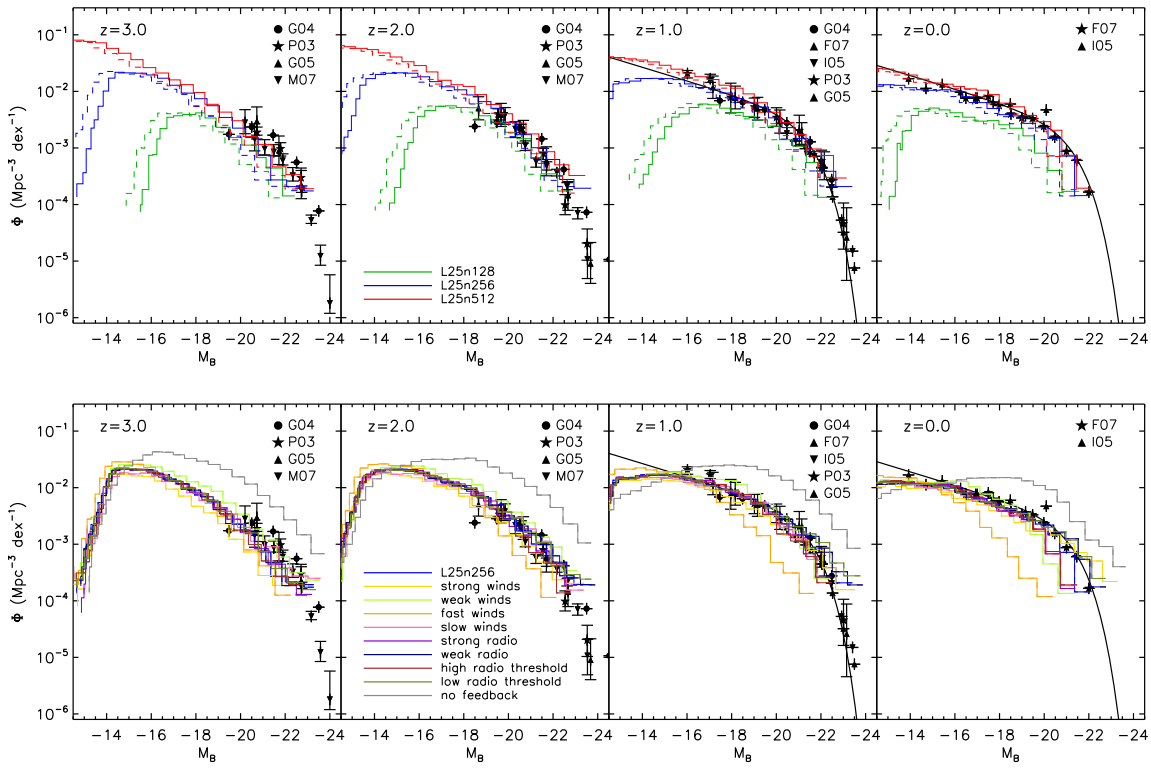

Figure 4.4.—: B-band luminosity functions compared against observational data at several redshifts for three different resolutions (top) and our varied feedback models (bottom). The solid lines assume no dust attenuation. The dashed lines (top panel only) show the attenuated luminosity function using the simple model of Charlot & Fall (2000). The varied physics models impact the simulated luminosity function similarly to the GSMF. The agreement between our simulations and observations is good for redshifts $0 \leq z \leq 2$, while the redshift $z = 3$ comparison shows a slight offset between the observations and simulations. As with the stellar mass function, we find an evolution toward somewhat steeper low luminosity slopes at high redshift for the simulation data.

Table 4.3:: Observational references for the luminosity function data used in Figure 4.4.

Source	Observed Redshift Ranges	Plotted Redshift Panel
Poli et al. (2003)	$0.7 < z < 1.0$	$z = 1$
	$1.3 < z < 2.5$	$z = 2$
	$2.5 < z < 3.5$	$z = 3$
Gabasch et al. (2004)	$0.8 < z < 1.2$	$z = 1$
	$1.75 < z < 2.5$	$z = 2$
	$2.5 < z < 3.4$	$z = 3$
Giallongo et al. (2005)	$0.7 < z < 1.0$	$z = 1$
	$1.3 < z < 2.5$	$z = 2$
	$2.5 < z < 3.5$	$z = 3$
Ilbert et al. (2005)	$0.05 < z < 0.2$	$z = 0$
	$1.0 < z < 1.3$	$z = 1$
Faber et al. (2007)	$0.2 < z < 0.4$	$z = 0$
	$1.0 < z < 1.2$	$z = 1$
Marchesini et al. (2007)	$2.0 < z < 2.5$	$z = 2$
	$2.5 < z < 3.5$	$z = 3$

4.3.2 Stellar Mass vs. Halo Mass

Within the past decade, abundance matching models have brought together measurements of the galaxy stellar mass functions with detailed numerical models of structure formation (Conroy et al. 2006; Conroy & Wechsler 2009; Moster et al. 2010; Guo et al. 2010; Moster et al. 2013; Behroozi et al. 2013). By relying on a simple central assumption to pair the population of simulated dark matter haloes to observed galaxies (e.g., based on mass), a more detailed link between observed galaxies and their host dark matter haloes has been established along with an understanding of how galaxies and their host haloes evolve together in time. In particular, one of the central results from these models is a parameterised relationship describing the evolution of the stellar mass to halo mass (SMHM) ratio as a function of galaxy mass and redshift. Comparing directly to abundance matching results – rather than using just the GSMF comparison in the previous section – has the added advantage that abundance matching models account for the asymmetric impact of observational errors on the stellar mass functions, while also inferring additional galaxy properties such as their star formation rates.

It has been shown in Paper I that the feedback physics included in our simulations produces a reasonable match to the abundance matching derived SMHM relationship at redshift $z = 0$ by reducing the efficiency of star formation in low mass and high mass haloes through efficient stellar and AGN feedback. Here, we focus on the evolution of the SMHM ratios for the simulated galaxies compared against the abundance matching models of Moster et al. (2013) and Behroozi et al. (2013) at several redshifts, as well as Guo et al. (2010) at redshift $z = 0$. Figure 4.5 shows the simulated galaxy stellar mass vs. halo mass relation for three different redshifts. The solid lines indicate the

median SMHM relation as a function of simulation resolution (top panel) and feedback model (bottom panel). In each figure, we show a two-dimensional histogram indicating the full distribution of simulated galaxies for the "L25n256" simulation (bottom panel) and "L25n512" simulation (top panel).

In the low mass regime at redshift $z = 0$, most of the feedback models yield SMHM relations clustered around the abundance matching results. The spread in these models can be attributed to changes in the adopted wind model, as discussed in Paper I. Briefly, we note that the "strong" wind model suppresses star formation in low mass systems too efficiently, leading to an underestimate of the SMHM relation. Conversely, the "weak" wind simulation overproduces stars in these same systems. As we consider these relations at higher redshift, a similar trend remains true. At redshifts $z = 1$ and $z = 2$ the "weak" wind and "strong" wind models bracket the abundance matching SMHM relation, with approximately the correct slope. The fiducial feedback model, which falls between these two cases, is in approximate agreement with the abundance matching results (although the slope may be somewhat steeper at redshift $z = 2$ in Behroozi et al. 2013).

For high mass systems at redshifts $z = 1$ and $z = 0$, the relationship between the abundance matching SMHM relation and the simulation result is heavily dependent on the adopted AGN feedback model. As discussed in Paper I, the location of the knee of the SMHM relation is set by the adopted AGN radio threshold; i.e. a high radio threshold pushes the knee location to lower masses. The adopted radio threshold value was set to get the redshift $z = 0$ SMHM relation knee in the right location. The same trend can be observed at redshift $z = 1$. Notably, the high and low radio threshold values bracket the desired location of the SMHM relation knee.

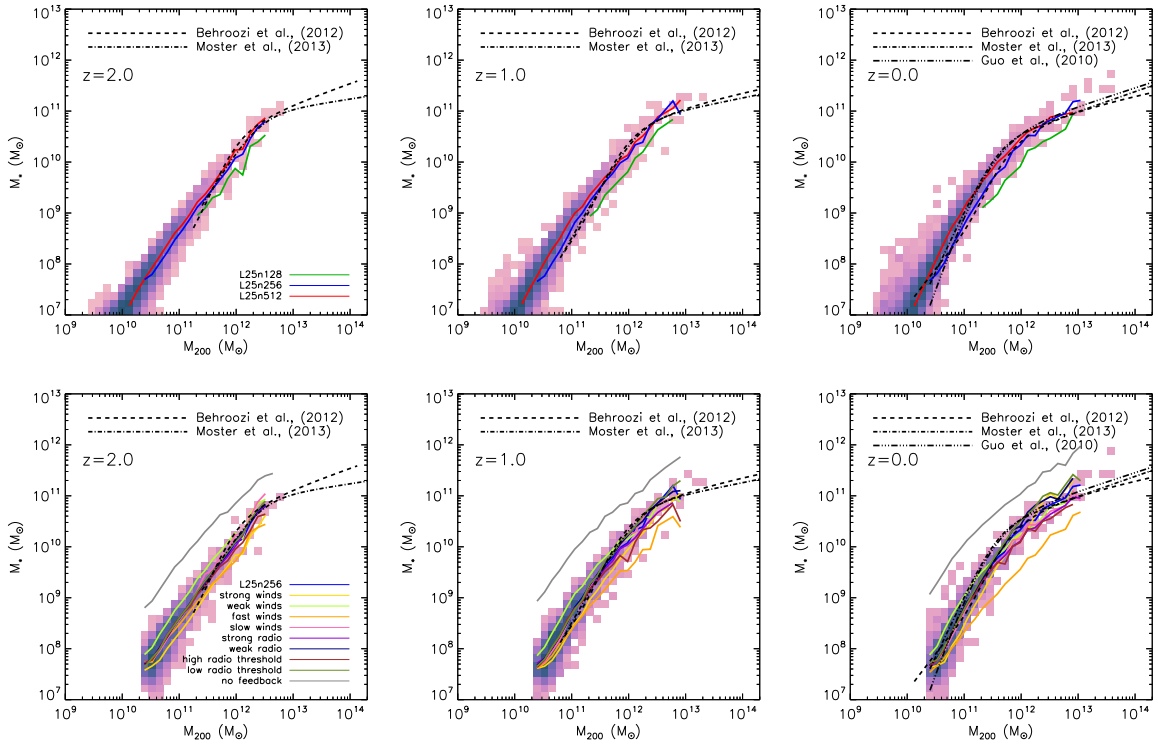

Figure 4.5.—: Binned median stellar-mass halo-mass relations are shown for three different resolutions (top) and our varied feedback models (bottom) as solid lines for redshifts $z = 2$, $z = 1$, and $z = 0$ from from left to right, respectively. In the background, two dimensional histograms show the distribution of simulated galaxy's stellar masses and halo masses, for the L25n512 (top) and L25n256 (bottom) simulations. Each panel also contains lines denoting the results of abundance matching studies, as labelled in the plotted regions.

The top panel of Figure 4.5 shows the resolution dependence of the simulated SMHM relation using our fiducial feedback model. While the redshift $z = 2$ SMHM relation is converged for the intermediate and high resolution simulation, the lowest mass systems show an offset between these two runs at redshift $z = 1$ which becomes more pronounced by redshift $z = 0$. There is a factor of ~ 2 offset in the stellar masses of the intermediate and high resolution runs for low mass systems at redshift $z = 0$. While the intermediate resolution simulation agrees well with the Behroozi et al. (2013) result, the high resolution simulation agrees better with the Moster et al. (2013) result. Although the "strong winds" simulation suppressed star formation too efficiently in low mass systems in the intermediate resolution simulation, it may provide a good fit to the SMHM relation at high resolution.

Interestingly, the high resolution simulation (red line) SMHM relation is in good agreement with the Moster et al. (2013) abundance matching relation at redshifts $z = 0$ and $z = 2$, but is slightly offset from the Moster et al. (2013) relation at redshift $z = 1$. At redshift $z = 1$, the simulated low mass galaxies have more stellar mass than we would expect from abundance matching models. The offset between the simulations and abundance matching results is roughly a factor of two in stellar mass. This is directly related to the flat evolution of the number density of low mass systems demonstrated in Figure 4.2, and is another indication that the simulated low mass galaxies are building up stellar mass too rapidly at or around redshift $z = 1$. As discussed previously, stronger star formation driven winds can suppress stellar masses buildup in these systems leading to better agreement at redshift $z = 1$. However, this comes at the expense of the agreement between the abundance matching and simulation redshift $z = 0$ SMHM relationship. It is therefore interesting to consider whether alternative galactic wind

implementations which have successfully reproduced the normalization, slope, and scatter of the SMHM relation at intermediate and high redshift will achieve similar agreement at low redshifts (e.g., Kannan et al. 2014).

We conclude that our fiducial feedback model is capable of reproducing the abundance matching derived SMHM relation to within a factor of two in galaxy stellar mass at all plotted redshifts. This is an important result because it implies that we can compare simulated galaxies against observed galaxies by matching them based on their stellar mass. This also implies that the galaxies in our simulations are building up their stellar mass similarly to what is inferred via abundance matching models (modulo the discussion of the low mass systems around redshift $z = 1$). We note that Moster et al. (2013) highlighted the fact that while many simulations reproduce the redshift $z = 0$ SMHM relation correctly, their intermediate and high redshift SMHM relations lie far from abundance matching results. Although our fiducial model slightly overproduces the stellar mass content of low mass galaxies at early times, we emphasize that the magnitude of this overproduction is an improvement over many previous results (Moster et al. 2013).

4.4 SFR Relations

In the previous section we examined the simulated GSMF and SMHM relationships, finding that our feedback models are capable of producing galaxy populations that build up stellar mass broadly consistent with observations. To further differentiate the performance of our various feedback model choices, we consider additional constraints on how and when galaxies build up their stellar mass from direct observations of the

evolution of the global star formation rate and star formation main sequence. We contrast the results of our various feedback models with those observations in the following subsections.

4.4.1 Cosmic SFR Density

The global cosmic SFR density (SFRD) has been measured out to high redshift in several bands including the UV (Yoshida et al. 2006; Salim et al. 2007; Bouwens et al. 2009; van der Burg et al. 2010; Robotham & Driver 2011; Bouwens et al. 2011; Cucciati et al. 2012), radio (Smolčić et al. 2009; Karim et al. 2011), UV/IR (Zheng et al. 2007), and FIR (Rujopakarn et al. 2010). There is an increasingly clear picture for the cosmic SFRD emerging, where the SFRD increases substantially from redshift $z \sim 10$ to $z \sim 2$ (Madau et al. 1998; Bouwens et al. 2008), reaches a peak value around redshift $z = 2 - 3$, and then begins to decline rapidly thereafter (Lilly et al. 1996; Schiminovich et al. 2005; Hopkins & Beacom 2006; Villar et al. 2008). while the SFRD is generally limited by the growth rate of dark matter haloes at high redshift (e.g., Hernquist & Springel 2003), the location of the turnover of the SFRD function as well as the steepness of the subsequent decline depend heavily on the implementation of feedback physics (e.g., Springel & Hernquist 2003b; Schaye et al. 2010; Crain et al. 2009; Bower et al. 2012). The role of feedback in shaping the SFRD for the particular set of simulations used in this paper has been discussed in Paper I. Here, we extend the discussion of Paper I by identifying which haloes have had their star formation rates impacted the most by feedback and relating this to the build-up of stellar mass discussed in the previous section. We note that although the simulation box used here is relatively small, it has been previously

shown that this box should be sufficiently large to capture the proper late time evolution of the cosmic SFRD (Springel & Hernquist 2003b).

Figure 4.6 shows the global cosmic SFRD as a function of redshift, broken down as a function of galaxy stellar mass. The three panels show three distinct feedback models: "no feedback" (top left), "no AGN" (top right), and "L25n256" (bottom). The "no feedback" simulated SFRD substantially overshoots the observed data points at all redshifts. At early times (i.e. $z \gtrsim 3$) the largest contribution to the SFRD is from relatively "low mass" galaxies. These systems do not yet harbour sufficiently massive black holes to regulate their growth via AGN feedback. Instead, we find that including star formation driven winds is sufficient to regulate the early SFRD to an observationally consistent level, as demonstrated in the central panel of Figure 4.6. The impact of introducing winds can be seen very clearly by identifying the blue/green lines which trace the SFRD contributions from low mass systems. Galactic winds: (i) reduce the early peak SFRs in low mass systems and (ii) increase the SFR contributions from low mass systems at late times.

Correcting the late time behaviour of the SFRD evolution requires the introduction of AGN feedback to regulate the growth of massive systems (e.g., Schaye et al. 2010). Without strong AGN feedback, the SFRD continues to rise past redshift $z = 2$ with dominant contributions from systems with $M_* > 10^{10} M_\odot$ as seen in the central panel of Figure 4.6. In fact, Figure 4.6 shows that the contributions from the most massive systems *alone* are enough to exceed the observed global cosmic SFRD limits. When we introduce AGN feedback into our models, as shown in the right panel of Figure 4.6, star formation is suppressed in haloes with stellar masses $M_* > 10^{10.5} M_\odot$ allowing our models to pass through the observational data points with the correct late time slope (e.g.,

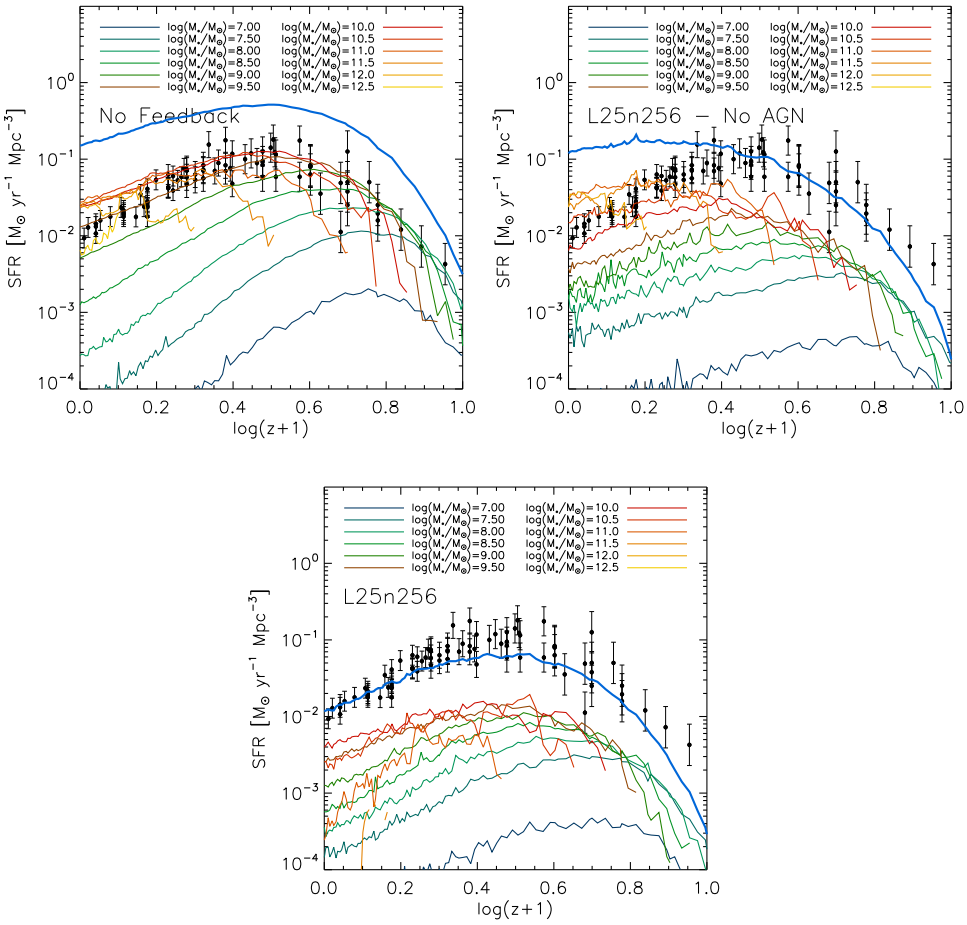

Figure 4.6.—: Cosmic star formation rate density as a function of redshift (blue thick line) along with a collection of observational constraints compiled in Behroozi et al. (2013). The three panels show the "no feedback" simulation (top left), the standard model with AGN feedback turned off (top right), and the fiducial L25n256 model (bottom). Contributions to the SFR density from various mass bins (of size ± 0.25 dex) are shown. At early times the shape of the SFR density evolution is dominated by the most massive galaxies. At late times the decline in the SFR density is determined by the suppression of star formation via AGN feedback in the most massive haloes. Star formation driven winds regulate the SFR density at early times, while AGN feedback is critical past redshift $z = 2$.

Bower et al. 2012). Importantly, we note that the mass scale where AGN feedback must kick in to regulate the cosmic SFRD evolution at late times is the same mass scale where star formation must be suppressed in order to reproduce the observed location of the "knee" of the GSMF.

As was concluded in Paper I, we find reasonable agreement of our fiducial feedback model's simulated SFRD with the measured cosmic SFRD. The late time shape is mainly regulated by AGN feedback, whereas the early build-up of stellar mass is mainly limited through stellar feedback.

4.4.2 Star Formation Main Sequence

The star formation main sequence (SFMS) describes the relationship between galactic stellar mass and star formation rate (e.g., Noeske et al. 2007; Daddi et al. 2007; Elbaz et al. 2007; Salim et al. 2007; Peng et al. 2010; Whitaker et al. 2012). Not only is there a clear correlation between stellar mass and star formation rate, but the normalization of this relationship evolves with redshift while the slope remains nearly constant (Daddi et al. 2007; Dutton et al. 2010). Moreover, as a result of the observed small scatter, it has been argued that galaxies spend the vast majority of their lives on or close to this relationship, and thus the SFMS is the primary avenue along which galaxies accumulate their stellar mass (Noeske et al. 2007). Comparing against the observed SFMS provides an additional constraint on the build-up of stellar mass in our simulations.

Figure 4.7 shows the SFMS for our various feedback models at redshifts $z = 2$, $z = 1$, and $z = 0$. In each panel, we show a two-dimensional histogram denoting the distribution of galaxies from the "L25n256" simulation (bottom panels) and the

"L25n512" simulation (top panels). Additionally, we show coloured lines marking the binned median SFMS for the various feedback models (bottom) and resolutions (top, as noted in the plotted legend). Observational SFMS measurements are shown within the figures for comparison against our models. We note that we have not made any attempt to remove or seperate passive galaxies, as is often done in the observational data sets against which we are comparing. This issue will be addressed in more detail in subsequent work using larger simulation volumes.

All feedback models recover a positive correlation between the galaxy stellar mass and star formation rate. To parametrise and quantify this relationship, we adopt a functional form for the SFMS of

$$\log\left(\frac{\mathrm{SFR}}{\mathrm{M}_{\odot}\mathrm{yr}^{-1}}\right) = \log\left(\frac{\mathrm{SFR}_{10}}{\mathrm{M}_{\odot}\mathrm{yr}^{-1}}\right) + b\log\left(\frac{M}{10^{10}\mathrm{M}_{\odot}}\right) \tag{4.1}$$

where SFR_{10} and b set the normalization and slope of the relation, respectively. A best fit is found via RMS minimisation of the simulated galaxies in a given simulation. The derived best fit for the "L25n256" simulation (bottom) and the "L25n512" simulation (top) is shown as a solid black line in Figure 4.7, with the best fit parameters printed within the plotted region. We fit Gaussian curves to this residual distribution, and present the one sigma standard deviation within the plotted region to indicate the intrinsic spread in the simulated relations. Although it is not explicitly shown for all cases, these relations tend to have a fairly tight scatter. The scatter about this relationship is $\sigma_{\mathrm{MS}} \sim 0.3$ dex for both the "L25n256" and "L25n512" simulations, which is very similar to the observed scatter (Noeske et al. 2007; Salmi et al. 2012). Our fiducial feedback models naturally recover a SFMS with an intrinsic scatter that is similar to observations. Here, we consider how the normalization and slope of the simulated SFMS

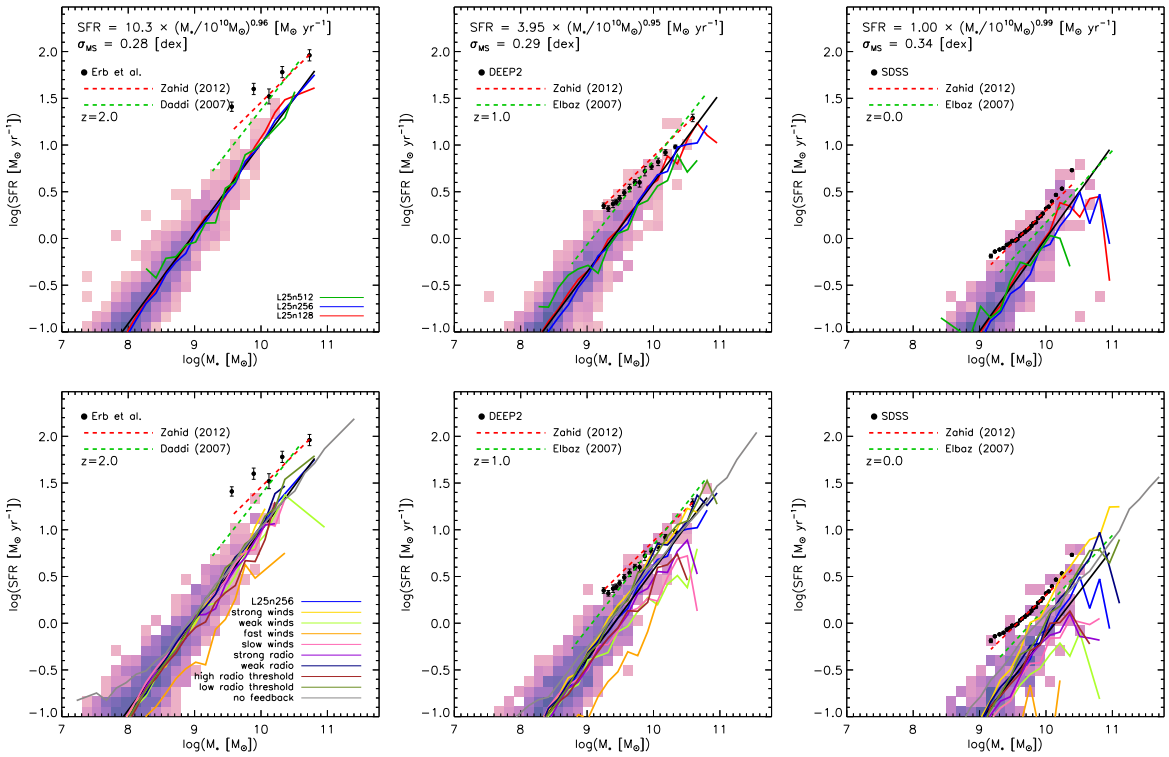

Figure 4.7.—: Binned median star formation main sequence relations are shown for three different resolutions (top) and our varied feedback models (bottom) as solid lines for redshifts $z = 2$, $z = 1$, and $z = 0$ from from left to right, respectively. In the background, two dimensional histograms show the galaxy distribution for the L25n512 (top) and L25n256 (bottom) simulations. The dark solid line shows the linear best fit to the simulated star formation main sequence relation, with the best fit parameters noted within the plotted region. For comparison, we shown the appropriate observational data taken from SDSS DR7 (Abazajian et al. 2009), DEEP2 (Davis et al. 2003), and Erb et al. (2006a) at redshifts $z = 0$, 0.8, and 2 as compiled in Table 1 of Zahid et al. (2012), along with best fit SFMS relations from Elbaz et al. (2007) and Daddi et al. (2007).

compare to observations and the role that our feedback model plays in achieving this result.

Most of our feedback models fall slightly below the observed SFMS normalizations. This generalisation includes models with both strong/weak winds and strong/weak radio mode AGN. In particular, if we examine redshift $z = 2$ results, we find that all of our models (except for the "fast wind" simulation, which is clearly the worst fit) produce very similar SFMS relations which are all about 0.3 dex below the observed relation and all have a slope of close to unity, which is steeper than the observed relation. In most of the previously discussed plots, the "no feedback" run was a fairly extreme outlier. However, for the SFMS we find that the "no feedback" run produces results consistent with the bulk of our feedback model simulations.

A similar set of conclusions holds for the redshift $z = 1$ and $z = 0$ SFMS. From redshift $z = 2$ to $z = 1$ and redshift $z = 1$ to $z = 0$ there is a significant decrease in the normalization of the observed and simulated SFMS. However, the redshift $z = 1$ and $z = 0$ simulated SFMS relations are still at or below the observed relations and have slopes (near unity) which are steeper than observations. This trend can be seen more explicitly in Figure 4.8, which shows the median specific star formation rate evolution for galaxies in the mass bin $10^{9.75} M_{\odot} < M_{*} < 10^{10.25} M_{\odot}$ along with the observational data listed in Dutton et al. (2010). We find good agreement between the late time decline in the specific SFR normalization in the simulations and observations. Feedback (in particular, galactic winds) plays a role in determining the normalization of this relation. Stronger star formation driven winds lead to higher SFMS normalizations. This trend – which can be seen in both Figures 4.7 and 4.8 – is driven by two effects: (i) strong winds suppress the stellar mass growth of galaxies, moving them "to the left" in Figure 4.7 and

(ii) by reducing star formation in low mass systems, strong winds increase the amount of star forming gas that is available to more massive systems at later times. The second of these points can also be seen as an increase in the bright end on the luminosity function shown in Figure 4.4. However, most of the feedback models show the same overall trend with redshift, which is driven by the reduction in the accretion rate with redshift which scales roughly as $\dot{M}_{\rm acc} \propto (1+z)^{2.25}$ (Birnboim et al. 2007; Genel et al. 2008; Dutton et al. 2010).

The resolution dependence of these results is demonstrated in the top panel of Figure 4.7 where we show the SFMS for our fiducial feedback model at three different resolutions and the left panel of Figure 4.8 which shows the SFMS normalization evolution for the same simulations. There is a weak resolution dependence in the derived SFMSs. This is especially true for the intermediate and high mass SFMS relations, which are nearly identical at all plotted redshifts.

We conclude that our galaxy formation model predicts a star formation main sequence which is in reasonable agreement with the observations. This result is similar to that found in other recent studies (e.g., Davé et al. 2011b; Puchwein & Springel 2013; Kannan et al. 2014). Generally, simulations have difficulties obtaining a SFMS with a slope substantially shallower than unity and often have SFMSs that are mildly depressed in their normalization relative to observations. Neither of these issues can be easily corrected without introducing problems in the simulated GSMF – especially at the low mass end. The offset between the simulated and observational SFMS is fairly minor, but it should be noted that improving the agreement here would give rise to tension in other observationally constrained relations.

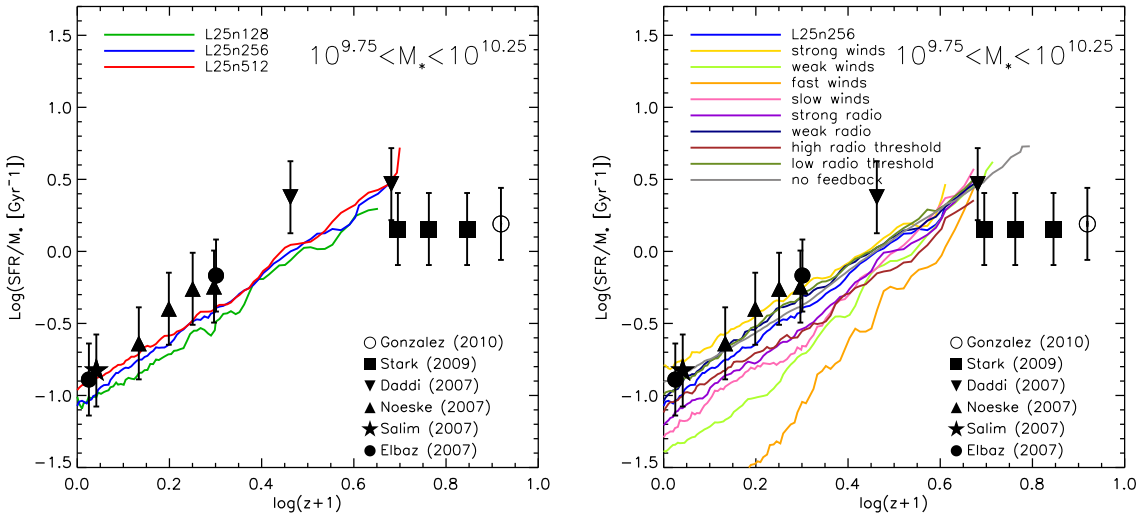

Figure 4.8.—: The median specific star formation rate for galaxies with stellar masses $10^{9.75} M_\odot < M_* < 10^{10.25} M_\odot$ is shown as a function of redshift along with observational data for three different resolutions of our fiducial feedback model (left) and variations of our fiducial feedback model parameters (right). We plot curves only where we have at least 10 galaxies in the selected mass bin. Observational data is taken from González et al. (2010), Stark et al. (2009), Daddi et al. (2007), Noeske et al. (2007), Salim et al. (2007), and Elbaz et al. (2007). There is a clear evolution toward higher specific star formation rates in the past as seen in the data. Feedback – particularly our wind model – is partially responsible for the normalization of this relation. There is a normalization offset between the models and the observations, which slowly increases with time.

4.5 Galaxy Properties

The previous two sections focused on examining the buildup of stellar mass in our simulations. We have shown that our feedback models are capable of producing galaxy populations that form and evolve over time consistently with a wide range of observational constraints. In this section, we explore the simulated Tully-Fisher and mass-metallicity relations.

4.5.1 Tully-Fisher

The Tully-Fisher (TF) relation describes the observed correlation between galactic mass (or luminosity) and rotational velocity (Tully & Fisher 1977). This is an important indicator of galactic structure because it combines information about galactic mass, concentration, and angular momentum. It is a major goal of galaxy formation models to explain the slope, zero-point, scatter, and redshift evolution of the TF relation (e.g. Silk 1997; Steinmetz & Navarro 1999; van den Bosch 2000, 2002; Sommer-Larsen et al. 2003; Dutton et al. 2007). We showed already in Paper I, that our galaxy formation model reproduces the $z = 0$ TF relations. In this section, we examine the TF relation at several redshifts and explore how our model evolves with respect to observational constraints.

Figure 4.9 shows the Tully-Fisher relations for the various feedback models at redshifts $z = 2$, $z = 1$, and $z = 0$. We show the binned median Tully-Fisher relation for the various feedback models (bottom) and resolutions (top) along with a two dimensional histogram denoting the distribution of galaxies for the "L25n256" (bottom) and "L25n512" (top) simulations. For comparison, observational Tully-Fisher relations

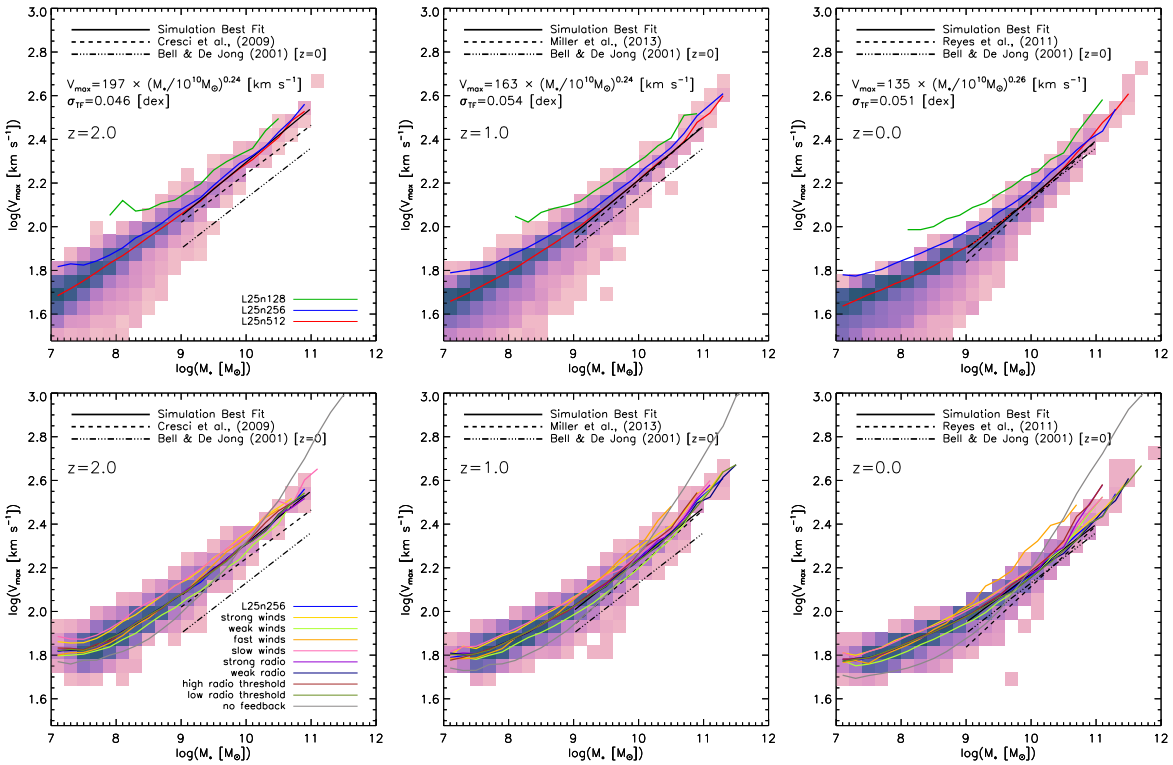

Figure 4.9.—: Binned median Tully-Fisher relations are shown for three different resolutions (top) and our varied feedback models (bottom) as solid lines for redshifts $z = 2$, $z = 1$, and $z = 0$ from from left to right, respectively. Bins of width $\Delta M_* = 0.2$ [dex] were used, with a minimum of 3 galaxies per bin. In the background, two dimensional histograms show the galaxy distribution for the L25n512 (top) and L25n256 (bottom) simulations. The dark solid line shows the best fit to the simulated TF relation with the best fit parameters noted within the plotted region for the L25n512 (top) and L25n256 (bottom) simulations.

are also shown.

The simulated galaxy populations do contain positive correlations between the galaxy stellar mass and $V_{\rm max}$. To parameterise our results, we adopt a functional form for the TF relation

$$\log\left(\frac{V_{\rm max}}{\rm km\ sec^{-1}}\right) = \log\left(\frac{V_{\rm max,10}}{\rm km\ sec^{-1}}\right) + b\log\left(\frac{M_*}{10^{10}{\rm M}_\odot}\right) \quad (4.2)$$

where M_* is the stellar mass, and $V_{\rm max}$ is the circular velocity at twice the stellar half mass radius. A best fit relation is found at each redshift via RMS minimisation of all galaxies with stellar masses $10^9 M_\odot < M_* < 10^{11} M_\odot$. The best fit is plotted within Figure 4.9 as a solid black line and the parameters are printed within the plotted region for the "L25n256" (bottom) and "L25n512" (top) simulations.

Feedback is required to obtain a proper slope and normalization for the Tully-Fisher relation at any of the plotted redshifts, as seen in the bottom panel of Figure 4.9. The simulated "no feedback" Tully-Fisher relation is too steep and extends to substantially higher rotational velocities than are seen observationally. Most of the feedback models produce consistent Tully-Fisher relation slopes, but there is some variability in the normalization as has been discussed already in Paper I. At redshift $z = 0$ the L25n512 simulation $M_* - V_{\rm max}$ relation has a slope of $b = 0.26$ which is similar the recent measurements of Reyes et al. (2011, $b = 0.27$) (but slightly above the TF relation slope found by Bell & de Jong (2001, $b \approx 0.23$)). As we consider the evolution to higher redshift, the L25n512 simulation retains a nearly constant $M_* - V_{\rm max}$ relation slope of $b = 0.24$, which is reasonably consistent with the observed redshift $z = 1$ TF slope (Miller et al. 2012, $b = 0.26$). Although we do not list their slopes explicitly, the other feedback models explored here all yield similar slopes (with the exception of the "no feedback"

simulation).

All of feedback simulations show a slight evolution in the normalization of the Tully-Fisher relation towards higher rotational velocities at a fixed stellar mass at higher redshifts. Since this evolution is somewhat subtle (compared to e.g., the SFMS evolution), we have included the redshift $z = 0$ TF relation in all redshift plots. The normalization evolution is similar to that found in high redshift disk-dominated samples (e.g., Miller et al. 2013; Cresci et al. 2009). We note that while a number of previous studies have indicated that there is an offset in the high redshift TF relation relative to the local TF relation that increases with redshift (Puech et al. 2008; Cresci et al. 2009; Gnerucci et al. 2011; Vergani et al. 2012; Miller et al. 2013), there is also evidence suggesting that no such evolution occurs in the TF normalization (Miller et al. 2011, 2012). It is unclear exactly what drives the discrepancy in the observed normalization evolution. However, one possibility is that the offset is sensitive to galaxy morphology (Miller et al. 2013) which could explain why the rotationally dominated selected samples (e.g., Cresci et al. 2009) found clear TF relation offsets.

The resolution dependence of these inferences can be seen in the top panel of Figure 4.9 where we show the simulated Tully-Fisher relation for our fiducial feedback model at three different resolutions. There is a noticeable offset between the low and intermediate resolution simulations at all redshifts, with the intermediate resolution simulation having lower rotational velocities at a fixed stellar mass. The magnitude of this offset decreases between the intermediate and high resolution simulations, and is particularly small for the most massive systems at all redshifts. This indicates that the simulated Tully-Fisher relation is numerically converging for our highest resolution simulations. Moreover, we note that the highest resolution simulations are converging to

a Tully-Fisher relation which is consistent with the marked observational relations at all redshifts. While the measured slope of the simulated intermediate resolution simulation remained fixed at $b = 0.22 - 0.23$ over the plotted redshift range, the slope of the high resolution simulation remains nearly fixed at a slightly larger value of $b = 0.24 - 0.26$ – which is still consistent with the local and high redshift measured TF slopes.

Overall, we find that our fiducial feedback galaxy formation model describes the evolution of the slope and normalization of the stellar TF relation reasonably well (certainly much better than our model without feedback). Our results are consistent with the conclusions of several previous simulation based studies that examined the local Tully-Fisher relation (e.g., Portinari & Sommer-Larsen 2007; Croft et al. 2009; de Rossi et al. 2010, 2012; McCarthy et al. 2012b). Typically, it is found that including feedback is critical to obtaining the correct TF normalization (e.g., Governato et al. 2007) because it reduces buildup of stellar material in a central, compact component. We do not find any significant evolution in the slope of the TF relation with redshift, but we do find an evolution in the normalization which is consistent with both observational results and previous simulation work (de Rossi et al. 2010).

4.5.2 Mass Metallicity Relation

After metals are returned to the ISM from aging stellar populations, they can be retained in the ISM, locked into future generations of stars, or ejected from the galaxy via outflow processes driven by stellar winds or AGN activity. Although not all of these processes are directly observable, HII region nebular emission line diagnostics allow for observational estimates of the metallicity of star-forming gas in galaxies. This provides information

that can constrain the character of outflow models. Although it is critical to many of the results presented in the previous sections that strong winds must operate on low mass galaxies in order for their stellar mass build-up to mimic observations, these same winds will carry metals along with them and can potentially deplete a substantial fraction of a galaxy's metal content. On the other hand, in the absence of any strong feedback we expect that galaxies will be unable to eject any metals which they produce, potentially leading to an overproduction of metals.

Figure 4.10 shows the MZ relations for our various feedback models at redshifts $z = 2$, $z = 1$, and $z = 0$. The metallicities have been determined by finding the average star formation rate weighted oxygen abundance in each galaxy, which places an emphasis on star-forming gas as is done through metallicity estimates via nebular emission lines. In each figure, we show a two-dimensional histogram denoting the distribution of galaxies for the "L25n256" (bottom panel) and "L25n512" (top panel) simulations. Additionally, we show coloured lines marking the binned median MZ relation for the various feedback models (bottom) and resolutions (top) as noted in the legend. Mass bins of $\Delta M = 0.2$ dex are used, and median lines are shown if the mass bin contains at least 3 galaxies. Observational MZ relations are shown within the figures for comparison. We include MZ data from SDSS DR7 (Abazajian et al. 2009), DEEP2 (Davis et al. 2003), and Erb et al. (2006a) at redshifts $z = 0$, 0.8, and 2 as compiled in Table 1 of Zahid et al. (2012) for comparison against the simulation results. There are uncertainties in the overall normalization of the observed metallicity abundance measurements, so we apply the empirical conversion of Kewley & Ellison (2008) and plot the observed MZ data using the Kobulnicky & Kewley (2004, hereafter: KK04) and Pettini & Pagel (2004, hereafter: PP04) diagnostics.

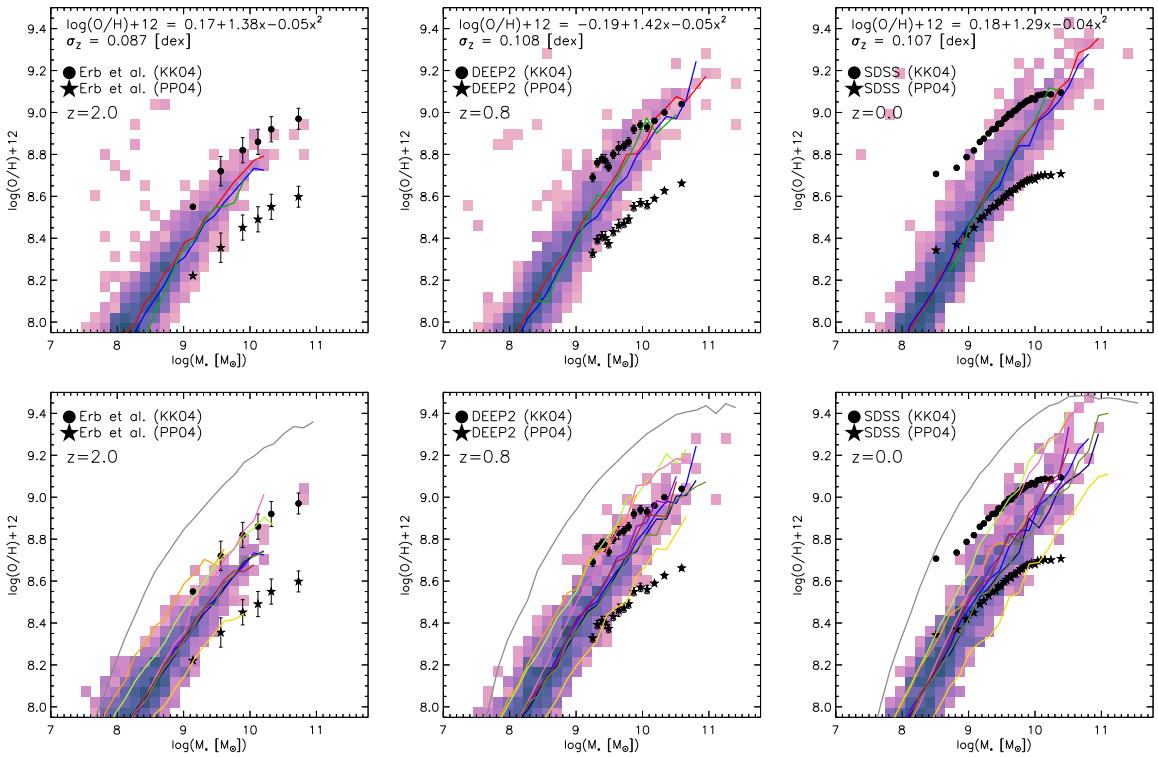

Figure 4.10.—: Binned median mass-metallicity relations are shown for three different resolutions (top) and our varied feedback models (bottom) as solid lines for redshifts $z = 2$, $z = 1$, and $z = 0$ from from left to right, respectively. In the background, two dimensional histograms show the galaxy distribution for the L25n512 (top) and L25n256 (bottom) simulations. The observational MZ relations are taken from SDSS DR7 (Abazajian et al. 2009), DEEP2 (Davis et al. 2003), and Erb et al. (2006a) as compiled in Table 1 of Zahid et al. (2012). We show the observational MZ relations using the KK04 diagnostic, as well as the PP04 diagnostic, to demonstrate systematic uncertainties in observational nebular emission line determinations.

The metal content of galaxies is strongly dependent on the adopted feedback model, as demonstrated in the bottom panel of Figure 4.10. At redshift $z = 2$, all of the models (except for the "no feedback" case) produce MZ relations that are fairly similar in shape. There is some dispersion in their normalizations. Simulations with strong feedback are efficient at ejecting metals out of galaxies, and tend to have lower MZ relation normalizations. Conversely, simulations with weak winds tend to have higher MZ relation normalizations. At the low mass end, the offset between the "strong winds" and "weak winds" simulations is about 0.3 dex, with the fiducial feedback model (L25n256) falling right in-between. Changes in the AGN feedback do not have a major impact on the high redshift MZ relation. In any case, at redshift $z = 2$ all of the feedback models fall between in the PP04 and KK04 measured MZ relations, and so we cannot rule out any of the models clearly (except for the "no feedback" case).

At redshift $z = 0.8$, the observed MZ relation has shifted slightly upward toward higher metallicities at all mass scales. Many of the feedback simulations show a similar shift. However, the simulations evolve toward higher metallicities preferentially for massive systems, which steepens the simulated MZ relation relative to the observed relation. As a result, all of the feedback runs now have slopes that are slightly steeper than the observed relations. Two of the runs ("weak winds" and "slow winds") are well in excess of the observed KK04 MZ relation. Most of the other runs, however, are still situated between the PP04 and KK04 observational relations. Overall, the most notable missing feature from the simulated MZ relation is the flattening of the MZ relation for some of the more massive systems. While the observed MZ relation flattens for basically all metallicity diagnostics at all observed redshifts, our simulated MZ relation does not show a similar behaviour.

At redshift $z = 0$, the simulated MZ relation is now clearly distinct in shape from the observed MZ relation. The three main descriptive features of the observed MZ relations are the low mass slope, the high mass flattening, and the overall normalization. None of the feedback models accurately reproduce the low mass slope or the high mass flattening. Instead, most of the feedback models produce a constant slope MZ relation that is steeper than the observed relation. There remains a clear dispersion in the normalization of the MZ relation for the various feedback models. Most of the models lie between the PP04 and KK04 MZ relations in the galaxy mass range $10^9 M_\odot < M_* < 10^{10} M_\odot$. However, owing to the their steep slopes, most of the models have both insufficiently low metallicity galaxies at the low mass end and overly enriched galaxies at the high mass end. The significance of the overproduction of metals for massive galaxies is not immediately clear. This flattening at the massive end has been interpreted as saturation of the gas phase metallicity when production of metals from star formation nearly balances the locking up of metals in long lived stellar populations (Edmunds 1990; Savaglio et al. 2005; Zahid et al. 2013). Our simulations should recover such a flattening where the closed box model explanation holds. Instead, it maybe possible that the lack of a flat slope at high metallicities could be caused by inefficient expulsion of metals from massive systems due to the diminishing mass loading factor for winds in massive haloes. Alternatively, there is on-going discussion regarding the validity of nebular emission line diagnostics for high metallicity values (e.g., Nicholls et al. 2013). Updated metallicity diagnostics that take into account non-equilibrium electron energy distributions may show a continued slope of the MZ relation for higher metallicity values, as found in our simulations. For this reason, we avoid further discussion about the discrepancy between the slope of the MZ relation for massive galaxies.

The resolution dependence of the simulated MZ relation can be seen in the upper panel of Figure 4.10. There are no major or systematic changes in the simulated MZ relation between the different resolution simulations. This consistency holds true for all of the plotted redshifts, indicating that the MZ relation is well converged. Any issues with the shape of the simulated MZ relation are not likely to substantially change if we moved to higher resolution simulations.

The origin of the steep MZ slope in our simulations is the low metal retention efficiency of low mass galaxies owing to galactic winds with large mass loadings. Strong winds facilitate the mixing of the central metal rich disk gas with the metal poor hot halo gas. In low mass galaxies – where the mass loading factors for winds are very high – this prevents a substantial buildup of metal mass, which ultimately leads to the steep redshift $z = 0$ MZ relation shown in Figure 4.10. We note that this effect is stronger if we do not treat the mass and metal loading for our winds independently. As described above and in Paper I, we have adopted a wind metal loading factor in our model, which determines the metallicity of the wind material relative to the local ISM metallicity from where the wind is launched. Even with a reduced metal loading factor, which helps galaxies maintain a larger fraction of the metals they produce, we still find that the lowest mass galaxies have gas-phase metallicities that are at or below the lowest of observational expectations. This exposes an interesting tension between our need for high wind efficiencies to reduce the buildup of stellar mass in low mass galaxies, and the need for low mass galaxies to be relatively efficient at retaining their metal content (Zahid et al. 2012). The solution to this tension likely either lies in: (i) fundamentally reducing the accretion efficiency of low mass galaxies via some feedback mechanism that is able to disrupt and heat the IGM around these systems or (ii) a more detailed wind model that

self consistently handles the entrainment of low metallicity material as winds propagate out of galaxies (e.g., Hopkins et al. 2012a).

We conclude that many of our feedback models are capable of producing an MZ relation which has an appropriate slope and normalization at high redshift, but is notably steeper than observations at low redshift (albeit with reasonable normalizations). Several previous studies have been successful at reproducing the MZ relation at both redshift $z = 0$ (e.g., Brooks et al. 2007; de Rossi et al. 2007) and higher redshifts (Brooks et al. 2007; Kobayashi et al. 2007; de Rossi et al. 2007; Tassis et al. 2008) and we note that the MZ results presented in this section are somewhat different from what has been found previously (in particular Davé et al. 2011a, which is of practical interest because of the similarities in our wind models). There are three principle sources of differences between our models and earlier ones, which are all numerical in nature.

First, the gas fractions of the galaxies formed in the simulations presented are generally higher than those of Davé et al. (2011a). This is partially due to differences in the way galaxies accrete gas (Nelson et al. 2013) and form central gas reservoirs (Torrey et al. 2012), which makes it difficult to separate out particular aspects of the calculations that lead to results that are different from ours. Higher gas fractions lead to diluted/lowered metallicity values, which is partially responsible for the lower metallicity values of low mass galaxies found in our simulations. Second, while mixing is numerically suppressed in SPH simulations, it can be artificially enhanced in grid based simulations due to poor resolution. Employing a moving mesh hydro solver minimises the impact of artificial mixing significantly (Springel 2010a; Genel et al. 2013). Nevertheless, mixing in our simulations is more efficient than in previous SPH simulations, which will lead to a systematic lowering (or dilution via mixing) of the central galactic gas phase

metallicity. Third, the wind prescriptions used in Davé et al. (2011a) are momentum conserving, which scale less steeply with galaxy mass than the energy conserving wind models adopted here. These effects translate into a shallower MZ relation, which would be in better agreement with the redshift $z = 0$ observed MZ slope, as was found in Davé et al. (2011a). The overall picture observed in our simulations of mixing dominating the reduction in the observed metallicity of low mass systems is similar to that presented in Tassis et al. (2008), except in our case this process is too efficient to reproduce observations. This places constraints on the character of our wind model which will be considered in future work.

4.6 Discussion and Conclusions

Simulating the formation and evolution of the galaxy population in a fully cosmological context is an inherently difficult numerical task. It requires a very large dynamic range such that galactic structural scales can be resolved within a full cosmic volume simulation box. Furthermore, it requires numerically well-posed modelling of the complex baryon physical processes to yield realistic galaxy populations.

In Paper I we introduced a new feedback module into the simulation code AREPO which is intended to regulate the growth of galaxies by introducing star formation driven winds and AGN feedback. It was shown that – with this feedback module included – our simulations are able to match a number of redshift $z = 0$ observed galaxy relations. The primary goal of this paper is to extend the work presented in Paper I by presenting a summary of high redshift galaxy properties as realised in a set of large-volume, high-resolution cosmological hydrodynamical simulations with varied assumptions for

the star formation driven winds and AGN feedback.

The critical point of including feedback in our models is to regulate when and where galaxies build up their stellar mass. The performance of any such model can be directly tested by comparing against observations at several epochs. As we have attempted to demonstrate throughout this paper, we have constructed a reasonably self-consistent model, where galactic stellar mass measurements, star formation rate measurements, and structural measurements are broadly reproduced by our fiducial feedback model without major violations of observational constraints. However, our implementation of feedback is not unique, and it is worth discussing some of the more subtle tensions that exist in our models that might provide information about how we can improve upon them in the future.

Our currently implemented star formation driven wind prescription is based on the hydrodynamically decoupled wind model of Springel & Hernquist (2003a) with a modification to allow for variable wind speeds based on the local dark matter velocity dispersion (Oppenheimer & Davé 2006; Okamoto et al. 2010). In our models, these winds are critical for reproducing the evolving low mass slope of the GSMF and regulating the magnitude of global star formation rate density in low mass haloes in the early Universe. The two free parameters in this model (the energy normalization and the wind speed) have been set based on their ability to reproduce the evolving SFRD and redshift $z = 0$ GSMF (and, similarly, the redshift $z = 0$ SMHM relation). Our fiducial model employs a very strong energy normalization (the full amount of energy available from core collapse supernovae, as discussed in Paper I). Such a high energy normalization may be reasonable given the many physical processes (e.g., photoionization of gas, radiation pressure from young stars, etc.) for which η is intended to be a proxy. However, even

with such a strong energy normalization we found there is an overproduction of stellar mass in these systems at redshift $z = 0$ for the high resolution simulations as shown in Figure 4.1. This offset cannot be fully corrected by simply introducing a larger energy normalization for our wind model because of the characteristic flat evolution in the number density of low mass systems in all of our feedback model simulations at late times.

Similarly all of our simulations tend to mildly undershoot the observed SFMS normalization with a slope that is systematically steeper than SFMS observational measurements. This makes the disagreement between our simulations and observations the worst for low mass galaxies. Introducing stronger winds does tend to increase the normalization of the SFMS. However, the normalization shift is most pronounced at late times (after previously ejected wind material has had time to re-accrete), while the normalization offset between observations and simulations is most dramatic at high redshift (i.e. $z = 2$).

Nevertheless, our fiducial feedback model matches a wide range of observational metrics. We note that our model only slightly overshoots in the mass buildup of low mass galaxies (by a factor of ~ 2) and only slightly undershoots the observed star formation rates of low mass galaxies (by, again, a factor of ~ 2). Given that observational uncertainties on, e.g., stellar mass measurements (Mitchell et al. 2013) or star formation rate determinations can be of this same order, we would not stress this as being a critical issue to our model. However, we emphasise that within the context of our adopted kinetic wind model there are not any immediate or clear alternative parameter choices that will allow us to simultaneously reduce these tensions further.

One clue regarding the nature of our wind model can be obtained from comparisons with observed MZ relations. The large wind mass loading factors that are required to regulate the growth of low mass systems double back as very efficient mechanisms to eject metals from galaxies. This gives rise to an important, yet seemingly unappreciated, tension. Empirical estimates of the total oxygen content of low mass galaxies indicate that these systems can eject only some reasonably small fraction (e.g., 30%) of their metals (Zahid et al. 2012). Yet, when cosmological simulations tune their wind prescriptions to match, e.g., the galaxy stellar mass function, they often adopt very strong wind mass loading factors that substantially exceed this limit under the traditional assumption that the metallicity of wind material is the same as the metallicity of the local ISM from where the wind was launched.

There are two clear ways to resolve this issue. The first is to reduce the efficiency with which material is ejected out of galaxies. This can be achieved very straightforwardly in our models by lowering the energy normalization for our winds. However, doing so would immediately increase the masses of all galaxies, ruining the agreement with the GSMF, SMHM relation, and early SFRD evolution. A more robust solution would be to allow winds to have a more disruptive effect on the accretion of gas into low mass galaxies. By, for example, allowing winds to be pushed by cosmic ray streaming (Uhlig et al. 2012) or to carry along with them some thermal energy, it may be possible to reduce the star formation rates in low mass galaxies by disrupting the IGM around these systems. The second possible solution is to modify our sub-grid picture for the wind structure, as we have done in this paper. Substantially higher resolution simulations on the origin of galactic winds indicate that: (i) wind mass loading factors far in excess of unity are physically plausible and (ii) the origin and composition of ejected material can

depend on the physical mechanism responsible for launching the wind (Hopkins et al. 2012a). By accounting for the impact of low metallicity gas entrainment that might occur as a wind propagates out of the systems, the evolution of the MZ relation can be brought back into reasonable agreement with observations. It is likely that both of these issues are partially responsible for the MZ relation tension, and it will be interesting to consider how alternative galactic wind formulations and modifications of our currently employed hydrodynamically decoupled wind prescriptions can resolve this issue.

An additional interesting issue with our simulated MZ relations is that they fail to reproduce the observed flattening seen in the observed MZ relation for massive galaxies. As discussed previously, the detailed cause of this discrepancy is unclear. However, it should also be noted that recent papers have called into question the validity of the standard nebular emission line metallicity diagnostics for very high metallicity values (Nicholls et al. 2013).

The most promising next step to be taken with these models is to extend their application to larger simulation volumes at comparable mass and spatial resolution to the runs we have employed here. The $L = 25h^{-1}$ Mpc boxes used in this paper have served as excellent testbeds for understanding the impact of our feedback models. Within these volumes we can already find a wide variety of galaxy properties and demonstrate the success of our model in reproducing basic observational constraints like the GSMF and cosmic SFRD. However, this (relatively small) simulation box does not do an adequate job of sampling different density environments or of producing a sufficiently large number of massive galaxies, groups, and clusters to perform detailed statistical modeling. For this reason, our ability to discuss the high redshift cutoff the GSMF or the turnover in the SMHM relation is limited. Moreover, our ability to do

detailed morphological classification and perform environment studies is limited. This can be remedied by moving to larger simulation volumes (ideally without sacrificing mass or spatial resolution). Using larger simulation volumes, many additional science question can be addressed including correlations between galactic star formation rate and environment, correlations between galactic morphology and physical properties, or the predominant formation venues for massive elliptical and star forming disk galaxies.

Chapter 5

Illustris Simulation Observatory: A Catalog of Mock Galaxy Images and Spectra

P. Torrey, G. Snyder, M. Vogelsberger, C. Hayward, S. Genel, D. Sijacki, V. Springel, & L. Hernquist

> "If you want to win something, run 100 meters. If you want to experience something, run a marathon."
>
> — Emil Zatopek

5.1 Introduction

In the currently favored Λ cold dark matter (ΛCDM) paradigm, structure formation is driven by the gravitational collapse of dark matter haloes (White & Rees 1978; Fall &

Efstathiou 1980; Blumenthal et al. 1984). Galaxies form within these haloes when gas cools and collapses into their potential wells. The formation of dark matter haloes has been studied extensively using numerical dark matter only simulations (e.g., Springel et al. 2005c; Boylan-Kolchin et al. 2009; Fosalba et al. 2008; Teyssier et al. 2009; Klypin et al. 2011). Applying the findings from dark matter only simulations to build a theory of galaxy formation requires a method to link the formation of dark matter haloes to observable galaxy properties. Hydrodynamical simulations are the most direct method for modeling the co-evolution of dark matter and baryons (e.g. Katz et al. 1992, 1996; Weinberg et al. 1997; Murali et al. 2002; Springel & Hernquist 2003b; Kereš et al. 2005; Ocvirk et al. 2008; Crain et al. 2009; Croft et al. 2009; Schaye et al. 2010; Oppenheimer et al. 2010; Vogelsberger et al. 2012). By directly including hydrodynamics in structure formation simulations one can gain insight into the thermal state and column density distribution of the intergalactic medium (IGM) via the Lyman-α forest (Cen et al. 1994; Zhang et al. 1995; Hernquist et al. 1996; Theuns et al. 1998), phase structure and heavy element composition of the circumgalactic medium (CGM) and IGM (Aguirre et al. 2001; Cen & Fang 2006; van de Voort & Schaye 2012b; Shen et al. 2013), and accretion rates/properties of dark matter and baryons into galaxies (Kereš et al. 2005; van de Voort et al. 2011; Nelson et al. 2013). Since hydro simulations follow the dynamics of both the dark matter and baryons self-consistently, predictions can be made about the internal structure of galaxies, including the distribution of gas (Kereš et al. 2012; Torrey et al. 2012) and the formation of stellar disks and bulges (Abadi et al. 2003; Governato et al. 2004; Agertz et al. 2011; Marinacci et al. 2014). As a result of this detailed information, simulations are a valuable tool for interpreting observational data and placing observed galaxies into a more complete evolution based cosmological context.

One limiting factor when making comparisons between hydrodynamical simulations and observations is translating results into a common language to facilitate even-handed comparisons (e.g., Conroy et al. 2010). Many important galaxy properties – such as stellar mass – have substantial uncertainties associated with their measurement (e.g., Conroy & Wechsler 2009; Conroy & Gunn 2010, and references therein). These uncertainties can be physical in origin (e.g., the slope of the IMF, treatment of the thermally pulsating asymptotic giant branch phase, etc.) or due to assumptions made during the spectral energy distribution (SED) fitting procedures (Papovich et al. 2001; Wuyts et al. 2007; Gallazzi & Bell 2009; Michałowski et al. 2012; Banerji et al. 2013). Accurately estimating physical galaxy properties based on 10's of broadband photometric data points (or even full SEDs) is difficult because observed galaxy SEDs contain contributions from stars with a complex distribution of stellar ages and metallicities. Simplifying assumptions regarding the functional form of the star formation history or a uniform stellar metallicity are often assumed. These assumptions can lead to systematic errors on the derived galaxy stellar mass, independent of physical uncertainties (e.g., Mitchell et al. 2013). Similarly, derived galaxy structural properties – such as bulge-to-disk decompositions or galaxy sizes – are often determined inconsistently in simulations and observations (Scannapieco et al. 2010).

A powerful way to facilitate direct comparisons is to convert simulated galaxy populations into mock observations. This can be achieved in simulations by adopting stellar population synthesis (SPS) models to assign light to all star particles within a galaxy based on their age and metallicity distributions (Tinsley 1972; Bruzual A. 1983; Buzzoni 1989; Bruzual A. & Charlot 1993; Worthey 1994; Maraston 1998; Leitherer et al. 1999; Bruzual & Charlot 2003; Thomas et al. 2003; Maraston 2005). When produced in

this fashion mock observations inherit the same physical uncertainties mentioned above, but can be used to address issues with the way SED fitting or photometric analysis is performed. A large body of literature already exists within the idealized merger simulation community: Lotz et al. (2008) used mock broadband images of idealized merger simulations (Cox et al. 2006b) to determine the conversion from observed galaxy pair counts into merger rates. Wild et al. (2009) and Snyder et al. (2011) used mock galaxy SEDs of idealized mergers to determine the lifetime and redshift dependent abundance of K+A galaxies. Snyder et al. (2013) used synthetic galaxy spectra to propose a new Mid-IR diagnostic of AGN. Similar work exists within the semi analytic community including the production of mock galaxy luminosity functions (e.g., Henriques et al. 2011; Somerville et al. 2012) and mock light-cone data (Kitzbichler & White 2007; Henriques et al. 2012; Overzier et al. 2013) based on dark matter only simulations (Springel et al. 2005c).

In this paper, we describe the production of a mock galaxy image catalog based on the recent Illustris simulation (Vogelsberer et al 2014). The Illustris project has two basic principles. First, a comprehensive feedback module was adopted to allow galaxy populations to regulate their stellar mass growth appropriately. The central components of this feedback model were first presented in Vogelsberger et al. (2013) and demonstrated to regulate galaxy populations appropriately at several epochs in Torrey et al. (2014). Adopting this feedback model ensures that simulations run as part of the Illustris project will match a wide range of galaxy observable properties such as the cosmic star formation rate density, the evolving galaxy stellar mass function, and the star formation main sequence (Genel 2014). The second component of the Illustris project is to apply these feedback models on full hydro simulations in large cosmological

volumes (i.e. in periodic boxes of size $L \sim 100$ Mpc), with sufficiently high mass and spatial resolution (i.e. $M_{\rm Bar} \sim 10^6 M_\odot$ and $\epsilon \lesssim 1$ kpc) to resolve a wide range of galaxy structures. In contrast to "zoom-in" style simulations of individual objects, large-volume simulations allow populations of resolved galaxies to evolve – naturally facilitating comparisons to observational survey data. Using results from the Illustris simulation, we employ stellar population synthesis (SPS) templates to produce mock broadband galaxy images and integrated SEDs. These mock images encode information about the spatial distribution and formation history of galactic stellar components. This enables color image production, SED fitting, morphology classification, and measurements of galaxy structure. In this paper, we detail our methods for producing these images, demonstrate some initial science cases, and explain how one will be able to access these images.

This paper is outlined as follows: In §5.2 we describe the simulation that has been used to produce our mock image catalog as well as our methods for producing the mock galaxy image catalog based on its output. In §5.3 we describe the format for the mock galaxy images, and demonstrate multi-band image generation. In §5.4 we provide a detailed application of this data, by determining stellar mass measurements using a popular SED fitting code to compare the SED derived stellar masses against the simulation based stellar mass determination. In §5.6 we summarize and conclude.

5.2 Methods

In this section we describe of our procedure for producing mock galaxy SEDs and photometric images. We provide details on the simulation that forms the basis of our mock image catalog, explain how light is assigned to each galaxy to produce mock

Table 5.1:: List of broadband filters used in the Illustris Virtual Observatory.

Filter	$\lambda_{\rm eff}$ (Å)	Field Number
GALAX FUV	1513.3	1
GALAX NUV	2300.5	2
SDSS-u	3573.1	3
SDSS-g	4724.1	4
SDSS-r	6201.4	5
SDSS-i	7524.7	6
SDSS-z	8917.3	7
IRAC1	35667.8	8
IRAC2	45023.2	9
IRAC3	56852.6	10
IRAC4	79040.1	11
Johnson-U	3650.9	12
Johnson-B	4449.0	13
Cousins-R	6599.4	14
Cousins-I	8061.5	15
Johnson-V	5506.9	16
Johnson-J	12269.0	17
Johnson-H	16466.8	18
Johnson-K	22008.3	20
2MASS-H	16567.4	19
2MASS-Ks	21620.0	21
ACS-F435	4329.2	22
ACS-F606	5929.7	23
ACS-F775	7712.9	24
ACS-F850	9071.6	25

Continued on next page

Table 5.1 – continued from previous page

f105w	10539.9	26
f125w	12449.4	27
f160w	15314.6	28
NIRCAM-F070W[a]	6955.5	29
NIRCAM-F090W	9031.3	30
NIRCAM-F115W	11515.3	31
NIRCAM-F150W	15064.8	32
NIRCAM-F200W	19831.5	33
NIRCAM-F277W	27728.0	34
NIRCAM-F356W	35751.1	35
NIRCAM-F444W	44292.7	36

[a] Preliminary JWST/NIRCAM filter curves were obtained from www.stsci.edu/jwst/instruments/nircam/instrumentdesign/filters

images, and outline the resulting data product format.

5.2.1 The Illustris Simulation

All mock images are produced based on galaxies formed in the Illustris simulation. A detailed description of the Illustris simulation can be found in Vogelsberer et al (2014). We briefly summarize the simulation properties below.

The Illustris simulation is a large-volume cosmological hydrodynamical simulation that was run in a periodic box of size $L = 75h^{-1}$ Mpc with $N_{\rm DM} = 1820^3$ dark matter particles ($M_{\rm DM} = 6.3 \times 10^6 M_\odot$) and $N_{\rm Bar} \approx 1820^3$ baryon resolution elements ($M_b \approx 1.3 \times 10^6 M_\odot$). Cosmological parameters consistent with the latest Wilkinson Microwave Anisotropy Probe (WMAP)-9 measurements were adopted ($\Omega_M = 0.2726$, $\Omega_\Lambda = 0.7274$, $\Omega_b = 0.0456$, $\sigma_8 = 0.809$, $n_s = 0.963$, and $H_0 = 100\ h$ km s^{-1} Mpc^{-1} with $h = 0.704$). The Illustris simulation was run using the moving mesh code AREPO which, in addition to gravity and hydrodynamics (Springel 2010a), includes a comprehensive physics and feedback module allowing for radiative gas cooling (Katz et al. 1996; Wiersma et al. 2009a), star formation with associated feedback (Springel & Hernquist 2003a), mass and metal return to the interstellar medium from aging stellar populations (Wiersma et al. 2009b), and active galactic nuclei (AGN) feedback (Sijacki & Springel 2006; Sijacki et al. 2007) as described in detail in Vogelsberger et al. (2013). The feedback included in the Illustris simulation was tuned to match the redshift $z = 0$ galaxy stellar mass function and evolving cosmic star formation rate density (Vogelsberger et al. 2013), but has also been shown to produce galaxy populations that evolve consistently with observations (Torrey et al. 2014).

Galaxies are defined in the simulation via the SUBFIND halo finder (Springel et al. 2001). For each galaxy, we identify all associated particles (gas, stars, and dark matter) and produce a 'mini-snapshot' file that contains all particle information for each galaxy. Mini-snapshots files are technically an unnecessary replication of the simulation data, however they are produced to make the data for each galaxy more easily accessible (each full Illustris snapshot is 2Tb, and therefore it can be rather slow to extract individual galaxy data). These mini-snapshots can be opened and processed very easily and are in the natural format for simulation post-processing analysis tools that have been designed to run on individual galaxies.

We employ the radiative transfer code SUNRISE[1] (Jonsson 2006; Jonsson et al. 2010) to produce galaxy images based on the mini-snapshot files. We use SUNRISE to (i) assign full spectra to each star particle based on its age and metallicity, (ii) redshift the spectra appropriately, (iii) generate images of arbitrary field of view and pixel size for arbitrary camera positions, and (iv) convolve spectra with arbitrary (pre-tabulated) broadband filter transmission functions. In the present work, we do not apply the dust absorption, scattering, or emission functionality of SUNRISE. While these are important considerations for SED modeling, we do not expect the SUNRISE radiative transfer results to be fully converged for the mass and spatial resolutions employed by the Illustris simulation (Jonsson et al. 2010). Instead, we use only a simple empirically motivated dust obscuration correction (described below) and leave a more complete examination of dust and its consequence for mock images to future studies. Although we do not directly perform radiative transfer, using SUNRISE allows us to reuse an existing, tested, publicly

[1]Sunrise is freely available and documented at http://code.google.com/p/sunrise/.

available code, and to prepare our pipeline software for use on future hydro simulations where full dust modeling may be appropriate. We further assume no contribution to the galaxy SEDs from accreting supermassive black holes.

We run SUNRISE on all galaxies in the simulation with more than 500 simulation stellar particles. We adopt this lower limit because we expect integrated galaxy quantities (e.g., stellar mass or color) to be well defined for these systems. Although this 500 particle lower limit is almost an order of magnitude higher than most other numerical studies, a 500 particle galaxy will not be sufficiently well resolved to study internal galaxy structure. Thus, we save integrated galaxy SEDs and integrated broadband photometry for all systems with more than 500 stellar particles, and only save spatially resolved galaxy images for systems with stellar masses $M_* > 10^{9.5} M_\odot$ ($N_* \gtrsim 3,500$).

5.2.2 Stellar Light

For each galaxy, light is assigned to all constituent star particles based on their mass, age, and metallicity using stellar population synthesis model SEDs. We adopt the STARBURST99 (SB99) single age population model which includes an SED grid resolved with 1221 wavelength bins at 308 age and 25 metallicity values (Leitherer et al. 1999; Vázquez & Leitherer 2005; Leitherer et al. 2010). A single SED is assigned to each star particle out of this grid, scaled according to its formation mass. Figure 5.1 shows the age dependent SEDs for three stellar metallicity values in the SB99 templates.

In our current simulations, each star particle has a stellar mass of $M_* \approx 1.3 \times 10^6 M_\odot$ and represents an unresolved full stellar population. As a result, it is not immediately clear how to distribute the associated stellar light. When radiative transfer is not

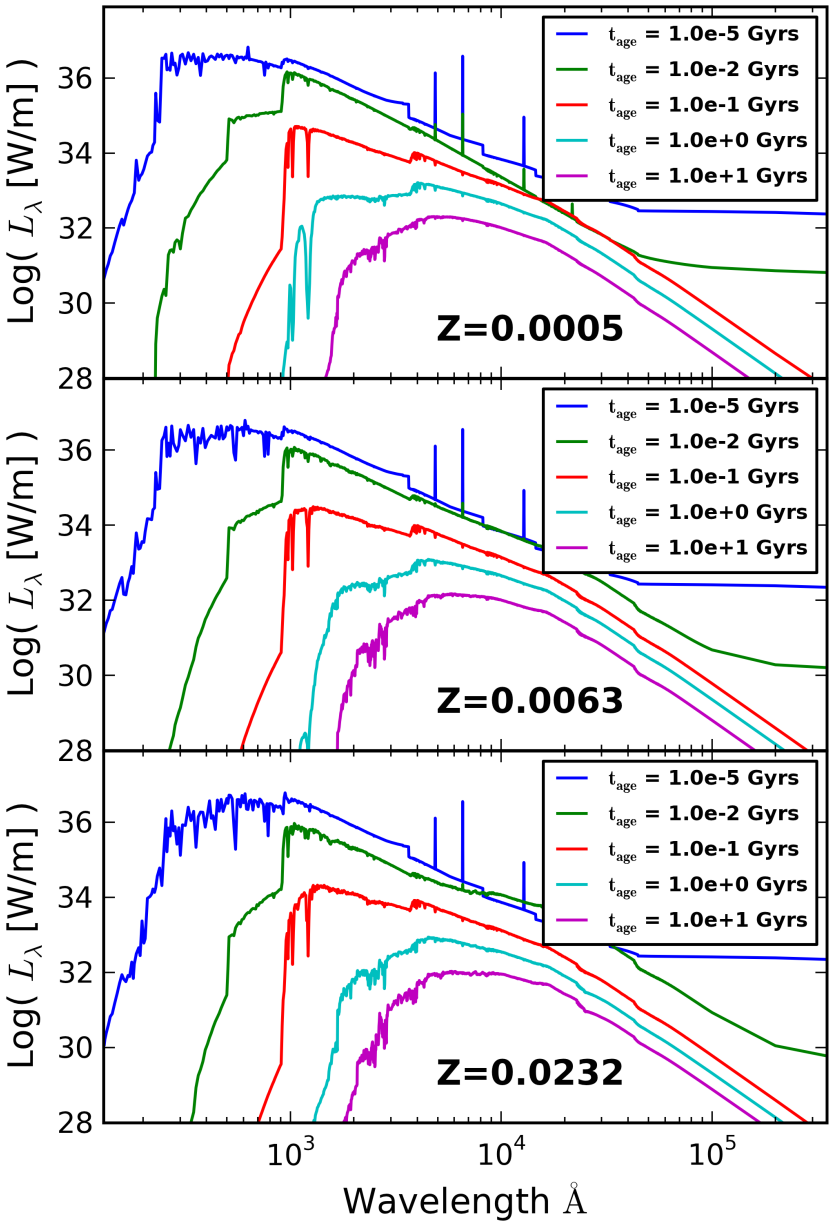

Figure 5.1.—: Input SEDs based on the SB99 stellar population synthesis models. We show SEDs for Z=0.0005 (top), 0.0063 (middle), and 0.0232 (bottom) at several times, as noted in the legend of the figure. Each star particle in the simulation is assigned a single SED by finding the nearest available SED in age-metallicity space. All SEDs used in this paper assume Chabrier IMFs.

considered, adopting an appropriate scheme for spreading stellar light is unimportant for integrated quantities (e.g., the integrated galaxy SED) but can impact visual interpretation of galactic structure and bias quantitive measures. Over smoothing of stellar light will lead to modification/deformation of, e.g., galaxy light profiles – which should obviously be avoided. Under smoothing light can also have adverse consequences for the resulting galaxy images. Consider, for example, a population of individual (simulation) star particles on the far outskirts of a galactic disk. Assigning all stellar light to a single pixel (i.e. assuming each simulation star particle is best represented by a point source) will result in a population of easily identified bright pixels in the galactic outskirts. Smoothing the light from these star particles over several pixels will result in a reduction in the surface brightness of each pixel (perhaps causing the light from these star particles to fall below surface brightness detection limits). Importantly, changing the pixel number for a smoothed light distribution will not change the image attributes as the light will still be smoothed over the same spatial extent, and therefore have the same surface brightness (as long as the pixel scale is smaller than the smoothing scale). Under smoothing of stellar light sources can bias our mock galaxy images toward easy detection of diffuse light components which may only be revealed in very deep observations.

We consider six choices for spreading the stellar light as described below, and demonstrate them in Figure 5.2. The top left panel of Figure 5.2 assigns point source light distributions for each star particle. Point source light distributions require no additional assumptions, but leads to pixilated images where all light from any star particle is always contained within a single pixel. Image pixilation becomes particularly noticeable in the outskirts of the galaxy. This pixilation is not realistic since each star particle represents a *population* of stars, which should have some finite spatial

distribution. Artificial pixilation can be reduced by spreading the light from each star particle over a Gaussian kernel distribution. One natural choice for the smoothing length is the gravitational softening length, and an example resulting image is shown in the second to left panel of Figure 5.2. Employing this fixed smoothing length results in structure in the center of the galaxy being washed out while the galaxy outskirts are dominated by circular stellar light distributions. Increasing the fixed smoothing length further, as shown in the right panel of Figure 5.2, leads to a smooth distribution of light in the galaxy outskirts, but washes out most of the internal galaxy structure, as one might expect.

Based on visual inspection, adaptive light spreading based on the local density of star particles is yield a smooth and well resolved distribution of light from the inner to outer parts of the galaxy. In practice we set the light spreading scale based on the distance for each star to its N^{th} neighbor. In the bottom three panels of Figure 5.2, we show examples of this adaptive light smoothing for three choices of the neighbor number ($N_{\rm NGB} = \{4, 16, 32\}$). We have modified SUNRISE to include the same tree build and neighbor finding steps included in GADGET-2 (Springel 2005) to facilitate efficient neighbor finding for all systems.

None of the light distribution options are formally any more or less valid than the others. We do not rule out that a more physical size light assignment algorithm may be possible. In all subsequent analysis in this paper and for the publicly accessible database, we adopt $N_{NGB} = 16$ as our fiducial choice for the adaptive light smoothing.

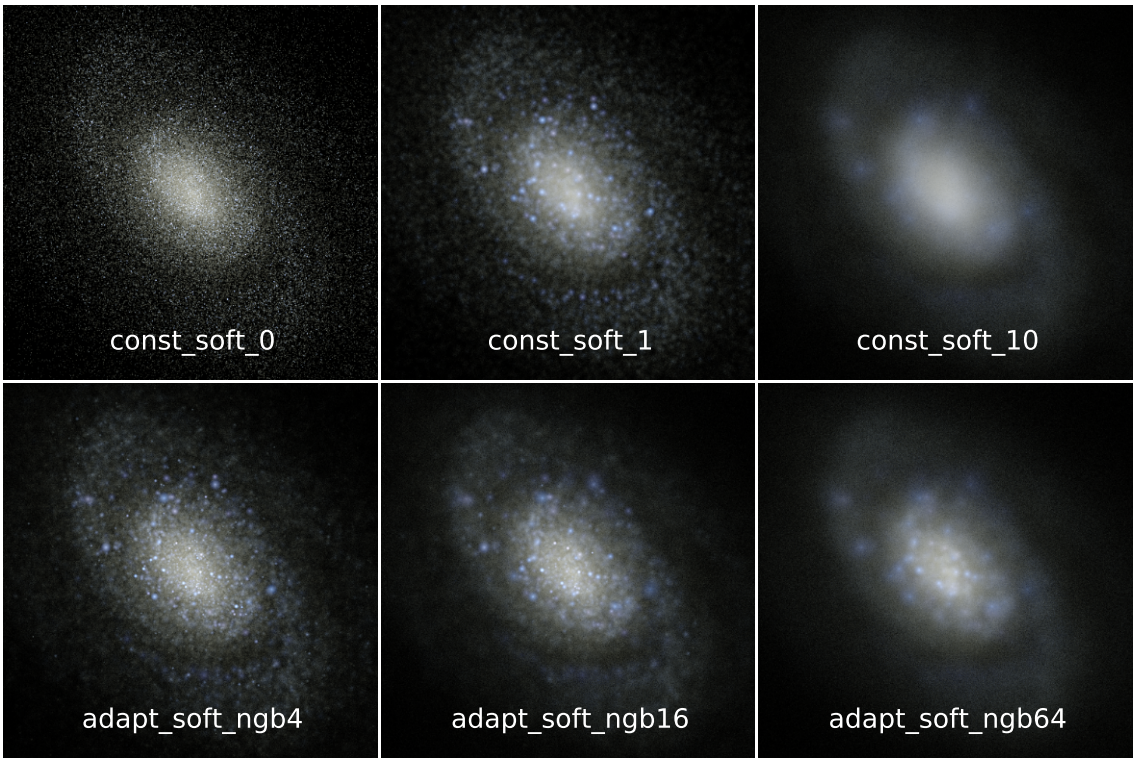

Figure 5.2.—: Montage of images based on several options for the smoothing of stellar light for a single galaxy. The top row shows constant smoothing, with point like source (top left), smoothing set equal to the gravitational softening (top middle), and smoothing set equal to ten times the gravitational softening (top right). The bottom row shows adaptive smoothing, with $N_{NGB} = 4$, $N_{NGB} = 16$, and $N_{NGB} = 64$. We adopt $N_{NGB} = 16$ for all subsequent figures and analysis.

5.2.3 Nebular Emission

Our fiducial galaxy images contain only stellar light. We choose to start with only stellar light because stars dominate the rest-frame optical SED in most local galaxies and non-stellar light sources introduce additional uncertainties in our SED modeling. However, line emission from gas in HII regions (e.g., H-α) can contribute substantially to the flux in certain broadband filters which can have a substantial impact on inferred ages and stellar masses especially for high redshift galaxies where the average star formation rates are much higher than in the local universe (Zackrisson et al. 2008; Schaerer & de Barros 2009; Ono et al. 2010; Stark et al. 2013). We re-calculate the integrated broadband magnitudes for the galaxy population with a model that accounts for the environment around young stellar populations. A complete description of the model can be found in Jonsson et al. (2010). In summary, young stars are assumed to still be partially obscured by their birth clouds. As a result, SUNRISE reassigns the intrinsic SEDs of young star particles assuming a partially obscured young stellar spectra with added contributions from HII regions (Dopita et al. 2005, 2006a,b) as calculated in Groves et al. (2008) via the MAPPINGS-III 1-D photoionization and radiative transfer code (Binette et al. 1985; Sutherland & Dopita 1993; Groves et al. 2004a,b). The MAPPINGS model replaces SB99 emission for all young ($t_{age} < 10^7$ yrs) star particles. The spatial distribution of light for our simulated galaxies with and without the MAPPINGS model is fairly similar. Therefore, to save storage space, we store only integrated quantities for this model.

5.2.4 Dust Obscuration

Our fiducial galaxy images do not contain any dust obscuration because a proper treatment of dust in modifying observed galaxy spectra depends on the distribution of gas and dust on small scales relative to young stellar populations. Given the $\sim$ kpc scale resolution of the Illustris simulation, is it not immediately clear how to best perform dust obscuration. However, in addition to the dust free galaxy images, we do consider the simple empirical dust model of Charlot & Fall (2000, hereafter CF00). The CF00 model accounts for the effects of dust by applying an effective absorption curve proportional to $\lambda^{-0.7}$ to the standard SB99 SED. The normalization of the absorption curve is lowered by a factor of three when stars are assumed to no longer be embedded within their birth clouds after stars are older than $t_{\rm age} > 3 \times 10^7$ yrs. The only parameter in this model is stellar age; no knowledge of the local ISM conditions (including the local gas density or metallicity) are taken into account. The CF00 models have a spatial distribution of light which is similar to the fiducial non-dusty images so we store only integrated quantities for this model.

5.2.5 Image Production and Broadband Definitions

Images are produced by projecting the stellar light using pinhole cameras with a resolution of 256×256 pixels without any noise, foreground stars, or other complicating issues. Each galaxy is viewed from 4 viewing angles which are randomly aligned with respect to the rotation axis of each galaxy. The image field-of-view is set to be 10 times the stellar half mass radius for each galaxy with the galactic potential minimum placed at the center of the image and the camera is assumed to be 50 Mpc away, regardless of

the galaxy's intrinsic redshift. This results in the production of a mock integral field unit (IFU) data cube – with full spectra being associated with each pixel. We convolve the IFU mock data cubes with 36 broadband filter transmission functions – as listed in Table 5.1 – to produce broadband images for each galaxy, assuming the source is at rest with respect to the observer. The resulting broadband images can be used to generate RGB images based on various filter combinations or to facilitate quantitative comparisons with observations.

5.3 Results: Galaxy Images, SEDs, and other data products

The redshift z=0 galaxy population has been run through the SUNRISE pipeline producing a catalog of 40,000 galaxy spectra and 10,000 galaxy images with associated photometric data. This data will be made publicly accessible upon this paper being accepted through a web-based SQL database.[2]

The photometric data for each galaxy is contained in a single, multi-extension FITS file. Each file contains four image extensions, corresponding to the four cameras. Each camera extension has dimensionality of $N_{\rm bands} \times N_{\rm pixels} \times N_{\rm pixels}$. The ordering of the broadband filters can be found in Table 5.1 as well as in the first field in the FILTERS extension. Image units, pixel count, and other relevant details are stored in each camera extension header. This initial release closely follows the SUNRISE output format, for which additional information and documentation was presented by Jonsson (2006);

[2] www.illustris-project.org/dev/image_pipeline.com

Table 5.2:: FITS file content overview. Bracket quantities indicated multiple fields. See SUNRISE documentation and papers for additional information.

Extension Name Field Name	Extension Number	Notes
CAMERA[0,1,2,3]-PARAMETERS	2-5	
Header Info:		
cameradist		Camera to galaxy dist [kpc]
linear_fov		Image FOV [kpc]
CAMPOS[X,Y,Z]		Camera Position [kpc]
CAMDIR[X,Y,Z]		Camera Viewing Direction
CAMUP[X,Y,Z]		Camera Up Direction
INTEGRATED_QUANTITIES	7	
Header Info:		
TTYPE[1-12]		Names of included data fields
TUNIT[1-12]		Units for included data fields
L_bol_grid		Bolometric Luminosity [W]
Data Fields:		
lambda		SED λ array [m]
L_lambda		SED L_λ array [W/m]
FILTERS	13	
Header Info:		
TTYPE[1-20]		Names of included data fields
TUNIT[1-20]		Units for included data fields
Data Fields:		
Filter Name List		Broadband filter names
Effective Wavelengths		$\lambda_{\rm eff}$ for each filter [m]
AB_mag_nonscatter[0,1,2,3]		Absolute magnitudes in each band
CAMERA[0,1,2,3]-BROADBAND -NONSCATTER	14-17	
Header Info:		
IMUNIT		Units for included images
Data Fields:		
data		Contains all broadband images

Jonsson et al. (2010).

5.3.1 Galaxy Images

Color galaxy images produced from our image pipeline were first presented in Figure 13 of Vogelsberer et al (2014) which shows 42 blue star forming galaxies and 42 red, passive galaxies as viewed through the SDSS-g, -r, -i bands using the Lupton et al. (2004) asinh scaling. In addition to making qualitatively realistic RGB images, we can consider the visual appearance of this galaxy set as viewed through different filters or from different angles. Figure 5.3 shows an example galaxy as seen through 12 of the broadband filters, as labeled within the figure. Each image has been scaled independently using an "asinh" scaling, with the non-linear transition set to the mean pixel intensity for that band. Bands decrease in wavelength from top left to lower right (effective wavelengths associated with each band can be found in Table 5.1). UV bands are strongly influenced by emission young star particles. The spherical emission from young star particles can be easily identified in the short wavelength bands, where emission is dominated by a small number of particles. Longer-wavelengths bands trace stellar mass more efficiently and present with much less variation from one band to another.

Figure 5.4 shows RGB color images of two disk galaxies made using the SDSS-g, -r, -i bands as viewed from 5 different viewing angles to demonstrate the impact of viewing angle on perceived galactic morphology. The left (right) most image is aligned (anti-aligned) with the angular momentum vector for the stars in the galaxy. The central images uniformly transition between these two polar views. While the top galaxy is relatively axisymmetric, the bottom galaxy has a prominent bar. The observable

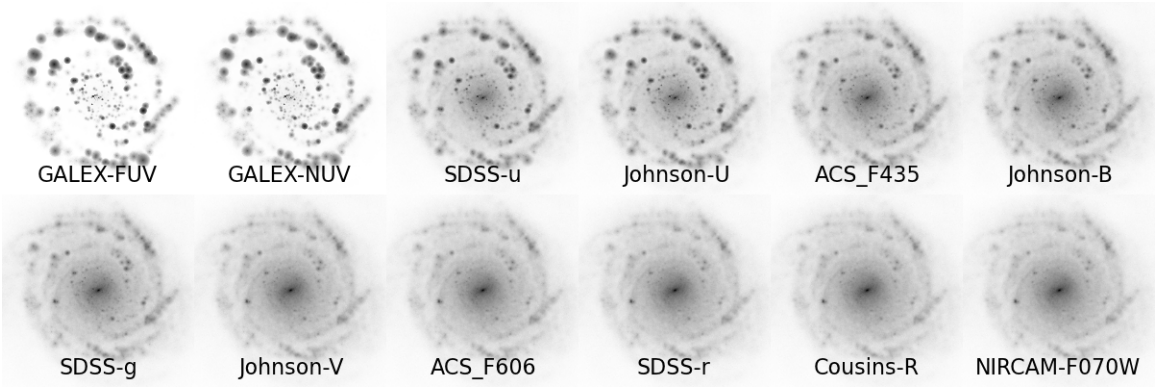

Figure 5.3.—: Montage of a sample simulated disk galaxy in 12 bands as labeled within the figure. Each image has been scaled independently using an "asinh" scaling, with the non-linear transition is set to the mean pixel intensity for that band. Bands decrease in wavelength from top left to lower right. UV bands are strongly impacted by localized emission young star particles. Longer-wavelengths bands trace stellar mass efficiently.

strength of the bar feature is a function of viewing angle, with the bar appearing strongest when viewed face on and being completely unidentifiable when the galaxy is viewed edge on. Although this may have been evident a priori, we would point out that these mock images can be used to derive visually classified bar strength correction factors to determine what fraction of strongly barred systems would have been classified as having weak bars, or no bars altogether, based on viewing angle. Figure 5.5 shows an analogous exploration of two sample elliptical galaxies. While the visual classification of disk systems can change substantially based on viewing angle, a less substantial change is seen in the characteristics of the elliptical systems except for perhaps a slight modification to the system's perceived ellipticity.

5.3.2 Integrated SEDs

Spatially resolved galaxy images are only stored in 36 bands because storing the spatially resolved SED information would greatly increase (by over an order of magnitude) the storage requirements for the mock image catalog and, at the same time, maintaining this extra information for most galaxies would not be immediately useful for most science applications. However, we do store integrated global SEDs for each galaxy under the IntegratedQuantities field. Example SEDs are shown in Figure 5.6 for one star forming blue galaxy (blue line), and one quiescent red galaxy (red line). The two galaxies have noticeably different SED slopes with the star forming galaxy having substantially more UV emission despite being similar in stellar mass with the quiescent system.

As with all broadband quantities, the fiducial SEDs do not take into account dust, which implies that the UV luminosities are likely overestimated due to missing SED

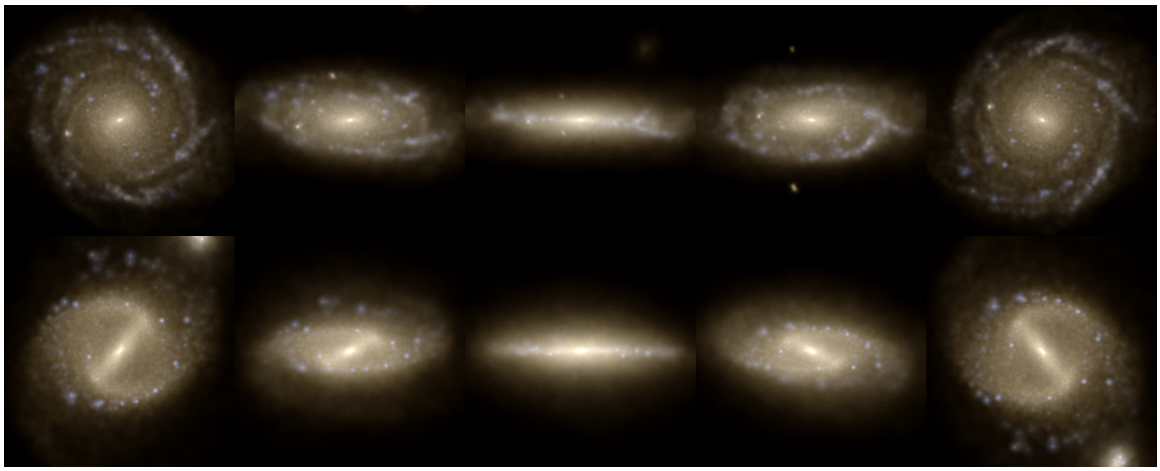

Figure 5.4.—: Montage of a two disk galaxies without a bar (top) and with a bar (bottom) viewed from 5 different viewing angles. The observable strength of the bar depends on viewing angle.

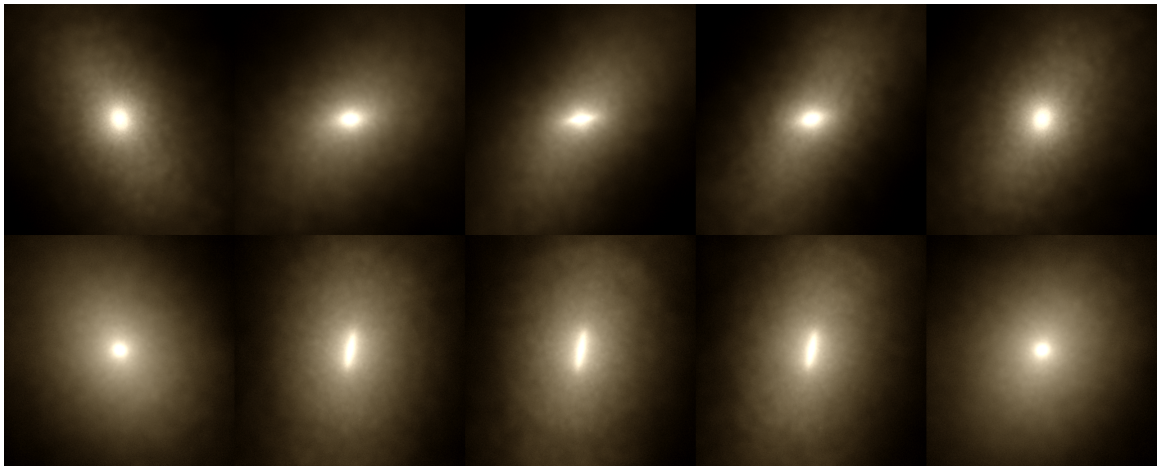

Figure 5.5.—: Montage of two elliptical galaxies. Aside from perhaps a small change in the observed elongation, visual classification of the elliptical systems is nearly invariant to changes in the viewing angle.

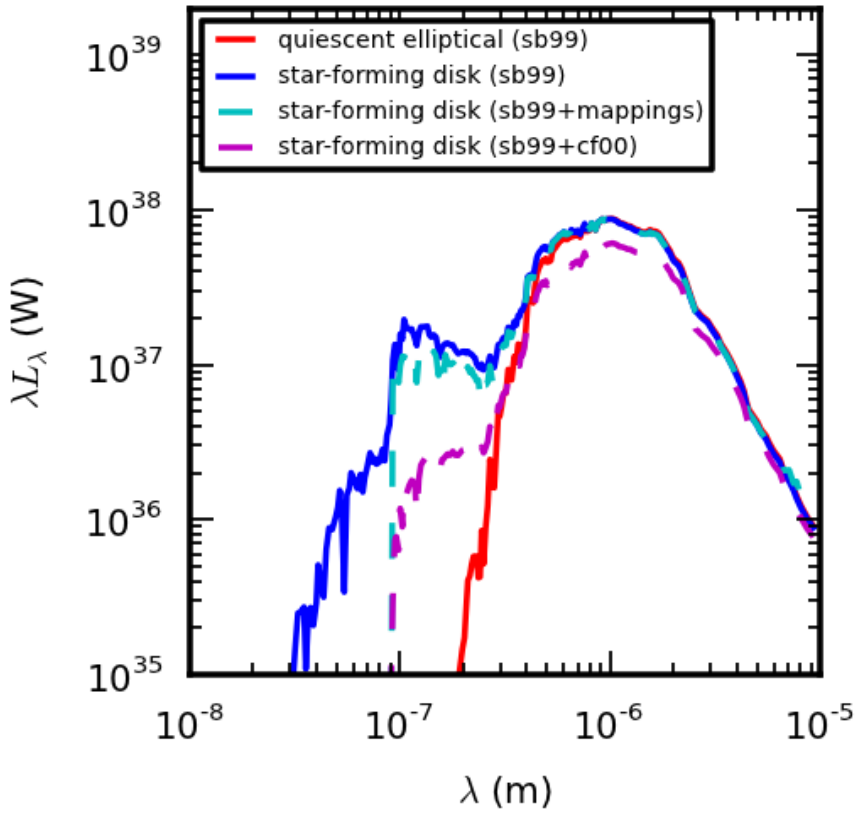

Figure 5.6.—: Integrated SEDs are shown for a quiescent elliptical (red line) and star forming disk (blue line) of similar stellar mass. Due to the younger stellar population, the star forming disk has substantially more UV emission. We also show the star forming disk's SED when using the MAPPINGS HII region model (cyan), and the CF00 empirical dust correction (magenta). Both of these models reduce the UV luminosity substantially.

attenuation, while the FIR luminosities maybe underestimated due to neglected thermal dust emission. This is demonstrated in Figure 5.6, where the cyan and magenta lines show the star forming galaxy's SED when applying the MAPPINGS HII region model and the CF00 empirical dust correction, respectively In both cases, these models substantially reduce the UV luminosity by approximating the obscuration of young stellar spectra. At optical wavelengths, the CF00 model depresses the SED by $\sim 20\%$, while the MAPPINGS model is nearly coincident with the pure SB99 spectra.

5.3.3 Auxiliary Images

Deriving galaxy images from simulation data allows us to construct and present additional "auxiliary" images extracted directly from the simulation output (Jonsson et al. 2010). Figure 5.7 shows a series of these fields including: h-band light using an sinh scaling with the non-linear transition set to the mean pixel value (top), stellar mass surface density (second from top), mass weighted average projected stellar age (third from top), and mass weighted average projected stellar metallicity (bottom). These derived quantities are produced using an identical method for the stellar light, including the adaptive smoothing procedure to determine the effective size of star particles. However, rather than spreading the light contributions from each star particle, the age, metallicity, etc., values are calculated. These derived quantities are intended to be used as supplementary information to the photometric maps, and can be applied to a number of questions including the mass-to-light ratios as a function of morphological type or the evolution of stellar metallicity gradients.

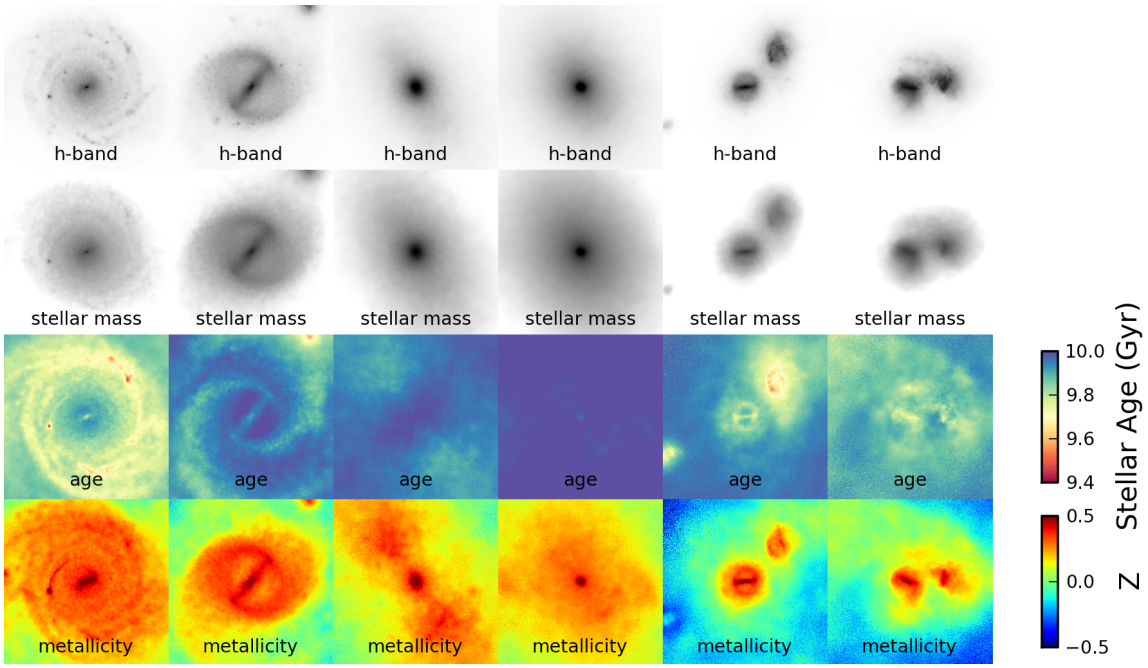

Figure 5.7.—: Projections of simulation derived physical quantities are shown for six example galaxies. Rows show: (top) h-band light using an sinh scaling with the non-linear transition set to the mean pixel value, (second from top) stellar mass surface density, (third from top) mass weighted average projected stellar age, and (bottom) mass weighted average projected stellar metallicity.

5.4 Example Scientific Application: Derived Stellar Masses

The Illustris Simulation Observatory has a number of applications including studying the distribution of galaxies of various morphological types as a function of mass and redshift, the morphology-environment relation, and the role of mergers in driving morphological evolution. Some of these topics will be studied directly in a companion paper (Snyder et al 2014). In this section we provide one example application of the image pipeline catalog: stellar mass estimates based on broadband photometry fitting.

As outlined in detail in the previous sections: galaxy SEDs are calculated by assigning stellar light to each star particle based on its age and metallicity. Each galaxy is then assigned an SED that is the sum of all constituent star particles, which therefore properly reflects its star formation history with self-consistent contributions from starbursts, mergers, and periods of quiescence. We can now use these galaxy SEDs or broadband photometry to derive stellar masses for each galaxy, and compare this against the "true" galaxy mass based on the simulation.

For real observational data, stellar masses are often determined by assuming one of a few commonly adopted functional forms for the star formation history and finding the best fit stellar mass, galaxy age, star formation timescale, and metallicity to the observed SED. One common assumption is an exponentially declining star formation history which is characterized by three free parameters: the galaxy formation time, star formation timescale, and metallicity. The simplest method for constraining these parameters is to perform a chi-squared minimization of the observed SED or broadband

photometry relative to a grid of mock SEDs which sample different values in the free parameter space. This is the general approach that is taken in, e.g., FAST (Kriek et al. 2009).

To perform this exercise we assign light to a galaxy based on a theoretical stellar population synthesis template (e.g., the SB99 model), and then use the same (or a similar) stellar population synthesis model to find a best fit to the SED. One might therefore worry that this is a circular argument, which will not shed any light on the validity of "true" galaxy mass estimates. Indeed, there are important systematic factors (e.g., the slope of the IMF) that may be different in real galaxies compared to the stellar population synthesis models that cannot be probed with our analysis. However, this is still an interesting exercise because the star formation history for our simulated galaxies is "known" and properly reflected in the integrated galaxy SED, while the observational models must assume a functional form for the star formation history. The simple question we can therefore ask is: How well do broadband fitting routines recover the stellar mass from the simulations? Similar topics have been addressed using semi-analytic models in the past (e.g., Mitchell et al. 2013).

5.4.1 Comparison: FAST vs. SUBFIND stellar masses

We employ the code FAST (Kriek et al. 2009) to fit stellar population synthesis models to the artificially generated image pipeline broadband photometry. Our fiducial comparison setup uses FAST assuming exponentially decaying star formation history ($\psi \propto \exp(-t/\tau)$) to determine stellar masses based on the stellar-light-only galaxy photometry from the image pipeline. In this case, the mock galaxy photometry use the

SB99 SPS templates while FAST uses the BC03 templates. The mock galaxy photometry is made without any dust attenuation and we restrict FAST fits to neglect attenuation as well. FAST input files are generated by calculating rest-frame broadband fluxes for the five SDSS band (u, g, r, i, z) converted to units of flux density assuming the galaxies are at redshift $z = 0.01$ using the same cosmology employed in the Illustris simulation. Although FAST has the ability to determine spectroscopic/photometric redshifts, in our initial comparison we supply correct redshifts to FAST to avoid this causing errors. We note that it is slightly inconsistent to use rest-frame broadband fluxes for input into FAST (which assumes redshifted fluxes), but we have checked that error is minimal for such a low redshift. We compare the stellar mass derived from FAST (hereafter FAST mass) against the simulation determined stellar mass found in the SUBFIND galaxy catalog (hereafter SUBFIND mass) for all galaxies with integrated spectra in the image pipeline.

The left panel of Figure 5.8 shows a two dimensional histogram indicating the relationship between the FAST photometrically derived stellar mass and the SUBFIND tabulated stellar mass for all 41,517 galaxies with more than 500 star particles at redshift z=0. The black line indicates a perfect 1:1 relationship (i.e. the FAST masses exactly equal the SUBFIND masses). There is a tight relationship between these two quantities that nearly follows the ideal 1:1 scaling, with a slight offset and scatter. Out of the 41,517 galaxies for which we perform this fitting, 1755 (4%) disagree by more than a factor of two and 10 (0.02%) disagree by more than a factor of five.

The right panel of Figure 5.8 shows the ratio of the FAST masses to the SUBFIND masses as a function of the SUBFIND mass which helps to identify some residual trends in the derived FAST masses. There is a mass dependence in the FAST mass offset value

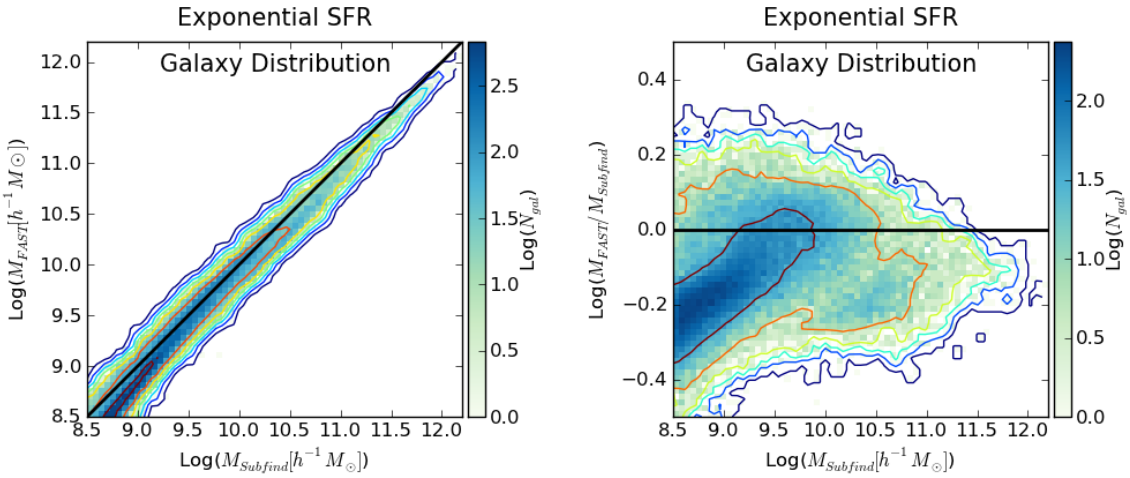

Figure 5.8.—: Two-dimensional histograms depicting the distribution of stellar mass derived from FAST and intrinsic stellar mass from SUBFIND (left) and the ratio of these two values as a function of galaxy mass (right) are shown. In both cases, the color of the pixel denotes the number of galaxies in that pixel as noted in the colorbar. The general agreement between the derived stellar masses and the "true" simulation mass is generally very good, with $> 95\%$ of systems obtaining the correct mass within a factor of two. The ratio of the intrinsic value to derived value does show some bifurcation and mass dependent trends, as discussed in the main text.

which is highlighted by the large distribution of galaxies outlined by the maroon contour line. Additionally, there is a bifurcation in the distribution of derived mass values, with a second locus of derived mass values being present for systems with SUBFIND stellar masses of $M_* \sim 10^{10.5} M_\odot$.

The principle origin of the bifurcated derived galaxy masses can be attributed to the discrete and sparse metallicity values that are sampled in the FAST BC03 stellar population synthesis templates. The standard BC03 templates used in FAST draw from discrete metallicities values of $Z = [0.004,\ 0.008,\ 0.02,\ 0.05]$ without interpolation. The left panel of Figure 5.9 shows the average (mean) template metallicity that FAST applied to galaxies in each pixel. Since FAST is forced to pick one of these sparsely populated metallicity values, the two galaxy locus can be seen to clearly correlate with different FAST metallicity values. The right panel of Figure 5.9 shows the mass weighted average stellar metallicity for these same galaxies. The simulated galaxies tend to have higher metallicities at higher mass values, and a comparison of the left and right panels shows that FAST nearly recovers this mass dependent behavior. However, since the template metallicity spacing is so sparse, the result is a discrete jump in the derived stellar masses depending on which template metallicity is applied. We have further checked that if we restrict FAST to using only a single metallicity ($Z = 0.02$) template, all derived galaxy masses fall along a single continuous relation, albeit with an offset from the desired $M_{\rm FAST} = M_{\rm SUBFIND}$ relation.

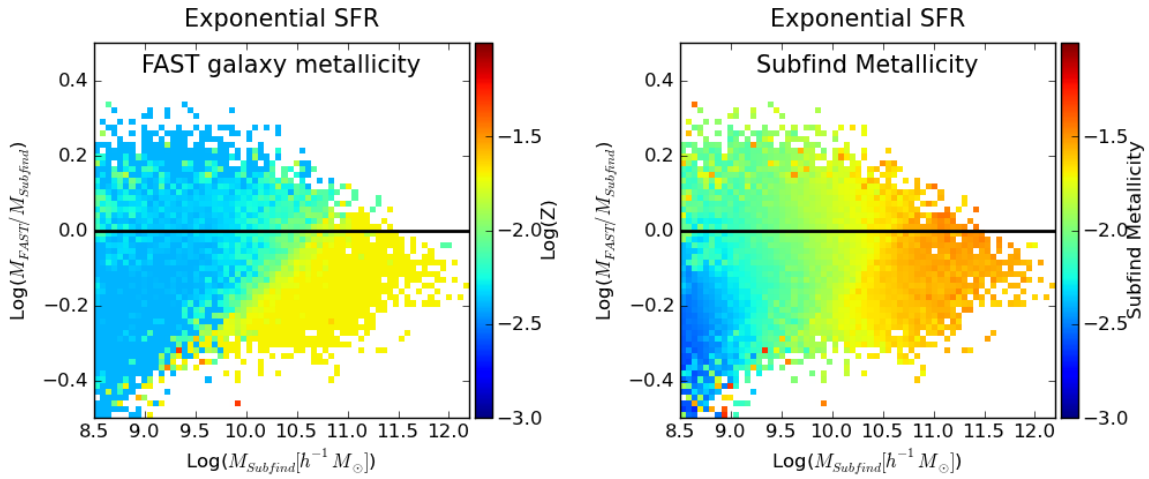

Figure 5.9.—: Two-dimensional histograms depicting the average metallicity template applied by FAST (left) and average galaxy metallicity based on the simulation data (right) are shown. In both cases, the color of the pixel denotes an average (mean) metallicity for all galaxies in that pixel, with the legend indicating the quantitative metallicity values. While the simulation galaxy metallicity smoothly varies with mass, the FAST metallicities show a segregated distribution due to the sparsely spaced metallicity templates.

5.4.2 Alternative Assumed Star Formation Histories

Here we re-compute FAST masses by employing a delayed or truncated star formation history in FAST. Both the delayed and truncated star formation histories are described by two parameters: a galaxy formation time and star formation timescale, τ. The galaxy formation time gives the lookback time when the galaxy started forming stars (i.e. for all times before this, the star formation rate is assumed to be zero). In the case of the delayed star formation history ($\psi \propto t \exp(-t/\tau)$), the star formation timescale modulates the decay timescale for the late time star formation rate decline. In the case of the truncated star formation history, the star formation rate is assumed to be constant after the galaxy formation time for one star formation timescale, after which it drops back to zero.

Figure 5.10 shows the ratio of the FAST mass to the SUBFIND mass as a function of the SUBFIND mass for the delayed star formation history (left) and truncated star formation history (right). The distribution of galaxies in the delayed star formation history space looks very similar to what was found for the previously assumed exponential star formation history. By examining a number of "best fit" star formation histories from the exponential and delayed models shows that the FAST is assuming a very similar (and young) star formation history in many cases, explaining why the distribution of derived galaxy masses is so similar.

The distribution of derived galaxy masses for the truncated star formation rate history is more complicated. Figure 5.11 show the average metallicity (left) and age (right). There are three metallicities assigned to galaxies, causing mass estimate continuity issues as discussed above. The metallicity alone cannot explain the bimodal

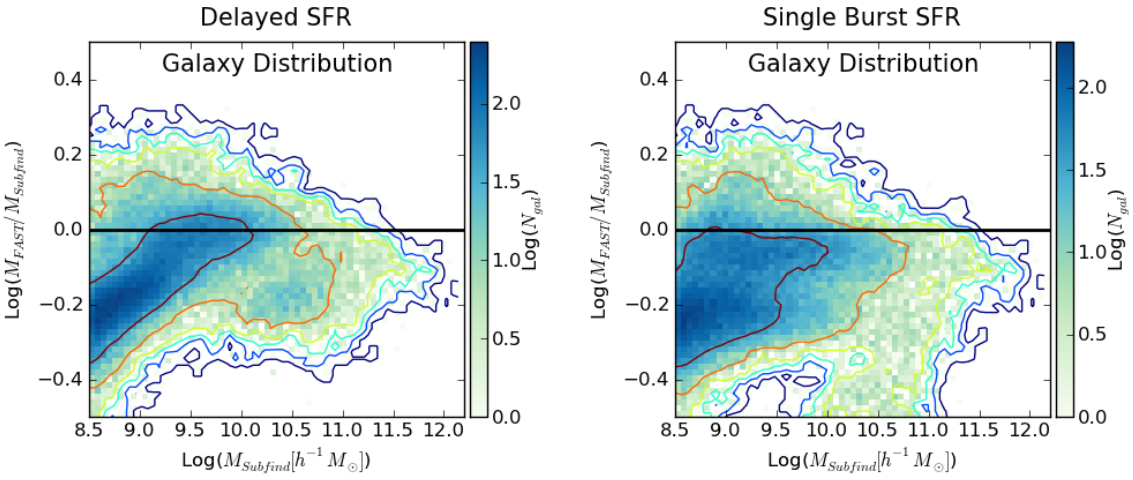

Figure 5.10.—: Two dimensional histograms depicting the distribution of derived FAST masses versus intrinsic masses for a delayed star formation history (left) and truncated or constant star formation history (right) are shown. The distribution of derived galaxy masses for the delayed star formation history shows only subtle differences from the exponential star formation history. The distribution of derived galaxy masses for the truncated star formation history is notably different from the exponential or delayed star formation histories.

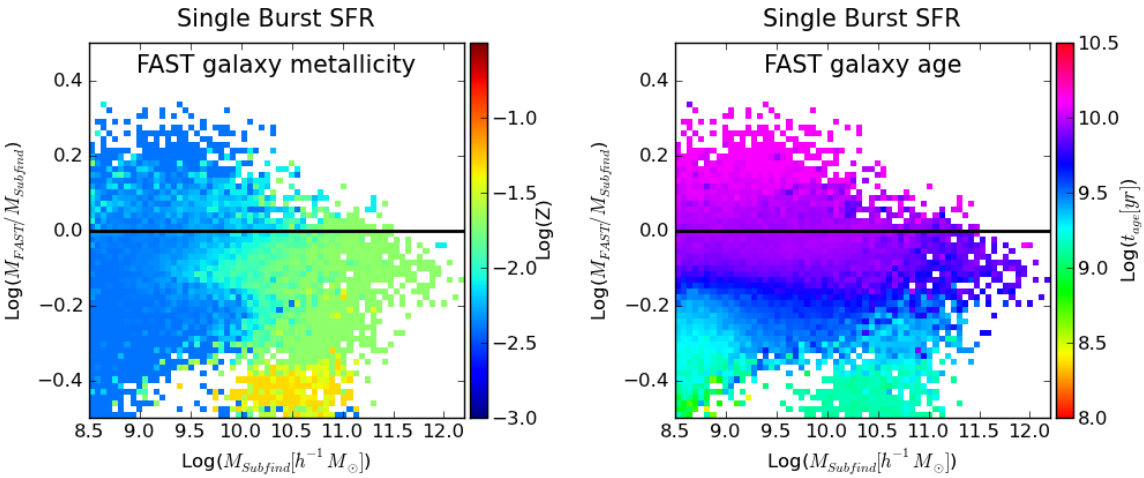

Figure 5.11.—: Two dimensional histograms depicting the distribution of average metallicity (left) and average galaxy age (right) for the truncated star formation history. The sparse metallicity template spacing is only partially responsible for the structure seen in the distribution of galaxies in Figure 5.10. There is a large assumed age gradient, with galaxies that are assumed to be very young being assigned mass that are too small.

galaxy population at $M_{SUBFIND} \approx 10^9 M_\odot$. The right panel of Figure 5.11 shows that there is a large age gradient between the two galaxy populations. Galaxies that are assigned old ages (and long star formation timescales) yield larger derived mass estimates (since they would straightforwardly have larger mass to light rates). It is not immediately clear why FAST is assigning a bimodal distribution of ages to this low mass galaxy population – though this is likely tied to the recent star formation histories of these low mass systems which can substantially impact the best fit SED that FAST selects. When bursty systems are fit with single-component SFHs, their stellar masses can be significantly underestimated (e.g., Michałowski et al. 2012; Michalowski et al 2014). In any case, when FAST assigns a very young age to a galaxy it is likely that the galaxy's mass will be underestimated. A more detailed analysis of this particular subject is readily possible using the publicly available mock image catalog.

5.5 Discussion

The Illustris Simulation Observatory is distinct from any previously released mock image catalog. To our knowledge it forms the largest publicly available mock image catalog constructed directly from hydrodynamical simulations. The Illustris Simulation Observatory can be applied to address issues that are inaccessible via real data. Potential applications include the viewing angle dependence of bar classification or the fraction of merging systems at redshift z=2 that are missed due to poor image quality and resolving power. Large mock data catalogs have been produced by semi-analytic models of galaxy formation based on dark matter only simulations in the past (e.g., Kitzbichler & White 2007; Henriques et al. 2012; Overzier et al. 2013). These models have the advantage

that they can be run on very large volume N-body only simulations – allowing them to produce large mock light-cones and mock survey data. However, the underlying galaxy formation models apply prescriptions to account for the role that galactic dynamics (e.g., galaxy bars, major/minor mergers, disk instabilities, etc.) play in morphological evolution. In contrast, hydrodynamical models attempt to handle these same dynamical processes self-consistently. A central distinction of the Illustris Simulation Observatory from previous semi-analytic model based mock observations is that the self-consistent buildup of galaxy stellar components will be properly reflected in the mock galaxy images. For this reason, it is particularly interesting to used the Illustris Simulation Observatory to study issues where spatially resolved distribution of stars is important.

There are limitations to the current models: the redshift $z = 0$ gravitational softening is $\epsilon = 0.5\ h^{-1}$ kpc in our simulations, making small systems and small-scale features within large systems poorly resolved. As an example, our gravitational softening might prevent galaxy bars from forming via small scale disk instabilities (Kaufmann et al. 2007). Additionally, our current models make use of a pressurized equation of state to handle the multi-phase ISM in a sub-grid fashion (Springel & Hernquist 2003a). Features that are expected to be induced by detailed ISM physics – such as spiral arm structure driven by pressure waves in the ISM – will not be properly captured in our simulations. The mass resolution of our models may also impact results. Given our gas/star particle mass resolution of $M_* = 1.3 \times 10^6 M_\odot$, young stellar populations will be stochastically sampled with a small number of particles. This has been shown in the past to potentially bias non-parametric fitting parameters, such as the Gini coefficient (Lotz et al. 2008; Jonsson et al. 2010).

The scope of this initial data release has been determined to circumvent some

potential problems tied to the large dataset size. Including only the broadband images with four viewing angles and integrated SEDs, the current dataset is $\sim$ 5.6 Tb. This storage requirement will grow quickly as one expands to higher redshifts, or as one includes additional image fields (e.g., kinematic maps, projected stellar ages, etc.). A cursory estimation of the disk requirements to store all galaxies with more than $N_* > 500$ star particles at all redshifts including all auxiliary fields is $\sim$ 5 Pb. We plan to continue investigating efficient distribution solutions, so that we can make larger chunks of this dataset available in the future.

5.6 Conclusions

The main point of this paper is the presentation of a large, publicly available mock galaxy image catalog based on a high-resolution full-volume cosmological hydrodynamical simulation. We described our method for building this image catalog, including how light was assigned to each star particle within each galaxy. We have made publicly available >40,000 galaxy images in 36 broadbands plus integrated SEDs. We have demonstrated that these broadband images can be used to generate high quality galaxy images with a variety of morphological types.

We showed that the SED fitting code FAST is able to derive the "correct" galaxy mass within a factor of 2 for >95% of galaxies in our idealized sample. We also uncovered some residual trends in the stellar mass estimates and argued that sparsely populated stellar population synthesis template metallicity values are responsible for bifurcating the photometrically derived galaxy mass values. Although our idealized comparison cannot address systematic uncertainties such as the dependence of the mass-to-light ratio for a

galaxy population depending on the shape of the IMF, we have used our mock image pipeline to show that overall FAST is able to derive reasonably accurate galaxy stellar masses for complex star formation histories using a relatively simplistic assumed star formation histories.

Our goal when constructing this mock galaxy image database is that it may serve as a useful tool for observers when interpreting extragalactic data. In principle, the FITS file format of our mock galaxy images should make it easy to process these images with existing image analysis tools. This should facilitate galaxy selection from our catalog using selection criteria matched to observational targets. The spatially resolved galaxy properties (e.g., half-light-radii, bulge-to-disk ratios, etc.) can be derived using the same photometric image decomposition or fitting techniques.

A few additional applications of the mock image pipeline are currently under way. We are undertaking automated non-parametric measurements of galaxy morphology for direct comparison with survey data (Snyder et al., in prep). Among other goals, this will allow us to quantitatively assess the extent to which the morphological mix of the simulated galaxies match reality. Visual classification of the galaxy population for galaxies with $> 10^5$ stellar particles is also planned. This gives us a sample of $\sim$1000 galaxies with stellar masses $M_* \gtrsim 5 \times 10^{10} M_\odot$ which we have verified contains both disks and elliptical systems. Visual classification will give us an alternative to the automated non-parametric classifications and let us directly address whether, e.g., the disk-to-elliptical fraction for simulated galaxies is comparable to the measured values from SDSS via efforts such as GalaxyZoo (Lintott et al. 2008). By making even handed comparisons to galaxy surveys, we can begin to observe the origins of galaxy structure according to theory in ever-larger simulations. This includes not only determining the

observability of bars, interaction, and disk evolution as a function of redshift, but also identifying their triggers within the simulations.

Chapter 6

Conclusions and Future Directions

> "I put a piece of paper under my pillow, and when I could not sleep I wrote in the dark."
>
> — Henry David Thoreau

The work presented in this thesis contributed to galaxy formation modeling by (i) broadening the capabilities of the numerical simulations to include new and relevant physical processes, (ii) pioneering the impact of an important new hydro method on the formation of galactic gas disks, and (iii) making concrete model predictions against currently observable galaxy properties. Here I summarize the main conclusions and highlight directions for future projects.

Conclusions

Toward a more complete cosmological context

Mergers and interactions are an important component of galaxy formation and evolution. In Chapter 2 we studied the metallicity evolution of interacting galaxies using idealized merger simulations. The idealized merger setup used for that study remains a useful tool for systematically exploring merger parameter space as well as variations of the fiducial physics model. The end result of our study was a clear picture for the gas-phase metal content of galaxies to evolve during interactions. We concluded that the observed metallicity depression in interacting galaxies can be attributed to kiloparsec scale gas inflow triggered by tidal encounters. Extensions of the galaxy merger suite presented in Torrey et al. (2012) have been used in Rich et al. (2012), Scudder et al. (2012), and Patton et al. (2013) to explain the presence of increased star formation rates and decreased nuclear metallicities in close pair galaxies within the Sloan Digital Sky Survey and local (ultra) luminous infrared galaxies.

A limitation of the idealized merger models is their lack of cosmological context which manifests in artificially constructed initial conditions and an absence of circumgalactic and intergalactic material. This prohibits study of interesting questions such as the size evolution of galaxies or the physical origin of the mass-metallicity relation. Avoiding these limitations can be achieved by moving to cosmological simulations where information about the buildup of all galaxy types is naturally contained within a hierarchal galaxy assembly picture. We could have generalized and extended the work presented in Chapter 2 of this thesis by examining the metallicity evolution of

galaxies across cosmic time in cosmological simulations. However, this was not possible because cosmological simulations have historically struggled to produce realistic galaxy populations. One of the most glaring issues is the lack of morphological diversity in simulated galaxy populations. Few simulations have been able to simultaneously form late-type and early-type galaxies. Since the buildup of disk galaxies – including the formation of gas disks, metallicity gradients, etc. – could not be reliably studied, it was not possible to immediately extend Chapter 2 of this thesis into a fully cosmological context. Instead we turned our attention to the more fundamental problem of forming realistic galaxy populations – including the simultaneous formation of late-type and early-type systems – in cosmological simulations.

The two most basic physical components of galaxy formation models are gravity and hydrodynamics. Accurate gravity solvers that give consistent results are implemented in most cosmological simulation codes (but see O'Shea et al. 2005, for a more detailed critique). The same level of accuracy or agreement has not been achieved for hydro solvers (e.g., Frenk et al. 1999). Despite being able to unambiguously write down the relevant inviscid equations of motion, the results obtained in hydrodynamic simulations depend on the adopted hydro discretization scheme. Differences between methods become most pronounced when resolution is limited, as is almost always the case in cosmological simulations. In Chapter 3 of this thesis, we compared two different hydro solvers to understand how the adopted discretization scheme can impact the properties of gas disks formed in cosmological simulations. The timing of this study was opportunistic since the first simulations using AREPO and its novel moving-mesh hydro solver had only recently been completed (Vogelsberger et al. 2012). We found a very clear distinction: gas disks formed in AREPO were systematically larger and more rotationally supported

than the gas disks formed in GADGET. We attributed the differences to known numerical issues found in the standard density based formulation of SPH. We argued that caution should be used when interpreting the results of galaxy formation simulations that have employed this type of hydro solver.

Some disagreement lingers in the galaxy formation community regarding the relative importance of hydrodynamics to galaxy formation. It has been argued that feedback is the dominant mechanism that drives galaxy formation (e.g., Scannapieco et al. 2012), and therefore it is more important to implement a realistic feedback scheme than include accurate hydrodynamics. The simulations employed in Chapter 3 neglected strong feedback in order to facilitate a clean numerical comparison. Despite the AREPO simulation's improved handling of the hydrodynamics, the resulting simulated galaxy populations formed stars far too efficiently to match even the most basic observational constraints such as the galaxy stellar mass function or cosmic star formation rate density. We agree that feedback is an important component of galaxy formation models but believe implementing an accurate hydrodynamical scheme should take precedence. While the accuracy of hydro solver implementations can be rigorously benchmarked against test problems with known analytic solutions (e.g., Agertz et al. 2007; Sijacki et al. 2012), star formation and AGN feedback methods are highly uncertain (e.g., Scannapieco et al. 2012). It has been unambiguously shown that deficiencies exist in the hydro solvers that are included in some of the most widely used cosmological hydrodynamical simulation codes (Agertz et al. 2007; Sijacki et al. 2012). We have specifically shown in Chapter 3 of this thesis that these deficiencies severely impact galaxy formation simulations. These deficiencies can be objectively corrected by employing a more accurate hydro solver. A similar level of objective validation does not exist for feedback models, given our current

understanding of how they operate.

The uncertainty in feedback models is exacerbated because feedback is sourced based on the already uncertain gas distribution in galaxies. The two most commonly implemented feedback sources in simulations are star formation driven winds and AGN feedback. The distribution of star formation as well as the fueling rates of black holes are determined directly from the distribution of gas. Errors in the gas distribution seeded by an inaccurate treatment of the hydrodynamics will have consequences for the strength of feedback injection. To provide a concrete example: artificial clumping of CGM gas – as was shown to occur in Chapter 3 of this thesis for the standard density formulation of SPH – leads to extra cold gas being delivered to the central galaxy and central black hole driving up the amount of feedback contributed from both sources. It follows that one should aim to first ensure the hydrodynamic evolution of gas is being carried out in the most accurate way possible before implementing methods for injecting feedback based on the gas distribution. Authors have proposed modifications to the standard density based SPH formulation to help circumvent some of the most crucial pitfalls presented in Chapter 3 (e.g., Saitoh & Makino 2013; Hopkins 2013; Read & Hayfield 2012; Hobbs et al. 2012). Implementing these code modifications is a minimal step that should be taken to improve the standard density based SPH hydro solver accuracy before focusing on the more ambiguous feedback model development.

Toward a more complete galaxy formation model

We have argued that implementing an accurate hydro solver should take precedence over studying uncertain feedback processes. However, this is not to be interpreted as saying

that feedback is unimportant. Strong feedback is a requisite simulation component in order to produce model galaxy populations that resemble observations. After validating the performance of the AREPO hydro solver in Chapter 3, we incorporated a comprehensive feedback module into AREPO as described in Vogelsberger et al. (2013). In Chapter 4 of this thesis, we considered the the evolution of galaxy properties under varied assumptions for this feedback model in a series of cosmological simulations. The main points of this chapter are (i) to show that AREPO is now equipped with a feedback module that is capable of reproducing a wide range of galaxy relations at several redshifts, (ii) to demonstrate the relative importance of star formation driven winds and AGN feedback in our model as a function of galaxy mass and redshift, and (iii) to identify areas of residual tension between our current best galaxy formation model and observations.

Since they were first employed nearly two decades ago, hydrodynamical simulations have generally failed to produce robust matches to observed galaxy properties due to incomplete feedback implementations. For example, several widely cited galaxy formation simulations that were published in past few years adopt feedback implementations that fail to capture either the low mass end slope of the galaxy stellar mass function or exponential high mass end cutoff (e.g., Crain et al. 2009; Davé et al. 2011b; Khandai et al. 2014). Meanwhile, decade-old semi-analytic models (e.g., Croton et al. 2006; Somerville et al. 2008; Guo et al. 2011) have produced robust matches to the redshift dependent galaxy stellar mass function, and many other observed galaxy relations. The historical superiority of semi-analytic models when matching observed galaxy relations has resulted in their widespread use over hydro models. We are now reaching a point where hydro simulations are producing galaxy populations that match observed galaxy

properties equally well with semi-analytic models. This equality has been facilitated by the implementation of more "complete" feedback models in hydro simulations (Puchwein & Springel 2013; Vogelsberger et al. 2013; Torrey et al. 2014). The simulations and feedback models presented in Vogelsberger et al. (2013) and analyzed in Chapter 4 of this thesis among the first full-volume galaxy formation cosmological simulations that can reliably produce the main observationally established galaxy relations.

In the results of Chapter 4, we find that using an energetically plausible stellar wind model the normalization and slope of the low mass end of the galaxy stellar mass function can be appropriately regulated within a standard ΛCDM simulation. We found that an energy conserving star formation driven wind scheme with an energy input per supernova of $\sim 10^{51}$ ergs matches the slope of the abundance matching derived stellar mass halo mass relation. The requisite wind mass loading factors are very high: about 5 for a Milky Way type galaxy at redshift $z = 0$. Within this model, wind speeds nearly equal to (but below) the halo escape velocity provide the best galaxy stellar mass function match. Our models support the existence of a galactic fountain in almost all galaxies, with star formation driven winds expelling a substantial amount of gas and heavy elements into the CGM and IGM around galaxies as they form stars. Additional constrains on the validity of our adopted star formation driven wind model can be obtained by comparing the heavy element distribution in the haloes of simulated galaxies against observations (Suresh et al., in prep). Star formation driven winds are insufficient to quench star formation in the most massive systems. A more energetic form of feedback is required to replicate the exponential cutoff at the massive end in the galaxy stellar mass function. Our simulations recover an appropriate "knee" in the galaxy stellar mass function when we include AGN feedback – radio mode AGN feedback in particular. Combining our star

formation driven wind model with our AGN feedback model results in a galaxy stellar mass function, optical band luminosity functions, and stellar mass to halo mass relations that all broadly agree with observational constrains out to redshift $z = 3$.

The strongest tension between our galaxy formation model predictions and observations is the evolving mass-metallicity relation. While strong feedback is critically important to regulating the stellar mass growth of galaxies in our model, these same winds drive a large fraction of a galaxy's heavy element content out of the ISM. This results in a steep simulated mass-metallicity relation that is set by the mass loading of star formation driven winds. One way to reduce this tension is to lower the strength of winds within our simulations, which would in turn reduce the amount of metal content driven out of galaxies. Our feedback model is energetically plausible (i.e. we only assume 10^{51} erg per supernova), but the resulting mass loading factors are very high for low mass systems. We have tested that reducing the strength of star formation driven winds can improve the agreement with the observed mass-metallicity relation. However, reducing the feedback strength causes tension in the galaxy stellar mass function, making a simple reduction in the feedback strength alone an unfavorable solution. Another way to reduce the tension would be evoke feedback mechanisms or physical processes that could slow the gas accretion rates for low mass galaxies. For example, if star formation driven winds in low mass galaxies are able to efficiently shock heat the surrounding IGM to temperatures comparable to or above the halo virial temperature, then accretion can be temporarily halted. The net result is a substantial reduction in the star formation efficiency for low mass systems per unit metal mass expelled. This could potentially preserve the low star formation efficiency that is required by low mass systems, while allowing them to retain an appropriate metal mass fraction in their own ISM. While we

have clear ideas about how to improve our current feedback implementations, relieving the mass-metallicity relation tension in our models is going to require a more careful examination of star formation driven winds and their ability to re-distribute both mass and heavy elements in and around galaxies.

A new way of interpreting extragalactic survey data

Modulo the tension in the mass-metallicity relation, the galaxy formation models explored in Chapter 4 have achieved a level of agreement with observations that goes substantially beyond previous results. Broad agreement has now been achieved through tuning of the feedback model to match the observed galaxy stellar mass function evolution. The Tully-Fisher relation and star formation main sequence evolve consistently with the observed relations. Morphological diversity, including the formation of disk and ellipticals side-by-side in the same simulations, have now been achieved. A lingering limitation of these hydro models is their ability to simulate large galaxy populations at high mass and spatial resolution owing to large numerical cost. Practically speaking, small simulation volumes limit the number of simulated galaxies and make the simulation results (e.g., the cosmic star formation rate density) susceptible to cosmic variance. More importantly, the traditional periodic box simulation approach imposes an effective assumption that the Universe is homogenous on scales greater than the linear simulation box size. This can result in an underrepresentation of massive galaxy groups and clusters, missing non-linear mode evolution for modes comparable to or larger than the simulation box size, and inaccurate realization of large scale gravitational forces/torques that are responsible for imposing galaxy and halo spin. While the $L = 20 - 25h^{-1}$ Mpc

volumes used in Chapters 3 and 4 of this thesis allowed us to probe numerics and tune our feedback model efficiently, the validity of the redshift $z = 0$ results are limited by the small box size. Moving to bigger simulations boxes can remove many of these concerns.

The computational expense of bigger (e.g., $L = 75h^{-1}$ Mpc) simulation volumes including full hydrodynamics without sacrificing mass and spatial resolution is a computational challenge. The Illustris project made use of the testing and model validation in Chapter 4 to select a set of feedback parameters to be used in a single $L = 75h^{-1}$ Mpc simulation box. The Illustris project has similar box size and mass resolution to the dark matter only Millennium-II simulation (Boylan-Kolchin et al. 2009) making it the highest resolution full hydro simulation of its size to date. In contrast to dark matter only simulations – with their accompanying semi-analytic models – the Illustris simulation contains information and predictive power on the physical state of gas and stars in and around galaxies. For example, while semi-analytic models prescribe the morphological evolution of galaxies through merger and bar induced bulge formation, hydrodynamical models self-consistently follow stellar dynamics. This detailed model information can be useful to on-going and planned galaxy formation focused observational campaigns if have a way to efficiently and fairly compare the simulated and observed galaxy populations.

The last science chapter of this thesis focused on the problem of facilitating even handed comparisons between simulations and observations. We produced a catalog of 40,000 mock galaxy images and SEDs based on the Illustris simulation. A distribution pipeline – including a web based SQL queryable interface – has been developed. We have converted all data products into "observer-friendly" files (FITS format) such that analysis tools developed for large survey data sets can be quickly run on the mock data.

While previous mock image catalogs have been produced based on idealized galaxy merger simulations or semi-analytic models, the Illustris Simulation Observatory is the first attempt to make such a large mock image database directly from cosmological hydrodynamical simulations. The initial Illustris Simulation Observatory paper was structured as a data release paper, with limited direct science performed. However the potential applications for this image collection are fairly extensive, and we discuss some of the most interesting near term uses here.

A long standing problem in observational galaxy formation is linking galaxy populations together across different epochs. Conclusions about the size or mass evolution of galaxies is often determined under the assumption that galaxies of a common cosmic number density are the progenitors or decedents of one another. This linking method implicitly assumes that galaxies remain well ordered in their stellar mass content and that the total number of galaxies is not substantially changing due to mergers. Although it seems unlikely that either of these assumptions are widely inaccurate, the full validity of these assumptions are not rigorously known. The Illustris Simulation Observatory grants users direct access to the time domain of galaxy evolution. The size and mass evolution of galaxies from the high redshift Universe to the present day can be directly probed and compared against observations. For example: we can identify high redshift compact ellipticals via their effective radii as measured in Illustris Simulation Observatory and immediately identify their formation mechanisms and follow their subsequent evolution (Wellons et al., in prep). The Illustris Simulation Observatory provides us with a new tool to place extragalactic observations into a more complete cosmological context. Not only will this allow us to question the assumptions regarding the constant number density evolution, but this also lets us directly probe the physical

processes that are responsible for galaxy size and mass evolution.

Mergers are one of the processes that are important to the size and mass evolution of galaxies. The evolving importance of galaxy mergers is probed observationally through measurements of close pair and interacting galaxies from which one can infer the redshift dependent galaxy merger rate. Accurate determinations of the high redshift galaxy merger rate are hindered by difficulty in identifying high redshift interacting systems due to diminishing image quality. This effect has been measured by visually classifying artificially redshifted galaxy images from the local Universe. The fraction of galaxies tagged as mergers can be influenced by up to 30% for redshift $z = 2$ systems due to image degradation alone. Although one can state clearly that not all high redshift galaxy mergers can be identified even with deep HST imaging, a best method for correcting the observed high redshift galaxy merger rate into a real/physical galaxy merger rate is still not immediately clear. The Illustris Simulation Observatory can contribute by allowing us to image redshift $z = 0$ and $z = 2$ systems as if they were both at redshift $z = 0$ and both at redshift $z = 2$. While observations are inherently limited to artificially degrading the quality of their galaxy images in order to probe redshift dependent biases, we can employ the Illustris Simulation Observatory images to artificially degrade *and* enhance system images. We can measured the merger rate for the mock galaxy images as if they were observed any redshift – *independent of their actual redshift.* In addition to correcting the high redshift merger rate calculation, using the Illustris Simulation Observatory in this way can shed light on redshift dependent observational biases for measured galaxy sizes, masses, and morphological and kinematic classifications.

Future Directions

Three natural extensions to this thesis are discussed here: Extensions of the image pipeline, improvements to the simulation physics, and next generation simulations.

Extensions of image pipeline

We have only begun to scratch the surface of the observational comparisons that can be made with the Illustris Simulations Observatory presented in the Chapter 5 of this thesis. We have publicly released only the redshift $z = 0$ un-obscured stellar light galaxy images. This limited publicly released dataset can be used for a number of science applications including investigating the validity of common SED fitting routines as was conducted in Chapter 5.

A simple and exciting extension of the image pipeline is publicly releasing images for the high redshift progenitors of the $z = 0$ galaxy population. We can identify common trends in the morphological evolution of different galaxy types using the merger-tree data form the Illustris simulation. A sample set of galaxy evolution images can be found in Figures 6.1 and 6.2 where we show the evolution of 5 present day disks and ellipticals, respectively. From this simple example one can infer the nearly ubiquitous importance of mergers (both major and minor) in building up many of the massive redshift $z = 0$ elliptical systems. These galaxy images also contain rich information on, e.g., the formation and lifetime of stellar shells or galaxy color evolution. Modifying the existing web-based SQL framework to trace galaxy evolution using the merger tree relational database of Lemson & Springel (2006) tied to the image pipeline data is a

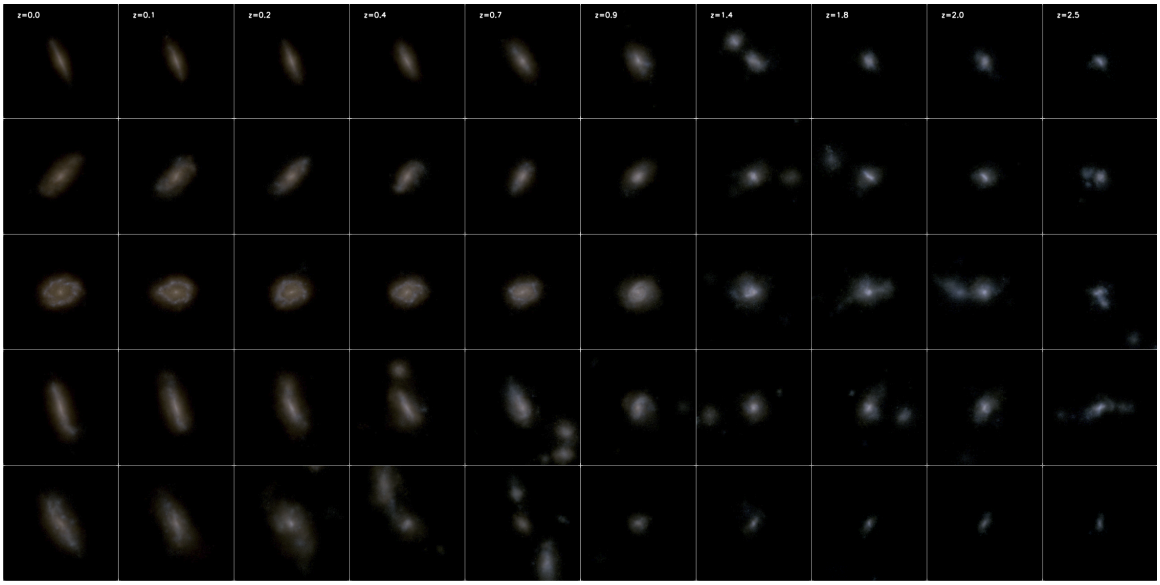

Figure 6.1.—: Morphological evolution of 5 galaxies identified as disk galaxies at redshift $z = 0$.

straightforward task. Doing so in practice will require a large amount of web-accessible storage, which will likely require some form of partnership with a data distribution center.

A separate extension the current image pipeline is through modifications to the light contributions in the current images. Specific example are (i) including AGN light, (ii) emission from shock excited gas, and (iii) obscuration and re-emission from dust. The first and second points can be implemented directly using the existing SUNRISE formalism. Specifically, new "light sources" can be defined to account for emission from AGN and shocked gas. Mean AGN input spectra can be adopted and the MAPPINGS shock models can be used to assign emission from shocked gas. Including dust obscuration and emission is perhaps the most interesting, but also most technically difficult. For the purposes of dust-obscuration, the simulated galaxies in Illustris can be considered semi-resolved: The gross distribution of gas and stars on $\sim$kpc scales is resolved. However, the detailed distribution of gas relative to young star clusters – which is critical to determining obscuration of young star forming regions – is not properly captured. As such, a brute force approach of performing pan-chromatic radiative transfer – as is implemented in SUNRISE – to determine the dust thermal state cannot be directly applied. However, we have substantially more information about the gas/dust distribution compared to semi-analytic models where it is common to assume a uniform dust screen based on the total neutral hydrogen gas column density in the galaxy. A detailed exploration of how to best perform dust obscuration on our semi-resolved galaxy population is underway and will be presented in an upcoming paper (Xu et al., in prep).

A final augmentation of the current image pipeline is the inclusion of simulation based projected images. Specific examples are (i) gaseous/stellar mass maps, (ii)

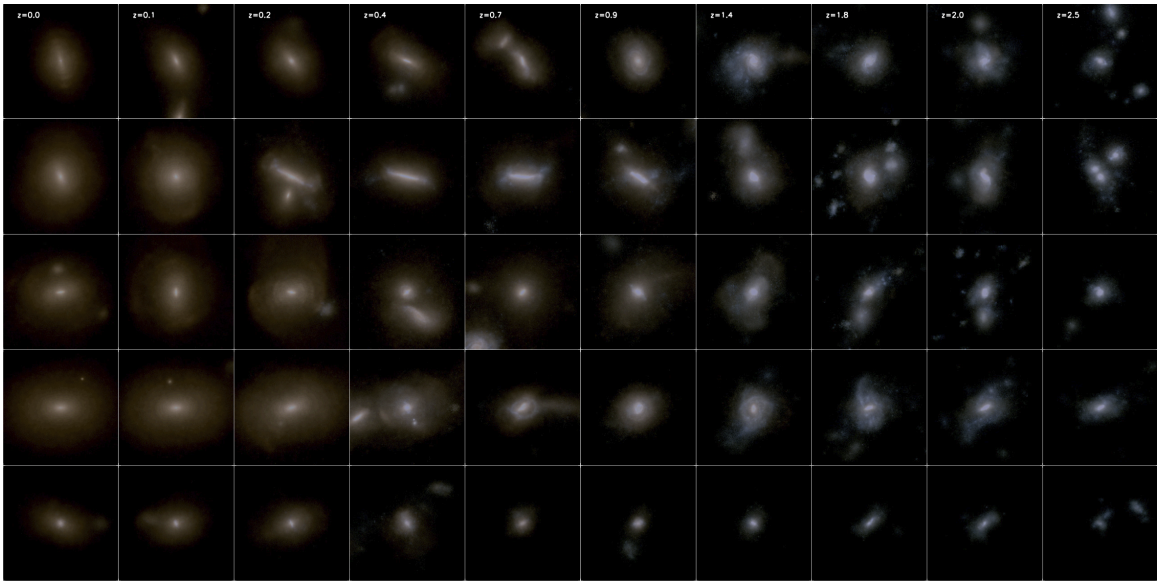

Figure 6.2.—: Morphological evolution of 5 galaxies identified as elliptical galaxies as redshift $z = 0$.

gaseous/stellar kinematic maps, (iii) gaseous/stellar metallicity maps, and (iv) stellar age maps. All of these quantities are indirectly accessible to observers, and are used in assembling a picture of galaxy formation. Some galaxy classifications (e.g., slow/fast rotator, disk/dispersion dominated, etc.) are based almost entirely on kinematic information. Auxiliary image pipeline maps could map observed galactic kinematic signatures to galaxy assembly histories. Auxiliary maps could also provide insight on present day counterparts and kinematic evolution of kinematically classified high redshift galaxies. Auxiliary images can be produced within the existing SUNRISE image pipeline framework, with a moderate amount of code modification.

Improvements to physics

While we consider the physical model implemented in the Illustris simulation to be state-of-the-art, several elements are worth improving for future simulations. The currently employed feedback model can be refined. In current galaxy formation models (including our best model as employed in Illustris), star formation driven winds are invoked to regulate the growth of low mass galaxies by tuning their strength until a reasonable match to the galaxy stellar mass function (GSMF) is achieved (e.g., Okamoto et al. 2010; Davé et al. 2011b; Puchwein & Springel 2013; Vogelsberger et al. 2013). While this crude approach is capable of producing models with positive matches to the GSMF, it has trouble reproducing the evolution of the mass-metallicity relation as well as the phase structure and chemical composition of the circumgalactic medium (CGM) (Torrey et al. 2014). There is an increasingly clear tension between the need for strong winds to reproduce the GSMF and the fact that these same winds efficiently expel a substantial

fraction of a galaxy's gas phase metal content (Zahid et al. 2013). Reconciling this tension requires revisiting our theoretical picture for how galactic outflows operate.

Recently it has been shown that winds can be launched in very high resolution simulations by directly including the feedback mechanisms that are associated with young stellar populations. In particular, momentum injection via radiation pressure as well as photoionization of gas in HII regions have been shown to be important for preventing the catastrophic collapse of cold, star-forming gas clouds (Hopkins et al. 2011; Agertz et al. 2013) while thermal feedback from supernovae and long range radiation pressure can help winds escape the galaxy (Hopkins et al. 2012a, 2013a,b). Whereas current large volume simulations employ ad hoc prescriptions to capture the mass loading of galactic winds, explicit ISM model simulations recover wind properties in a much more predictive sense. Unfortunately, the high resolution requirements restrict our ability to simulate more than a handful of objects with a detailed ISM model – which limits our ability to make broad observational predictions based on the model (e.g., for different masses, environments, or formation histories). However, the high resolution explicit ISM models can be used as a basis on which we refine the galaxy formation physics prescriptions that are employed in coarser resolution simulations of large galaxy populations. We need to develop a method to port the lessons learned from explicit ISM level simulations into larger-scale, lower-resolution simulations. By running zoom-in style simulations of a single galaxy at several resolutions, we can adopt a hybrid approach to derive wind prescriptions that allow low resolution simulations to recover broadly similar results compared against their high resolution (including the detailed-ISM model) counterparts. Similar statements can be made regarding the fueling of black holes and the resulting AGN feedback. By embedding reasonable feedback prescriptions for black holes in a

detailed multi-phase ISM model, we can investigate the origin and structure of black hole driven outflows including the observed high-velocity, multi-phase outflows seen around quasars (e.g., Laor et al. 1997; Crenshaw & Kraemer 2000; Tremonti et al. 2007).

We see the use of nested simulations as a viable way to build a more robust star formation driven wind and AGN driven feedback model that can improve the quality of the next generation of cosmological simulations. Whereas our current feedback model uses a direct mapping from galaxy halo mass to wind velocity with a constant wind temperature, we can incorporate probability distribution functions that describe appropriate velocities and temperatures based on the results of increasingly detailed simulations. Model validation can be performed using the same type of comparisons presented in Chapters 4 and 5 of this thesis.

Next Generation Simulations: Illustris-II

The historically motivated Moore's Law predicts a continued doubling every 24 months of the available computational power for running simulations. Combining increasing computational power with steady algorithmic improvements has lead to a doubling in the number of resolution elements used in hydrodynamic galaxy formation simulations every ~ 18 months (Vogelsberer et al 2014). Currently, the Illustris Simulation holds the record for the most resolution elements of any published galaxy formation simulation run down to redshift $z = 0$ – a record that will likely not last for very long. Other simulations using a similar box size ($L \sim 75h^{-1}$ Mpc) with a similar number of resolution elements have also been recently completed including the MassiveBlack-II simulation (Khandai et al. 2014) and the EAGLE simulation (Schaye et al., in prep). All of these simulations adopt

the approach of increasing the simulation box size while maintaining fairly aggressive target baryon mass resolution.

A natural path forward is to increase the particle count by a factor of eight within the next few years. This can be done in simulations of the same box size to increase the spatial resolution by a factor of two, or in boxes that are double the size with a constant mass/spatial resolution to improve the sampling of galaxy environment and group/cluster resolution. Coupled with modest improvements in the feedback physics, either of these approaches could provide valuable new insight into galaxy formation. Specifically, larger box sizes would improve our probing of galaxy environments and our understanding of group/cluster formation while better resolved simulations could help us resolve lower mass galaxies and better resolve the internal structure of massive systems. However, the Illustris simulation consumed 16 million CPU hours to evolve from a starting redshift of $z = 127$ to $z = 0$ spread over 8192 MPI-tasks with a peak memory usage of 25 terabytes and produced 200 terabytes of data split over 135 simulation output snapshots. Blindly increasing the particle count by a factor of eight will boost the expected compute cost, memory consumption, and final data storage size to rather uncomfortably high values.

Nevertheless, compute allocations for such massive simulations are currently available through nationally operated compute facilities. The limiting factor is not the available compute power, but rather our own preparedness for running such simulations. Ensuring the success of these very expensive next generation simulations requires that we first gain a more complete understanding of the successes and failures of the current Illustris Simulation. The Illustris Simulation Observatory is specifically designed to help in this area by facilitating direct comparisons to galaxy survey data in a format that can be re-applied on next generation simulations. Second, we must

continue to refine our physical models within the simulations. Physical model refinement can be targeted to either correct some of the most glaring issues identified through our analysis of the existing Illustris simulation or to implement lessons learned from more-detailed ISM modeling. Improving and refining our physical modeling of feedback is a rich research area, and one where I anticipate spending much of my time over the coming several years. Third, we must maintain focus on improving the scaling and performance of our simulation codes. Extending simulation codes to run with $\sim$ 100,000 MPI tasks is technically challenging and will require substantial time to be spent on the less-glamourous backend code development. Moreover, some of the largest modern super-computing facilities are increasing their floating-point operations per second (FLOPS) by adding compute accelerator cards such as graphical processing units (GPUs). Most of the currently employed galaxy formation simulation codes – including AREPO – do not yet take advantage of accelerator cards.

The Illustris-II simulation will likely not be a single simulation with eight times more particles but rather a suite of simulations. It is important that we push to better spatial and mass resolution without sacrificing large galaxy population statistics or proper large scale structure environment. The best suited simulations may be smaller high resolution boxes (perhaps as small as $L = 25h^{-1}$ Mpc with $M_{\rm bar} \sim 10^5 h^{-1} M_\odot$) embedded in low resolution large volumes ($L \sim 75h^{-1}$ Mpc). In principle, several sub-volumes can be simulated to sample different environments. This is a similar approach as adopted in the GIMIC simulation suite, where sub-volumes were re-simulated from the Millennium simulations (Crain et al. 2009). In the case of Illustris-II, one could sub-sample and re-simulate regions from the original Illustris Simulation, or another large-volume dark matter only simulation if a larger parent volume is required. Pushing toward higher

mass and spatial resolution is key to establishing a more robust picture for how feedback processes couple to the gas in and around galaxies of different masses and in different environments. Successful extensions of the Illustris Simulation and Illustris Simulation Observatory resulting in increasingly accurate and detailed mock observational catalogs have the potential to greatly expand our understanding of the processes that drive galaxy formation, while ushering in a paradigm shift in the way that we model and physically interpret extragalactic observations.

References

Abadi, M. G., Navarro, J. F., Steinmetz, M., & Eke, V. R. 2003, ApJ, 597, 21

Abazajian, K. N., et al. 2009, ApJS, 182, 543

Abel, T. 2011, MNRAS, 413, 271

Agertz, O., Kravtsov, A. V., Leitner, S. N., & Gnedin, N. Y. 2013, ApJ, 770, 25

Agertz, O., Teyssier, R., & Moore, B. 2011, MNRAS, 410, 1391

Agertz, O., et al. 2007, MNRAS, 380, 963

Aguirre, A., Hernquist, L., Schaye, J., Katz, N., Weinberg, D. H., & Gardner, J. 2001, ApJ, 561, 521

Baldry, I. K., Glazebrook, K., & Driver, S. P. 2008, MNRAS, 388, 945

Balogh, M. L., Pearce, F. R., Bower, R. G., & Kay, S. T. 2001, MNRAS, 326, 1228

Banerji, M., et al. 2013, MNRAS, 431, 2209

Barnes, J. E., & Hernquist, L. 1996, ApJ, 471, 115

Barnes, J. E., & Hernquist, L. E. 1991, ApJ, 370, L65

Bauer, A., & Springel, V. 2012, MNRAS, 423, 2558

Behroozi, P. S., Wechsler, R. H., & Conroy, C. 2013, ApJ, 770, 57

Bell, E. F., & de Jong, R. S. 2001, ApJ, 550, 212

Belley, J., & Roy, J. 1992, ApJS, 78, 61

Binette, L., Dopita, M. A., & Tuohy, I. R. 1985, ApJ, 297, 476

Birnboim, Y., Dekel, A., & Neistein, E. 2007, MNRAS, 380, 339

Blumenthal, G. R., Faber, S. M., Primack, J. R., & Rees, M. J. 1984, Nature, 311, 517

Booth, C. M., & Schaye, J. 2009, MNRAS, 398, 53

Bouwens, R. J., Illingworth, G. D., Franx, M., & Ford, H. 2008, ApJ, 686, 230

Bouwens, R. J., et al. 2009, ApJ, 690, 1764

—. 2011, ApJ, 737, 90

Bower, R. G., Benson, A. J., & Crain, R. A. 2012, MNRAS, 422, 2816

Boylan-Kolchin, M., Springel, V., White, S. D. M., Jenkins, A., & Lemson, G. 2009, MNRAS, 398, 1150

Brooks, A. M., Governato, F., Booth, C. M., Willman, B., Gardner, J. P., Wadsley, J., Stinson, G., & Quinn, T. 2007, ApJ, 655, L17

Bruzual, G., & Charlot, S. 2003, MNRAS, 344, 1000

Bruzual A., G. 1983, ApJ, 273, 105

Bruzual A., G., & Charlot, S. 1993, ApJ, 405, 538

Buzzoni, A. 1989, ApJS, 71, 817

Catinella, B., et al. 2010, MNRAS, 403, 683

Cen, R., & Fang, T. 2006, ApJ, 650, 573

Cen, R., Miralda-Escudé, J., Ostriker, J. P., & Rauch, M. 1994, ApJ, 437, L9

Chabrier, G. 2003, PASP, 115, 763

Charlot, S., & Fall, S. M. 2000, ApJ, 539, 718

Chartas, G., Brandt, W. N., Gallagher, S. C., & Garmire, G. P. 2002, ApJ, 579, 169

Commerçon, B., Hennebelle, P., Audit, E., Chabrier, G., & Teyssier, R. 2008, A&A, 482, 371

Conroy, C., & Gunn, J. E. 2010, ApJ, 712, 833

Conroy, C., Gunn, J. E., & White, M. 2009, ApJ, 699, 486

Conroy, C., & Wechsler, R. H. 2009, ApJ, 696, 620

Conroy, C., Wechsler, R. H., & Kravtsov, A. V. 2006, ApJ, 647, 201

Conroy, C., White, M., & Gunn, J. E. 2010, ApJ, 708, 58

Courteau, S., Dutton, A. A., van den Bosch, F. C., MacArthur, L. A., Dekel, A., McIntosh, D. H., & Dale, D. A. 2007, ApJ, 671, 203

Cox, T. J., Dutta, S. N., Di Matteo, T., Hernquist, L., Hopkins, P. F., Robertson, B., & Springel, V. 2006a, ApJ, 650, 791

Cox, T. J., Jonsson, P., Primack, J. R., & Somerville, R. S. 2006b, MNRAS, 373, 1013

Crain, R. A., et al. 2009, MNRAS, 399, 1773

Crenshaw, D. M., & Kraemer, S. B. 2000, ApJ, 532, L101

Cresci, G., et al. 2009, ApJ, 697, 115

Croft, R. A. C., Di Matteo, T., Springel, V., & Hernquist, L. 2009, MNRAS, 400, 43

Croton, D. J., et al. 2006, MNRAS, 365, 11

Cucciati, O., Tresse, L., Ilbert, O., Le Fèvre, O., Garilli, B., & Le Brun, V. 2012, A&A, 539, A31

Daddi, E., et al. 2007, ApJ, 670, 156

Dalla Vecchia, C., & Schaye, J. 2008, MNRAS, 387, 1431

—. 2012, MNRAS, 426, 140

Danovich, M., Dekel, A., Hahn, O., & Teyssier, R. 2012, MNRAS, 422, 1732

Davé, R., Finlator, K., & Oppenheimer, B. D. 2006, ArXiv Astrophysics e-prints

—. 2011a, MNRAS, 416, 1354

Davé, R., Oppenheimer, B. D., & Finlator, K. 2011b, MNRAS, 415, 11

Davidzon, I., et al. 2013, A&A, 558, A23

Davis, M., et al. 2003, in Society of Photo-Optical Instrumentation Engineers (SPIE) Conference Series, Vol. 4834, Society of Photo-Optical Instrumentation Engineers (SPIE) Conference Series, ed. P. Guhathakurta, 161–172

de Rossi, M. E., Tissera, P. B., & Pedrosa, S. E. 2010, A&A, 519, A89

—. 2012, A&A, 546, A52

de Rossi, M. E., Tissera, P. B., & Scannapieco, C. 2007, MNRAS, 374, 323

Debuhr, J., Quataert, E., & Ma, C.-P. 2011, MNRAS, 412, 1341

Dekel, A., & Silk, J. 1986, ApJ, 303, 39

Di Matteo, T., Colberg, J., Springel, V., Hernquist, L., & Sijacki, D. 2008, ApJ, 676, 33

Di Matteo, T., Springel, V., & Hernquist, L. 2005, Nature, 433, 604

D'Onghia, E., Vogelsberger, M., Faucher-Giguere, C., & Hernquist, L. 2010, ApJ, 725, 353

Dopita, M. A., et al. 2005, ApJ, 619, 755

—. 2006a, ApJ, 647, 244

—. 2006b, ApJS, 167, 177

Drory, N., Bender, R., & Hopp, U. 2004, ApJ, 616, L103

Dubois, Y., Devriendt, J., Slyz, A., & Teyssier, R. 2012, MNRAS, 420, 2662

Dubois, Y., & Teyssier, R. 2008, A&A, 477, 79

Dutton, A. A., van den Bosch, F. C., & Dekel, A. 2010, MNRAS, 405, 1690

Dutton, A. A., van den Bosch, F. C., Dekel, A., & Courteau, S. 2007, ApJ, 654, 27

Edmunds, M. G. 1990, MNRAS, 246, 678

Ekta, B., & Chengalur, J. N. 2010, MNRAS, 406, 1238

Elbaz, D., et al. 2007, A&A, 468, 33

Ellison, S. L., Patton, D. R., Simard, L., & McConnachie, A. W. 2008, AJ, 135, 1877

Erb, D. K., Shapley, A. E., Pettini, M., Steidel, C. C., Reddy, N. A., & Adelberger, K. L. 2006a, ApJ, 644, 813

Erb, D. K., Steidel, C. C., Shapley, A. E., Pettini, M., Reddy, N. A., & Adelberger, K. L. 2006b, ApJ, 646, 107

Faber, S. M., et al. 2007, ApJ, 665, 265

Fall, S. M. 1983, in IAU Symposium, Vol. 100, Internal Kinematics and Dynamics of Galaxies, ed. E. Athanassoula, 391–398

Fall, S. M., & Efstathiou, G. 1980, MNRAS, 193, 189

Faucher-Giguère, C.-A., Lidz, A., Hernquist, L., & Zaldarriaga, M. 2008a, ApJ, 688, 85

Faucher-Giguère, C.-A., Lidz, A., Zaldarriaga, M., & Hernquist, L. 2009, ApJ, 703, 1416

Faucher-Giguère, C.-A., Prochaska, J. X., Lidz, A., Hernquist, L., & Zaldarriaga, M. 2008b, ApJ, 681, 831

Ferland, G. J., Korista, K. T., Verner, D. A., Ferguson, J. W., Kingdon, J. B., & Verner, E. M. 1998, PASP, 110, 761

Ferland, G. J., et al. 2013, Rev. Mexicana Astron. Astrofis., 49, 137

Few, C. G., Gibson, B. K., Courty, S., Michel-Dansac, L., Brook, C. B., & Stinson, G. S. 2012, A&A, 547, A63

Font, A. S., McCarthy, I. G., Crain, R. A., Theuns, T., Schaye, J., Wiersma, R. P. C., & Dalla Vecchia, C. 2011, MNRAS, 416, 2802

Fosalba, P., Gaztañaga, E., Castander, F. J., & Manera, M. 2008, MNRAS, 391, 435

Frenk, C. S., et al. 1999, ApJ, 525, 554

Gabasch, A., et al. 2004, A&A, 421, 41

Gabor, J. M., Davé, R., Oppenheimer, B. D., & Finlator, K. 2011, MNRAS, 417, 2676

Gallazzi, A., & Bell, E. F. 2009, ApJS, 185, 253

Genel, S. 2014, in prep

Genel, S., Vogelsberger, M., Nelson, D., Sijacki, D., Springel, V., & Hernquist, L. 2013, MNRAS, 435, 1426

Genel, S., et al. 2008, ApJ, 688, 789

Giallongo, E., Salimbeni, S., Menci, N., Zamorani, G., Fontana, A., Dickinson, M., Cristiani, S., & Pozzetti, L. 2005, ApJ, 622, 116

Gnerucci, A., et al. 2011, A&A, 528, A88

González, V., Labbé, I., Bouwens, R. J., Illingworth, G., Franx, M., Kriek, M., & Brammer, G. B. 2010, ApJ, 713, 115

Governato, F., Willman, B., Mayer, L., Brooks, A., Stinson, G., Valenzuela, O., Wadsley, J., & Quinn, T. 2007, MNRAS, 374, 1479

Governato, F., et al. 2004, ApJ, 607, 688

—. 2010, Nature, 463, 203

Groves, B., Dopita, M. A., Sutherland, R. S., Kewley, L. J., Fischera, J., Leitherer, C., Brandl, B., & van Breugel, W. 2008, ApJS, 176, 438

Groves, B. A., Dopita, M. A., & Sutherland, R. S. 2004a, ApJS, 153, 9

—. 2004b, ApJS, 153, 75

Guedes, J., Callegari, S., Madau, P., & Mayer, L. 2011, ApJ, 742, 76

Guo, Q., White, S., Angulo, R. E., Henriques, B., Lemson, G., Boylan-Kolchin, M., Thomas, P., & Short, C. 2013, MNRAS, 428, 1351

Guo, Q., White, S., Li, C., & Boylan-Kolchin, M. 2010, MNRAS, 404, 1111

Guo, Q., et al. 2011, MNRAS, 413, 101

Hahn, O., Teyssier, R., & Carollo, C. M. 2010, MNRAS, 405, 274

Hatton, S., Devriendt, J. E. G., Ninin, S., Bouchet, F. R., Guiderdoni, B., & Vibert, D. 2003, MNRAS, 343, 75

Heckman, T. M., Lehnert, M. D., Strickland, D. K., & Armus, L. 2000, ApJS, 129, 493

Henriques, B., Maraston, C., Monaco, P., Fontanot, F., Menci, N., De Lucia, G., & Tonini, C. 2011, MNRAS, 415, 3571

Henriques, B. M. B., White, S. D. M., Lemson, G., Thomas, P. A., Guo, Q., Marleau, G.-D., & Overzier, R. A. 2012, MNRAS, 421, 2904

Henriques, B. M. B., White, S. D. M., Thomas, P. A., Angulo, R. E., Guo, Q., Lemson, G., & Springel, V. 2013, MNRAS, 431, 3373

Hernquist, L. 1990, ApJ, 356, 359

Hernquist, L., & Katz, N. 1989, ApJS, 70, 419

Hernquist, L., Katz, N., Weinberg, D. H., & Miralda-Escudé, J. 1996, ApJ, 457, L51

Hernquist, L., & Springel, V. 2003, MNRAS, 341, 1253

Heß, S., & Springel, V. 2010, MNRAS, 406, 2289

Hobbs, A., Read, J., Power, C., & Cole, D. 2012, ArXiv e-prints

Hoeft, M., Yepes, G., Gottlöber, S., & Springel, V. 2006, MNRAS, 371, 401

Hopkins, A. M., & Beacom, J. F. 2006, ApJ, 651, 142

Hopkins, P. F. 2013, MNRAS, 428, 2840

Hopkins, P. F., Cox, T. J., Dutta, S. N., Hernquist, L., Kormendy, J., & Lauer, T. R. 2009a, ApJS, 181, 135

Hopkins, P. F., Cox, T. J., Hernquist, L., Narayanan, D., Hayward, C. C., & Murray, N. 2013a, MNRAS, 430, 1901

Hopkins, P. F., Cox, T. J., Kereš, D., & Hernquist, L. 2008a, ApJS, 175, 390

Hopkins, P. F., Cox, T. J., Younger, J. D., & Hernquist, L. 2009b, ApJ, 691, 1168

Hopkins, P. F., & Hernquist, L. 2006, ApJS, 166, 1

Hopkins, P. F., Hernquist, L., Cox, T. J., Di Matteo, T., Robertson, B., & Springel, V. 2006, ApJS, 163, 1

Hopkins, P. F., Hernquist, L., Cox, T. J., Dutta, S. N., & Rothberg, B. 2008b, ApJ, 679, 156

Hopkins, P. F., Hernquist, L., Cox, T. J., & Kereš, D. 2008c, ApJS, 175, 356

Hopkins, P. F., Hernquist, L., Cox, T. J., Robertson, B., & Krause, E. 2007a, ApJ, 669, 45

—. 2007b, ApJ, 669, 67

Hopkins, P. F., Kereš, D., Murray, N., Hernquist, L., Narayanan, D., & Hayward, C. C. 2013b, MNRAS, 433, 78

Hopkins, P. F., Lauer, T. R., Cox, T. J., Hernquist, L., & Kormendy, J. 2009c, ApJS, 181, 486

Hopkins, P. F., Quataert, E., & Murray, N. 2011, MNRAS, 417, 950

—. 2012a, MNRAS, 421, 3522

—. 2012b, MNRAS, 421, 3488

Ilbert, O., Tresse, L., Zucca, E., & et al. 2005, A&A, 439, 863

Iono, D., Yun, M. S., & Mihos, J. C. 2004, ApJ, 616, 199

Jonsson, P. 2006, MNRAS, 372, 2

Jonsson, P., Groves, B. A., & Cox, T. J. 2010, MNRAS, 403, 17

Joung, M. R., Bryan, G. L., & Putman, M. E. 2012, ApJ, 745, 148

Jungwiert, B., Combes, F., & Palouš, J. 2001, A&A, 376, 85

Kang, X., Jing, Y. P., Mo, H. J., & Börner, G. 2005, ApJ, 631, 21

Kannan, R., Stinson, G. S., Macciò, A. V., Brook, C., Weinmann, S. M., Wadsley, J., & Couchman, H. M. P. 2014, MNRAS, 437, 3529

Karakas, A. I. 2010, MNRAS, 403, 1413

Karim, A., et al. 2011, ApJ, 730, 61

Katz, N., & Gunn, J. E. 1991, ApJ, 377, 365

Katz, N., Hernquist, L., & Weinberg, D. H. 1992, ApJ, 399, L109

Katz, N., Weinberg, D. H., & Hernquist, L. 1996, ApJS, 105, 19

Kauffmann, G., Colberg, J. M., Diaferio, A., & White, S. D. M. 1999, MNRAS, 303, 188

Kauffmann, G., et al. 2003, MNRAS, 341, 33

Kaufmann, T., Mayer, L., Wadsley, J., Stadel, J., & Moore, B. 2006, MNRAS, 370, 1612

—. 2007, MNRAS, 375, 53

Kawata, D. 2001, ApJ, 558, 598

Kawata, D., & Gibson, B. K. 2003, MNRAS, 340, 908

—. 2005, MNRAS, 358, L16

Kennicutt, Jr., R. C. 1998, ApJ, 498, 541

Kereš, D., & Hernquist, L. 2009, ApJ, 700, L1

Kereš, D., Katz, N., Fardal, M., Davé, R., & Weinberg, D. H. 2009, MNRAS, 395, 160

Kereš, D., Katz, N., Weinberg, D. H., & Davé, R. 2005, MNRAS, 363, 2

Kereš, D., Vogelsberger, M., Sijacki, D., Springel, V., & Hernquist, L. 2012, MNRAS, 425, 2027

Keshet, U., Waxman, E., Loeb, A., Springel, V., & Hernquist, L. 2003, ApJ, 585, 128

Kewley, L. J., & Ellison, S. L. 2008, ApJ, 681, 1183

Kewley, L. J., Geller, M. J., & Barton, E. J. 2006, AJ, 131, 2004

Kewley, L. J., Rupke, D., Jabran Zahid, H., Geller, M. J., & Barton, E. J. 2010, ApJ, 721, L48

Khandai, N., Di Matteo, T., Croft, R., Wilkins, S. M., Feng, Y., Tucker, E., DeGraf, C., & Liu, M.-S. 2014, ArXiv e-prints 1402.0888

Kim, J., Wise, J. H., & Abel, T. 2009, ApJ, 694, L123

Kitzbichler, M. G., & White, S. D. M. 2007, MNRAS, 376, 2

Klypin, A. A., Trujillo-Gomez, S., & Primack, J. 2011, ApJ, 740, 102

Kobayashi, C., Springel, V., & White, S. D. M. 2007, MNRAS, 376, 1465

Kobulnicky, H. A., & Kewley, L. J. 2004, ApJ, 617, 240

Komatsu, E., et al. 2011, ApJS, 192, 18

Kriek, M., van Dokkum, P. G., Labbé, I., Franx, M., Illingworth, G. D., Marchesini, D., & Quadri, R. F. 2009, ApJ, 700, 221

Kurosawa, R., & Proga, D. 2009, MNRAS, 397, 1791

Laor, A., Fiore, F., Elvis, M., Wilkes, B. J., & McDowell, J. C. 1997, ApJ, 477, 93

Le Borgne, D., Rocca-Volmerange, B., Prugniel, P., Lançon, A., Fioc, M., & Soubiran, C. 2004, A&A, 425, 881

Leitherer, C., Ortiz Otálvaro, P. A., Bresolin, F., Kudritzki, R.-P., Lo Faro, B., Pauldrach, A. W. A., Pettini, M., & Rix, S. A. 2010, ApJS, 189, 309

Leitherer, C., et al. 1999, ApJS, 123, 3

Leitner, S. N., & Kravtsov, A. V. 2011, ApJ, 734, 48

Lemson, G., & Springel, V. 2006, in Astronomical Society of the Pacific Conference Series, Vol. 351, Astronomical Data Analysis Software and Systems XV, ed. C. Gabriel, C. Arviset, D. Ponz, & S. Enrique, 212

Lequeux, J., Peimbert, M., Rayo, J. F., Serrano, A., & Torres-Peimbert, S. 1979, A&A, 80, 155

Lia, C., Portinari, L., & Carraro, G. 2002, MNRAS, 330, 821

Lilly, S. J., Le Fevre, O., Hammer, F., & Crampton, D. 1996, ApJ, 460, L1

Lintott, C. J., et al. 2008, MNRAS, 389, 1179

Lotz, J. M., Jonsson, P., Cox, T. J., & Primack, J. R. 2008, MNRAS, 391, 1137

Lupton, R., Blanton, M. R., Fekete, G., Hogg, D. W., O'Mullane, W., Szalay, A., & Wherry, N. 2004, PASP, 116, 133

MacArthur, L. A., Courteau, S., Bell, E., & Holtzman, J. A. 2004, ApJS, 152, 175

Madau, P., Pozzetti, L., & Dickinson, M. 1998, ApJ, 498, 106

Maiolino, R., et al. 2008, A&A, 488, 463

Maller, A. H., & Dekel, A. 2002, MNRAS, 335, 487

Maraston, C. 1998, MNRAS, 300, 872

—. 2005, MNRAS, 362, 799

Marchesini, D., van Dokkum, P. G., Förster Schreiber, N. M., Franx, M., Labbé, I., & Wuyts, S. 2009, ApJ, 701, 1765

Marchesini, D., et al. 2007, ApJ, 656, 42

—. 2010, ApJ, 725, 1277

Marinacci, F., Binney, J., Fraternali, F., Nipoti, C., Ciotti, L., & Londrillo, P. 2010, MNRAS, 404, 1464

Marinacci, F., Pakmor, R., & Springel, V. 2014, MNRAS, 437, 1750

Marri, S., & White, S. D. M. 2003, MNRAS, 345, 561

Martin, C. L. 2005, ApJ, 621, 227

Martínez-Serrano, F. J., Serna, A., Domínguez-Tenreiro, R., & Mollá, M. 2008, MNRAS, 388, 39

McCarthy, I. G., Font, A. S., Crain, R. A., Deason, A. J., Schaye, J., & Theuns, T. 2012a, MNRAS, 420, 2245

McCarthy, I. G., Schaye, J., Font, A. S., Theuns, T., Frenk, C. S., Crain, R. A., & Dalla Vecchia, C. 2012b, MNRAS, 427, 379

McCarthy, I. G., et al. 2010, MNRAS, 406, 822

McGee, S. L., & Balogh, M. L. 2010, MNRAS, 403, L79

McKee, C. F., & Ostriker, J. P. 1977, ApJ, 218, 148

McQuinn, M., Lidz, A., Zaldarriaga, M., Hernquist, L., Hopkins, P. F., Dutta, S., & Faucher-Giguère, C.-A. 2009, ApJ, 694, 842

Michałowski, M. J., Dunlop, J. S., Cirasuolo, M., Hjorth, J., Hayward, C. C., & Watson, D. 2012, A&A, 541, A85

Michalowski et al. 2014, in prep

Michel-Dansac, L., Lambas, D. G., Alonso, M. S., & Tissera, P. 2008, MNRAS, 386, L82

Mihos, J. C., & Hernquist, L. 1994a, ApJ, 437, L47

—. 1994b, ApJ, 431, L9

—. 1996, ApJ, 464, 641

Miller, S. H., Bundy, K., Sullivan, M., Ellis, R. S., & Treu, T. 2011, ApJ, 741, 115

Miller, S. H., Ellis, R. S., Sullivan, M., Bundy, K., Newman, A. B., & Treu, T. 2012, ApJ, 753, 74

Miller, S. H., Sullivan, M., & Ellis, R. S. 2013, ApJ, 762, L11

Mitchell, P. D., Lacey, C. G., Baugh, C. M., & Cole, S. 2013, MNRAS, 435, 87

Mo, H. J., Mao, S., & White, S. D. M. 1998, MNRAS, 295, 319

Montuori, M., Di Matteo, P., Lehnert, M. D., Combes, F., & Semelin, B. 2010, A&A, 518, A56

Mortlock, A., Conselice, C. J., Bluck, A. F. L., Bauer, A. E., Grützbauch, R., Buitrago, F., & Ownsworth, J. 2011, MNRAS, 413, 2845

Moster, B. P., Naab, T., & White, S. D. M. 2013, MNRAS, 428, 3121

Moster, B. P., Somerville, R. S., Maulbetsch, C., van den Bosch, F. C., Macciò, A. V., Naab, T., & Oser, L. 2010, ApJ, 710, 903

Murali, C., Katz, N., Hernquist, L., Weinberg, D. H., & Davé, R. 2002, ApJ, 571, 1

Murante, G., Giovalli, M., Gerhard, O., Arnaboldi, M., Borgani, S., & Dolag, K. 2007, MNRAS, 377, 2

Murante, G., et al. 2004, ApJ, 607, L83

Navarro, J. F., & Benz, W. 1991, ApJ, 380, 320

Navarro, J. F., & Steinmetz, M. 1997, ApJ, 478, 13

Navarro, J. F., & White, S. D. M. 1994, MNRAS, 267, 401

Nelson, D., Vogelsberger, M., Genel, S., Sijacki, D., Kereš, D., Springel, V., & Hernquist, L. 2013, MNRAS, 429, 3353

Nicholls, D. C., Dopita, M. A., Sutherland, R. S., Kewley, L. J., & Palay, E. 2013, ApJS, 207, 21

Noeske, K. G., Weiner, B. J., Faber, S. M., & et, a. 2007, ApJ, 660, L43

Ocvirk, P., Pichon, C., & Teyssier, R. 2008, MNRAS, 390, 1326

Oey, M. S. 2003, in IAU Symposium, Vol. 212, A Massive Star Odyssey: From Main Sequence to Supernova, ed. K. van der Hucht, A. Herrero, & C. Esteban, 620–+

Okamoto, T., Eke, V. R., Frenk, C. S., & Jenkins, A. 2005, MNRAS, 363, 1299

Okamoto, T., Frenk, C. S., Jenkins, A., & Theuns, T. 2010, MNRAS, 406, 208

Okamoto, T., Jenkins, A., Eke, V. R., Quilis, V., & Frenk, C. S. 2003, MNRAS, 345, 429

Okamoto, T., Nemmen, R. S., & Bower, R. G. 2008, MNRAS, 385, 161

Ono, Y., Ouchi, M., Shimasaku, K., Dunlop, J., Farrah, D., McLure, R., & Okamura, S. 2010, ApJ, 724, 1524

Oppenheimer, B. D., & Davé, R. 2006, MNRAS, 373, 1265

—. 2008, MNRAS, 387, 577

Oppenheimer, B. D., Davé, R., & Finlator, K. 2009, MNRAS, 396, 729

Oppenheimer, B. D., Davé, R., Kereš, D., Fardal, M., Katz, N., Kollmeier, J. A., & Weinberg, D. H. 2010, MNRAS, 406, 2325

O'Shea, B. W., Nagamine, K., Springel, V., Hernquist, L., & Norman, M. L. 2005, ApJS, 160, 1

Overzier, R., Lemson, G., Angulo, R. E., Bertin, E., Blaizot, J., Henriques, B. M. B., Marleau, G.-D., & White, S. D. M. 2013, MNRAS, 428, 778

Papovich, C., Dickinson, M., & Ferguson, H. C. 2001, ApJ, 559, 620

Patton, D. R., Torrey, P., Ellison, S. L., Mendel, J. T., & Scudder, J. M. 2013, MNRAS, 433, L59

Peeples, M. S., Pogge, R. W., & Stanek, K. Z. 2009, ApJ, 695, 259

Peng, Y.-j., et al. 2010, ApJ, 721, 193

Perez, J., Michel-Dansac, L., & Tissera, P. B. 2011, MNRAS, 417, 580

Perez, M. J., Tissera, P. B., Scannapieco, C., Lambas, D. G., & de Rossi, M. E. 2006, A&A, 459, 361

Pérez-González, P. G., et al. 2008, ApJ, 675, 234

Pettini, M., & Pagel, B. E. J. 2004, MNRAS, 348, L59

Pierini, D., Maraston, C., Gordon, K. D., & Witt, A. N. 2005, MNRAS, 363, 131

Planck Collaboration et al. 2013, ArXiv e-prints 1303.5076

Poli, F., et al. 2003, ApJ, 593, L1

Portinari, L., Chiosi, C., & Bressan, A. 1998, A&A, 334, 505

Portinari, L., & Sommer-Larsen, J. 2007, MNRAS, 375, 913

Pounds, K. A., Reeves, J. N., King, A. R., Page, K. L., O'Brien, P. T., & Turner, M. J. L. 2003, MNRAS, 345, 705

Price, D. J. 2008, Journal of Computational Physics, 227, 10040

Puchwein, E., & Springel, V. 2013, MNRAS, 428, 2966

Puchwein, E., Springel, V., Sijacki, D., & Dolag, K. 2010, MNRAS, 406, 936

Puech, M., et al. 2008, A&A, 484, 173

Quinn, T., Katz, N., & Efstathiou, G. 1996, MNRAS, 278, L49

Rahmati, A., Pawlik, A. H., Raičevič, M., & Schaye, J. 2013, MNRAS, 430, 2427

Read, J. I., & Hayfield, T. 2012, MNRAS, 422, 3037

Read, J. I., Hayfield, T., & Agertz, O. 2010, MNRAS, 405, 1513

Reeves, J. N., O'Brien, P. T., & Ward, M. J. 2003, ApJ, 593, L65

Reyes, R., Mandelbaum, R., Gunn, J. E., Pizagno, J., & Lackner, C. N. 2011, MNRAS, 417, 2347

Rich, J. A., Dopita, M. A., Kewley, L. J., & Rupke, D. S. N. 2010, ApJ, 721, 505

Rich, J. A., Torrey, P., Kewley, L. J., Dopita, M. A., & Rupke, D. S. N. 2012, ApJ, 753, 5

Ritchie, B. W., & Thomas, P. A. 2001, MNRAS, 323, 743

Robertson, B., Bullock, J. S., Cox, T. J., Di Matteo, T., Hernquist, L., Springel, V., & Yoshida, N. 2006a, ApJ, 645, 986

Robertson, B., Cox, T. J., Hernquist, L., Franx, M., Hopkins, P. F., Martini, P., & Springel, V. 2006b, ApJ, 641, 21

Robertson, B., Hernquist, L., Cox, T. J., Di Matteo, T., Hopkins, P. F., Martini, P., & Springel, V. 2006c, ApJ, 641, 90

Robertson, B., Yoshida, N., Springel, V., & Hernquist, L. 2004, ApJ, 606, 32

Robotham, A. S. G., & Driver, S. P. 2011, MNRAS, 413, 2570

Rubin, V. C., Ford, Jr., W. K., & Whitmore, B. C. 1984, ApJ, 281, L21

Rudick, C. S., Mihos, J. C., & McBride, C. 2006, ApJ, 648, 936

Rujopakarn, W., et al. 2010, ApJ, 718, 1171

Rupke, D. S., Veilleux, S., & Sanders, D. B. 2002, ApJ, 570, 588

—. 2005a, ApJS, 160, 87

—. 2005b, ApJS, 160, 115

Rupke, D. S. N., Kewley, L. J., & Barnes, J. E. 2010a, ApJ, 710, L156

Rupke, D. S. N., Kewley, L. J., & Chien, L.-H. 2010b, ApJ, 723, 1255

Rupke, D. S. N., Veilleux, S., & Baker, A. J. 2008, ApJ, 674, 172

Saitoh, T. R., & Makino, J. 2013, ApJ, 768, 44

Sales, L. V., Navarro, J. F., Theuns, T., Schaye, J., White, S. D. M., Frenk, C. S., Crain, R. A., & Dalla Vecchia, C. 2012, MNRAS, 423, 1544

Salim, S., et al. 2007, ApJS, 173, 267

Salmi, F., Daddi, E., Elbaz, D., Sargent, M. T., Dickinson, M., Renzini, A., Bethermin, M., & Le Borgne, D. 2012, ApJ, 754, L14

Santini, P., et al. 2012, A&A, 538, A33

Savaglio, S., et al. 2005, ApJ, 635, 260

Scalo, J., & Elmegreen, B. G. 2004, ARA&A, 42, 275

Scannapieco, C., Gadotti, D. A., Jonsson, P., & White, S. D. M. 2010, MNRAS, 407, L41

Scannapieco, C., Tissera, P. B., White, S. D. M., & Springel, V. 2005, MNRAS, 364, 552

—. 2008, MNRAS, 389, 1137

Scannapieco, C., et al. 2012, MNRAS, 423, 1726

Schaerer, D., & de Barros, S. 2009, A&A, 502, 423

Schaye, J., et al. 2010, MNRAS, 402, 1536

Schechter, P. 1976, ApJ, 203, 297

Schiminovich, D., et al. 2005, ApJ, 619, L47

Schmidt, M. 1959, ApJ, 129, 243

Scudder, J. M., Ellison, S. L., Torrey, P., Patton, D. R., & Mendel, J. T. 2012, MNRAS, 426, 549

Shen, S., Madau, P., Guedes, J., Mayer, L., Prochaska, J. X., & Wadsley, J. 2013, ApJ, 765, 89

Shen, S., Wadsley, J., & Stinson, G. 2010, MNRAS, 407, 1581

Shields, G. A. 1990, ARA&A, 28, 525

Sijacki, D., & Springel, V. 2006, MNRAS, 366, 397

Sijacki, D., Springel, V., Di Matteo, T., & Hernquist, L. 2007, MNRAS, 380, 877

Sijacki, D., Springel, V., & Haehnelt, M. G. 2009, MNRAS, 400, 100

Sijacki, D., Vogelsberger, M., Kereš, D., Springel, V., & Hernquist, L. 2012, MNRAS, 424, 2999

Silk, J. 1997, ApJ, 481, 703

Smolčić, V., et al. 2009, ApJ, 690, 610

Snyder, G. F., Cox, T. J., Hayward, C. C., Hernquist, L., & Jonsson, P. 2011, ApJ, 741, 77

Snyder, G. F., Hayward, C. C., Sajina, A., Jonsson, P., Cox, T. J., Hernquist, L., Hopkins, P. F., & Yan, L. 2013, ApJ, 768, 168

Snyder et al. 2014, in prep

Sol Alonso, M., Michel-Dansac, L., & Lambas, D. G. 2010, A&A, 514, A57+

Somerville, R. S., Gilmore, R. C., Primack, J. R., & Domínguez, A. 2012, MNRAS, 423, 1992

Somerville, R. S., Hopkins, P. F., Cox, T. J., Robertson, B. E., & Hernquist, L. 2008, MNRAS, 391, 481

Sommer-Larsen, J., Götz, M., & Portinari, L. 2003, ApJ, 596, 47

Spergel, D. N., et al. 2003, ApJS, 148, 175

Springel, V. 2005, MNRAS, 364, 1105

—. 2010a, MNRAS, 401, 791

—. 2010b, ARA&A, 48, 391

Springel, V., Di Matteo, T., & Hernquist, L. 2005a, ApJ, 620, L79

—. 2005b, MNRAS, 361, 776

Springel, V., & Hernquist, L. 2002, MNRAS, 333, 649

—. 2003a, MNRAS, 339, 289

—. 2003b, MNRAS, 339, 312

Springel, V., White, M., & Hernquist, L. 2001, ApJ, 549, 681

Springel, V., & White, S. D. M. 1999, MNRAS, 307, 162

Springel, V., et al. 2005c, Nature, 435, 629

Stark, D. P., Ellis, R. S., Bunker, A., Bundy, K., Targett, T., Benson, A., & Lacy, M. 2009, ApJ, 697, 1493

Stark, D. P., Schenker, M. A., Ellis, R., Robertson, B., McLure, R., & Dunlop, J. 2013, ApJ, 763, 129

Steinmetz, M., & Mueller, E. 1994, A&A, 281, L97

Steinmetz, M., & Navarro, J. F. 1999, ApJ, 513, 555

Stinson, G., Seth, A., Katz, N., Wadsley, J., Governato, F., & Quinn, T. 2006, MNRAS, 373, 1074

Stinson, G. S., Brook, C., Macciò, A. V., Wadsley, J., Quinn, T. R., & Couchman, H. M. P. 2013, MNRAS, 428, 129

Sutherland, R. S., & Dopita, M. A. 1993, ApJS, 88, 253

Tacconi, L. J., et al. 2010, Nature, 463, 781

Tassis, K., Kravtsov, A. V., & Gnedin, N. Y. 2008, ApJ, 672, 888

Tepper-García, T., Richter, P., Schaye, J., Booth, C. M., Dalla Vecchia, C., & Theuns, T. 2012, MNRAS, 425, 1640

Tepper-García, T., Richter, P., Schaye, J., Booth, C. M., Dalla Vecchia, C., Theuns, T., & Wiersma, R. P. C. 2011, MNRAS, 413, 190

Teyssier, R. 2002, A&A, 385, 337

Teyssier, R., et al. 2009, A&A, 497, 335

Thacker, R. J., & Couchman, H. M. P. 2000, ApJ, 545, 728

—. 2001, ApJ, 555, L17

Thacker, R. J., Scannapieco, E., & Couchman, H. M. P. 2006, ApJ, 653, 86

Theuns, T., Leonard, A., Efstathiou, G., Pearce, F. R., & Thomas, P. A. 1998, MNRAS, 301, 478

Thielemann, F.-K., Nomoto, K., & Yokoi, K. 1986, A&A, 158, 17

Thomas, D., Maraston, C., & Bender, R. 2003, MNRAS, 339, 897

Tinsley, B. M. 1972, ApJ, 178, 319

Tittley, E. R., Pearce, F. R., & Couchman, H. M. P. 2001, ApJ, 561, 69

Toomre, A., & Toomre, J. 1972, ApJ, 178, 623

Tornatore, L., Borgani, S., Dolag, K., & Matteucci, F. 2007, MNRAS, 382, 1050

Torrey, P., Vogelsberger, M., Genel, S., Sijacki, D., Springel, V., & Hernquist, L. 2014, MNRAS, 438, 1985

Torrey, P., Vogelsberger, M., Sijacki, D., Springel, V., & Hernquist, L. 2012, MNRAS, 427, 2224

Tremonti, C. A., Moustakas, J., & Diamond-Stanic, A. M. 2007, ApJ, 663, L77

Tremonti, C. A., et al. 2004, ApJ, 613, 898

Tuffs, R. J., Popescu, C. C., Völk, H. J., Kylafis, N. D., & Dopita, M. A. 2004, A&A, 419, 821

Tully, R. B., & Fisher, J. R. 1977, A&A, 54, 661

Uhlig, M., Pfrommer, C., Sharma, M., Nath, B. B., Enßlin, T. A., & Springel, V. 2012, MNRAS, 423, 2374

Vale, A., & Ostriker, J. P. 2004, MNRAS, 353, 189

van de Voort, F., & Schaye, J. 2012a, MNRAS, 2882

—. 2012b, MNRAS, 423, 2991

van de Voort, F., Schaye, J., Altay, G., & Theuns, T. 2012, MNRAS, 421, 2809

van de Voort, F., Schaye, J., Booth, C. M., Haas, M. R., & Dalla Vecchia, C. 2011, MNRAS, 414, 2458

van den Bosch, F. C. 2000, ApJ, 530, 177

—. 2002, MNRAS, 332, 456

van der Burg, R. F. J., Hildebrandt, H., & Erben, T. 2010, A&A, 523, A74

Vázquez, G. A., & Leitherer, C. 2005, ApJ, 621, 695

Veilleux, S., Cecil, G., & Bland-Hawthorn, J. 2005, ARA&A, 43, 769

Vergani, D., et al. 2012, A&A, 546, A118

Villar, V., Gallego, J., Pérez-González, P. G., Pascual, S., Noeske, K., Koo, D. C., Barro, G., & Zamorano, J. 2008, ApJ, 677, 169

Vogelsberer et al. 2014, in prep

Vogelsberger, M., Genel, S., Sijacki, D., Torrey, P., Springel, V., & Hernquist, L. 2013, MNRAS, 436, 3031

Vogelsberger, M., Sijacki, D., Kereš, D., Springel, V., & Hernquist, L. 2012, MNRAS, 425, 3024

Wadsley, J. W., Veeravalli, G., & Couchman, H. M. P. 2008, MNRAS, 387, 427

Weil, M. L., Eke, V. R., & Efstathiou, G. 1998, MNRAS, 300, 773

Weinberg, D. H., Hernquist, L., & Katz, N. 1997, ApJ, 477, 8

Weinmann, S. M., Pasquali, A., Oppenheimer, B. D., Finlator, K., Mendel, J. T., Crain, R. A., & Macciò, A. V. 2012, MNRAS, 426, 2797

Whitaker, K. E., van Dokkum, P. G., Brammer, G., & Franx, M. 2012, ApJ, 754, L29

White, S. D. M., & Frenk, C. S. 1991, ApJ, 379, 52

White, S. D. M., & Rees, M. J. 1978, MNRAS, 183, 341

Wiersma, R. P. C., Schaye, J., & Smith, B. D. 2009a, MNRAS, 393, 99

Wiersma, R. P. C., Schaye, J., Theuns, T., Dalla Vecchia, C., & Tornatore, L. 2009b, MNRAS, 399, 574

Wild, V., Walcher, C. J., Johansson, P. H., Tresse, L., Charlot, S., Pollo, A., Le Fèvre, O., & de Ravel, L. 2009, MNRAS, 395, 144

Worthey, G. 1994, ApJS, 95, 107

Wuyts, S., et al. 2007, ApJ, 655, 51

Yoshida, M., et al. 2006, ApJ, 653, 988

Younger, J. D., Hopkins, P. F., Cox, T. J., & Hernquist, L. 2008, ApJ, 686, 815

Zackrisson, E., Bergvall, N., & Leitet, E. 2008, ApJ, 676, L9

Zahid, H. J., Dima, G. I., Kewley, L. J., Erb, D. K., & Davé, R. 2012, ApJ, 757, 54

Zahid, H. J., Geller, M. J., Kewley, L. J., Hwang, H. S., Fabricant, D. G., & Kurtz, M. J. 2013, ApJ, 771, L19

Zaritsky, D., Kennicutt, Jr., R. C., & Huchra, J. P. 1994, ApJ, 420, 87

Zhang, Y., Anninos, P., & Norman, M. L. 1995, ApJ, 453, L57

Zheng, X. Z., Dole, H., Bell, E. F., Le Floc'h, E., Rieke, G. H., Rix, H.-W., & Schiminovich, D. 2007, ApJ, 670, 301

Zibetti, S., White, S. D. M., Schneider, D. P., & Brinkmann, J. 2005, MNRAS, 358, 949